BOTTOM UP SYNTHESIS OF STRUCTURALLY PRECISE TWO-DIMENSIONAL POLYMERS FOR ORGANIC PHOTOVOLTAICS

A Dissertation

Presented to the Faculty of the Graduate School

of Cornell University

In Partial Fulfillment of the Requirements for the Degree of

Doctor of Philosophy

by

John William Colson

August 2014

BOTTOM UP SYNTHESIS OF STRUCTURALLY PRECISE TWO-DIMENSIONAL POLYMERS FOR ORGANIC PHOTOVOLTAICS

John William Colson, Ph. D.

Cornell University 2014

Abstract

Polymerization methods that provide linear or branched macromolecules with outstanding functional group tolerance and molecular weight control are well studied. In contrast, polymerization strategies that yield two-dimensional (2D) periodic structures remain in their infancy (Chapter 1). Two-dimensional covalent organic frameworks (COFs) are polymer networks that organize molecular building blocks into well-defined porous, layered structures linked by covalent bonds. These materials are usually synthesized as insoluble and unprocessable powders, limiting their utility in applications such as organic optoelectronics. This dissertation describes efforts to overcome the challenges associated with this powder morphology. Initially, COF films were prepared using single-layer graphene (SLG) as a substrate (Chapter 2) and these conditions generalized to a family of 2D COFs with tunable pore size (Chapter 3). Synthetic conditions were developed that provide access to patterned COFs (Chapter 4). COF films that incorporate semiconductors may serve as important precursors for organic optoelectronics. As proof-of-concept, organic photovoltaics fabricated using a variety of COF active-layers were fabricated and characterized (Chapter 5). These results provide a blueprint for incorporating COFs as materials in organic optoelectronic devices.

BIOGRAPHICAL SKETCH

Born and raised in Fort Worth, Texas, John spent his formative years as a musician playing piano and percussion. While attending the University of Oklahoma (Norman, Oklahoma) on an academic and music scholarship, John took an organic chemistry class which completely changed his life. He immediately joined the laboratory of Prof. Ronald Halterman to learn and develop as a synthetic chemist. Following two successful years in that lab, John spent a summer doing research at IBM Almaden Research Center in San Jose, California, where polymers stole his heart; the love affair continues to this day. After returning to the University of Oklahoma to graduate with a B.S. in Chemistry, *summa cum laude*, John abandoned the heat and took up residence in Ithaca, New York to attend Cornell University, where he joined the laboratory of Prof. William Dichtel as a member of his second cohort of graduate students. At Cornell, John has worked to develop porous polymers for applications in electronics. Following completion of his Ph.D. degree, John will join the laboratories of Prof. Matthew Tirrell and Prof. Paul Nealey at the University of Chicago as a postdoctoral fellow. When not in lab unlocking the secrets of the universe, John is an avid runner, with a personal best of 2 hours, 59 minutes, and 41 seconds in the marathon. He considers one of his proudest moments when he crossed the finish line at the 2013 Boston Marathon.

Dedicated to the victims, survivors, and first responders of the 2013 Boston Marathon.

You are always in my heart.

ACKNOWLEDGMENTS

I am indebted to my advisor, Prof. William Dichtel, whose mentorship and support have helped me to grow and flourish as a scientist. I would also like to thank the other members of my Ph.D. committee, Prof. Geoffrey Coates and Prof. Héctor Abruña, for their support and willingness to serve as members.

The work in this dissertation was highly collaborative, and I must thank all of my coauthors and collaborators in other departments including Dr. Arthur Woll (CHESS, Cornell), Mark Levendorf and Prof. Jiwoong Park (Chemistry, Cornell), Virgil Shields and Prof. Michael Spencer (Electrical Engineering, Cornell), as well as David Moore and Prof. Tobias Hanrath (Chemical Engineering, Cornell). I also had the opportunity to travel overseas and work with Florian Auras, Mona Calik, and Prof. Thomas Bein (Chemistry, LMU-Munich) without whom Chapter 5 would not exist.

Financial support for this work came from the NSF in the form of a Graduate Research Fellowship as well as awards CHE-1056657 and CHE-1124754. Additional support was provided by a Sloan Research Fellowship, the Arnold and Mabel Beckman Foundation, and the Research Corporation for Science Advancement.

This work leveraged the vast resources made available to researchers at Cornell through the CCMR (NSF DMR-1120296), the CNF (NSF ECCS-0335765) and CHESS (NSF DMR-0936384).

Finally, I would like to thank the Dichtel Research Group and all its members for the scientific partnerships, conversations, and adventure these past 5 years.

TABLE OF CONTENTS

LIST OF FIGURES

CHAPTER ONE

CHAPTER TWO

CHAPTER TWO - APPENDIX

CHAPTER THREE

CHAPTER THREE – APPENDIX

CHAPTER 1

RATIONALLY SYNTHESIZED TWO-DIMENSIONAL POLYMERS

Abstract

Synthetic polymers access diverse and useful property sets and influence most aspects of modern life. Many polymerization methods provide linear or branched macromolecules, frequently with outstanding functional group tolerance and molecular weight control. In contrast, extending polymerization strategies to two-dimensional periodic structures is in its infancy, and successful examples have emerged only recently through molecular framework, surface science, and crystal engineering approaches. This chapter describes successful 2D polymerization strategies, as well as seminal research that inspired their development. These methods include the synthesis of 2D covalent organic frameworks as layered crystals and thin films, surface-mediated polymerization of polyfunctional monomers, and solid-state topochemical polymerizations. Early application targets of 2D polymers include gas separation and storage, optoelectronic devices, and membranes, each of which might benefit from predictable long-range molecular organization inherent to this macromolecular architecture.

This chapter was first published in *Nature Chemistry*: Colson, J. W. & Dichtel, W.R. *Nature Chem.* **5,** 453 (2013) and is reproduced with permission.

Introduction

Synthetic polymers comprise most commercial products and are synthesized industrially on a hundred-million ton annual scale. Recently developed controlled polymerization methods[1-4] provide increasingly well-defined chain lengths, excellent functional group tolerance, and access to diverse block copolymer and novel architectures. In contrast, comparatively few polymerization methods provide periodic two-dimensional (2D) structures, a challenge that lies at the interface of polymer science and molecular self-assembly. Diverse strategies have emerged to synthesize and characterize 2D polymers from a disparate range of research traditions, including surface science, crystal engineering, scanning probe microscopy, and molecular frameworks. These advances will inspire further synthetic innovation, enable the first rigorous investigations of the properties unique to this topology, and finally provide a means for organic chemists to design within extended 2D and 3D space.

A 2D polymer is a covalently linked network of monomers with periodic bonding in two orthogonal directions. These polymers have been isolated in three forms: layered crystals, multilayer and monolayer[5-8] films on surfaces, and free-standing sheets. Individual or disordered 2D polymer sheets are a subset of 2D crystals, and periodic layered 2D polymers are three-dimensional crystals, in which covalent bonding is confined to two dimensions and noncovalent interactions direct their organization in the third. It should also be noted that multiple definitions of 2D polymers have been employed historically. The term “2D polymer” has been used more broadly to include linear polymerizations performed at interfaces or in layered noncovalent assemblies, or to irregularly cross-linked polymers confined to surfaces or

layered films. Each of these methods provides 2D objects that lack periodic bonding[9,10]. However, spatially confined polymerizations represent pioneering examples of controlled reactions within organized molecular assemblies, an important step towards 2D polymerization. The term "2D polymer" was also defined more restrictively to include only materials isolated as single sheets[11], a milestone that was achieved only recently[12]. We describe polymers with 2D topologies in all of the above isolated forms, just as we consider a linear polymer to be inherently one-dimensional whether it is found in the bulk, dissolved in solution, or isolated as an individual macromolecule. However, we consider 2D networks linked by coordination bonds or other noncovalent interactions to be outside the scope of this Review.

Graphite, graphene[13], and hexagonal boron nitride[14,15] are prototypical 2D polymers whose optical, electronic, and mechanical properties have attracted intense contemporary interest. These materials feature distinct properties from other 2D materials, such as ionic 2D crystals[16], as a result of their covalent bonding. These 2D polymers are prepared via exfoliation[17], epitaxial growth[18], or pyrolytic decomposition[19,20] techniques, which preclude rational modification of their structure. A wide variety of nanometer-size graphene fragments[21] have also been synthesized using both top-down and bottom-up approaches. Structurally precise "nanographenes"[22], the largest of which contains 222 carbon atoms[23], are derived from multistep synthetic pathways rather than a single polymerization reaction. Such approaches are likely to prove inefficient for preparing significantly larger systems. Nevertheless, these hydrocarbons are useful models of structurally precise graphene

subunits and exhibit desirable optoelectronic properties as a consequence of quantum confinement and their specific edge structure.

Although the properties of synthetic 2D polymers are only now being explored, they offer several features that distinguish them from linear macromolecules. For example, 2D polymers derive their topology from the directionality of their covalent linkages and offer a means to organize chemical functionality with atomic precision over long distances. In contrast, subtle changes in chemical structure can dramatically and unpredictably affect the solid-state structure of molecular compounds[24,25] and linear polymers[26-28]. Many noncovalent assemblies show similar structural order[29-32], but 2D polymers promise to be far more robust. The mechanical properties and stability of both free-standing 2D polymer sheets and their multilayer assemblies are as yet untested, but should reflect their covalently bonded structure, in contrast to the interchain interactions of entangled 1D polymers (Figure 1.1). 2D polymers also frequently feature permanent pores of defined size and shape, providing high specific surface areas and free volume suitable for postsynthetic functionalization. As such, they might prove useful as membranes and for filtration, molecular recognition and sensing, catalysis, optoelectronic devices, and many other applications that leverage specific molecular organization. Realizing these opportunities will require general and robust methods to synthesize, isolate, and characterize 2D polymers in their various forms.

Two-dimensional polymerizations are distinct from their linear counterparts in that they must precisely control monomer assembly before or during covalent bond formation. Otherwise, aperiodic, cross-linked networks are obtained. Two strategies

provide such control: Thermodynamic approaches perform monomer assembly and polymerization simultaneously under dynamic bond forming conditions (Figure 1.1c), providing 2D polymers commonly known as covalent organic frameworks (COFs). Kinetic approaches (Figure 1.1d) polymerize building blocks preorganized into 2D assemblies, and are thus compatible with irreversible reactions. Both approaches rely on shape-persistent monomers and directional interactions to enforce specific bonding geometries, and all existing examples employ an interface or layered crystal to template the formation of the desired 2D structure. This chapter describes emerging 2D polymerization methods and highlight important developments that influenced these approaches.

Thermodynamic Synthesis of 2D Polymers: Covalent Organic Frameworks

The most general existing 2D polymerization strategy provides layered periodic networks linked by covalent bonds known as covalent organic frameworks. COFs are synthesized by condensing appropriately designed monomers under reversible bond-forming conditions. The dimensionality (2D or 3D) and topology of the COF result from the shape of the monomers and the relative orientations of their reactive groups (Figure 1.2). COF synthesis is modular, as chemically distinct monomers provide identical network topologies provided that these design criteria are preserved. No other 2D polymerization strategy currently provides comparable scope and a straightforward means to predict and tune the network structure.

COF synthesis was informed by prior advances in other classes of framework materials and designed noncovalent assemblies. Seminal work by Lehn[33,34], Robson[35], Wuest[36,37], and Fujita[38] established the connection between network structure and

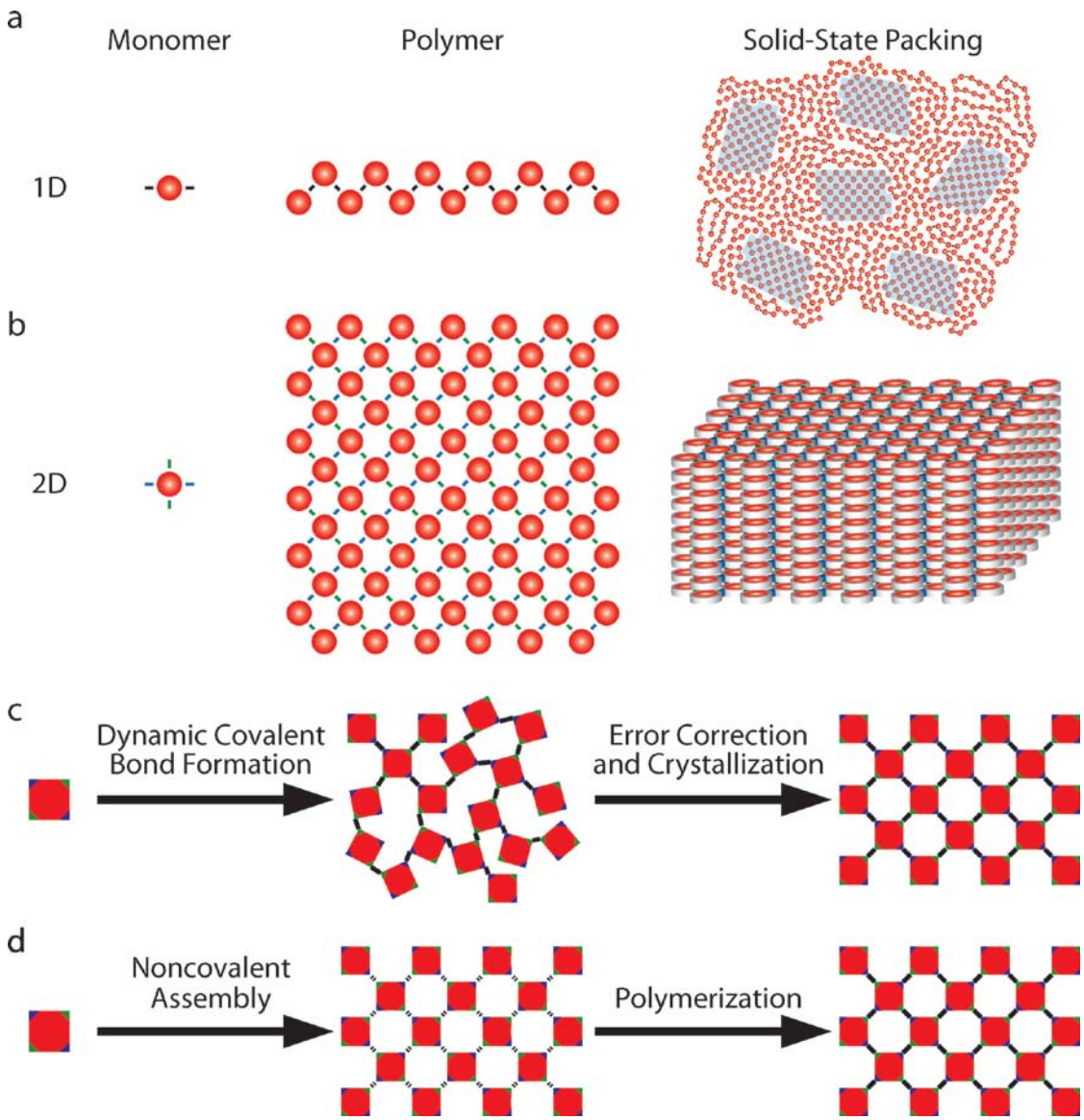

Figure 1.1 | Schematic illustration of the structures of **a)** one-dimensional and **b)** two-dimensional polymers and **(c,d)** strategies for 2D polymerization. **a)** Some 1D polymers pack into crystalline domains (blue shaded regions) within a disordered matrix while others are amorphous in the solid-state. **b)** 2D polymers can be isolated as multilayer crystals (shown) or as individual sheets. **c)** 2D polymerization under thermodynamic control, in which bond formation and crystallization occur simultaneously. **d)** 2D polymerization under kinetic control relies on monomer assembly prior to bond formation.

coordination geometry within 2D coordination networks, 3D coordination polymers, 3D hydrogen-bonded networks, and coordination cages, respectively. These concepts were elaborated to synthesize permanently porous 3D coordination polymers known

as metal-organic frameworks (MOFs)[39] or porous coordination polymers (PCPs)[40]. These high surface-area materials have attracted intense recent interest for gas storage, separation, and catalysis. The MOF/PCP approach has proven to be remarkably versatile, with thousands of new materials reported in the last decade[41-45].

One of the challenges of extending MOF design concepts to covalently linked polymers is that many organic functional groups do not undergo dynamic exchange processes as readily as coordination complexes, which typically possess lower bond strengths. COF synthesis relies on reversible covalent bond-forming reactions, such as condensations that furnish boroxines or imines. These and other equilibria have been used in various dynamic molecular and polymeric systems. Relevant examples include the concept of dynamic covalent chemistry[46], in which a single receptor is amplified from a complex, equilibrating mixture in the presence of a template, as well as in the syntheses of organic polyhedra[47-49], ladder polymers[50,51], and reorganizing, self-repairing polymers[52-54]. COF synthesis expands on these examples of dynamic covalent bond formation to achieve predictable long-range order in 2D or 3D.

Yaghi and coworkers synthesized the first COFs, which were two distinct 2D COFs containing 1,4-phenylenebisboronic acid (PBBA)[55]. A boronate ester-linked network designated COF-5 (Figure 1.2a), obtained from condensing PBBA and 2,3,6,7,10,11-hexahydroxytriphenylene (HHTP), represents a prototypical 2D COF structure. COF-5 adopts a hexagonal unit cell ($a = b = 2.97$ nm) whose macromolecular sheets stack in an eclipsed fashion, similar to that found in hexagonal boron nitride, with a 0.34 nm interlayer spacing, similar to that of graphite. This structure, as well as all subsequent COFs, was assigned by comparing its refined

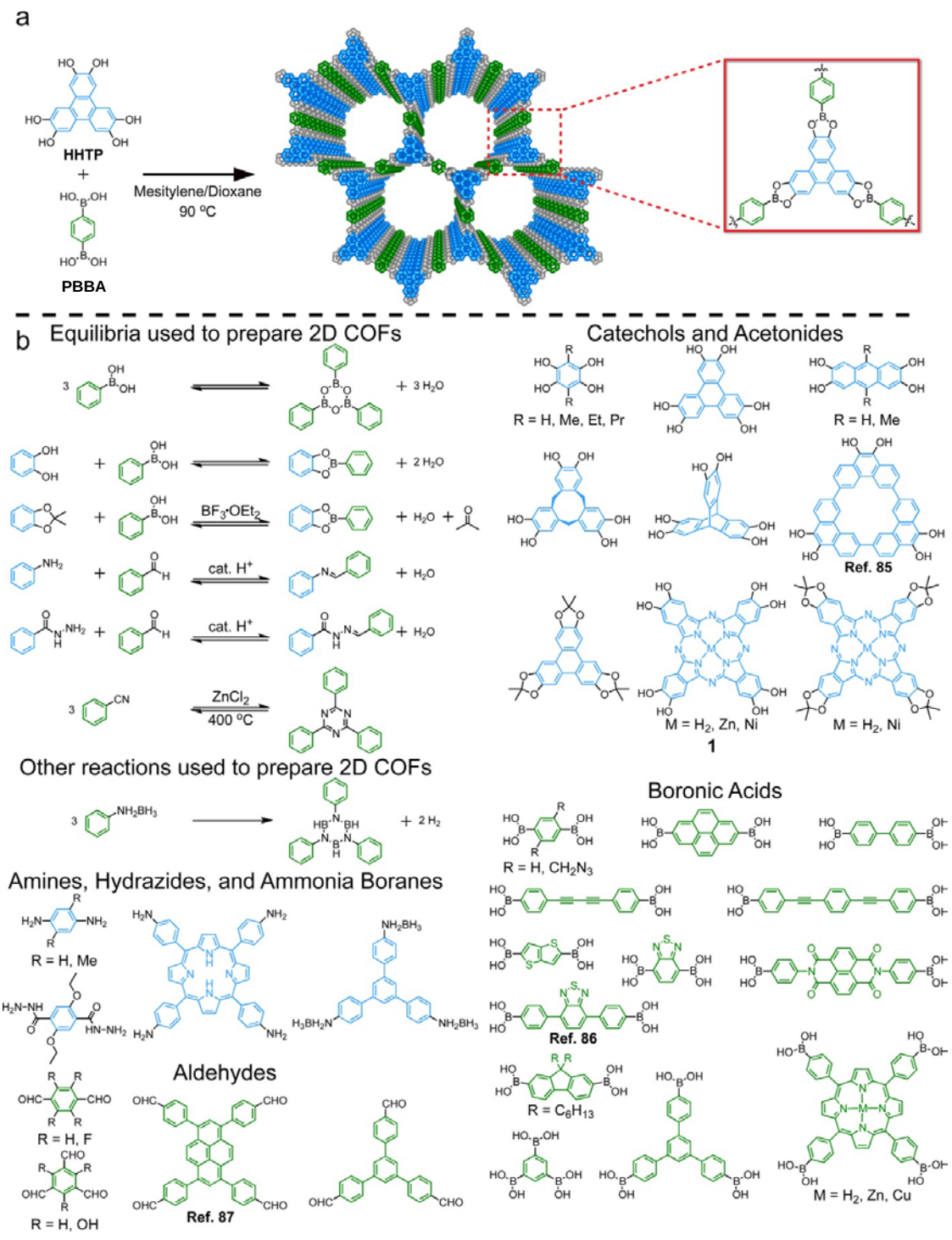

Figure 1.2 | a) Condensation of **HHTP** and **PBBA** provides a prototypical 2D COF (COF-5). Its topology and chemical structure (inset) are displayed. **b)** Equilibria that have provided bulk 2D COFs are given, as well as all monomers used to synthesize layered 2D COFs by the date of acceptance (March 7, 2013). Materials derived from monomers not discussed in the text are given with references.

powder X-ray diffraction (PXRD) pattern with simulated patterns of eclipsed and staggered stacking arrangements; no single-crystal X-ray structure of a 2D COF has been reported to date. COF-5 exhibits permanent porosity with high surface area (1590 m^2 g^{-1}), a narrow pore size distribution, and excellent thermal stability (>350 ºC). COF-1, a 2D COF derived from the dehydration of PBBA, was reported simultaneously with COF-5, and remains the single example of staggered interlayer stacking. Its benzene subunits are arranged above boroxine rings in adjacent layers, likely due to the size and electronic complementarity of its boroxine and benzene subunits not found in networks with larger aromatic surfaces[56].

Several recent computational studies have investigated the structure of 2D COFs in greater detail than has been possible to measure experimentally. Aromatic systems do not typically crystallize into fully eclipsed cofacial structures, as suggested by refinement of 2D COF PXRD data. It is likely that they adopt slightly offset structures that balance attractive forces with repulsive electrostatic interactions. Indeed, density functional theory calculations (Figure 1.3) by Clancy[57], Heine[58,59], and Zhou[60], identified offset structures as energy minima. Clancy and coworkers also correlated the preferred offset to the density of boron-oxygen linkages in each COF[61], suggesting that interlayer boron-oxygen or boron-aromatic interactions may also influence COF structure. These offsets have no single preferred direction with a minimum energy observed in a symmetric ring in the potential energy surface (Figure 1.3b). This finding indicates that the layers likely adopt random offsets from a vector normal to the stacking direction. However, these offsets have yet to be confirmed experimentally because peak broadening in powder samples is too large to

differentiate between eclipsed and slightly offset structures. High-resolution microscopy or complementary spectroscopy will be necessary to confirm these calculations in lieu of higher resolution X-ray diffraction. Recently, Jiang and coworkers further engineered COF offsets by incorporating arene-perfluoroarene interactions[62], which are expected induce closer interlayer packing.

Thirty-seven unique 2D COFs have now been synthesized as layered crystals, most linked by boronate esters, including several 3D networks[63-65] outside the scope of this review. Monomers utilized in 2D COFs are shown in Figure 1.2b. Most are planar, though Zheng and coworkers crystallized a 2D COF using a bowl-shaped

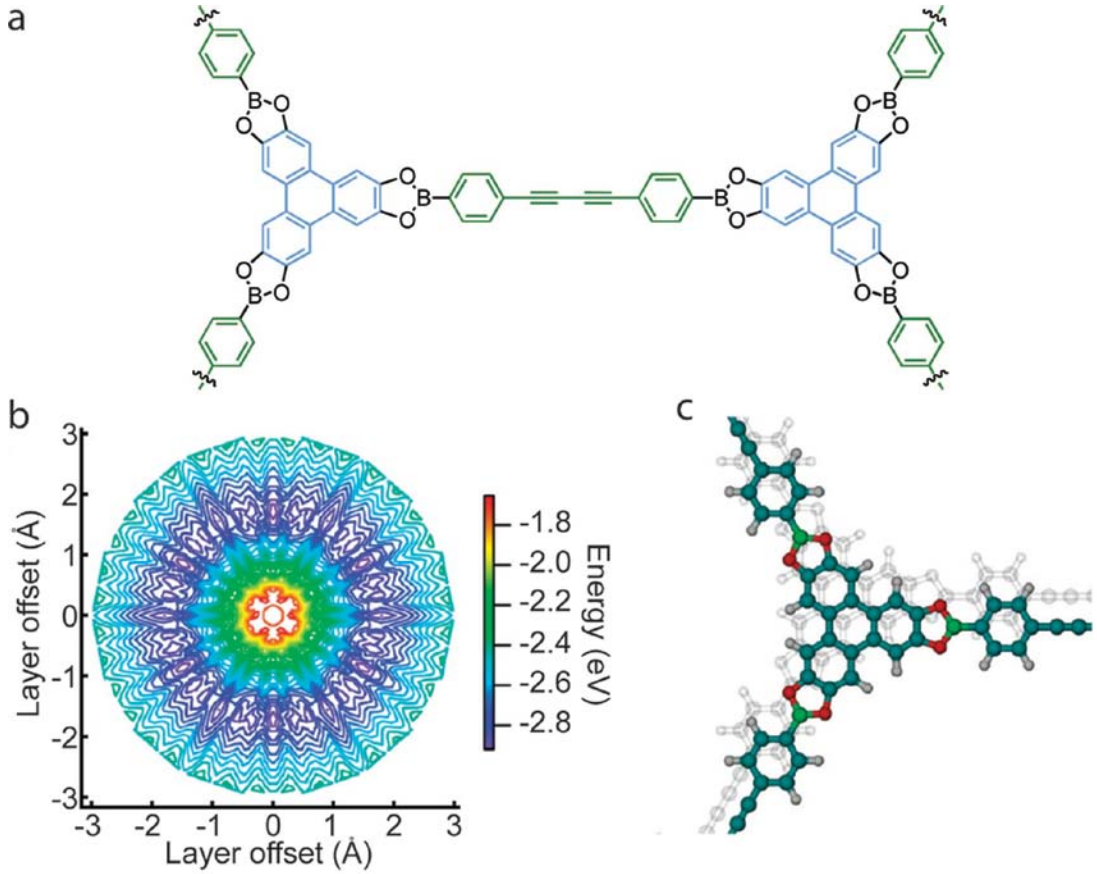

Figure 1.3 | a) Partial structure of a 2D COF whose preferred interlayer offsets were calculated using DFT. **b)** Potential energy surface as a function of interlayer offset of the COF in **a)**. **c)** The lowest energy structure of the COF represented in **a)**. Fig. **b)** and **c)** were adapted from ref. 57.

monomer, hexahydroxycyclotricatechylene (CTC), linked by PBBA (CTC-COF)[66]. Adjacent columns of stacked CTC units face in opposite directions, forming rippled, rather than planar, 2D polymer sheets. A 2D COF incapable of cofacial stacking that incorporated hexahydroxytriptycene linked by PBBA (TDCOF-5)[67] was reported by El-Kaderi and colleagues, which exhibited an out-of-plane lattice parameter commensurate with this difference in packing. Many polyfunctional boronic acids have provided 2D COFs, but the structural diversity of the catechol component has remained limited. Only HHTP[55,68-71], octahydroxyphthalocyanine **1**[72-74], and 1,2,4,5-tetrahydroxybenzene[75-78] have been incorporated into multiple materials. The low solubility and oxidative sensitivity of planar polyfunctional catechols complicates large-scale synthesis and storage, and oxidized catechol building blocks are known contaminants of isolated frameworks. Spitler and Dichtel developed an alternative method[73] in which boronate esters are formed from soluble and bench-stable catechol acetonides in the presence of the Lewis acid catalyst $BF_3{\cdot}OEt_2$. This method provided square free-base and Ni phthalocyanine-containing frameworks, as well as COF-5 and the HHTP-biphenyl network known as COF-10[68]. A mechanistic study of boronate ester formation[79] revealed several complex equilibria, including non-productive $BF_3{\cdot}ArB(OH)_2$ complexes, suggesting that alternative Lewis acids might further improve this approach.

Though boronic acid condensations now dominate the 2D COF literature, other equilibria also provide 2D crystalline networks. Trimerization of the nitrile moieties of 1,4-dicyanobenzene under ionothermal conditions (molten $ZnCl_2$, 400 ºC) yields a hexagonal triazine-linked framework[80]. However, this COF showed limited

crystallinity, and these reaction conditions are unlikely to tolerate many functional groups. This contrasts with triazine formation under mild acid-catalyzed conditions, which is irreversible, providing high surface area, but amorphous, porous polymers. Carbonyl condensation reactions also show promise, as demonstrated by 2D imine[81] and hydrazone-linked[82] COFs synthesized under solvothermal acid-catalyzed conditions. Notably, two enamine-linked COFs derived from the condensation of linear diamines and triformylglucinol exhibited enhanced stability to concentrated aqueous acid and boiling water[83]. Borazine-linked frameworks have also been reported, which were synthesized from the thermal decomposition of an ammonia-borane precursor[84]. Other reversible reactions might also provide crystalline networks, and broadening the range of COF linkage chemistries represents an important challenge to increase the scope of 2D polymerization.

Inspired by intense interest in MOFs and other high surface area materials for storing, sequestering, or separating technologically relevant gases, 2D COFs were initially evaluated for these applications. COFs are comprised of lightweight elements that could provide improved gravimetric storage capacity and many adsorb significant amounts of CH_4, CO_2, and H_2[88,89]. COF-10 demonstrated notable NH_3 uptake[90], outperforming zeolite 13X, sulfonic acid-containing polymer Amberlyst 15, and mesoporous silica MCM-41. The strong interaction between the COF and NH_3 derives from the Lewis acidity of its boronate ester linkages. Decreased NH_3 uptake observed over three adsorption-desorption cycles was attributed to turbostratic disorder induced into the 2D layered crystals, suggesting that using Lewis acidic 3D COFs might improve performance. Generally, two-dimensional COFs display smaller surface areas

than their 3D counterparts and many MOFs[88], in part because their 2D architectures are inherently more dense.

Post-synthetic modification of 2D COFs leverages the periodicity of the framework to organize secondary functionality, either through covalent or coordinative bonding. Wang and coworkers[81] prepared a 2D imine-linked framework, COF-LZU1, by condensing 1,3,5-benzenetricarboxaldehyde and 1,4-diaminobenzene. COF-LZU1 adopts a nearly eclipsed layered crystal with 1.8 nm-wide pores and is hypothesized to bind metal ions through bidentate coordination to proximal N atoms in adjacent layers. For example, 0.5 equivalents of Pd^{2+} per unit cell were incorporated by soaking COF-LZU1 in a solution of $Pd(OAc)_2$, inducing only minor changes to its PXRD pattern. The resulting Pd-loaded COF is a highly active catalyst for the Suzuki-Miyaura cross-coupling reaction, achieving high yields (often >97%) at low catalyst loadings (≤1 mol% Pd). Control experiments suggested that bound Pd ions were the active catalysts, and the insoluble COFs were easily recovered and recycled at least four times without loss of activity. This study demonstrates a promising future for 2D polymer catalysts to combine specific metal-coordination environments, the operational simplicity of heterogeneous catalysis, and substrate selectivity imparted by the pore structure, though further improvements in stability are needed. Another example of COF functionalization was reported by Jiang and coworkers[70], who performed Cu-catalyzed azide-alkyne cycloaddition (CuAAC) reactions within the pores of 2D COFs bearing azide moieties. Several cycloaddition partners and functionalization densities demonstrate the versatility of this strategy to distribute external functionality throughout the porous crystal.

A distinctive aspect of 2D layered COFs is their long-range π-orbital overlap in the stacking direction, which gives rise to high exciton and charge mobilities of interest for optoelectronic devices. First, their pores run parallel to the stacking direction, providing an opportunity to introduce complementary organic or inorganic semiconductors. The resulting vertically aligned p-n junctions embody a morphology long thought to be ideal for photovoltaic performance[91]. Second, the stacked π-systems found in COFs adopt zero degree dihedral angles between layers, maximizing their orbital interactions, in contrast to discotic liquid crystals, which often stack into less ideal twisted interlayer structures due to steric crowding of their pendant mesogens. Finally, COFs generally show excellent thermal stability and do not undergo thermal phase transitions, unlike polymeric semiconductors, which frequently require thermal or solvent annealing to attain morphologies suitable for reasonable photovoltaic performance.

Jiang and coworkers reported the first photoconductive COFs, each based on 2,7-pyrene diboronic acid, either self-condensed into a boroxine-linked structure[92] (Figure 1.4a) or co-crystallized with HHTP to yield a boronate ester-linked material[69]. Photoconductivity observed in devices consisting of the COF powder sandwiched between Au and Al electrodes (Figure 1.4a, red trace) suggested long-range exciton delocalization, presumably through the stacked pyrene moieties. Charge mobilities of phthalocyanine- and porphyrin-based COFs were later studied using laser flash-photolysis time-resolved microwave conductivity, which measures the intrinsic charge-carrier mobility of the material independent of defects or impurities. Phthalocyanine-based COFs display hole mobilities[72] as high as 1.3 $cm^2\ V^{-1}\ s^{-1}$, while

mobilities as high as 8.1 $cm^2\ V^{-1}\ s^{-1}$ were reported for a porphyrin-containing imine-linked COF[93]. Charge separation in COFs has been studied both for COFs in which the donor and acceptor are both incorporated into the framework[94], or for noncovalent post-synthetic functionalization using a soluble fullerene derivative acceptor[95]. In both cases, ultra-fast charge transfer on the time-scale of picoseconds occurred from the electron donor to the acceptor. Charge separated states with long-lived lifetimes of 1.5 μs at 280 K and 1500 μs at 80 K, respectively, were observed in the donor-acceptor framework[94]. Additionally, the first COF-based photovoltaic device was reported[95] using a thienothiophene-containing 2D COF/fullerene hybrid, albeit with an unoptimized photoconversion efficiency of 0.053%.

An outstanding issue in studies of COF charge mobility is how interlayer offsets impact their optoelectronic properties. For example, calculations suggest that HHTP-containing COFs with perfectly eclipsed stacking could potentially delocalize charge carriers over the entirety of the HHTP pillar[96], resulting in band-like charge transport with mobility as high as 10 $m^2\ V^{-1}\ s^{-1}$. However, the degree of lateral sliding (e.g. offset) between adjacent HHTP molecules in a pillar strongly affects the transfer integral between layers[97]. Charge is delocalized to the greatest extent when the lateral offset approaches 3 Å, while offsets of 1 Å between layers have extremely small transfer and overlap integrals, resulting in charge localization to a single HHTP molecule in a stack. Therefore, controlling the nature of interlayer stacking in 2D COFs is likely to strongly influence their charge transport properties.

One of the most attractive aspects of COFs for optoelectronic applications is that their 2D layered structures are preserved even as the molecular structure of the

monomers is varied. In contrast, even subtle changes in structure often induce dramatic changes in the packing behavior of molecular[24] and polymeric[26] semiconductors. For example, Dichtel and coworkers systematically increased the pore size of a square Zn phthalocyanine framework to diagonal widths of 2.7, 3.4, 4.0, and 4.4 nm by employing increasingly long and structurally diverse diboronic acid linkers[98]. Similarly, hexagonal COF lattices have also been expanded[57,99] to 4.0 and 4.7 nm. These larger pore sizes might accommodate complimentary semiconductors or other functional guests. Jiang and coworkers leveraged the modularity of COF synthesis to characterize the charge mobility of various cofacially-stacked (Figure

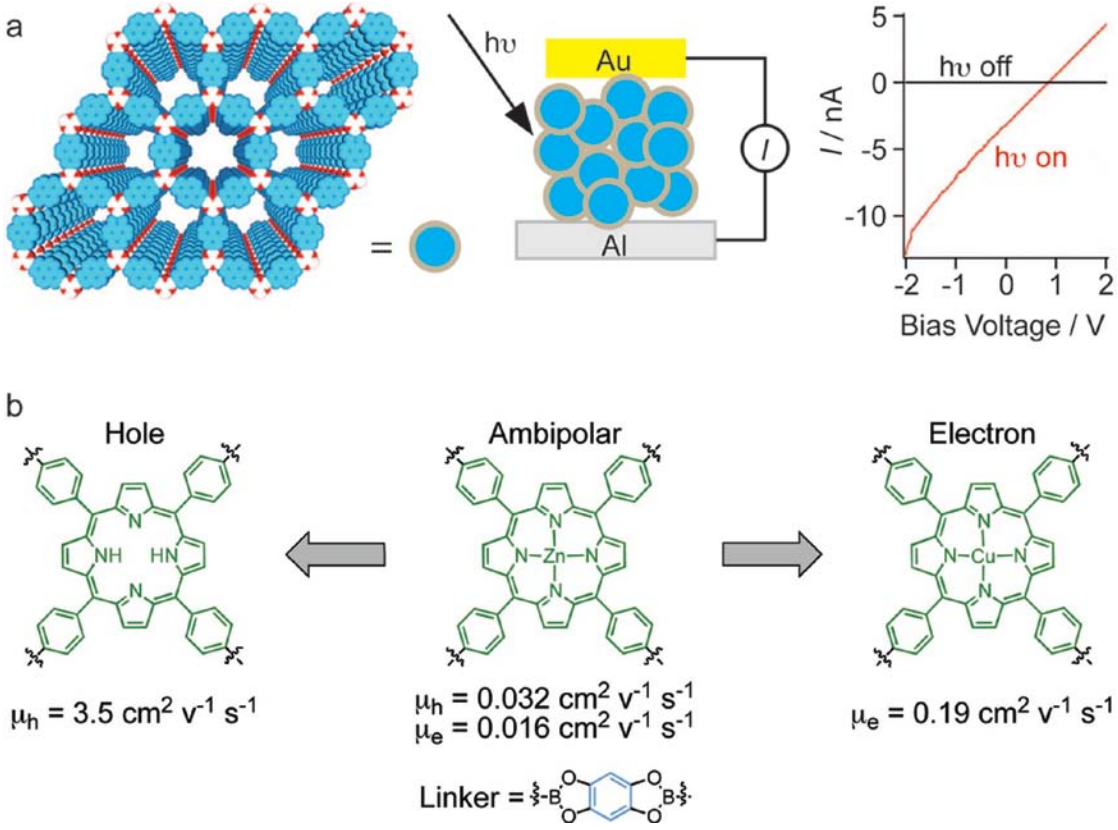

Figure 1.4 | 2D COFs exhibit photoconductivity and variations in charge transport as a function of their structure. **a)** 2,7-pyrene diboronic acid self-condenses into a boroxine-linked 2D COF (left). Crystalline powder sandwiched between two electrodes (middle) exhibits photoconductivity (right). Adapted from ref. 92. **b)** The nature of charge transport through 2D porphyrin COFs depends on the presence or identity of the coordinated metal ion. Adapted from ref. 100.

1.4b) π-systems[100]. They found the semiconducting properties of porphyrin-containing 2D COFs to depend strongly on the identity of the central metal ion: the free-base porphyrin COF conducts holes, Zn porphyrin COFs are ambipolar, and Cu porphyrin COFs conduct electrons. Separately, Jiang and coworkers co-condensed complementary triphenylene donors and benzothiadiazole acceptors into a framework which retained its 2D layered morphology, a rare example of self-segregated donor-acceptor systems capable of simultaneous hole and electron conduction[101].

Their high intrinsic mobilities and structural versatility confirm the promise of 2D COFs as novel organic semiconductors and set the stage for incorporating these materials into working devices. The performance of molecular or polymeric semiconductors in working devices is strongly affected by impurities and local disorder, and the identity and prevalence of relevant defects and impurities within 2D COFs remain largely uncharacterized. Such measurements will be facilitated by preparing these materials as thin films on both conducting and insulating surfaces.

Surface-supported 2D polymers: Thermodynamic and Kinetic Approaches

2D COFs are typically obtained as insoluble powders, an isolated form that limits their utility. Microcrystalline powders are suitable for many applications traditionally associated with porous materials, including gas storage, separations, and catalysis. However, their crystallites are randomly oriented and are not easily interfaced to surfaces, including electrodes. 2D polymer membranes and scaffolds will demand few-layer, free-standing, or surface-bound materials with controlled orientation. Likewise, interfacing COFs reliably to electrodes and insulators will be necessary to realize their optoelectronic potential. Therefore, methods to synthesize multilayer or

monolayer 2D polymer films are of great contemporary interest. Surfaces also offer a natural interface to template molecular assembly and polymerization in two dimensions.

Using the same solvothermal conditions that produce COF powders, Dichtel and coworkers grew COF thin films on single-layer graphene (SLG) functionalized substrates[102]. Figure 1.5 compares grazing incidence X-ray diffraction (GIXD) data of powders and films, revealing their topologies to be identical. However, diffraction from powders is observed as an isotropic ring of intensity from low out-of-plane angle ($Q_\perp$) to high out-of-plane angle, including the out-of-plane COF stacking, observed in the powder at 1.84 $Å^{-1}$. In contrast, diffraction from thin films is localized to small $Q_\perp$, and the stacking peak is absent. These experiments indicate that the π-systems of the COF film are oriented normal to the substrate. Scanning electron microscopy (SEM) and focused ion beam (FIB) milling of the thin films revealed a continuous COF film that conf $_{PBBA}$ to the substrate. This method was generalized to pyrene- and several

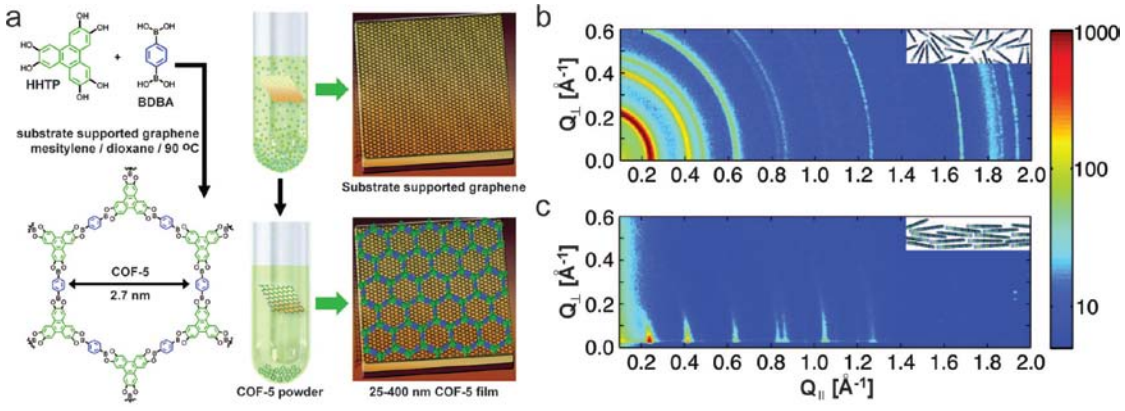

Figure 1.5 | a) 2D COF thin films were prepared by including a single-layer graphene-functionalized substrate in the polymerization solution. **b)** Grazing incidence x-ray diffraction (GIXD) of a 2D COF powder, whose crystallites are randomly oriented (inset). **c)** GIXD of the corresponding film, whose crystallites are oriented with the stacking direction normal to the graphene surface (inset). Adapted from ref. 102.

phthalocyanine-based COFs, which each crystallized as an oriented thin film. One of the attractive features of this approach is that SLG can be transferred to arbitrary substrates and has shown promise as a transparent electrode material[103]. For example, SLG was deposited onto fused SiO_2, after which COF films were grown and characterized spectroscopically in transmission mode. The generality of this procedure will open new applications and characterization methods for 2D COFs that are unavailable in their powder forms. This method also represents a means to incorporate COFs into optoelectronic devices.

The above solvothermal conditions produce multilayer COF films that range in thickness from 20 – 400 nm but have not accessed crystalline few-layer or monolayer films. COF islands consisting of 10 – 25 layers were isolated by Zamora and coworkers[104] by sonochemically exfoliating bulk COF powders. These multilayers were dispersed in solvent and deposited onto highly oriented pyrolytic graphite (HOPG), where their thickness was measured by atomic force microscopy (AFM). These results suggest that other 2D COFs might also be exfoliated to few or single layers, and the properties and stability of materials isolated in this way remain an open question.

Individual 2D COF layers have been grown on metal surfaces through ultra-high vacuum (UHV) deposition of the monomers[8,105,106], an approach pioneered by Porte and coworkers[8]. These single-layer 2D polymers are typically characterized using scanning tunneling microscopy (STM), which provides atomic scale resolution of the polymer structures and periodicity over *ca*. 100 x 100 nm field of view (Figure 1.6). For example, macrocyclic pentagon and heptagon defects were observed[107] in

COF-1 monolayers alongside the expected fused hexagons. Zamora and coworkers[108] optimized the deposition parameters of acid chloride and alcohol monomers to synthesize a single-layer polyester COF that was defect-free over 100 nm^2 areas. This example demonstrates that fine control of monomer deposition can provide long-range order even in the absence of reversible bond formation, as this reaction is unlikely to be reversible and no polyester COFs have been prepared in bulk form. COF monolayers were also synthesized by evaporating boroxines with pendant aryl bromides onto a Au surface to provide noncovalent dimers, which undergo aryl-aryl coupling to yield a hexagonal lattice upon heating[109]. UHV preparation of COFs is a 2D polymerization technique under kinetic control, in contrast to solvothermal polymerizations under thermodynamic control.

Alternative methods for forming surface-bound COF monolayers utilize reversible bond formation to access or improve the long-range order of the polymer.

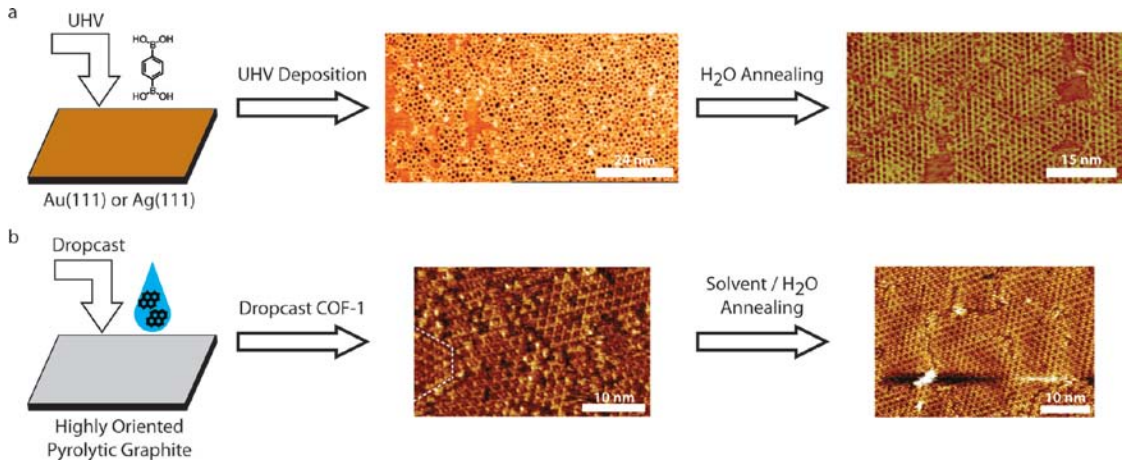

Figure 1.6 | a) PBBA self condenses onto crystalline metal surfaces following UHV deposition. STM image (middle) shows formation of COF-1 monolayers containing various 5- and 7-membered ring defects. Annealing this film in a humid environment improves the order of the film (right). Middle image adapted from ref. 8. Right image adapted from ref. 111. **b)** COF-1 nanocrystals dropcast on to HOPG (middle) were similarly annealed to provide a monolayer with improved long-range order (right). Adapted from ref. 5.

Such approaches tolerate a variety of monomer deposition or initial polymerization strategies, followed by a final annealing procedure. Dienstmaier and coworkers pioneered this approach by depositing COF-1 nanocrystals of 7.8 nm average diameter onto HOPG[5] (Figure 1.6b). These crystallites were annealed in a humid environment, enabling dynamic hydrolysis and reformation of the boroxine linkages. Under these conditions, the few-layer, small crystallites ripen into a COF monolayer with ~40 nm crystalline domains. Similar COF monolayers were obtained when the PBBA monomer itself was used in place of the nanocrystal seeds. The generality of this method was subsequently demonstrated for monolayer COFs with pore sizes as large as 3.8 nm by lengthening the diboronic acid monomer[110]. Wan and coworkers also improved the order of UHV-deposited monolayers upon annealing in the presence of trace amounts of water released by heating a hydrated metal salt at pressure[111]. These results demonstrate that reactivating dynamic bond exchange processes provides a means to anneal COF monolayers and improve their long-range order, while also mitigating the need to deposit COF monomers under careful conditions.

Monolayer and multilayer COF films offer a wide range of opportunities for further study. First, the full range of linkage chemistries used in COF powders has yet to be generalized to oriented thin films. Likewise, the nucleation processes of COFs are unknown; control of domain size, film thickness, and selective growth on patterned substrates might follow from improved understanding. The porosity of multilayer films is also undemonstrated. Ultimately, COF multilayer and monolayer films will enable many advanced functions for these materials, and properties such as

their ionic and electronic conductivity, dielectric constants, etch resistance, patternability, and hydrolytic stability are each areas of immediate interest.

Molecular Networks and Polymerizations Mediated by Surfaces

Another strategy for synthesizing single-layer 2D polymers involves depositing shape-persistent monomers onto a crystalline metal surface. The surface is then heated to speed molecular diffusion and activate covalent bond-forming reactions, often aryl-aryl couplings. The resulting 2D polymers remain adsorbed to the substrate and are characterized by STM, revealing their structure, defects, and domain sizes with atomic precision. This 2D polymerization strategy emerged from pioneering STM studies of 2D molecular crystallization and directed noncovalent assembly, which have been reviewed previously[32,112]. Covalent networks have appeared comparatively recently and remain much more rare.

Hecht and Grill reported the first covalent two-dimensional polymers of this type by developing the above approach to various halogenated porphyrins[6]. The substitution pattern of the porphyrin monomer determines the dimensionality of the resulting coupled products. For example, a porphyrin bearing a single aryl-bromide dimerizes on the surface, and linear disubstituted monomers provide 1D polymers, a method recently applied to surface-bound molecular wires[113-115] and graphene nanoribbons[116]. Tetrafunctional porphyrins produce 2D polymers with dimensions of approximately 5 x 5 monomers (Figure 1.7). The authors later modified this approach to perform sequential polymerizations based on the lower activation temperature of aryl-iodides relative to aryl-bromides[7]. Heating 5,15-bis(4′-bromophenyl)-10,20-bis(4′-iodophenyl)porphyrin on Au(111) to 120 °C initiates polymerization at the trans

aryl-iodide positions, providing linear porphyrin polymers that retain their aryl-bromide moieties. These aryl-bromides are activated upon increasing the temperature to 250 °C. The resulting 2D polymers were more extended than the single-step approach (8 x 8 monomer units and larger) due to the preorganization of the intermediate 1D polymer chains in the subsequent 2D crosslinking step. This two-step protocol also afforded the opportunity to incorporate additional dibrominated monomers selectively during the second polymerization, although the resulting materials were not periodic in two dimensions.

Abel and coworkers demonstrated 2D polymerization of 1,2,4,5-tetracyanobenzene (TCB), which tetramerizes to form phthalocyanine networks on Au(111), Ag(111), or NaCl/Ag(100) surfaces when coevaporated with Fe[117]. The polymerization depended strongly on the TCB:Fe stoichiometry. At a 1:2 ratio, complete cyclization to a 2D polymer was observed, with domain sizes on the order of 400 nm^2, or about 8 – 12 phthalocyanines per side. A 1:4 TCB:Fe ratio instead provided isolated phthalocyanines with pendant nitrile groups, which assemble into periodic noncovalent arrays. The nature of the surface also played a key role in network formation, as polymerizations that took place on Au or Ag gave small domain sizes, while, remarkably, those on NaCl formed a single polymeric domain (10^3–10^4 nm^2). This large domain size is notable for a 2D polymer synthesized under kinetic control and illustrates the large effect of the nature of the surface on the polymerization outcome. Future studies of the optoelectronic properties of these conjugated phthalocyanine polymers will also be of great interest.

Much like COFs, a key advantage of surface-mediated 2D polymerizations is that their topology is predictable based on monomer structure. While the scalability of these methods is inherently limited, their characterization by STM provides direct evidence of their structure, domain size, and defects. These studies also motivate fundamental studies of molecular diffusion on surfaces. For example, Müllen and Fasel correlated surface mobility and degree of polymerization as a function of monomer size and structure[118], though it is not fully understood how this mobility changes during the polymerization. Surface-mediated reactions have since expanded in scope to include imide[119], imine[120], and urea[121] condensations, which might also be amenable to forming 2D periodic networks. Additional opportunities for these polymers include organizing guest molecules into periodic arrays, as was shown for C_{60} by Champness and coworkers[122]. Transferring these polymers to insulating substrates might facilitate their electronic characterization and use as templates or

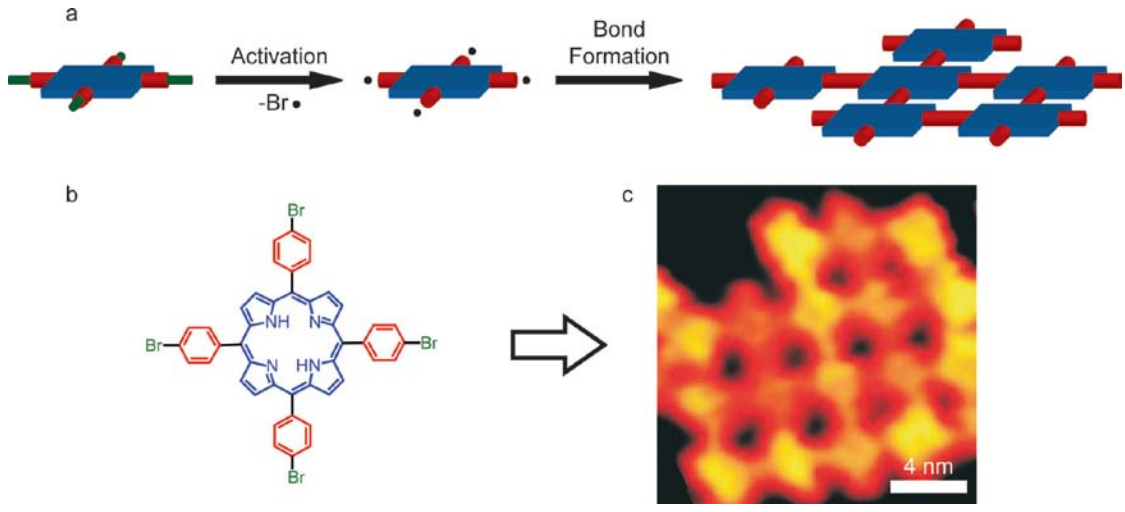

Figure 1.7 | Two-dimensional polymers prepared via surface-catalyzed aryl-aryl coupling. **a)** Surface-mediated 2D polymerization scheme of the tetrafunctional porphyrin monomer in **b)**. **c)** STM image of resulting 5 x 5 2D networks. Adapted from ref. 6.

coatings, particularly as larger 2D polymers are accessed through on-surface polymerization.

Reactions in Organized 2D Assemblies

Noncovalent 2D assemblies can organize monomers to place reactive groups in close proximity for subsequent polymerization. Such assemblies can derive their 2D form from layered crystals, surface confinement, or amphiphile assembly in solution. This strategy offers a route to synthesize high molecular weight networks because molecular organization can occur over long length scales. The polymerization reaction must be efficient, selective, and sufficiently mild to preserve the assembly; however, it need not be reversible, greatly expanding the number of compatible bond-forming reactions as compared to solvothermal COF synthesis or surface-mediated polymerization.

Elaborating upon prior work in polymerization within organized assemblies, Stupp and coworkers confined two distinct polymerizations within spatially segregated domains of an organized molecular assembly[9]. Amphiphiles containing acrylate (A) and nitrile (B) polymerizable functionalities were incorporated into a mesogen that assembled into layered 2D sheets (Figure 1.8). Thermally-initiated acrylate and nitrile polymerizations cross-link the mesogens into a bilayer superstructure. Although the resulting polyacrylate and polynitrile chains lack periodicity in two dimensions, this example represents pioneering work towards 2D polymerizations within organized assemblies.

Ozaki and coworkers demonstrated a 2D polymerization within a crystalline monolayer of alkyne-containing monomer **2** on HOPG[123,124] (Figure 1.9). Notably, this

example is also the first true covalently-linked 2D polymer of which we are aware. STM analysis of the monolayers prior to polymerization indicated that both the internal diyne and terminal alkyne moieties were aligned appropriately for topochemical polymerization. Indeed, UV irradiation yielded a 2D polymer linked by two distinct types of polyacetylenes. The polymer was first characterized using Penning ionization electron spectroscopy[123] to show the change in electronic energy levels before and after polymerization. As determined by STM[124], the lattice parameters of the 2D polymer were nearly unchanged from the monomeric form, which is likely to be a key design criterion for polymerizations of this type. Müllen and coworkers[125] subsequently polymerized an isophthalic acid derivative using either light or an STM tip to prepare a similar 2D polymer linked by parallel polyacetylenes. Like other surface-mediated polymerization techniques, STM-tip induced polymerizations provide small quantities and are relatively rare. Additionally, care must be taken to characterize such polymerizations using complementary analyses, as the STM itself does not provide definitive proof that polymerization has occurred.

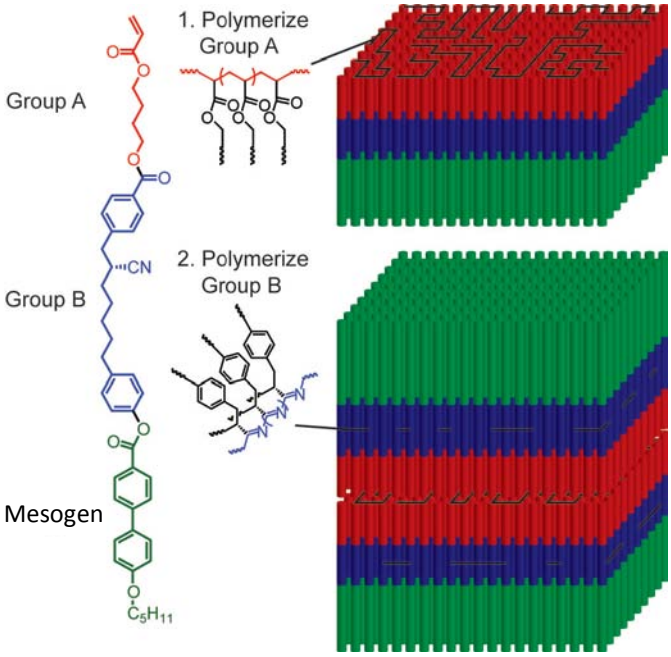

Figure 1.8 | Two distinct polymerizable groups A and B were incorporated into a mesogen. Thermal polymerization results in a bilayer superstructure with independent linear polymers confined to two distinct planes. Adapted from ref. 9

Nevertheless, this method does offer the possibility of patterning with nanometer scale resolution[126].

Sakamoto and coworkers[12] elegantly expanded the scope of topochemical 2D polymerizations to take place within layered crystals. Their design utilizes a trigonal cup-shaped monomer bearing reactive groups on each of its faces. The monomer crystallizes into a layered structure in which adjacent monomers face in opposite directions, placing an alkyne of one monomer near an anthracene of its neighbor. Irradiation of these crystals induced intermolecular [4+2] cycloaddition reactions,

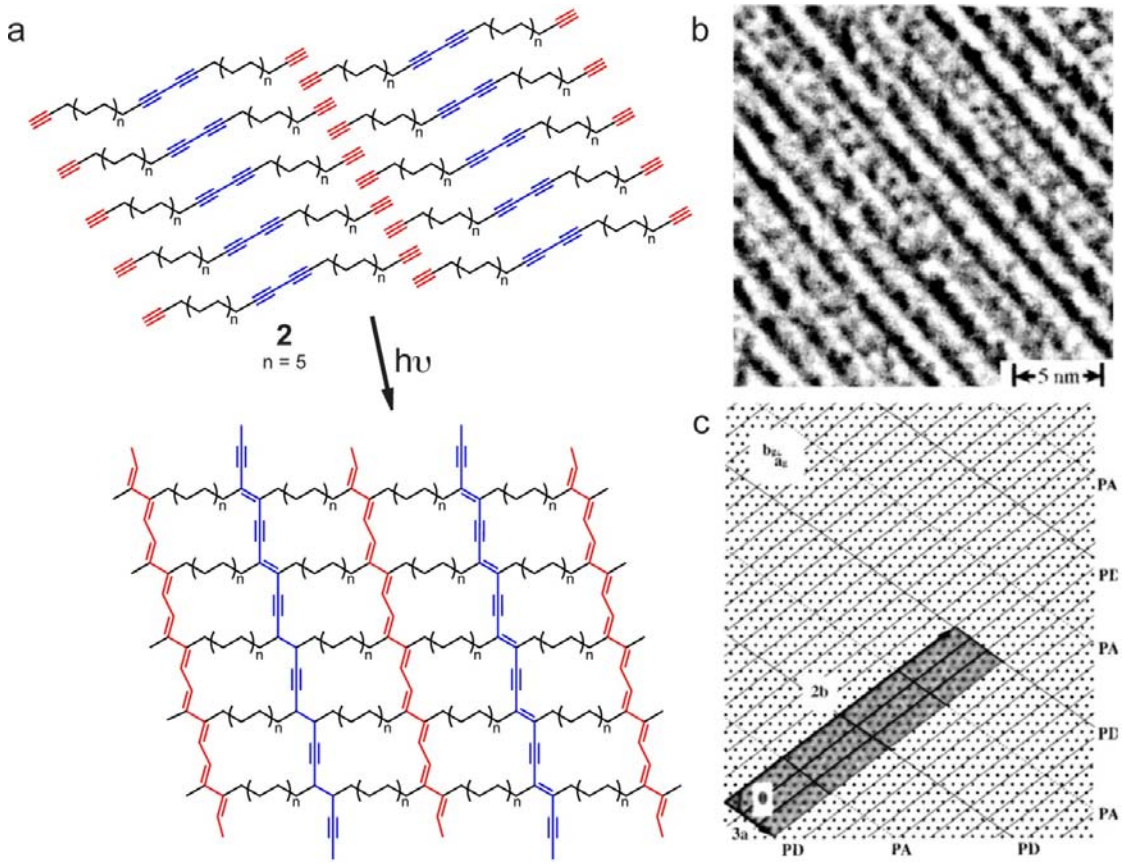

Figure 1.9 | a) Irradiation of alkyne-containing monomers induces simultaneous topochemical polymerizations that yield a 2D polymer comprised of linear polyacetylene and polydiacetylene chains linked by alkanes. **b)** STM image of the 2D polymer on graphite. **c)** The proposed structure of the 2D polymer on graphite generated from the Fourier transform of the image in **b)**. The dark lines represent the polydiacetylene, while the dotted lines represent the polyacetylene. Graphite is represented by dark periodic circles. Adapted from ref. 124.

providing a layered two-dimensional polymer (Figure 1.10). Remarkably, the 2D polymer multilayers were exfoliated to dispersed single-layers in suitable solvents, representing the first example of a rationally synthesized 2D polymer isolated as an

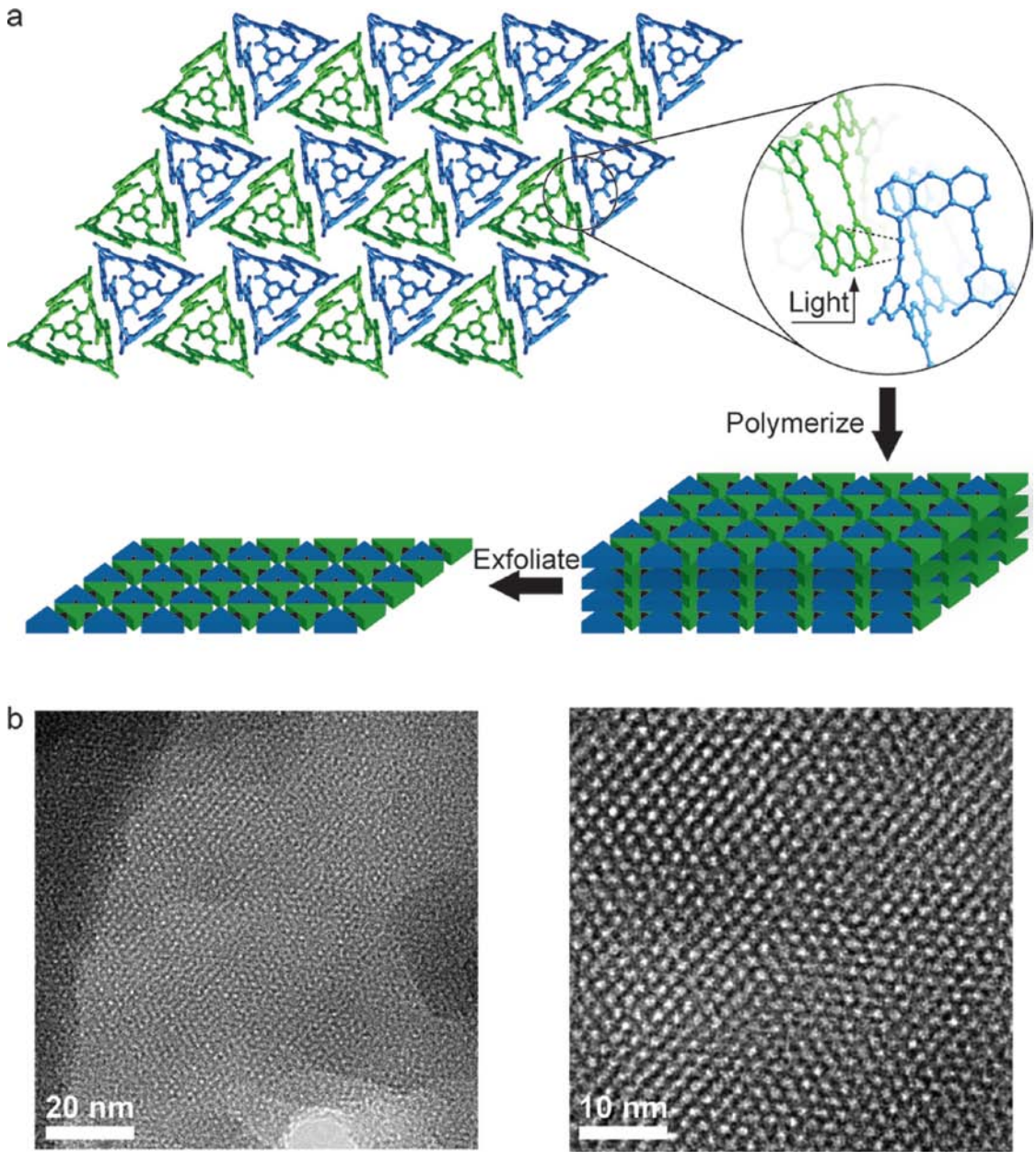

Figure 1.10 | a) Cup-shaped monomers crystallize with their reactive groups in close proximity between adjacent monomers. UV light-induced polymerization, followed by exfoliation, provided isolated single-layer 2D polymers. **b)** Large-view TEM of exfoliated few layer 2D polymer sheets (left). Higher magnification (right) reveals that the polymers maintain their trigonal shape and topology after irradiation. Adapted from ref. 12.

individual sheet. Transmission electron microscopy revealed few-layer bundles of polymer that sometimes retained the same macroscopic shape as the parent multilayer crystal, and selected area electron diffraction revealed that the covalently linked polymer retains the topology of its supramolecular precursor. Because molecular crystals can be large and synthesized in bulk quantities, this approach provides access to high molecular weight 2D polymers on preparative scale.

2D polymerizations in noncovalent assemblies, though rare, have been reinvigorated by the recent work of Sakamoto and coworkers. Demonstrating the generality of this approach is an important next step, as it remains difficult to predict molecular crystallization with the precision needed for successful topochemical reactions. The possibility of a monomer crystallizing into multiple polymorphs might also complicate design, although computational crystal structure prediction is improving rapidly.

Conclusion and Outlook

Synthesizing 2D polymers represents a longstanding challenge in polymer science. Several complementary strategies have emerged recently, fueled in part by advances in characterization that have enabled unambiguous structural information of these insoluble materials. Further advances will provide insight into the properties of these polymers, which will determine their applications and inspire new methods to produce them. Understanding the fundamental processes of chemical assembly that occur during 2D polymerization, including nucleation, error correction, and defect formation, are important chemical questions that remain poorly understood. Ultimately, 2D polymers represent an exciting class of materials with major

opportunities for fundamental study, the promise of novel properties that emerge from their unique topology and structural precision, and an as-yet undeveloped application space.

REFERENCES

1. Bielawski, C. W. & Grubbs, R. H. *Prog. Polym. Sci.* **32,** 1 (2007).

2. Matyjaszewski, K. *Macromolecules* **45,** 4015 (2012).

3. Matyjaszewski, K. & Tsarevsky, N. V. *Nature Chem.* **1,** 276 (2009).

4. Semsarilar, M. & Perrier, S. *Nature Chem.* **2,** 811 (2010).

5. Dienstmaier, J. F., Gigler, A. M., Goetz, A. J., Knochel, P., Bein, T., Lyapin, A., Reichlmaier, S., Heckl, W. M. & Lackinger, M. *ACS Nano* **5,** 9737 (2011).

6. Grill, L., Dyer, M., Lafferentz, L., Persson, M., Peters, M. V. & Hecht, S. *Nature Nanotech.* **2,** 687 (2007).

7. Lafferentz, L. Eberhardt, V., Dri, C., Africh, C., Comelli, G., Esch, F., Hecht, S. & Grill, L. *Nature Chem.* **4,** 215 (2012).

8. Zwaneveld, N. A. A., Pawlak, R., Abel, M., Catalin, D., Gigmes, D., Bertin, D. & Porte, L. *J. Am. Chem. Soc.* **130,** 6678 (2008).

9. Stupp, S. I., Son, S., Lin, H. C. & Li, L. S. *Science* **259,** 59 (1993).

10. Schultz, M. J., Zhang, X., Unarunotai, S., Khang, D. Y., Cao, Q., Wang, C., Lei, C., MacLaren, S., Soares, J. A., Petrov, I., Moore, J. S. & Rogers, J. A. *Proc. Natl. Acad. Sci. U.S.A.* **105,** 7353 (2008).

11. Sakamoto, J., van Heijst, J., Lukin, O. & Schluter, A. D. *Angew. Chem. Int. Ed.* **48,** 1030 (2009).

12. Kissel, P., Erni, R., Schweizer, W. B., Rossell, M. D., King, B. T., Bauer, T., Gotzinger, S., Schluter, A. D. & Sakamoto, J. *Nature Chem.* **4,** 287 (2012).

13. Geim, A. K. & Novoselov, K. S. *Nature Mater.* **6,** 183 (2007).

14. Whittell, G. R. & Manners, I. *Angew. Chem. Int. Ed.* **50,** 10288 (2011).

15. Golberg, D., Bando, Y., Huang, Y., Terao, T., Mitome, M., Tang, C. & Zhi, C. *ACS Nano* **4,** 2979 (2010).

16. Novoselov, K. S., Jiang, D., Schedin, F., Booth, T. J., Khotkevich, V. V., Morozov, S. V. & Geim, A. K. *Proc. Natl. Acad. Sci. U.S.A.* **102,** 10451 (2005).

17. Novoselov, K. S., Geim, A. K., Morozov, S. V., Jiang, D., Zhang, Y., Dubonos, S. V., Grigorieva, I. V. & Firsov, A. A. *Science* **306,** 666 (2004).

18. Berger, C., Song, Z., Li, X., Wu, X., Brown, N., Naud, C., Mayou, D., Li, T., Hass, J., Marchenkov, A. N., Conrad, E. H., First, P. N. & de Heer, W. A. *Science* **312,** 1191 (2006).

19. Li, X., Cai, W., An, J., Kim, S., Nah, J., Yang, D., Piner, R., Velamakanni, A., Jung, I., Tutuc, E., Banerjee, S. K., Colombo, L. & Ruoff, R. S. *Science* **324,** 1312 (2009).

20. Huang, P. Y., Ruiz-Vargas, C. S., van der Zande, A. M., Whitney, W. S., Levendorf, M. P., Kevek, J. W., Garg, S., Alden, J. S., Hustedt, C. J., Zhu, Y., Park, J., McEuen, P. L. & Muller, D. A. *Nature* **469,** 389 (2011).

21. Chen, L., Hernandez, Y., Feng, X. & Müllen, K. *Angew. Chem. Int. Ed.* **51,** 7640 (2012).

22. Pisula, W., Feng, X. & Müllen, K. *Chem. Mater.* **23,** 554 (2011).

23. Simpson, C. D., Brand, J. D., Berresheim, A. J., Przybilla, L., Räder, H. J. & Müllen, K. *Chem. Eur. J.* **8,** 1424 (2002).

24. Mas-Torrent, M. & Rovira, C. *Chem. Rev.* **111,** 4833 (2011).

25. Rivnay, J., Mannsfeld, S. C. B., Miller, C. E., Salleo, A. & Toney, M. F. *Chem. Rev.* **112,** 5488 (2012).

26. Peet, J., Senatore, M. L., Heeger, A. J. & Bazan, G. C. *Adv. Mater.* **21,** 1521 (2009).

27. Beaujuge, P. M. & Fréchet, J. M. J. *J. Am. Chem. Soc.* **133,** 20009 (2011).

28. Tsao, H. N. & Müllen, K. *Chem. Soc. Rev.* **39,** 2372 (2010).

29. Carlucci, L., Ciani, G., Proserpio, D. M. & Porta, F. *Angew. Chem. Int. Ed.* **42,** 317 (2003).

30. Dai, F., Dou, J., He, H., Zhao, X. & Sun, D. *Inorg. Chem.* **49,** 4117 (2010).

31. Finke, A. D., Gross, D. E., Han, A. & Moore, J. S. *J. Am. Chem. Soc.* **133,** 14063 (2011).

32. Bartels, L. *Nature Chem.* **2,** 87 (2010).

33. Lehn, J. M. Rigault, A., Siegel, J., Harrowfield, J., Chevrier, B. & Moras, D. *Proc. Natl. Acad. Sci. U.S.A.* **84,** 2565 (1987).

34. Baxter, P. N. W., Lehn, J.-M., Fischer, J. & Youinou, M.-T. *Angew. Chem. Int. Ed. Engl.* **33,** 2284 (1994).

35. Hoskins, B. F. & Robson, R. *J. Am. Chem. Soc.* **111,** 5962 (1989).

36. Simard, M., Su, D. & Wuest, J. D. *J. Am. Chem. Soc.* **113,** 4696 (1991).

37. Wang, X., Simard, M. & Wuest, J. D. *J. Am. Chem. Soc.* **116,** 12119 (1994).

38. Fujita, M., Yazaki, J. & Ogura, K. *J. Am. Chem. Soc.* **112,** 5645 (1990).

39. Stock, N. & Biswas, S. *Chem. Rev.* **112,** 933 (2012).

40. Bae, Y.-S. & Snurr, R. Q. *Angew. Chem. Int. Ed.* **50,** 11586 (2011).

41. Zhou, H.-C., Long, J. R. & Yaghi, O. M. *Chem. Rev.* **112,** 673 (2012).

42. Bétard, A. & Fischer, R. A. *Chem. Rev.* **112,** 1055 (2012).

43. Li, J.-R., Sculley, J. & Zhou, H.-C. *Chem. Rev.* **112,** 869 (2012).

44. Sumida, K., Rogow, D. L., Mason, J. A., McDonald, T. M., Bloch, E. D., Herm, Z. R., Bae, T.-H. & Long, J. R. *Chem. Rev.* **112,** 724 (2012).

45. Kreno, L. E., Leong, K., Farha, O. K., Allendorf, M., van Duyne, R. P. & Hupp, J. T. *Chem. Rev.* **112,** 1105 (2012).

46. Rowan, S. J., Cantrill, S. J., Cousins, G. R. L., Sanders, J. K. M. & Stoddart, J. F. *Angew. Chem. Int. Ed.* **41,** 898 (2002).

47. Mastalerz, M. *Angew. Chem. Int. Ed.* **49,** 5042 (2010).

48. Jin, Y., Jin, A., McCaffrey, R., Long, H. & Zhang, W. *J. Org. Chem.* **77,** 7392 (2012).

49. Nishiyabu, R., Kubo, Y., James, T. D. & Fossey, J. S. *Chem. Commun.* **47,** 1124 (2011).

50. Hartley, C. S., Elliott, E. L. & Moore, J. S. *J. Am. Chem. Soc.* **129,** 4512 (2007).

51. Hartley, C. S. & Moore, J. S. *J. Am. Chem. Soc.* **129,** 11682 (2007).

52. Lehn, J.-M. *Prog. Polym. Sci.* **30,** 814 (2005).

53. Maeda, T., Otsuka, H. & Takahara, A. *Prog. Polym. Sci.* **34,** 581 (2009).

54. Montarnal, D., Capelot, M., Tournilhac, F. & Leibler, L. *Science* **334,** 965 (2011).

55. Côté, A. P., Benin, A. I., Ockwig, N. W., O'Keeffe, M., Matzger, A. J. & Yaghi, O. M. *Science* **310,** 1166 (2005).

56. Zheng, C. & Zhong, C. *J. Phys. Chem. C* **114,** 9945 (2010).

57. Spitler, E. L., Koo, B. T., Novotney, J. L., Colson, J. W., Uribe-Romo, F. J., Gutierrez, G. D., Clancy, P. & Dichtel, W. R. *J. Am. Chem. Soc.* **133,** 19416 (2011).

58. Lukose, B., Kuc, A., Frenzel, J. & Heine, T. *Beilstein J. Nanotechnol.* **1,** 60 (2010).

59. Lukose, B., Kuc, A. & Heine, T. *Chem. Eur. J.* **17,** 2388 (2010).

60. Zhou, W., Wu, H. & Yildirim, T. *Chem. Phys. Lett.* **499,** 103 (2010).

61. Koo, B. T., Dichtel, W. R. & Clancy, P. *J. Mater. Chem.* **22,** 17460 (2012).

62. Chen, X., Addicoat, M., Irle, S., Nagai, A. & Jiang, D. *J. Am. Chem. Soc.* **135,** 546 (2013).

63. El-Kaderi, H. M., Hunt, J. R., Mendoza-Cortés, J. L., Côté, A. P., Taylor, R. E., O'Keeffe, M. & Yaghi, O. M. *Science* **316,** 268 (2007).

64. Hunt, J. R., Doonan, C. J., LeVangie, J. D., Côté, A. P. & Yaghi, O. M. *J. Am. Chem. Soc.* **130,** 11872 (2008).

65. Bunck, D. N. & Dichtel, W. R. *Angew. Chem. Int. Ed.* **51,** 1885 (2012).

66. Yu, J.-T., Chen, Z., Sun, J., Huang, Z.-T. & Zheng, Q.-Y. *J. Mater. Chem.* **22,** 5369 (2012).

67. Kahveci, Z., Islamoglu, T., Shar, G. A., Ding, R. & El-Kaderi, H. M. *CrystEngComm* **15,** 1524 (2013).

68. Côté, A. P., El-Kaderi, H. M., Furukawa, H., Hunt, J. R. & Yaghi, O. M. *J. Am. Chem. Soc.* **129,** 12914 (2007).

69. Wan, S., Guo, J., Kim, J., Ihee, H. & Jiang, D. *Angew. Chem. Int. Ed.* **47,** 8826 (2008).

70. Nagai, A., Guo, Z., Feng, X., Jin, S., Chen, X., Ding, X. & Jiang, D. *Nat. Commun.* **2,** 1 (2011).

71. Du, Y., Mao, K., Kamakoti, P., Ravikovitch, P., Paur, C., Cundy, S., Li, Q. & Calabro, D. *Chem. Commun.* **48,** 4606 (2012).

72. Ding, X., Guo, J., Feng, X., Honsho, Y., Seki, S., Maitarad, P., Saeki, A., Nagase, S., & Jiang, D. *Angew. Chem. Int. Ed.* **50,** 1289 (2011).

73. Spitler, E. L. & Dichtel, W. R. *Nature Chem.* **2,** 672 (2010).

74. Ding, X., Chen, L., Honsho, Y., Feng, X., Saengsawang, O., Guo, J., Saeki, A., Seki, S., Irle, S., Nagase, S., Parasuk, V. & Jiang, D. *J. Am. Chem. Soc.* **133,** 14510 (2011).

75. Feng, X., Chen, L., Dong, Y. & Jiang, D. *Chem. Commun.* **47,** 1979 (2011).

76. Tilford, R. W., Gemmill, W. R., zur Loye, H.-C. & Lavigne, J. J. *Chem. Mater.* **18,** 5296 (2006).

77. Tilford, R. W., Mugavero, S. J., Pellechia, P. J. & Lavigne, J. J. *Adv. Mater.* **20,** 2741 (2008).

78. Lanni, L. M., Tilford, R. W., Bharathy, M. & Lavigne, J. J. *J. Am. Chem. Soc.* **133,** 13975 (2011).

79. Spitler, E. L., Giovino, M. R., White, S. L. & Dichtel, W. R. *Chem. Sci.* **2,** 1588 (2011).

80. Kuhn, P., Antonietti, M. & Thomas, A. *Angew. Chem. Int. Ed.* **47,** 3450 (2008).

81. Ding, S. Y., Gao, J., Wang, Q., Zhang, Y., Song, W. G., Su, C. Y. & Wang, W. *J. Am. Chem. Soc.* **133,** 19816 (2011).

82. Uribe-Romo, F. J., Doonan, C. J., Furukawa, H., Oisaki, K. & Yaghi, O. M. *J. Am. Chem. Soc.* **133,** 11478 (2011).

83. Kandambeth, S., Mallick, A., Lukose, B., Mane, M. V., Heine, T. & Banerjee, R. *J. Am. Chem. Soc.* **134,** 19524 (2012).

84. Jackson, K. T., Reich, T. E. & El-Kaderi, H. M. *Chem. Commun.* **48,** 8823 (2012).

85. Feng, X., Dong, Y. & Jiang, D. *CrystEngComm* **15,** 1508 (2013).

86. Dogru, M., Sonnauer, A., Zimdars, S., Doblinger, M., Knochel, P. & Bein, T. *CrystEngComm* **15,** 1500 (2013).

87. Rabbani, M. G., Sekizkardes, A. K., Kahveci, Z., Reich, T. E., Ding, R. & El-Kaderi, H. M. *Chem. Eur. J.* **19,** 3324 (2013).

88. Han, S. S., Furukawa, H., Yaghi, O. M. & Goddard, W. A., III *J. Am. Chem. Soc.* **130,** 11580 (2008).

89. Furukawa, H. & Yaghi, O. M. *J. Am. Chem. Soc.* **131,** 8875 (2009).

90. Doonan, C. J., Tranchemontagne, D. J., Glover, T. G., Hunt, J. R. & Yaghi, O. M. *Nature Chem.* **2,** 235 (2010).

91. Benanti, T. & Venkataraman, D. *Photosynth. Res.* **87,** 73 (2006).

92. Wan, S., Guo, J., Kim, J., Ihee, H. & Jiang, D. *Angew. Chem. Int. Ed.* **48,** 5439 (2009).

93. Wan, S., Gándara, F., Asano, A., Furukawa, H., Saeki, A., Dey, S. K., Liao, L., Ambrogio, M. W., Botros, Y. Y., Duan, X., Seki, S., Stoddart, J. F. & Yaghi, O. M. *Chem. Mater.* **23,** 4094 (2011).

94. Jin, S., Ding, X., Feng, X., Supur, M., Furukawa, K., Takahashi, S., Addicoat, M., El-Khouly, M. E., Nakamura, T., Irle, S., Fukuzumi, S., Nagai, A. & Jiang, D. *Angew. Chem. Int. Ed.* **52,** 2017 (2013).

95. Dogru, M., Handloser, M., Auras, F., Kunz, T., Medina, D., Hartschuh, A., Knochel, P. & Bein, T. *Angew. Chem. Int. Ed.* **52,** 2920 (2013).

96. Patwardhan, S., Kocherzhenko, A. A., Grozema, F. C. & Siebbeles, L. D. A. *J. Phys. Chem. C* **115,** 11768 (2011).

97. Senthilkumar, K., Grozema, F. C., Bickelhaupt, F. M. & Siebbeles, L. D. A. *J. Chem. Phys.* **119,** 9809 (2003).

98. Spitler, E. L., Colson, J. W., Uribe-Romo, F. J., Woll, A. R., Giovino, M. R., Saldivar, A. & Dichtel, W. R. *Angew. Chem. Int. Ed.* **51,** 2623 (2012).

99. Dogru, M., Sonnauer, A., Gavryushin, A., Knochel, P. & Bein, T. *Chem. Commun.* **47,** 1707 (2011).

100. Feng, X., Liu, L., Honsho, Y., Saeki, A., Seki, S., Irle, S., Dong, Y., Nagai, A. & Jiang, D. *Angew. Chem. Int. Ed.* **51,** 2618 (2012).

101. Feng, X., Chen, L., Honsho, Y., Saengsawang, O., Liu, L., Wang, L., Saeki, A., Irle, S., Seki, S., Dong, Y. & Jiang, D. *Adv. Mater.* **24,** 3026 (2012).

102. Colson, J. W., Woll, A. R., Mukherjee, A., Levendorf, M. P., Spitler, E. L., Shields, V. B., Spencer, M. G., Park, J. & Dichtel, W. R. *Science* **332,** 228 (2011).

103. Pang, S., Hernandez, Y., Feng, X. & Müllen, K. *Adv. Mater.* **23,** 2779 (2011).

104. Berlanga, I., Ruiz-Gonzalez, M. L., Gonzalez-Calbet, J. M., Fierro, J. L., Mas-Ballesté, R. & Zamora, F. *Small* **7,** 1207 (2011).

105. Clair, S., Ourdjini, O., Abel, M. & Porte, L. *Adv. Mater.* **24,** 1252 (2012).

106. Gutzler, R., Walch, H., Eder, G., Kloft, S., Heckl, W. M. & Lackinger, M. *Chem. Commun.* **45,** 4456 (2009).

107. Ourdjini, O., Pawlak, R., Abel, M., Clair, S., Chen, L., Bergeon, N., Sassi, M., Oison, V., Debierre, J.-M., Coratger, R. & Porte, L. *Phys. Rev. B* **84,** 125421 (2011).

108. Marele, A. C., Mas-Ballesté, R., Terracciano, L., Rodríguez-Fernández, J., Berlanga, I., Alexandre, S. S., Otero, R., Gallego, J. M., Zamora, F. & Gómez-Rodríguez, J. M. *Chem. Commun.* **48,** 6779 (2012).

109. Faury, T., Clair, S., Abel, M., Dumur, F., Gigmes, D. & Porte, L. *J. Phys. Chem. C* **116,** 4819 (2012).

110. Dienstmaier, J. F., Medina, D. D., Dogru, M., Knochel, P., Bein, T., Heckl, W. M. & Lackinger, M. *ACS Nano* **6,** 7234 (2012).

111. Guan, C. Z., Wang, D. & Wan, L. J. *Chem. Commun.* **48,** 2943 (2012).

112. Slater, A. G., Beton, P. H. & Champness, N. R. *Chem. Sci.* **2,** 1440 (2011).

113. Lipton-Duffin, J. A., Ivasenko, O., Perepichka, D. F. & Rosei, F. *Small* **5,** 592 (2009).

114. Lipton-Duffin, J. A., Miwa, J. A., Kondratenko, M., Cicoira, F., Sumpter, B. G., Meunier, V., Perepichka, D. F. & Rosei, F. *Proc. Natl. Acad. Sci. U.S.A.* **107,** 11200 (2010).

115. Lafferentz, L., Ample, F., Yu, H., Hecht, S., Joachim, C. & Grill, L. *Science* **323,** 1193 (2009).

116. Cai, J., Ruffieux, P., Jaafar, R., Bieri, M., Braun, T., Blankenburg, S., Muoth, M., Seitsonen, A. P., Saleh, M., Feng, X., Müllen, K. & Fasel, R. *Nature* **466,** 470 (2010).

117. Abel, M., Clair, S., Ourdjini, O., Mossoyan, M. & Porte, L. *J. Am. Chem. Soc.* **133,** 1203 (2011).

118. Bieri, M., Nguyen, M. T., Groning, O., Cai, J., Treier, M., Ait-Mansour, K., Ruffieux, P., Pignedoli, C. A., Passerone, D., Kastler, M., Müllen, K. & Fasel, R. *J. Am. Chem. Soc.* **132,** 16669 (2010).

119. Treier, M., Richardson, N. V. & Fasel, R. *J. Am. Chem. Soc.* **130,** 14054 (2008).

120. Weigelt, S., Busse, C., Bombis, C., Knudsen, M. M., Gothelf, K. V., Laegsgaard, E., Besenbacher, F. & Linderoth, T. R. *Angew. Chem. Int. Ed.* **47,** 4406 (2008).

121. Jensen, S., Früchtl, H. & Baddeley, C. J. *J. Am. Chem. Soc.* **131,** 16706 (2009).

122. Blunt, M. O., Russell, J. C., Champness, N. R. & Beton, P. H. *Chem. Commun.* **46,** 7157 (2010).

123. Ozaki, H., Kasuga, M., Tsuchiya, T., Funaki, T., Mazaki, Y., Aoki, M., Masuda, S. & Harada, Y. *J. Chem. Phys.* **103,** 1226 (1995).

124. Takami, T., Ozaki, H., Kasuga, M., Tsuchiya, T., Ogawa, A., Mazaki, Y., Fukushi, D., Uda, M. & Aono, M. *Angew. Chem. Int. Ed. Engl.* **36,** 2755 (1997).

125. Miura, A., de Feyter, S., Abdel-Mottaleb, M. M. S., Gesquière, A., Grim, P. C. M., Moessner, G., Sieffert, M., Klapper, M., Müllen, K. & De Schryver, F. C. *Langmuir* **19,** 6474 (2003).

126. Okawa, Y. & Aono, M. *Nature* **409,** 683 (2001).

CHAPTER 2 - APPENDIX

SUPPLEMENTARY INFORMATION

A. Materials and Instrumentation. 1,4-phenylenebis(boronic acid) (PBBA) and 2,3,6,7,10,11-hexahydroxytriphenylene (HHTP), 1,4-dioxane, and mesitylene were purchased from commercial sources and used without further purification. Other solvents were purchased from commercial sources and purified using a custom-built activated alumina solvent purification system.

Fourier transform infrared spectroscopy (FTIR) was performed on a Thermo Nicolet iS10 spectrometer with a diamond ATR attachment. The spectra are uncorrected.

UV/Vis/NIR absorbance spectroscopy of powder samples was performed on a Cary 5000 spectrophotometer using a praying mantis diffuse reflectance accessory. The background was recorded using potassium iodide ground in a mortar and pestle. Transmission mode spectra were recorded of COF films grown on SLG/SiO_2 substrates (~1.5 cm^2). The background was recorded using a similar SLG/SiO_2 substrate without the COF film.

Photoemission and excitation experiments were performed on a Horiba Jobin Yvon Fluorolog-3 fluorescence spectrophotometer equipped with a 450 W Xe lamp, double excitation and double emission monochromators, a digital photon-counting photomultiplier, and a secondary InGaAs detector for the NIR range. Correction for variations in lamp intensity over time and wavelength was achieved with a solid-state silicon photodiode as the reference. The spectra were further corrected for variations in photomultiplier response over wavelength and for the path difference between the sample and the reference by multiplication with emission correction curves generated

on the instrument. Emission from COF films on SLG/SiO_2 was observed using a front face detection accessory.

Powder X-ray diffraction (PXRD) was performed on a Rigaku SmartLab X-Ray diffractometer in reflectance parallel beam/parallel slit alignment geometry. The measurement employed Cu Kα line focused radiation at 1760 W (40 kV, 44 mA) power and a Ge crystal detector fitted with a 1.0 mm radiation entrance slit. Samples were mounted on zero-background sample holders by dropping powders from a wide-blade spatula and then leveling the sample surface with a glass microscope slide. No sample grinding or sieving was used prior to analysis. Samples were observed using a 0.04º 2θ step scan from 2.0 – 34.0º with an exposure time of 0.4 s per step. No peaks could be resolved from the baseline for 2θ > 34º data and this region was not considered for further analysis.

Grazing incidence X-ray diffraction (GIXD) was performed at the G2 station at Cornell High Energy Synchrotron Source (CHESS) using a beam energy of 8.64 ± 0.01 keV (λ = 0.1435 nm), selected using a single-crystal Be crystal monochromator. Motorized slits were used to define a 0.2 × 3 (V×H) mm^2 beam, with a typical flux of 2×10^{10} photons/s. The data were collected using a 640-element 1D diode-array, of which each element incorporates its own pulse counting electronics capable of count rates of ~10^5 photons/s. A set of 0.1° Soller slits were used on the detector arm to define the in-plane resolution. The scattering geometry is described in detail elsewhere[1]. Each data set was collected by scanning the detector with the sample stationary. The incidence angle α between the beam and sample surface was 0.175°. Axes labels $Q_\perp$ and $Q_\parallel$ are defined using the GISAXS convention $Q_\perp = 4\pi/\lambda\sin(\delta/2)$

and $Q_{\|} = 4\pi/\lambda\sin(\nu/2)$, where δ and ν are the vertical and horizontal scattering angles, respectively[2]. At $\alpha=\delta=0$, $\hbar Q_{\|}$ and $\hbar Q_{\perp}$ (where $\hbar$ is Planck's constant) are the components of momentum transfer parallel and perpendicular to the sample surface, respectively.

Scanning electron microscopy (SEM) was performed on a FEI Strata 400 FESEM. Materials were deposited onto a sticky carbon surface on a flat aluminum platform sample holder. No metal sputtering of the sample was necessary.

Focused ion beam (FIB) patterning and milling was performed using a FEI Strata 400 FIB Ga^+ LIM system. A 1x10 μm Pt strip (~400 nm thickness) was deposited using the electron gun onto COF films grown on SLG/Cu and SLG/SiC substrates prior to exposing the sample to the FIB. The sample was then milled with the FIB using a cleaning cross-section. After milling, the samples were imaged at 5 keV using the electron gun. Cross-sectional images were obtained using a stage tilt angle of 52°. Thickness measurements made at this angle were corrected by multiplying by 1.26. SLG/SiO_2 substrates were grounded to the sample holder using sticky carbon prior to imaging to minimize charging. Top down and cross-sectional images at 2 keV were obtained in the same manner as the SLG/Cu and SLG/SiC substrates.

B. Methods. Graphene growth. Single-layer graphene was grown on Cu films using previously reported chemical vapor deposition methods[3,4]. For SLG/SiO_2 substrates, SLG was grown on 25 μm-thick copper foil. A layer of PMMA (50 nm) was spin-coated on top of the graphene and the copper was etched using aq. $FeCl_3$. The graphene was then transferred to fused SiO_2 and the PMMA removed by washing with $(CH_3)_2CO$. The SLG/SiO_2 was finally calcined at 300 °C for 2.5 h. Epitaxial SLG was grown on SiC using a modified cold wall CVD-type reactor with dual heater elements. Some samples were prepared under high vacuum growth conditions in the 10^{-6} to 10^{-5} torr range. Additional samples utilized a near atmospheric argon pressure growth environment. The temperature regime was 1300 – 1450 °C for growth in vacuum and 1350 – 1550 °C in a low argon flow (0.7 bar to 1.2 bar). Semi-insulating chemical-mechanical polished (CMP) 1.2 cm x 1.2 cm SiC wafer pieces were used as growth substrates.

General procedure COF-5 film growth on SLG. HHTP (16 mg, 0.049 mmol) and PBBA (25 mg, 0.15 mmol) were added to a 15 mL cylindrical pressure vessel and suspended in a mixture of mesitylene and 1,4-dioxane (v/v 1:1; 1.0 mL). After capping, the mixture was sonicated for 30 min and a graphene-containing substrate was added. The sealed vessel was heated in a 90 °C oven for a given reaction time. The vessel was cooled to room temperature and the resulting gray powder was recovered by filtration and dried under vacuum. The graphene-containing substrate was submerged in anhydrous toluene (10 mL) overnight, sonicated for 5 sec, and finally dried under vacuum. The PXRD, FTIR, and BET surface areas of the COF-5 powder samples matched the previous report[5].

General procedure for the growth of TP-COF film on SLG/SiO_2. The above procedure was followed using pyrene-2,7-diboronic acid[6] (50 mg, 0.17 mmol) and HHTP (35 mg, 0.11 mmol) reactants. Crystalline films were observed in as few as 2 hours. The PXRD and FTIR of the TP-COF powder matched the previous report[7]. These data, as well as the GIXD data and SEM images of the TP-COF thin films, are provided in section F.

General procedure for the growth of NiPc-PBBA COF film on SLG/SiO_2. The general growth procedure was followed using Ni octahydroxyphthalocyanine[8] (10 mg, 0.014 mmol) and PBBA (7.0 mg, 0.042 mmol) reactants and a mixture of 1,4-dioxane (1.0 mL) and MeOH (0.5 mL) as the solvent. The reaction vessel was heated to 120 °C in an oven for 18 h. PXRD and FTIR of the powders matched our own data of this material grown in the absence of SLG as well as recent published reports[9,10]. These data, as well as the GIXD data and SEM images of the NiPc-PBBA COF films on SLG/SiO_2, are provided in section G.

C. COF-5 Powder Characterization. The following PXRD and FTIR data are representative of COF-5 powders isolated from reaction mixtures that include an SLG/Cu substrate.

Figure S2.1. A representative PXRD pattern of an unwashed sample of COF-5 powder synthesized in the presence of an SLG/Cu substrate (14 h reaction time for this sample).

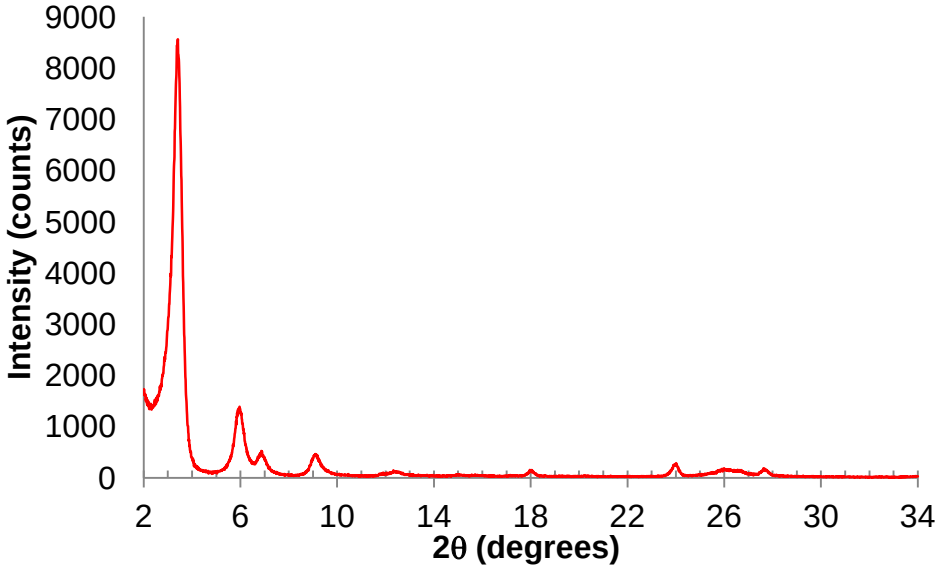

Figure S2.2. A representative FTIR spectrum of an unwashed sample of COF-5 powder synthesized in the presence of an SLG/Cu substrate (14 h reaction time for this sample). The OH-stretch region near 3350 cm^{-1} of this sample is more attenuated than in previous reports of this material.

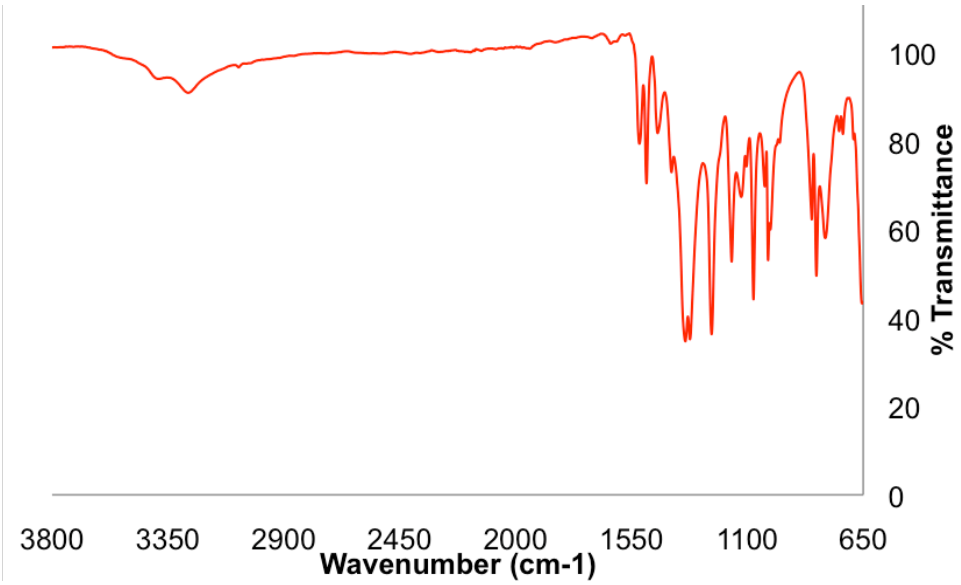

Formation of crystalline COF-5 as a function of reaction time and the presence of an SLG-containing substrate. As discussed in Chapter 2, we found that the formation of crystalline COF-5 required shorter reaction times than had been reported previously. The following PXRD data show the evolution of crystallinity of COF-5 as a function of reaction time in the presence of SLG/SiO_2. The COF-5 diffractions appear even at the earliest reaction times (compared to Fig. S2.1), though these data also show prominent residual starting materials. The diffraction patterns are dominated by COF-5 at reaction times of 1 h and longer both in the presence and absence of SLG/SiO_2 as shown in Fig. S2.4.

Figure S2.3. PXRD patterns of COF-5 powder synthesized in the presence of SLG/Cu for varying reaction times.

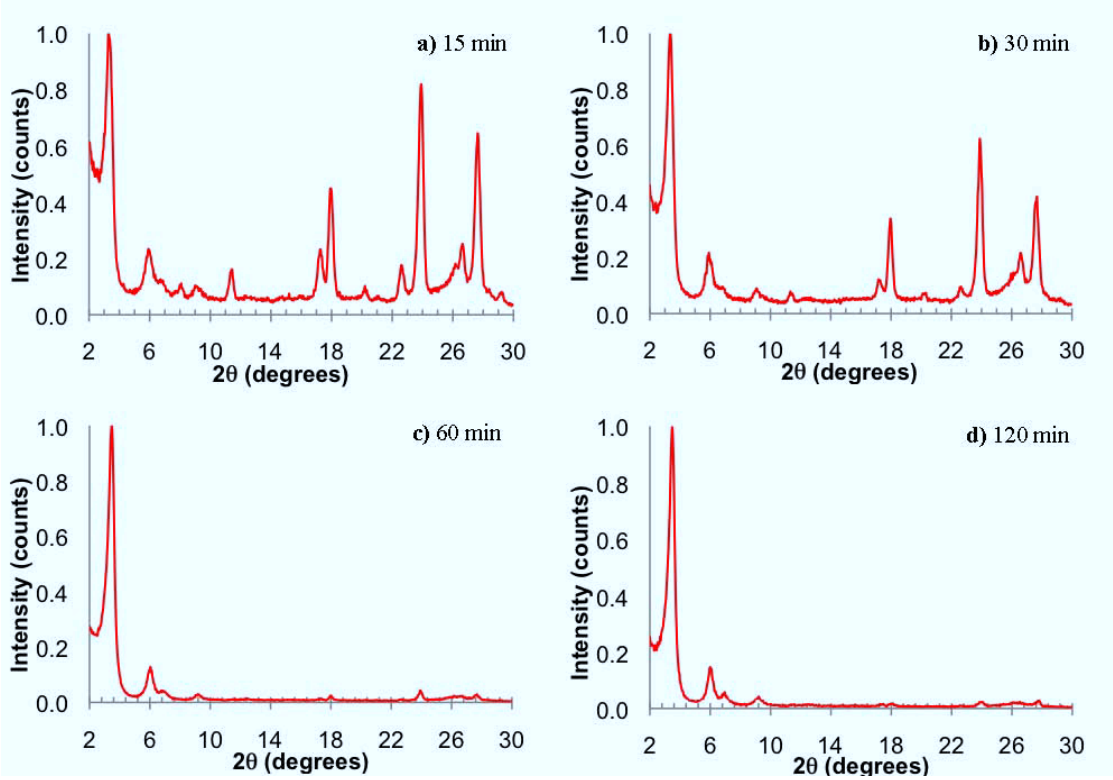

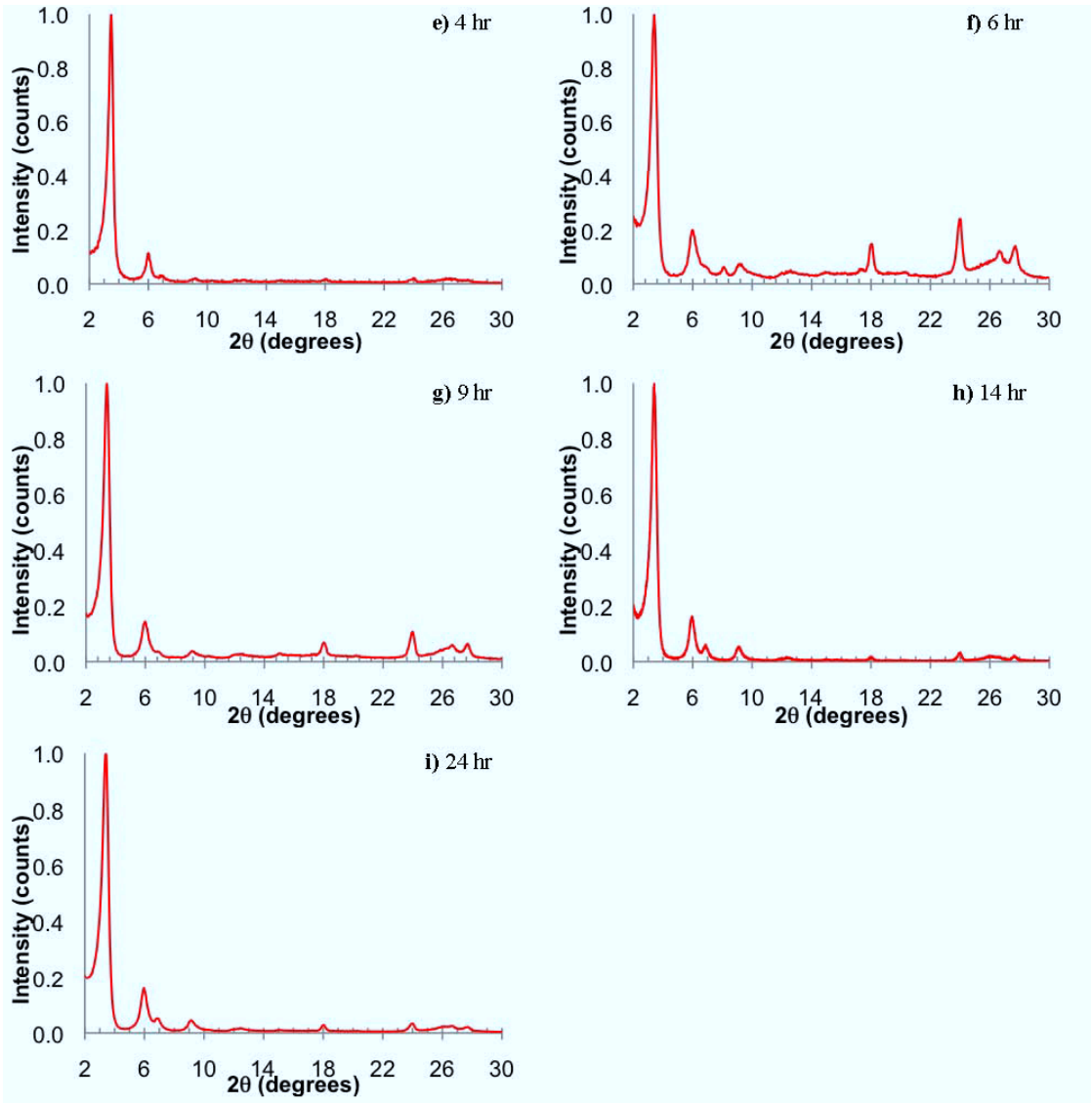

Figure S2.4. Three overlaid PXRD patterns of COF-5 powder synthesized in the absence (**a**) and presence (**b**) of SLG. All reaction times are 1 h.

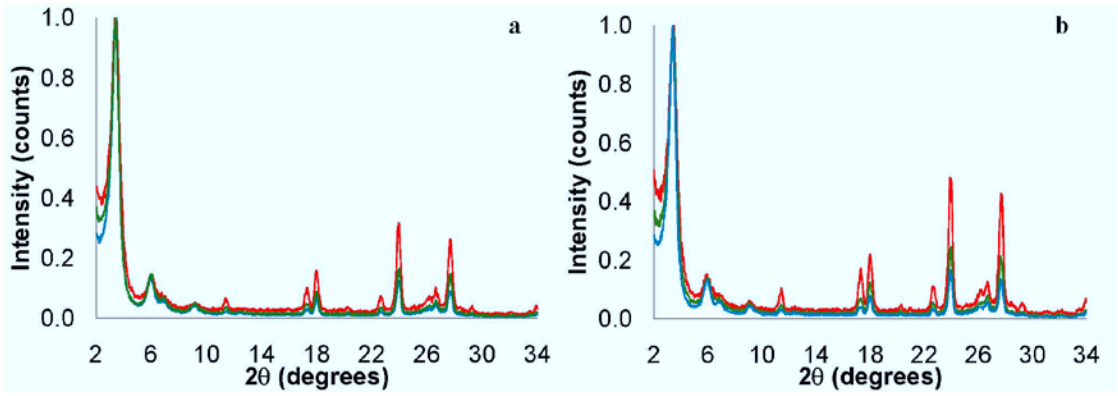

D. Mosaicity Estimate from GIXD. GIXD scans in Figs. 2.2, 2.3, and 2.4 indicate that the COF films described here have fiber texture: that is, the π-stacking direction is distributed about the substrate surface normal. To obtain an estimate of the angular distribution, the azimuthal position of 001 intensity in scans such as shown in Figure 2.2D is calculated as $\chi = \tan^{-1}(Q_{\parallel}/Q_{\perp})$. The scaled, background-subtracted results for each of the three films in Fig. 2.3 are shown in Figure S2.5, showing nearly identical distributions for each of the three films. The FWHM of these distributions is ~26°. Note that because these scans are obtained in grazing incidence rather than in specular geometry, they do not correspond to ideal pole figure scans[2]. Nevertheless, we believe these scans provide a reasonable estimate – or at worst an upper bound – of the orientational order in the films. Finally, we note that this estimate is in rough agreement with analysis of Figs. 2.3B, 2.3D, and 2.3F, based on azimuthal integration of in-plane Bragg peaks.

Figure S2.5. Azimuthal intensity distribution of (001) Bragg peaks from three COF-5 films grown on different substrates, based on scans identical to that shown in Fig. 2.2D.

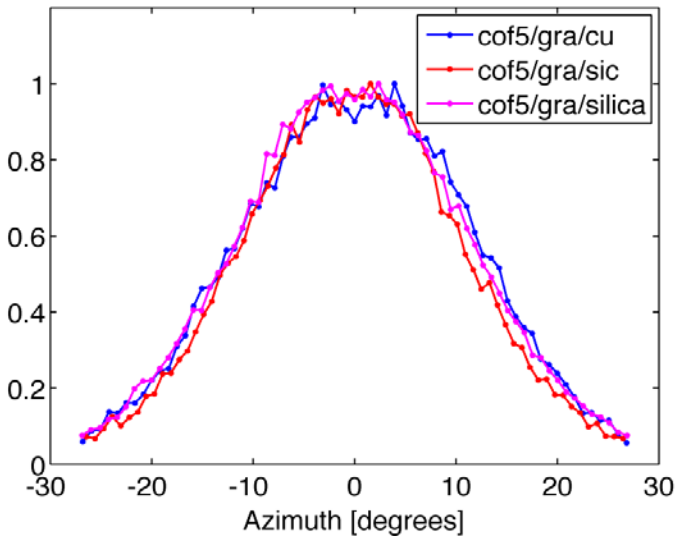

E. Micrographs of COF-5 Films on SLG/Cu, SLG/SiO_2, and SLG/SiC.

Figure S2.6. Top-down SEM image of COF-5 film on SLG/Cu (growth time: 30 min).

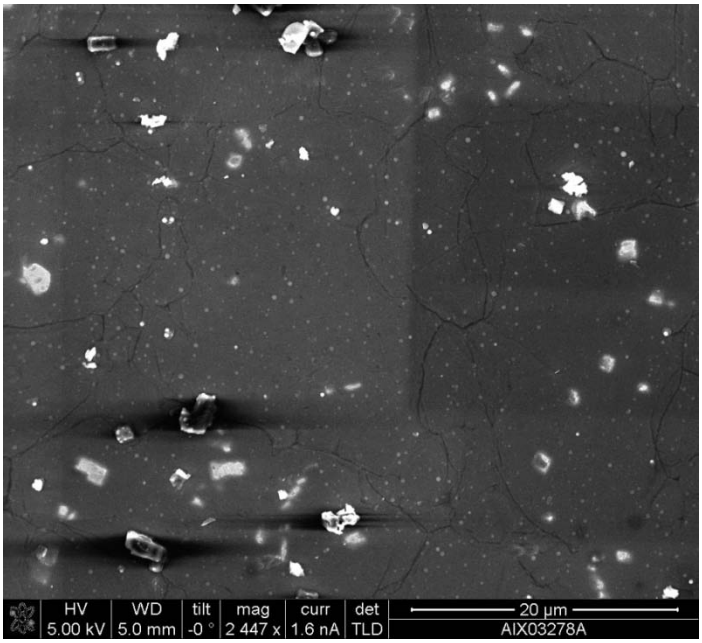

Figure S2.7. Cross-sectional SEM image of COF-5 film grown on SLG/Cu (growth time: 30 min). The film thickness was obtained by multiplying the measured values by 1.26. From top to bottom, the layers are Pt, COF-5 film, Cu, SiO_2, and Si.

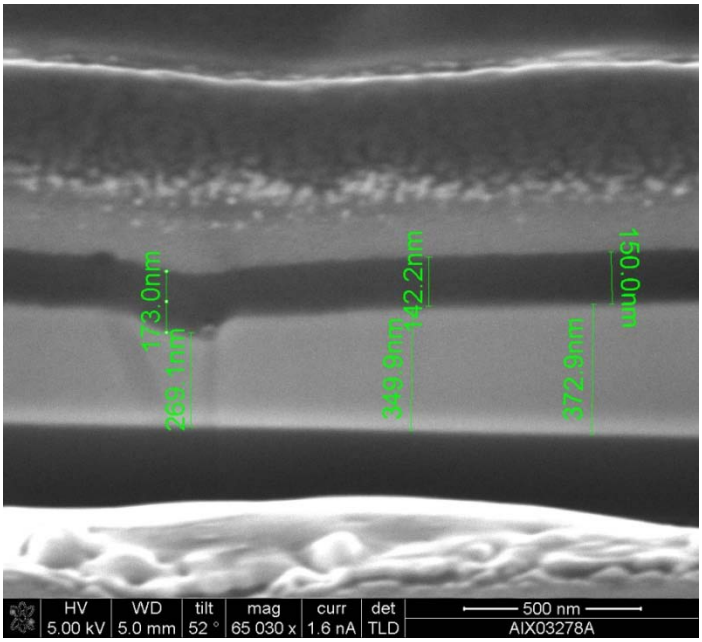

Figure S2.8. Top-down SEM image of COF-5 film on SLG/Cu (growth time: 2 h). The Pt bar (1 μm x 10 μm) was deposited on top of the film prior to milling.

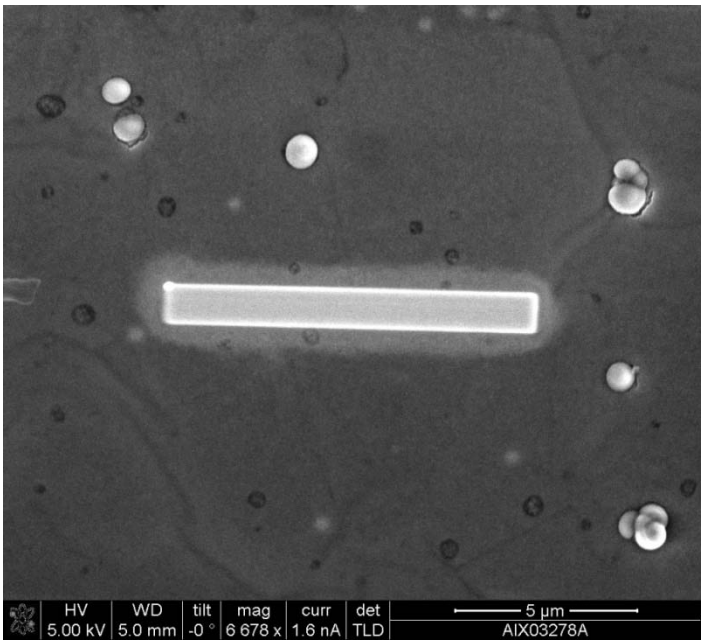

Figure S2.9. Cross-sectional SEM image of COF-5 film grown on SLG/Cu (growth time: 2 h). The film thickness was obtained by multiplying the measured values by 1.26. From top to bottom, the layers are Pt, COF-5 film, Cu, and SiO_2.

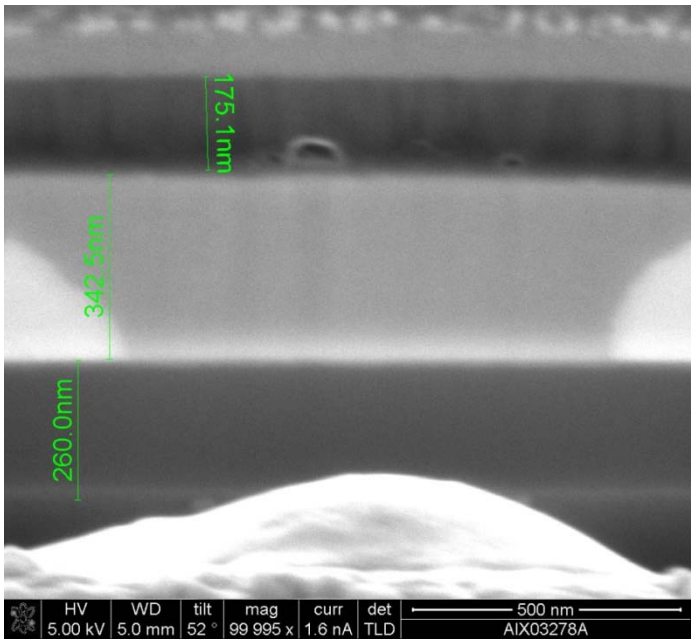

Figure S2.10. Top-down SEM image of COF-5 film grown on SLG/SiO_2 (growth time: 2 h).

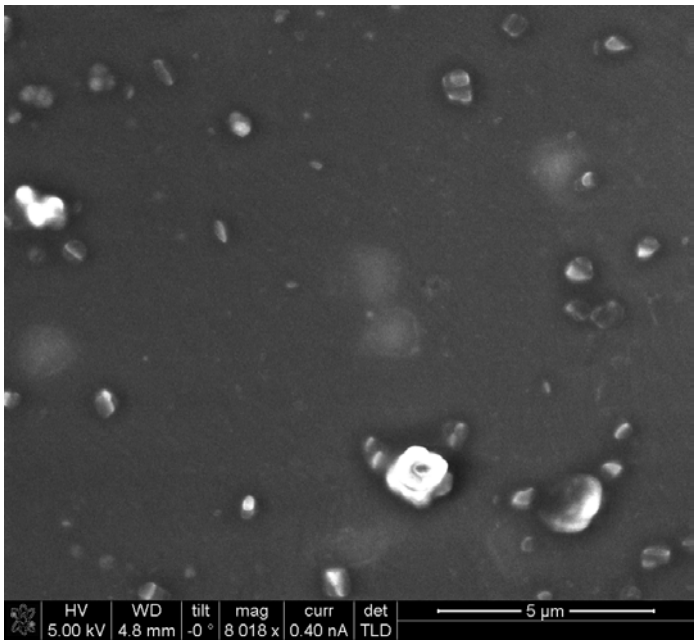

Figure S2.11. Cross-sectional SEM images of COF-5 films grown on SLG/SiO_2 (growth time: 2 h). The film thickness was obtained by multiplying the measured values by 1.26. From top to bottom, the layers are Pt, COF-5 film, and SiO_2.

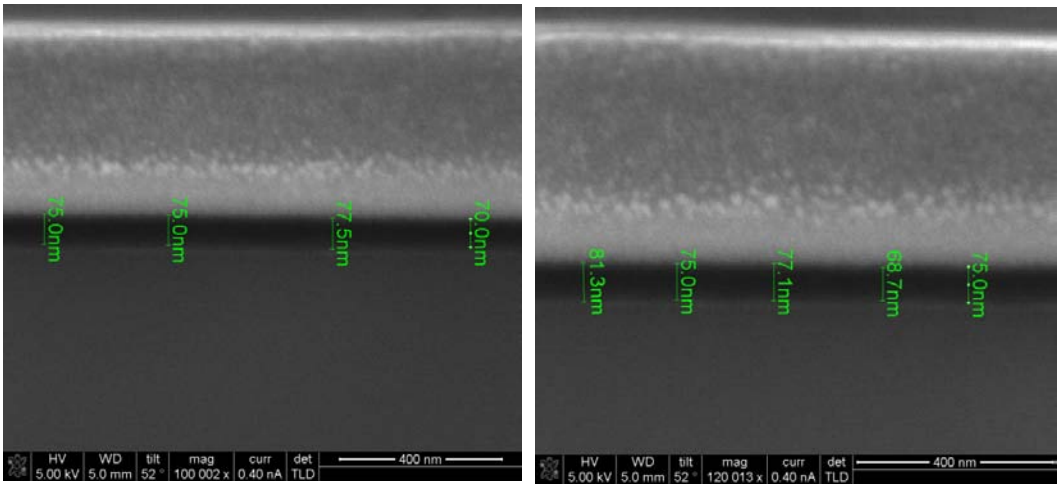

Figure S2.12. Top-down SEM image of COF-5 film grown on SLG/SiC (growth time: 8 h).

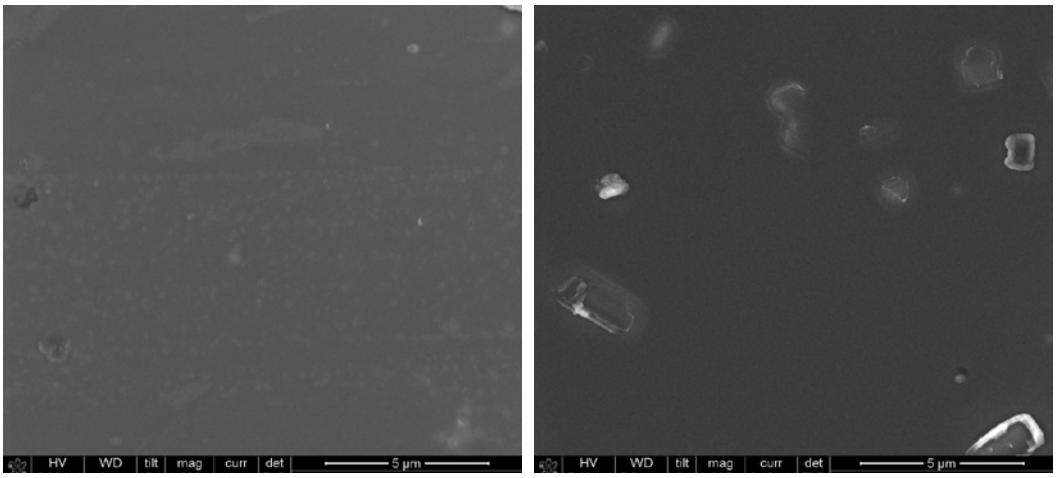

Figure S2.13. Cross-sectional SEM images at different magnifications of COF-5 film grown on SLG/SiC (growth time: 8 h). The film thickness was obtained by multiplying the measured values by 1.26. From top to bottom, the layers are Pt, COF-5 film, and SiC.

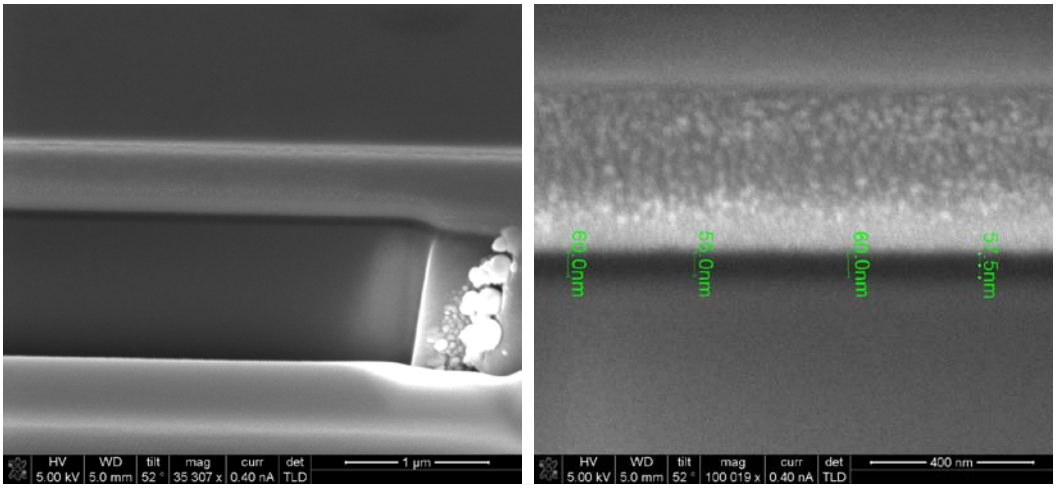

F. TP-COF Powder Characterization and Micrographs of Films.

Figure S2.14. PXRD pattern of an unwashed TP-COF powder synthesized in the presence of SLG/Cu (reaction time = 4 h).

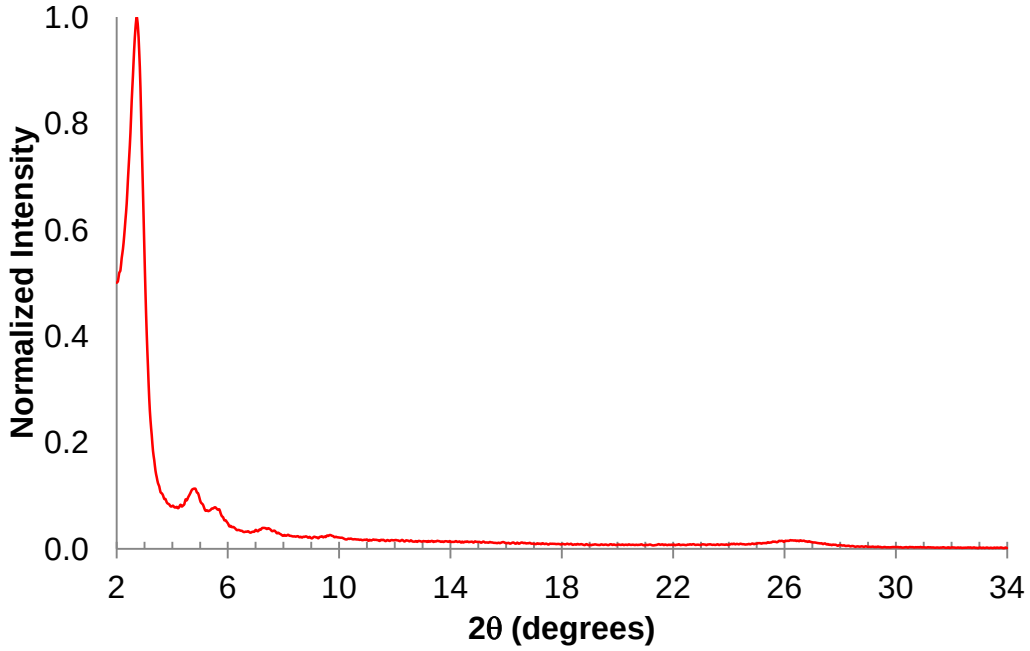

Figure S2.15. FTIR spectrum of an unwashed TP-COF powder synthesized in the presence of SLG/Cu (reaction time = 4 h).

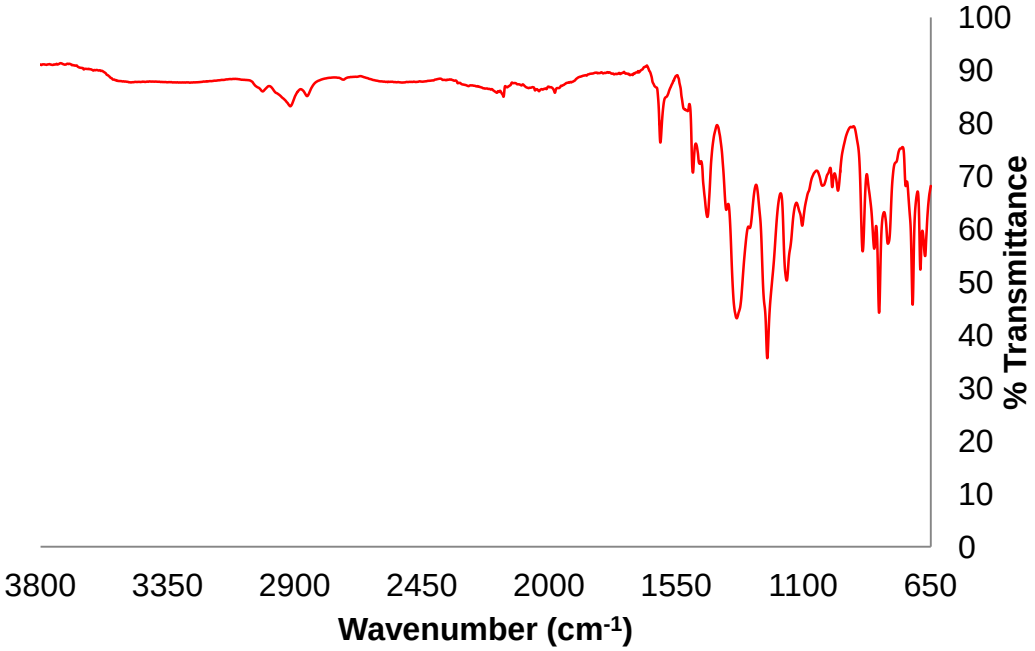

Figure S2.16. Top-down SEM of TP-COF film on SLG/SiO_2 (growth time: 4 h).

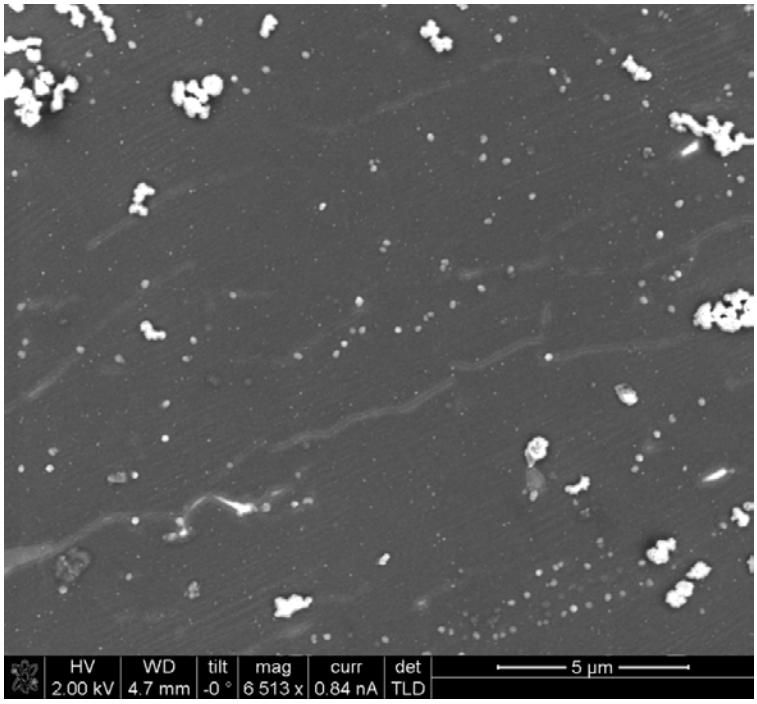

Figure S2.17. Cross-sectional SEM of TP-COF film on SLG/SiO_2 (growth time: 4 h). From top to bottom, the layers are Pt, C thin film, TP-COF film, SiO_2 (appears white due to charging).

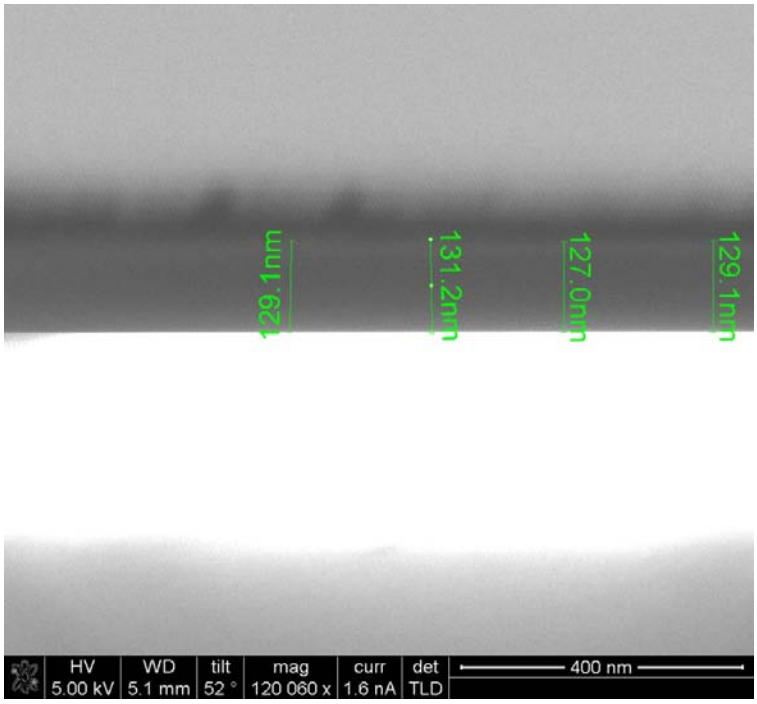

I. NiPc-PBBA COF Micrographs of Films and Powder Characterization

Figure S2.18. Top-down SEM of NiPc-PBBA COF film on SLG/SiO_2 (growth time: 18 h).

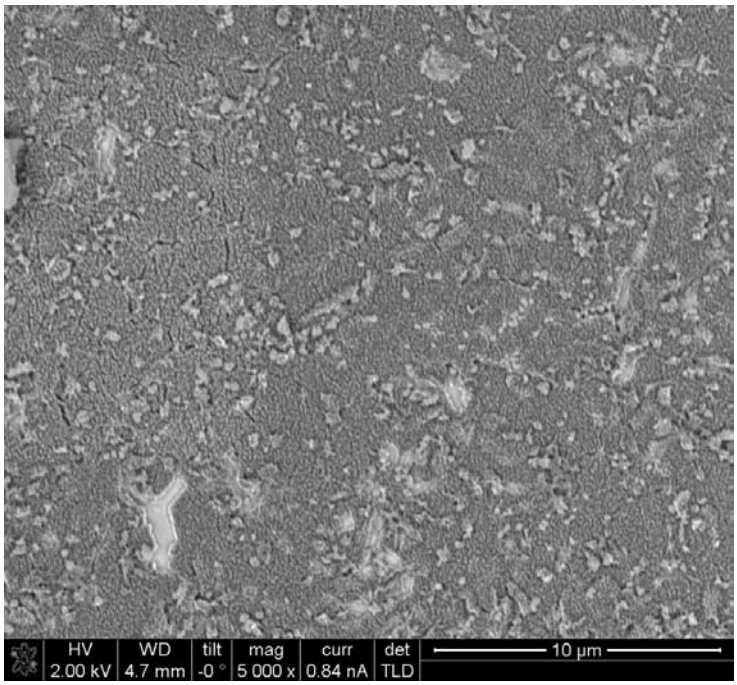

Figure S2.19. Cross-sectional SEM image of NiPc-PBBA COF grown on SLG/SiO_2 (growth time: 18 h).

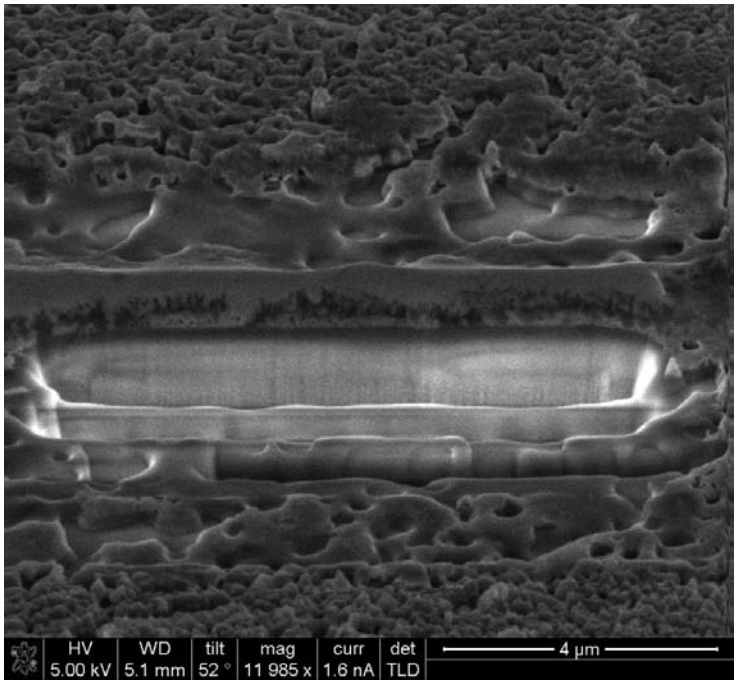

Figure S2.20. PXRD pattern of an unwashed NiPc-PBBA COF powder grown in the presence of SLG/SiO_2 (growth time: 18 h).

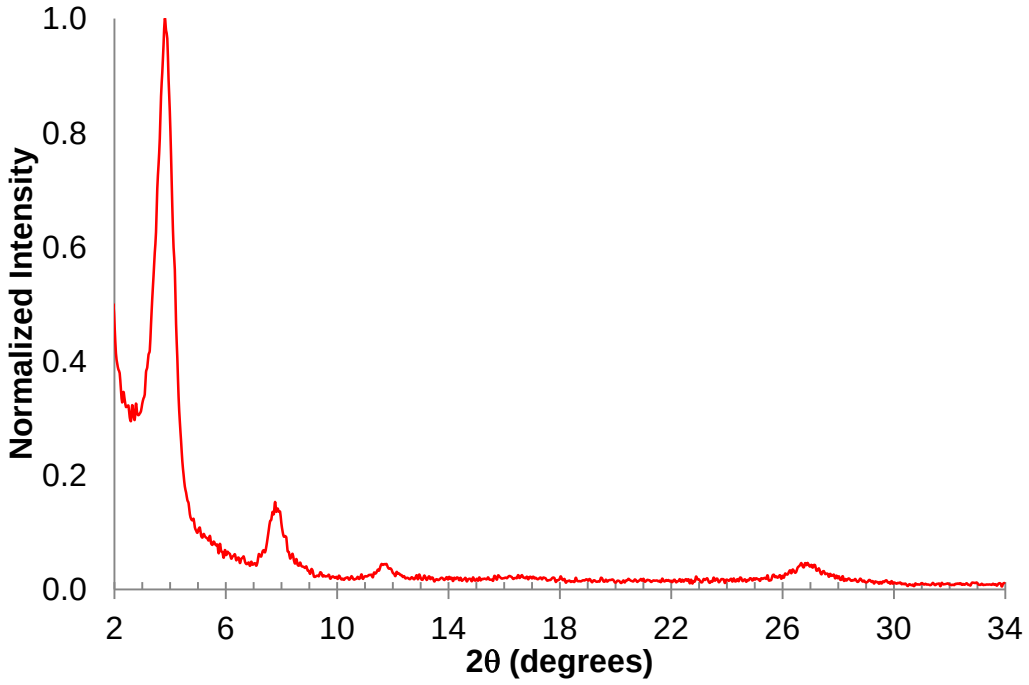

Figure S2.21. FTIR spectrum of an unwashed NiPc-PBBA COF powder grown in the presence of SLG/SiO_2 (growth time: 18 h).

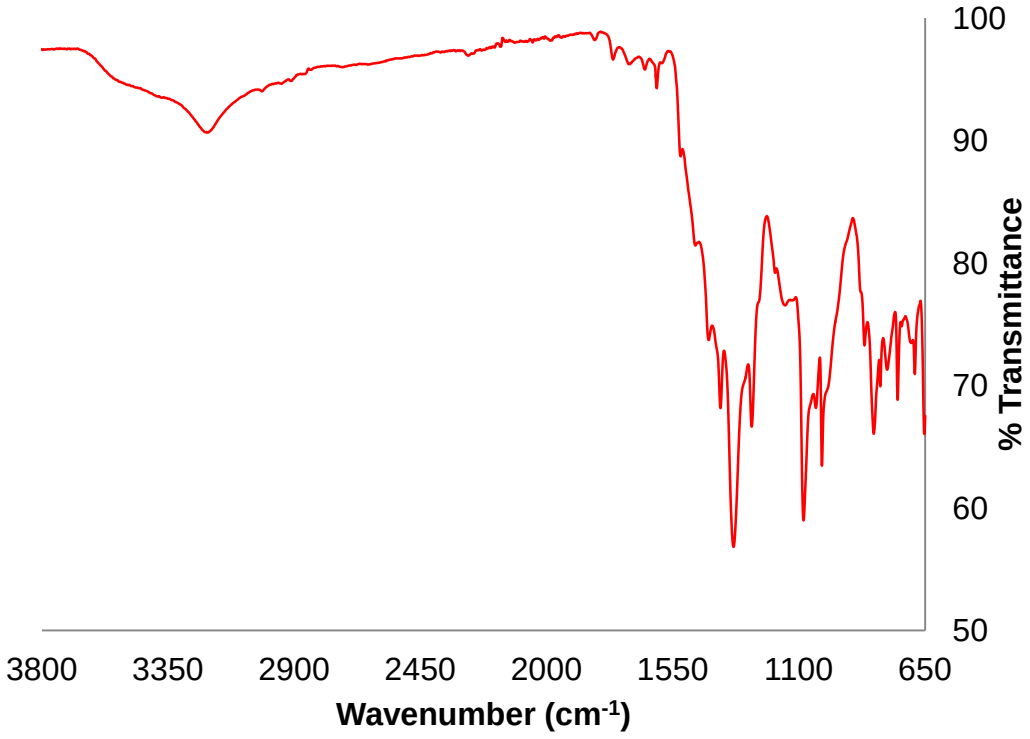

REFERENCES

1. Smilgies, D. M., Blasini, D. R., Hotta, S. & Yanagi, H. *J. Synchrotron Radiat.* **12**, 807 (2005).

2. Baker, J. L., Jimison, L. H., Mannsfeld, S., Volkman, S., Yin, S., Subramanian, V., Salleo, A., Alivisatos, A. P. & Toney, M. F. *Langmuir* **26**, 9146 (2010).

3. Li, X., Cai, W., An, J., Kim, S., Nah, J., Yang, D., Piner, R., Velamakanni, A., Jung, I., Tutuc, E., Banerjee, S. K., Colombo, L. & Ruoff, R. S. *Science* **324,** 1312 (2009).

4. Levendorf, M. P., Ruiz-Vargas, C. S., Garg, S. & Park, J. *Nano Lett.* **9**, 4479 (2009).

5. Côté, A. P., Benin, A. I., Ockwig, N. W., O'Keeffe, M., Matzger, A. J. & Yaghi, O. M. *Science* **310,** 1166 (2005).

6. Tzschucke, C. C., Murphy, J. M. & Hartwig, J. F. *Org. Lett.* **9**, 761 (2007).

7. Wan, S., Guo, J., Kim, J., Ihee, H., & Jiang, D. *Angew. Chem. Int. Ed.* **47**, 8826 (2008).

8. Baugh, S. D. P., Yang, Z. W., Leung, D. K., Wilson, D. M. & Breslow, R. *J. Am. Chem. Soc.* **123**, 12488 (2001).

9. Ding, X., Guo, J., Feng, X., Honsho, Y., Seki, S., Maitarad, P., Saeki, A., Nagase, S., & Jiang, D. *Angew. Chem. Int. Ed.* **50,** 1289 (2011).

10. Spitler, E. L., Giovino, M. R., White, S. A. & Dichtel, W. R. *Chem. Sci.* **2,** 1588 (2011).

CHAPTER 2

ORIENTED 2D COVALENT ORGANIC FRAMEWORK THIN FILMS ON SINGLE-LAYER GRAPHENE

Abstract

Covalent organic frameworks (COFs), in which molecular building blocks form robust, microporous networks, are usually synthesized as insoluble and unprocessable powders. We have grown two-dimensional (2D) COF films on single-layer graphene (SLG) under operationally simple solvothermal conditions. The layered films stack normal to the SLG surface and show improved crystallinity compared to COF powders. SLG surfaces supported on Cu, SiC, and transparent fused silica (SiO_2) substrates were used, enabling optical spectroscopy of COFs in transmission mode. Three chemically distinct COF films grown on SLG exhibit similar vertical alignment and long-range order, and two of these are of interest for organic electronic devices for which thin film formation is a prerequisite for characterizing their optoelectronic properties.

This work was done in collaboration with Arthur R. Woll at the Cornell High Energy Synchrotron Source, Mark P. Levendorf and Prof. Jiwoong Park in the Department of Chemistry at Cornell University, and Virgil B. Shields and Prof. Michael G. Spencer in the Department of Electrical Engineering at Cornell University. This chapter was first published in *Science*: Colson, J. W., Woll, A.R., Mukherjee, A., Levendorf, M.P., Spitler, E.L., Shields, V.B., Spencer, M.G., Park, J. & Dichtel, W.R. *Science* **332,** 228 (2011). Reproduced with permission from AAAS.

Methods for crystallizing organic subunits into predictable two-dimensional (2D) and three-dimensional covalent organic frameworks (COFs) remain in their infancy[1-4]. COFs organize molecular components into periodic networks linked by covalent bonds, providing predictable structures with long-range order usually only found in noncovalent assemblies. These materials exhibit many desirable properties, including outstanding thermal stability, permanent porosity with high specific surface area, and the lowest densities of any organic material[5]. However, the frameworks are inherently cross-linked and insoluble and are produced as either microcrystalline powders from solvothermal reactions or submonolayers by sublimation of the monomers onto crystalline metal surfaces[6-9]. The limited utility of these forms precludes many applications for COFs. For example, 2D layered COFs incorporate functional π-electron systems into ordered structures ideally suited for optoelectronic devices[10-13]. As unprocessable powders, these materials cannot be interfaced reliably to electrodes or incorporated into devices to harness or even quantify these properties. We now report the synthesis of oriented 2D layered COF films on single-layer graphene (SLG) surfaces.

The remarkable optical, electronic, and mechanical properties of SLG have attracted considerable interest, for example, as a possible replacement for tin-doped indium oxide transparent electrodes[14,15]. Its 2D, atomically precise structure is also well suited for interfacing to 2D layered networks. Large-scale graphene synthesis by metal-based chemical vapor deposition (CVD) has advanced dramatically in recent years[16-19], including the high-throughput growth of 30-inch wide samples supported on plastic substrates[20]. We demonstrate that oriented COF films form under operationally

simple solvothermal conditions on SLG supported by several different substrate materials: polycrystalline Cu films on Si wafers (SLG/Cu), fused SiO_2 (SLG/SiO_2), and SiC (SLG/SiC). The COF films are crystalline and oriented with their aromatic groups stacked perpendicular to the SLG surface on each substrate. Three boronate ester-linked COFs have been crystallized as thin films, including a square Ni phthalocyanine lattice of interest for organic photovoltaic devices[12,13].

The solvothermal condensation of 1,4-phenylenebis(boronic acid) (PBBA) and 2,3,6,7,10,11-hexahydroxytriphenylene (HHTP) in a mixture of mesitylene:dioxane (1:1 v/v) at 90 °C in the presence of SLG/Cu forms a framework known as COF-5

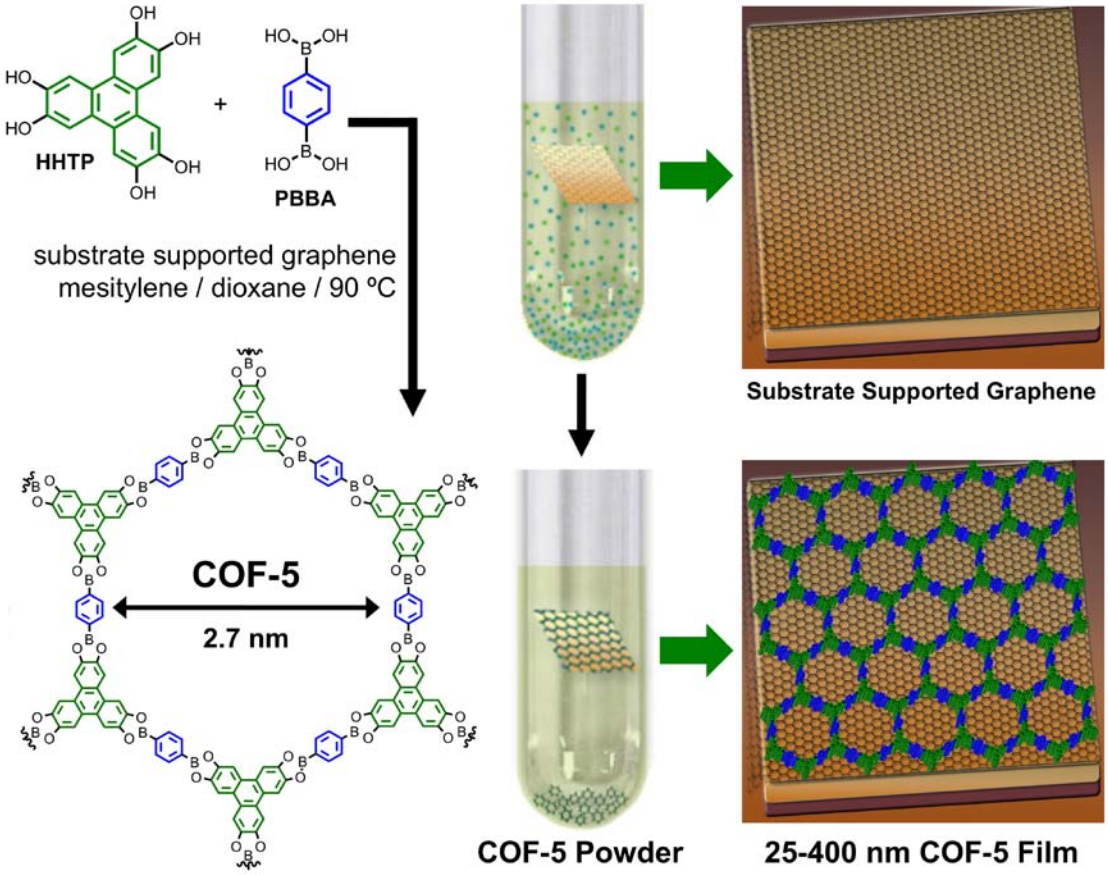

Figure 2.1 | The solvothermal condensation of HHTP and PBBA in the presence of a substrate supported single-layer graphene surface provides COF-5 as both a film on the graphene surface as well as a powder precipitated in the bottom of the reaction vessel.

(Fig. 2.1), both as an insoluble powder and as a continuous film on the graphene surface[21]. Powder x-ray diffraction (PXRD, see Chapter 2 appendix Fig. S2.1) and Fourier transform infrared spectroscopy (FTIR) of the unpurified powders (Fig. S2.2) indicated that crystalline COF-5 was obtained with only minor amounts of residual reactants in as little as 1 h (Fig. S2.3), faster than the 72 h reaction time used for its discovery[1]. These observations prompted us to investigate whether graphene catalyzes COF-5 powder formation, but we obtained similar results in the absence of SLG (Fig. S2.4). We conclude that long reaction times are not always necessary to produce COFs, suggesting that their films might be incorporated into devices more rapidly than previously thought.

The crystallinity of the COF-5 films and powders was compared using synchrotron X-ray diffraction. Figures 2.2A and 2B show 2D X-ray diffraction patterns obtained from a powder sample and a film grown on SLG/Cu, respectively, using identical incident beam and scan parameters. The data in Fig. 2.2A were collected in transmission mode by suspending a ~0.1 mm thick powder sample perpendicular to the incident beam. The Bragg peaks in Fig. 2.2A appear as rings because of the random orientation of grains in the sample (see inset). Figure 2.2B, as well as all subsequent diffraction data obtained from films use grazing incidence diffraction (GIXD), in which the substrate surface is horizontal and nearly parallel to the incident beam. Axes labels $Q_{\perp}$ and $Q_{\parallel}$ are defined using the convention $Q_{\perp} = 4\pi/\lambda\sin(\delta/2)$ and $Q_{\parallel} = 4\pi/\lambda\sin(\nu/2)$, where δ and ν are the vertical and horizontal scattering angles, respectively[22]. In contrast to Fig. 2.2A, the scattered intensity in Fig. 2.2B is concentrated near $Q_{\perp} = 0$, indicating that grains in the film exhibit fiber

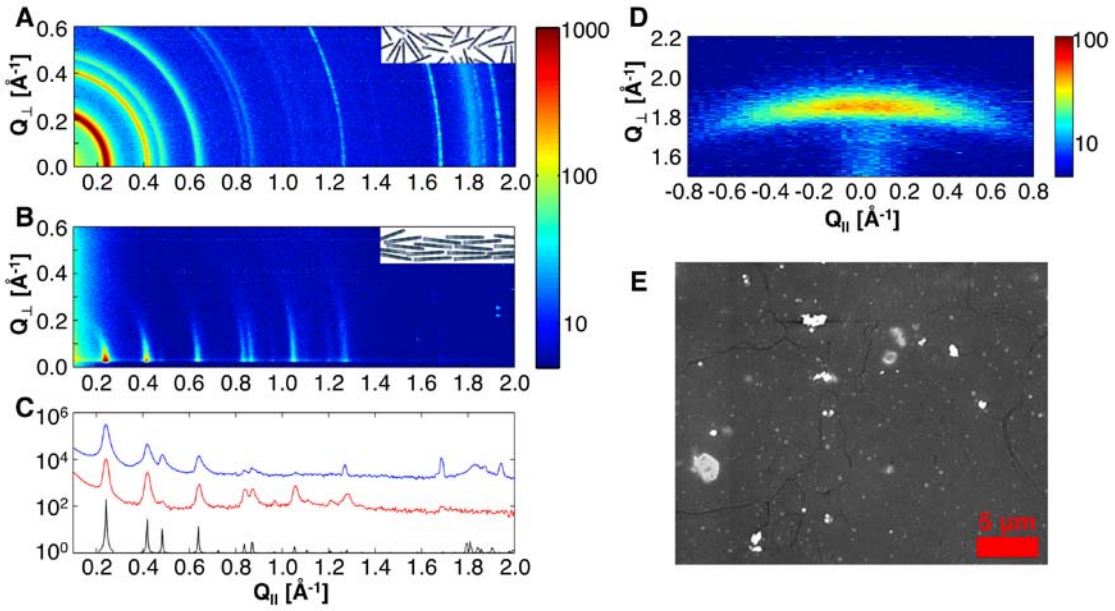

Figure 2.2 | (A) X-ray scattering data obtained from COF-5 powder; (inset) schematic of randomly oriented COF-5 grains in the powder, as indicated by **(A)**. **(B)** GIXD data from a COF-5 film on SLG/Cu; (inset) schematic of oriented COF-5 grains in the film, as indicated by **(B)**; **(C)** Projections of **A** (top/blue) and **B** (middle/red) near $Q_\perp$= 0, and the simulated powder diffraction spectrum (bottom/black) for COF-5; **(D)** GIXD data obtained at large $Q_\perp$, showing an off-specular projection of the COF-5 film (001) Bragg peak; **(E)** Top-down SEM image of the COF-5 thin film studied in **B**, **C**, and **D**.

texture: their *c*-axis orientations are centered about the surface normal, but they are randomly rotated about this axis (see inset). Projections of these data sets near $Q_\perp = 0$ (Fig. 2.2C) indicate peaks from both samples at 0.24, 0.42, 0.48, 0.64, 0.84, and 0.88 Å^{-1}, corresponding to 100, 110, 200, 210, 220, and 310 Bragg peaks of a hexagonal lattice with $a = b = 29.9$ Å, extremely close to the calculated (30.0 Å) and measured (29.7 Å) values previously reported for COF-5 powders[1]. The concentration of these peaks near $Q_\perp = 0$ in the film show that the hexagonal lattice of the COF-5 grains is aligned parallel to the substrate surface.

Figure 2.2C highlights additional peaks not shared by both samples. First, the film exhibits additional diffraction peaks at 0.97, 1.06, 1.21 and 1.27 Å^{-1} that are not

present in Fig. 2.2A or in reported PXRDs of COF-5 powder. These peaks correspond to the COF-5 400, 320, 500, and overlapping 330 and 420 Bragg peaks. Additionally, the 200 peak (at 0.48 $Å^{-1}$) is attenuated in the film compared to the powder. This difference can arise from trace impurities in the pores or from subtle differences in the horizontal offset between layers in the film compared to the powder[23]. Powder rings in Fig. 2.2A at 1.27, 1.68, 1.87, and 1.94 $Å^{-1}$ correspond to Bragg peaks from residual starting materials trapped in the pores of the unpurified powder samples. The broad powder ring in Fig. 2.2A centered at 1.83 $Å^{-1}$ corresponds to the 001 Bragg peak, and indicates that the stacked COF-5 sheets are in van der Waals contact (c = 3.43 Å). This peak is absent in Fig. 2.2B because the c-axes of grains in the film are oriented perpendicular to the substrate. Instead, the 001 peak of the film is observed (Fig. 2.2D) as a diffuse arc of scattering centered at $Q_{\perp}$ = 1.85 $Å^{-1}$ by obtaining additional measurements near $Q_{\parallel} = 0$ and large out-of-plane diffraction angle, corresponding to large $Q_{\perp}$. The width of this peak in $Q_{\parallel}$ provides a rough measure of the orientational order in the film[24], and indicates (see Chapter 2 appendix, page S2 - 10) that most grains orient their c-axes within ±13 degrees of the surface normal (Fig. S2.5). Debye-Scherrer analysis of Figs. 2.2B and 2.2D, taking instrumental resolution into account and assuming platelet-shaped grains[25], indicates that the grains are ~6.8 ± 0.3 nm tall x 46 ± 2 nm across, corresponding to approximately 20 unit cells laterally and vertically.

The coverage and thickness of the films on the SLG surface was evaluated by scanning electron microscopy (SEM). A top-down micrograph of a COF-5 film grown on SLG/Cu for 30 min (Fig. 2.2E) indicates complete coverage of the film over the graphene surface. A few bulk COF-5 crystallites are scattered on top of the film,

which are observed in greater frequency when longer reaction times are used. They are not strongly associated to the underlying film, and most are removed by sonicating the substrate in dry toluene for 10 s, after which the micrographs are uniform over ~100 μm^2 areas. Grain boundaries in the COF film appear in the micrograph as thin dark lines that we attribute to the roughness of the underlying polycrystalline Cu layer as they are not observed when COF-5 is grown on SLG on smoother substrates (for additional representative micrographs, see Figs. S2.6 to S2.9). Cross-sectional micrographs were obtained after depositing a protective layer of Pt (400 nm) and milling the sample using a Ga^+ focused ion beam (FIB). The cross-section of a film grown for 30 min (Fig. 2.3A) shows a continuous COF layer of 195 ± 20 nm thickness, corresponding to approximately 580 layers. The GIXD of this sample (Fig. 2.3B) was identical to that obtained from the 2 h film (Fig. 2.2B), indicating similar crystallinity and alignment. A discontinuity in the Cu is observed in Fig. 2.3A; though the structure of the graphene at this defect is not known, the COF film conforms to the indentation.

Although these studies were performed on SLG supported by its Cu growth metal, our synthetic method is general for SLG transferred to other substrates, including transparent fused SiO_2 (SLG/SiO_2). This flexibility facilitates studying the role of the underlying substrate on COF film growth, and provides a direct route for incorporating COFs into a wide range of devices. COF-5 shows similar structure and alignment on SLG/SiO_2 compared to SLG/Cu. The GIXD of a film (Fig. 2.3D, 2 h reaction time) exhibits the same 100, 110, 200, 210, 220, 310, 400, 320, 330, 420, and 500 Bragg peaks with diffraction intensities all localized near $Q_\perp = 0$. A cross-

sectional micrograph (Fig. 2.3C) of the film obtained after FIB milling shows a COF-5 film thickness of 94 ± 5 nm as well as a more uniform film/substrate interface compared to SLG/Cu. Top-down micrographs (Fig. S2.10) show fewer bulk crystallites and none of the cracks observed in the films grown on SLG/Cu. Films grown on SLG/Cu are consistently thicker than those grown on SLG/SiO_2 at equivalent reaction times (Fig. S2.11), suggesting that the Cu surface (including its defect sites) plays a role in COF nucleation. Since the graphene on each substrate is derived from the same CVD process, we conclude that the thickness and uniformity of the film is strongly affected by the quality of the underlying substrate.

COF-5 films also form on SLG derived from the thermal decomposition of SiC from its Si-terminated basal plane (SLG/SiC). SLG/SiC exhibits reduced surface roughness and larger graphene domains compared to SLG/Cu[26,27]. Top-down micrographs of COF-5 films grown for 8 h indicate the formation of continuous films with no visible grain boundaries and few bulk crystallites (Fig. S2.12). Cross-sectional micrographs obtained of FIB-milled samples indicate a uniform film with a thickness

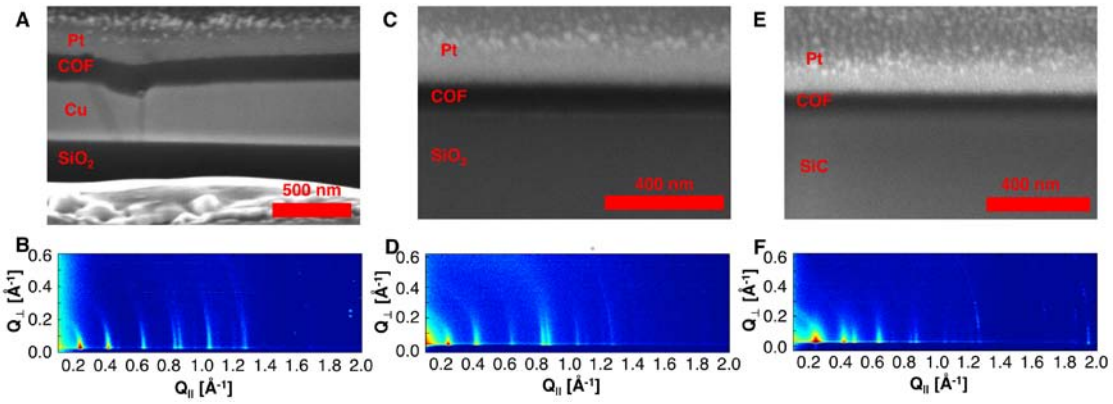

Figure 2.3 | (A) Cross-sectional SEM of a COF-5 film on SLG/Cu (30 min growth time, 195 ± 20 nm thickness) and **(B)** GIXD of the film; **(C)** Cross-section of a COF-5 film on SLG/SiO_2 (2 h growth time, 94 ± 5 nm thickness) and **(D)** GIXD of the film; **(E)** Cross-section of a COF-5 film on SLG/SiC (8 h growth time, 73 ± 3 nm thickness) and **(F)** GIXD of the film.

of 73 ± 3 nm (Figs. 2.3E and S2.13). The relatively thin COF film grown on SLG/SiC in 8 h follows the thickness trend observed for SLG/Cu and SLG/SiO_2. GIXD of the film indicates similar diffraction patterns as those grown on the other substrates, suggesting a highly crystalline, vertically oriented film. The epitaxial relation between SLG and the single-crystal SiC substrate allowed us to determine that the COF-5 film does not grow epitaxially with respect to the graphene, as rotation of the sample during the GIXD experiment did not reflect the six-fold symmetry of the COF lattice. This finding suggests that matching the COF lattice size and symmetry to the underlying graphene is not necessary to obtain crystalline films (see below).

The crystallinity and alignment of COF films on transparent SLG/SiO_2 substrates provides a means to organize functional π-electron systems within optoelectronic devices. Accordingly, films of two of the first COF semiconductors were grown on SLG/SiO_2. One of these frameworks, known as TP-COF[11], arises from incorporating a pyrene-2,7-diboronic acid linker in place of PBBA into the hexagonal COF-5 lattice (Fig. 2.4A). We obtained TP-COF in both thin film and powder form using similar conditions to those described above (see Figs. S2.14 to S2.15 for powder characterization and S2.16 to S2.17 for top-down and cross-sectional micrographs). The GIXD of the films (Fig. 2.4B) indicates similar vertical alignment of the 2D lattice, as judged by the attenuation of the signals with increasing $Q_\perp$ and the absence of the out-of-plane 001 diffraction. The increased pore size of TP-COF is apparent from the prominent 100 diffraction at 0.19 $Å^{-1}$, and the 110 (0.34 $Å^{-1}$), 200 (0.39 $Å^{-1}$), 210 (0.52 $Å^{-1}$) are also observed. Refinement of these data provided lattice parameters $a = b = 37.7$ Å in excellent agreement with those derived from PXRD data of TP-COF

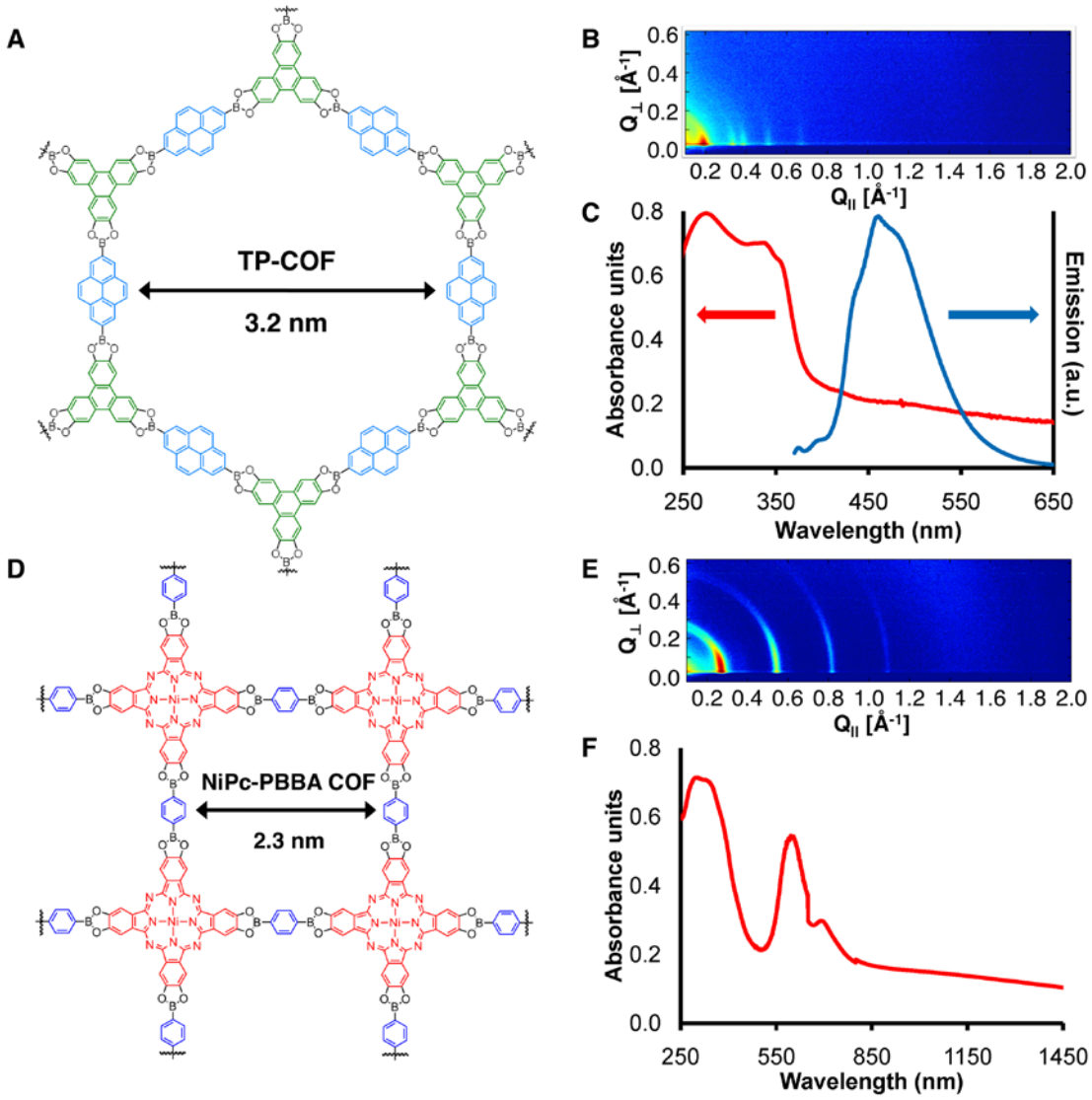

Figure 2.4 | (A) The TP-COF chemical structure, **(B)** GIXD of a film on SLG/SiO_2, **(C)** and transmission UV/Vis spectrum and emission spectrum (λ_{exc} = 352 nm) of the film. **(D)** The NiPc-PBBA COF chemical structure, **(E)** GIXD of a film on SLG/SiO_2, and **(F)** transmission UV/Vis/NIR spectrum of the film.

powders (37.5 Å)[11]. The transparent SLG/SiO_2 substrate enabled ultraviolet/visible/near infrared (UV/Vis/NIR) spectroscopy of a COF film in transmission mode for the first time (Fig. 2.4C, red trace). The spectrum is consistent with the presence of both HHTP and pyrene chromophores and shows improved vibrational resolution of the absorbance bands relative to the diffuse reflectance

spectrum of the powder sample. The photoluminescence of the film (Fig. 2.4C, blue trace) is characteristic of pyrene excimer emission over all excitation wavelengths, arising from efficient energy transfer from HHTP to pyrene that was observed in TP-COF powders.

Finally, we confirmed that COFs lacking hexagonal symmetry may also be crystallized on SLG by preparing a Ni phthalocyanine-PBBA COF on SLG/SiO_2 (Fig. 2.4D). GIXD of the film (Fig. 2.4E) again exhibited diffraction peaks localized near $Q_\perp = 0$ located at 0.27 $Å^{-1}$ (100), 0.55 $Å^{-1}$ (200), 0.81 $Å^{-1}$ (300), and 1.08 $Å^{-1}$ (400). These data correspond to a vertically aligned 2D square lattice with parameters $a = b =$ 23.0 Å that match those obtained from the characterization of the powder sample. Cross-sectional images indicated a continuous film of approximately 210 ± 25 nm thickness (Figs. S2.18 to S2.19). The translucent, turquoise films absorb strongly over the visible range of the spectrum as a consequence of the Ni phthalocyanine chromophores (Fig. 2.4F). Both the films and the powders are nonemissive, as is expected for H-aggregated phthalocyanines (see Figs. S2.20 to S2.21 for powder characterization). These vertically aligned, porous phthalocyanine COFs are intriguing precursors of ordered heterojunction films long thought to be ideal for organic photovoltaic performance[28].

REFERENCES

1. Côté, A. P., Benin, A. I., Ockwig, N. W., O'Keeffe, M., Matzger, A. J. & Yaghi, O. M. *Science* **310,** 1166 (2005).

2. Côté, A. P., El-Kaderi, H. M., Furukawa, H., Hunt, J. R. & Yaghi, O. M. *J. Am. Chem. Soc.* **129**, 12914 (2007).

3. Tilford, R. W., Gemmill, W. R., zur Loye, H. C. & Lavigne, J. J. *Chem. Mater.* **18**, 5296 (2006).

4. Perepichka, D. F. & Rosei, F. *Science* **323**, 216 (2009).

5. El-Kaderi, H. M., Hunt, J. R., Mendoza-Cortés, J. L., Côté, A. P., Taylor, R. E., O'Keeffe, M. & Yaghi, O. M. *Science* **316,** 268 (2007).

6. Grill, L., Dyer, M., Lafferentz, L., Persson, M., Peters, M. V. & Hecht, S. *Nature Nanotech.* **2,** 687 (2007).

7. Zwaneveld, N. A. A., Pawlak, R., Abel, M., Catalin, D., Gigmes, D., Bertin, D. & Porte, L. *J. Am. Chem. Soc.* **130,** 6678 (2008).

8. Gourdon, A. *Angew. Chem. Int. Ed.* **47**, 6950 (2008).

9. In't Veld, M., Iavicoli, P., Haq, S., Amabilino, D. B. & Raval, R. *Chem. Commun.*, 1536 (2008).

10. Wan, S., Guo, J., Kim, J., Ihee, H., & Jiang, D. *Angew. Chem. Int. Ed.* **48**, 5439 (2009).

11. Wan, S., Guo, J., Kim, J., Ihee, H., & Jiang, D. *Angew. Chem. Int. Ed.* **47**, 8826 (2008).

12. Spitler, E. L. & Dichtel, W. R. *Nature Chem.* **2**, 672 (2010).

13. Ding, X., Guo, J., Feng, X., Honsho, Y., Seki, S., Maitarad, P., Saeki, A., Nagase, S., & Jiang, D. *Angew. Chem. Int. Ed.* **50,** 1289 (2011).

14. Li X., Zhu, Y., Cai, W., Borysiak, M., Han, B., Chen, D., Piner, R. D. Colombo, L. & Ruoff, R. S. *Nano Lett.* **9**, 4359 (2009).

15. Kumar, A. & Zhou, C. *ACS Nano* **4**, 11 (2010).

16. Reina, A., Jia, X., Ho, J., Nezich, D., Son, H., Bulovic, V., Dresselhaus, M. S. & Kong, J. *Nano Lett.* **9**, 30 (2008).

17. Kim, K. S., Zhao, Y., Jang, H., Lee, S. Y., Kim, J. M., Kim, K. S., Ahn, J.-H., Kim, P., Choi, J.-Y. & Hong, B. H. *Nature* **457**, 706 (2009).

18. Li, X., Cai, W., An, J., Kim, S., Nah, J., Yang, D., Piner, R., Velamakanni, A., Jung, I., Tutuc, E., Banerjee, S. K., Colombo, L. & Ruoff, R. S. *Science* **324,** 1312 (2009).

19. Levendorf, M. P., Ruiz-Vargas, C. S., Garg, S. & Park, J. *Nano Lett.* **9**, 4479 (2009).

20. Bae, S., Kim, H., Lee, Y., Xu, X., Park, J.-S., Zheng, Y., Balakrishnan, J., Lei, T., Ri Kim, H., Song, Y. I., Kim, Y.-J., Kim, K. S. Ozyilmaz, B., Ahn, J.-H., Hong, B. H. & Iijima, S. *Nature Nanotech.* **5**, 574 (2010).

21. Methods and supplementary information can be found in the appendix immediately following Chapter 2.

22. Smilgies, D. M. & Blasini, D. R. *J. Appl. Crystallogr.* **40**, 716 (2007).

23. Lukose, B., Kuc, A. & Heine, T. *Chem. Eur. J.* **17**, 2388 (2011).

24. Baker, J. L., Jimison, L. H., Mannsfeld, S., Volkman, S., Yin, S., Subramanian, V., Salleo, A., Alivisatos, A. P. & Toney, M. F. *Langmuir* **26**, 9146 (2010).

25. Smilgies, D. M. *J. Appl. Crystallogr.* **42**, 1030 (2009).

26. Berger, C., Song, Z., Li, X., Wu, X., Brown, N., Naud, C., Mayou, D., Li, T., Hass, J., Marchenkov, A. N., Conrad, E. H., First, P. N. & de Heer, W. A. *Science* **312,** 1191 (2006).

27. Emtsev, K. V., Bostwick, A., Horn, K., Jobst, J., Kellogg, G. L., Ley, L., McChesney, J. L., Ohta, T., Reshanov, S. A., Rohrl, J., Rotenberg, E., Schmid, A. K., Waldmann, D., Weber, H. B. & Seyller, T. *Nature Mater.* **8**, 203 (2009).

28. Mayer, A. C., Scully, S. R., Hardin, B. E., Rowell, M. W. & McGehee, M. D. *Mater. Today* **10**, 28 (2007).

CHAPTER 3

LATTICE EXPANSION OF HIGHLY ORIENTED 2D PHTHALOCYANINE COVALENT ORGANIC FRAMEWORK FILMS

Abstract

Oriented 2D covalent organic framework (COF) films organize phthalocyanines into periodic, porous networks ideally suited for vertical charge transport. These films are precursors of ordered heterojunctions but their pores were previously too small to accommodate continuous networks of complementary electron acceptors. Here we increase the pore size of four phthalocyanine COFs well into the mesoporous regime. One of these films shows unprecedented crystallinity and nearly perfect vertical alignment.

Portions of this work were performed in collaboration with Brian T. Koo and Prof. Paulette Clancy in the School of Chemical and Biomedical Engineering at Cornell University. This chapter was published in full in *Angewandte Chemie International Edition* and the *Journal of the American Chemical Society*: Spitler, E. L., Colson, J. W., Uribe-Romo, F. J., Woll, A. R., Giovino, M. R., Saldivar, A. & Dichtel, W. R. *Angew. Chem. Int. Ed.* **51,** 2623 (2012) and Spitler, E. L., Koo, B. T., Novotney, J. L., Colson, J. W., Uribe-Romo, F. J., Gutierrez, G. D., Clancy, P. & Dichtel, W. R. *J. Am. Chem. Soc.* **133,** 19416 (2011). Both documents are reproduced with permission.

Directing the long-range order and orientation of organic semiconductors is critical to improving their performance[1]. Multicomponent films used in bulk heterojunction organic photovoltaic devices (OPVs) present the greatest difficulty, as the packing, alignment, and interfaces of two incompatible materials must be controlled in a systematic manner[2]. Strategies for manipulating molecular or polymer organization over micron length scales combine aspects of chemical design and processing techniques. Notable synthetic approaches include crystal engineering of acene-based organic semiconductors[3] and noncovalent assembly mediated by appended functionality[4], including discotic liquid crystals[5], or shape complementarity[6]. However, it remains extremely difficult to predict or design the packing of functional aromatic systems, as small chemical modifications often induce major changes in solid-state structure. Order and orientation over longer length scales are typically achieved during film formation or annealing through substrate patterning[7], electrical or magnetic field alignment[8], zone refining[9], or diblock copolymer phase separation[10].

Covalent organic frameworks (COFs) are an emerging class of materials that organize and align organic semiconductors predictably[11-14]. COF syntheses use reversible covalent bond-forming reactions to link molecular building blocks into periodic two-dimensional (2D) or three-dimensional networks. The 2D variants crystallize into layered structures containing stacked aromatic subunits ideal for interlayer exciton and charge transport[15-17]. 2D COFs exhibit several desirable and unique features: The length and relative orientation of their linking groups determine the lattice structure, in contrast to the unpredictable packing of traditional organic semiconductors. Also, their permanent porosity provides a continuous, high surface-

area interface for additional functionalization. COFs are typically isolated as insoluble and unprocessable powders not easily incorporated into devices, but we recently synthesized oriented COF thin films on single-layer graphene (SLG)[18]. These films would be well suited for ordered heterojunctions except their pores are too small to accommodate continuous domains of complementary semiconductors. Feasible lattice expansion is a tenet of reticular chemistry but is largely undemonstrated in COFs. Only the smallest possible pore width (2.3 nm) of the square phthalocyanine network most relevant for OPVs has been reported[13]. Here we describe 2D Zn phthalocyanine (ZnPc) COFs with expanded diagonal pore widths of 2.7, 3.4, 4.0, and 4.4 nm (Fig. 3.1), using the longest linkers incorporated into COFs thus far. We prepared each COF under similar reaction conditions, both as an insoluble powder and as an oriented film on SLG. One of the ZnPc COF films exhibits superior crystallinity and vertical

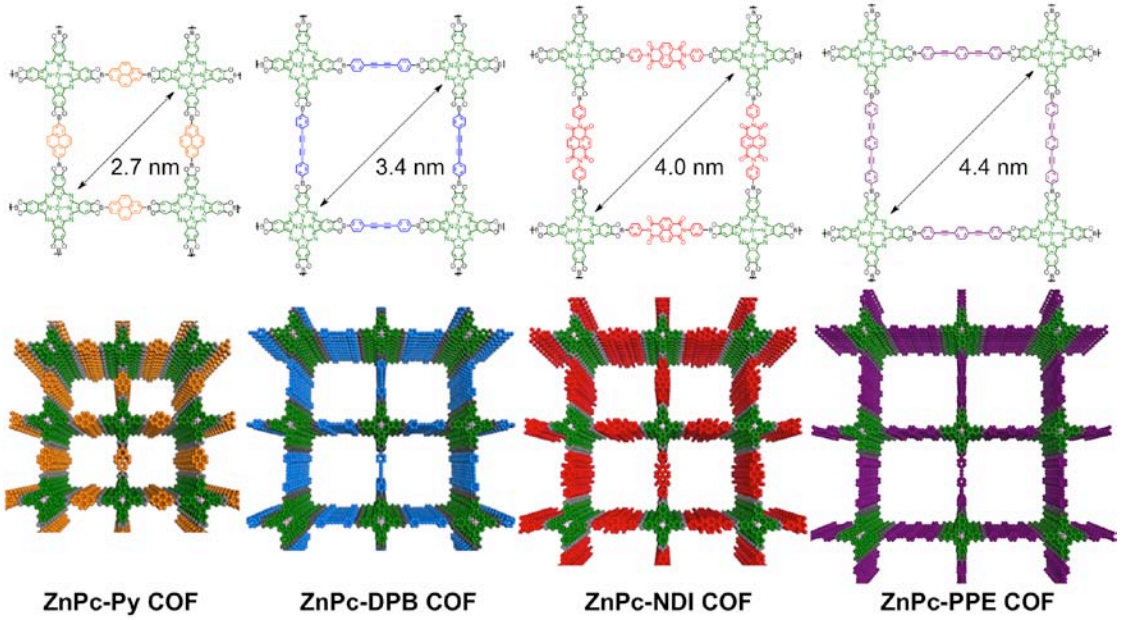

Figure 3.1 | Chemical and extended structures of the expanded ZnPc COFs. Each COF forms a two-dimensional layered network containing zinc phthalocyanines joined by (left to right) pyrene, diphenylbutadiyne, naphthalenediimide and phenylbis(phenylethynyl) units.

alignment compared to any other film we have prepared. Tuning the porosity and composition of these materials while maintaining their desirable topology demonstrates the versatility and power of the COF approach.

The COFs were synthesized as powders by condensing Zn octahydroxyphthalocyanine (**1**) with each of the four different linear diboronic acid linkers shown in Figure 3.2. The COF syntheses were performed in sealed glass ampoules in 2:1, 3:1, or 5:1 mixtures of dioxane:MeOH at 120 °C for 72 h. The COFs were reproducibly isolated as insoluble microcrystalline powders whose FT-IR spectra confirmed the formation of boronate ester linkages resonant near 1340 cm^{-1} and showed attenuated hydroxyl stretches (see Chapter 3 appendix Figs. S3.8 to S3.17). The COFs display excellent thermal stability, each retaining about 90% of its mass upon heating to 350 °C (Fig. S3.26). **ZnPc-Py COF** and **ZnPC-NDI COF** crystallize as needle-like structures, while **ZnPc-DPB COF** forms rough irregular sheets and **ZnPc-PPE COF** forms smooth µm-size aggregated spheroids, as observed by scanning electron microscopy (SEM, See Fig. S3.31).

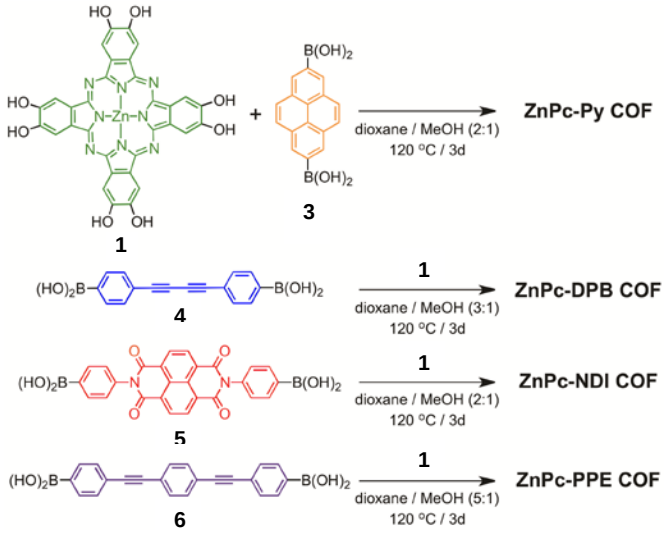

Figure 3.2 | Synthesis of 2D ZnPc covalent organic frameworks.

The crystallinity of the synthesized COFs was determined by powder X-ray diffraction (PXRD). As observed in Fig. 3.3, each of the COFs displays a PXRD

pattern with a large diffraction peak at 2θ (CuKα radiation) and *d*-spacings of 3.20° (27.6 Å) for **ZnPc-Py COF**, 2.67° (33.1 Å) for **ZnPc-DPB COF**, 2.44° (36.2 Å) for **ZnPc-NDI COF** and 2.36° (37.4 Å) for **ZnPc-PPE COF**. Additionally, all the COFs observed a small broad peak at 26.5° (*ca*. 3.35 Å); which is similar to those observed in other 2D COFs and other 2D layered materials such as graphite and boron nitride[19]. The diffraction peaks of each COF are consistent with a primitive tetragonal unit cell in which the (100), (200), (300), (400), (500) and (001) reflections were observed, as well as the weak (110) reflection for the **ZnPc-DPB** and **ZnPcPPE COFs**. Each COF is comprised of square-shaped ZnPc building blocks and linear linkers of varying length that form square planar sheets that stack in a highly symmetric eclipsed or nearly eclipsed fashion. Based on this hypothesis, we modeled t

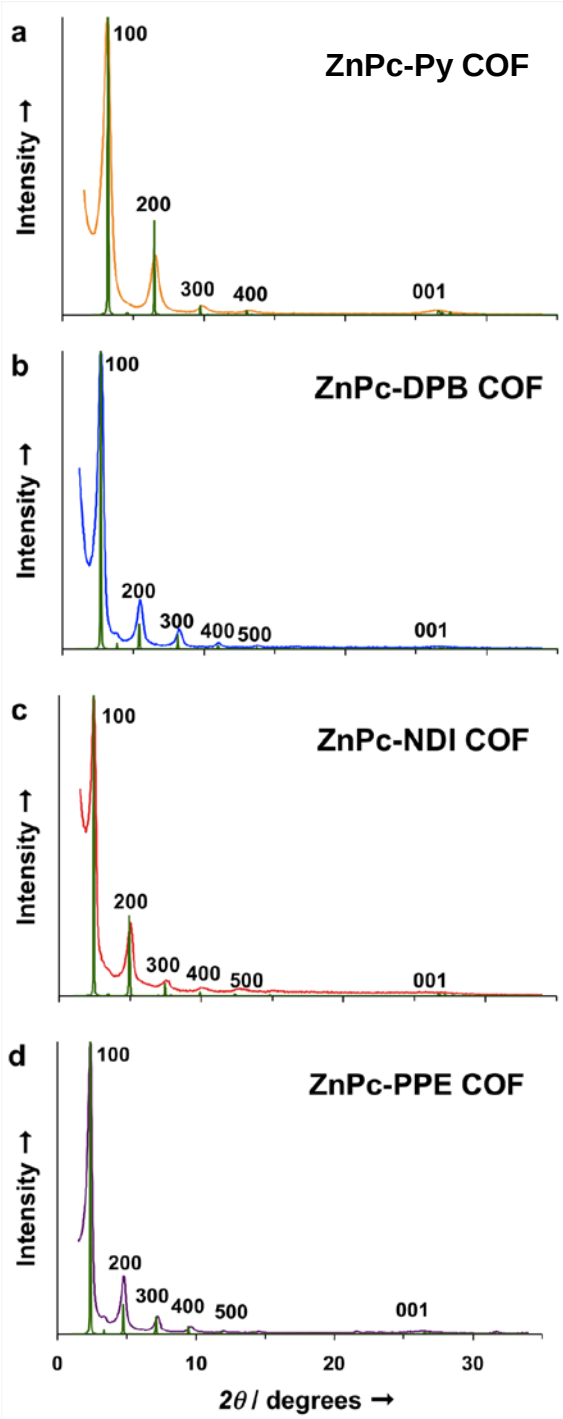

Figure 3.3 | Experimental vs. predicted (green) PXRD patterns of **a) ZnPc-Py COF**, **b) ZnPc-DPB COF**, **c) ZnPc-NDI COF** and **d) ZnPc-PPE COF**.

the eclipsed crystal structures of each material and simulated their powder X-ray diffraction patterns using the Materials Studio suite of programs. The COFs display diffraction patterns consistent with the simulations, crystallizing as cofacially-stacked two-dimensional sheets with *P*4/*mmm* symmetry, similar to the free base and Ni phthalocyanine COFs linked by phenylenebis(boronic acid)[13,14,16]. We also considered a staggered structure (*I*4/*mmm*) in which the ZnPc moieties in adjacent layers are offset by half a unit cell distance along the *a* and *b* axes (see Fig. S3.25). The simulated PXRD patterns of these structures do not match the experiments. The excellent agreement between simulated and observed patterns facilitated indexing of the observed peaks following Pawley refinement (see Figs. S3.21 to S3.24)[13,16]. The refined patterns resulted in unit cell parameters of a = 26.980 Å and c = 3.338 Å for **ZnPc-Py COF**; a = 32.183 Å and c = 3.356 Å for **ZnPc-DPB COF**; a = 35.701 Å and c = 3.361 Å for **ZnPc-NDI COF** and a = 38.533 Å and c = 3.367 Å for **ZnPc-PPE COF**. Despite the good crystallinity of these samples, the X-ray diffraction data do not preclude small deviations from perfectly eclipsed stacking. Based on typical π–π stacking geometries and DFT calculations performed on other boronate-linked 2D COFs[20], it is likely that adjacent layers are offset by around 1.7 Å. These calculations should be considered in future models of interlayer exciton and charge transport[17]. Diffuse reflectance absorbance spectroscopy of the COF powders (see Fig. S3.18) shows that each COF absorbs light throughout the visible and near-IR regions. The highly absorbent ZnPc chromophore dominates the spectrum of each material, and the spectra of the four COFs are very similar. They are red shifted relative to H_2Pc COFs

and very similar to the phenylene-linked NiPc COF, which was photoconductive under NIR excitation[16].

The porosity and surface areas of the ZnPc COFs were characterized by N_2 adsorption after activating the powders by washing with toluene and heating under vacuum. The COFs exhibit Type IV isotherms typical of mesoporous materials (Fig. 3.4), with initial adsorption into the pores at low relative pressures ($0.01 < P/P_o < 0.10$)[21]. Desorption follows the same general pathway, indicating reversible N_2 uptake.

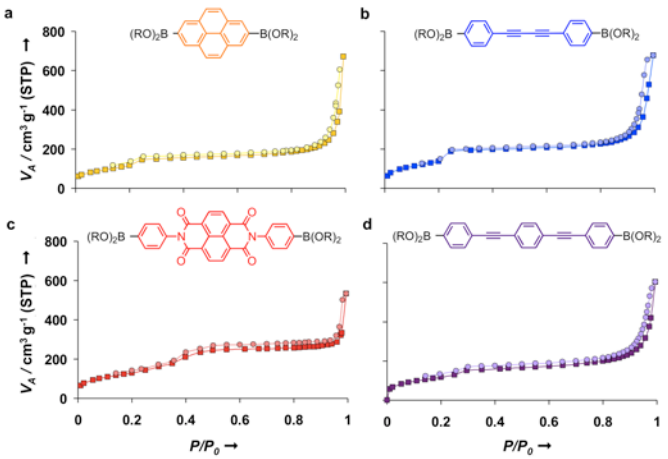

Figure 3.4 | N_2 uptake and surface area analysis of the ZnPc COFs. Adsorption (squares) & desorption (circles) isotherms for **a) ZnPc-Py COF** (gold), **b) ZnPc-DPB COF** (blue), **c) ZnPc-NDI COF** (red) and **d) ZnPc-PPE COF** (purple).

The Brunauer-Emmett-Teller (BET) surface-area model was applied to the $0.02 < P/P_o < 0.25$ region of the curves (see Figs. S3.27 to S3.30), which provided BET surface areas of 420 $m^2\ g^{-1}$ for **ZnPc-Py COF**, 485 $m^2\ g^{-1}$ for **ZnPc-DPB COF**, 490 $m^2\ g^{-1}$ for **ZnPc-NDI COF** and 440 $m^2\ g^{-1}$ for **ZnPc-PPE COF**. These surface areas are similar to previous H_2Pc and NiPc COFs[13,14,16]. Application of non-local density functional theory (NLDFT) models over the measured isotherms yielded pore-size distribution plots, from which average pore sizes were obtained (Figures S3.33 to S3.36). The average pore sizes determined were 31 Å, for **ZnPc-Py COF**, **ZnPc-DPB COF**, and **ZnPc-NDI COF**, and 34 Å for **ZnPc-PPE COF**, which correlate in reasonable agreement with the predicted numbers from the modeled crystal structures.

Despite their intriguing structures, COF powders are difficult to interface to electrodes or incorporate into devices. Thus, we grew each 2D ZnPc COF as a crystalline, vertically oriented thin film on a transparent SLG-functionalized fused silica substrate (SLG/SiO_2). For example, **ZnPc-Py COF** thin films were obtained by condensing **1** and **3** in a mixture of dioxane, MeOH, *N*,*N*-dimethylacetamide (DMA), and 1,2-dichlorobenzene (*o*-DCB) (3:1:2:1 *v*/*v*) in the presence of SLG/SiO_2. This solvent combination provided each of the ZnPc COFs as crystalline, oriented films and was modified from the DMA/*o*-DCB mixture employed by Jiang[16] for a NiPc COF powder. Interestingly, a DMA/*o*-DCB mixture lacking the other cosolvents provided crystalline COF films on the SLG whose grains showed no preferred orientation. The films were characterized using grazing incidence X-ray diffraction (GIXD, Fig. 3.5a) to assess their crystallinity and preferred orientation. The GIXD

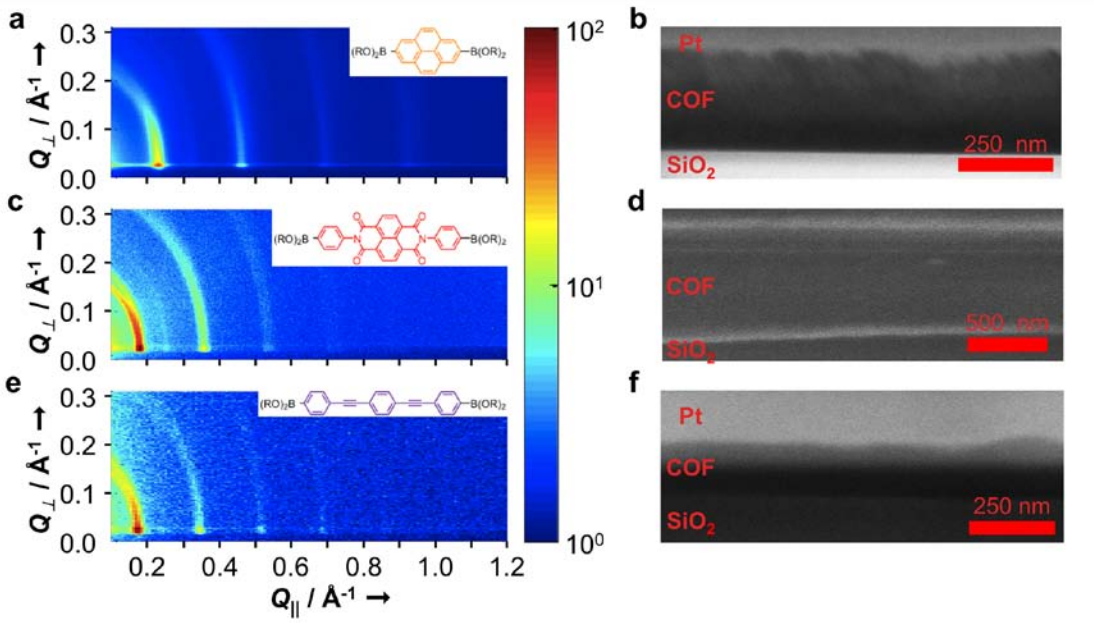

Figure 3.5 | Grazing incidence X-ray diffraction patterns and cross-sectional SEM for **ZnPc-Py COF** (**a,b**); **ZnPc-NDI COF** (**c,d**); **ZnPc-PPE COF** (**e,f**). The maximum intensity of each (100) Bragg peak is normalized to 100 counts.

pattern of the **ZnPc-Py COF** film shows scattering intensity at 0.22 $Å^{-1}$, 0.46 $Å^{-1}$, 0.69 $Å^{-1}$, 0.92 $Å^{-1}$, corresponding to the (100), (200), (300), and (400) peaks observed in the powder samples. This intensity is concentrated near $Q_{\perp} = 0$ $Å^{-1}$, indicating that the *c*-axis of the COF is oriented normal to the substrate surface. The (001) Bragg peak that appears at $Q_{||} = 1.83$ $Å^{-1}$ in powder samples, absent in the GIXD experiment, further confirms that the *c*-axis is oriented normal to the substrate. Instead, this peak is observed as a diffuse arc of scattering from $Q_{\perp} = 1.85$ to 1.90 $Å^{-1}$ in measurements performed at large out-of-plane diffraction angles (see Fig. 3.6d), indicating an angular spread of the stacking direction, or mosaicity, of ±11 degrees. Cross sectional SEM obtained by milling the sample with a Ga^{+} focused ion beam indicates a 400 ± 12 nm thick continuous film.

Similar crystalline, vertically oriented **ZnPc-NDI** and **ZnPc-PPE COF** thin films were obtained by condensing diboronic acid linkers **5** or **6** with **1** under similar conditions. GIXD patterns of these films are similar to that of **ZnPc-Py COF**, albeit with scattering intensity at smaller values of $Q_{||}$, corresponding to larger lattices. The (001) Bragg peak that appears at $Q_{||} = 1.83$ $Å^{-1}$ in each powder sample is again absent in the GIXD of each film but is found to be similar to that shown in Fig. 3.6D in out-of-plane scans. Cross-sectional SEM indicate 580 ± 84 nm and 200 ± 18 nm thick films for the **ZnPc-NDI** (Fig. 3.5d) and **ZnPc-PPE COF** (Fig. 3.5f), respectively.

Although grown under the same conditions, the **ZnPc-DPB COF** films show superior crystallinity and vertical alignment. The GIXD (Fig. 3.6a) of a 294 ± 6 nm thick film (Fig. 3.6b) indicates near complete localization of the scattering intensity near $Q_{\perp} = 0$ $Å^{-1}$. In contrast to Figs. 3.5a,c,e, the peak intensity at $Q_{\perp} = 0.028$ $Å^{-1}$ is

over 20 times higher than that in the diffuse arc of scattering extending towards larger $Q_\perp$, suggesting a mosaic spread below 0.2 degrees. Peaks at 0.19 $Å^{-1}$, 0.28 $Å^{-1}$, 0.39 $Å^{-1}$, 0.58 $Å^{-1}$, and 0.78 $Å^{-1}$ correspond to the (100), (110), (200), (300), and (400) peaks observed in the powders. (500) and (600) Bragg peaks not observed in the PXRD pattern (Fig. 3.3b) are observed at 0.97 $Å^{-1}$, and 1.16 $Å^{-1}$, respectively in the GIXD experiment. The off-specular (001) Bragg peak at $Q_{||}$ = 1.86 $Å^{-1}$ (Fig. 3.6c) is distinct from **ZnPc-Py COF** (Fig. 3.6d) or other 2D ZnPc COFs. First, the intensity distribution is flat, rather than curved, indicating that its width in $Q_{||}$ arises from finite lateral grain size, rather than mosaic spread. This observation is consistent with the low mosaic spread deduced from Fig. 3.6a. Second, the background-subtracted width of the peak along $Q_\perp$ is narrower than that in **ZnPc-Py COF** (Fig. 3.6d), indicating a longer correlation length along the stacking direction. This peak width is resolution-limited due to the geometric expansion of the beam as a consequence of the grazing incidence geometry. Additional scans (see Figs. S3.37 to S3.38) performed with

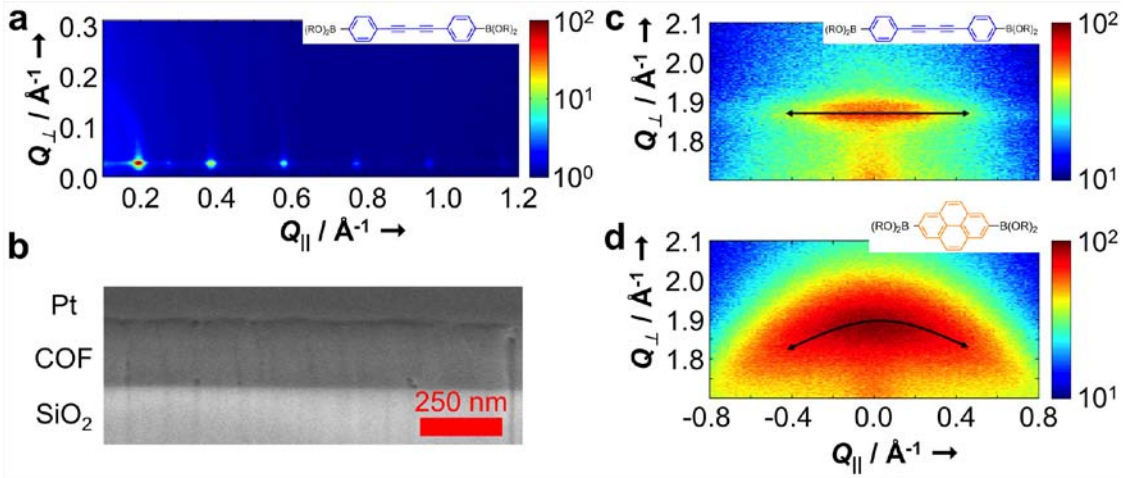

Figure 3.6 | Superior crystallinity and alignment of a **ZnPc-DPB COF** film. Grazing incidence X-ray diffraction pattern **a)** and cross-sectional SEM **b)** of **ZnPc-DPB COF**. The intensity of the off-specular projection of the (001) Bragg peak for **ZnPc-DPB COF c)** is flat with respect to $Q_\perp$, indicating nearly zero mosaicity, while that of the **ZnPc-Py COF d)** is representative of other COF films and shows an arc of scattering typical of less ideal vertical alignment.

improved resolution indicate a correlation length in the stacking direction of around 31 nm (*ca*. 94 layers), far exceeding that found in other COF films. For example, the **ZnPc-Py COF** data in Fig. 3.6d, which is not resolution-limited, gives a correlation length of *ca.* 4 nm or 12 layers. We attribute the **ZnPc-DPB COF**'s superior order partially to its diphenylbutadiyne linker, which can readily adopt a coplanar conformation needed during COF formation, although it may prove possible to obtain similar order in the other ZnPc COF films through further optimization.

A completementary crystalline, vertically oriented COF thin film known as **HHTP-DPB COF**[20c] with pore size of 4.7 nm can be prepared by condensing 2,3,6,7,10,11-hexahydroxytriphenylene (HHTP) and **4** using modified solvothermal conditions in the presence of SLG. GIXD (Figure 3.7A) indicates scattering intensity at 0.156 $Å^{-1}$, 0.271 $Å^{-1}$, 0.311 $Å^{-1}$, 0.411 $Å^{-1}$, 0.543 $Å^{-1}$, and 0.568 $Å^{-1}$, corresponding to the same (100), (110), (200), (210), (220) and (310) peaks observed in the powder samples[20c]. The intensity of these diffractions is concentrated near $Q_{\perp} = 0$, indicating that the *c*-axis of the COF is oriented normal to the substrate surface in the same manner as ZnPc-based COFs. Top-down SEM images indicate that the films are featureless over large areas and have only occasional bulk crystallites distributed across the surface (Figure S3.39). Cross-sectional micrographs obtained by milling the sample using a Ga^{+} focused ion beam indicate that the films are continuous across the substrate with thickness 132 ± 18 nm (Figure 3.7c). The large pore size obtained in the thin film morphology may also serve as a useful template for nanopatterning, as features in the 2–5 nm region are difficult to obtain using either standard lithographic techniques or block copolymer lithography[22].

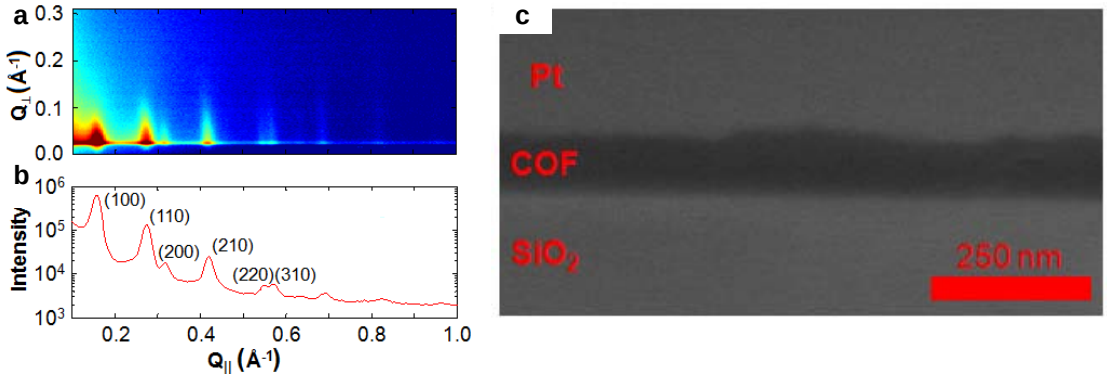

Figure 3.7 | a) Grazing incidence X-ray diffraction of **HHTP-DPB COF** thin film on SLG (growth time: 24 h). **b)** Projection of **a)** near $Q_{\perp} = 0$. **c)** Cross-sectional SEM image of the film.

COF films offer an unprecedented opportunity to organize and orient functional π-electron systems into robust periodic structures predictably through chemical synthesis. We have progressively expanded the pore size of the ZnPc lattice well into the mesoporous regime, such that many complementary materials, including ullerene acceptors, might form continuous nanostructured domains alongside the vertically stacked ZnPc macrocycles. The superior crystallinity and nearly zero mosaic spread of the diphenyl butadiyne-linked materials is particularly promising for forming nearly perfect ordered heterojunction structures.

REFERENCES

1. a) Tsao, H. N. & Müllen, K. *Chem. Soc. Rev.* **39,** 2372 (2010).

   b) Mas-Torrent, M. & Rovira, C. *Chem. Rev.* **111,** 4833 (2011).

2. a) Yang, X. & Loos, J. *Macromolecules* **40,** 1353 (2007).

   b) Thompson, B. C. & Fréchet, J. M. J. *Angew. Chem. Int. Ed.* **47** 58 (2008).

   c) Perez, M. D., Borek, C., Forrest, S. R. & Thompson, M. E. *J. Am. Chem. Soc.* **131** 9281 (2009).

   d) Groves, C., Reid, O. G. & Ginger, D. S. *Acc. Chem. Res.* **43,** 612 (2010).

3. a) Anthony, J. E. *Chem. Rev.* **106,** 5028 (2006).

   b) Briseno, A. L., Mannsfeld, S. C. B., Lu, X., Xiong, Y., Jenekhe, S. A., Bao, Z. & Xia, Y. *Nano Lett.* **7,** 668 (2007).

4. a) Schmidt-Mende, L., Fechtenkötter, A., Müllen, K., Moons, E., Friend, R. H. & MacKenzie, J. D. *Science* **293,** 1119 (2001).

   b) Percec, V., Glodde, M., Bera, T. K., Miura, Y., Shiyanovskaya, I., Singer, K. D., Balagurusamy, V. S. K., Heiney, P. A., Schnell, I., Rapp, A., Spiess, H. W., Hudson, S. D. & Duan, H. *Nature* **417,** 384 (2002).

   c) Kumaran, N., Veneman, P. A., Minch, B. A., Mudalige, A., Pemberton, J. E., O'Brien, D. F. & Armstrong, N. R. *Chem. Mater.* **22,** 2491 (2010).

   d) Berger, R., Resnati, G., Metrangolo, P., Weber, E. & Hulliger, J. *Chem. Soc. Rev.* **40,** 3496 (2011).

5. a) Kumar, S. *Chem. Soc. Rev.* **35,** 83 (2006).

   b) Sergeyev, S., Pisula, W. & Geerts, Y. H. *Chem. Soc. Rev.* **36,** 1902 (2007).

6. a) Gorodetsky, A. A., Chiu, C.-Y., Schiros, T., Palma, M., Cox, M., Jia, Z., Sattler, W., Kymissis, I., Steigerwald, M. & Nuckolls, C. *Angew. Chem. Int. Ed.* **49,** 7909 (2010).

7. a) Edwards, E. W., Montague, M. F., Solak, H. H., Hawker, C. J. & Nealey, P. F. *Adv. Mater.* **16** 1315 (2004).

   b) Gates, B. D., Xu, Q., Stewart, M., Ryan, D., Willson, C. G. & Whitesides, G. M. *Chem. Rev.* **105,** 1171 (2005).

c) Hoogboom, J., Garcia, P. M. L., Otten, M. B. J., Elemans, J. A. A. W., Sly, J., Lazarenko, S. V., Rasing, T., Rowan, A. E. & Nolte, R. J. M. *J. Am. Chem. Soc.* **127,** 11047 (2005).

8. a) Bushey, M. L., Nguyen, T.-Q. & Nuckolls, C. *J. Am. Chem. Soc.* **125,** 8264 (2003).

b) Shklyarevskiy, I. O., Jonkheijm, P., Stutzmann, N., Wasserberg, D., Wondergem, H. J., Christianen, P. C. M., Schenning, A. P. H. J., de Leeuw, D. M., Tomović, Ž., Wu, J., Müllen, K. & Maan, J. C. *J. Am. Chem. Soc.* **127,** 16233 (2005).

c) Monobe, H., Awazu, K., Shimizu, Y. *Adv. Mater.* **18,** 607 (2006).

9. Tracz, A., Jeszka, J. K., Watson, M. D., Pisula, W., Müllen, K. & Pakula, T. *J. Am. Chem. Soc.* **125,** 1682 (2003).

10. a) Segalman, R. A., McCulloch, B., Kirmayer, S. & Urban, J. J. *Macromolecules* **42,** 9205 (2009).

b) Ho, V., Boudouris, B. W., McCulloch, B. L., Shuttle, C. G., Burkhardt, M., Chabinyc, M. L. & Segalman, R. A. *J. Am. Chem. Soc.* **133,** 9270 (2011).

11. a) Côté, A. P., Benin, A. I., Ockwig, N. W., O'Keeffe, M., Matzger, A. J. & Yaghi, O. M. *Science* **310,** 1166 (2005).

b) Côté, A. P., El-Kaderi, H. M., Furukawa, H., Hunt, J. R. & Yaghi, O. M. *J. Am. Chem. Soc.* **129,** 12914 (2007).

c) Wan, S., Guo, J., Kim, J., Ihee, H., & Jiang, D. *Angew. Chem. Int. Ed.* **47,** 8826 (2008).

d) Feng, X., Chen, L., Dong, Y. & Jiang, D. *Chem. Commun.* **47,** 1979 (2011).

12. a) Tilford, R. W., Gemmill, W. R., zur Loye, H. C. & Lavigne, J. J. *Chem. Mater.* **18,** 5296 (2006).

b) Tilford, R. W., Mugavero, S. J., Pellechia, P. J. & Lavigne, J. J. *Adv. Mater.* **20,** 2741 (2008).

13. Spitler, E. L. & Dichtel, W. R. *Nature Chem.* **2**, 672 (2010).

14. Spitler, E. L., Giovino, M. R., White, S. A. & Dichtel, W. R. *Chem. Sci.* **2,** 1588 (2011).

15. Wan, S., Guo, J., Kim, J., Ihee, H., & Jiang, D. *Angew. Chem. Int. Ed.* **48**, 5439 (2009).

16. Ding, X., Guo, J., Feng, X., Honsho, Y., Seki, S., Maitarad, P., Saeki, A., Nagase, S., & Jiang, D. *Angew. Chem. Int. Ed.* **50,** 1289 (2011).

17. Patwardhan, S., Kocherzhenko, A. A., Grozema, F. C. & Siebbeles, L. D. A. *J. Phys. Chem. C* **115,** 11768 (2011).

18. Colson, J. W., Woll, A. R., Mukherjee, A., Levendorf, M. P., Spitler, E. L., Shields, V. B., Spencer, M. G., Park, J. & Dichtel, W. R. *Science* **332,** 228 (2011).

19. Sichel, E. K., Miller, R. E., Abrahams, M. S. & Buiocchi, C. J. *Phys. Rev. B* **13,** 4607 (1976).

20. a) Zhou, W., Wu, H. & Yildirim, T. *Chem. Phys. Lett.* **499,** 103 (2010).

    b) Lukose, B., Kuc, A. & Heine, T. *Chem. Eur. J.* **17,** 2388 (2011).

    c) Spitler, E. L., Koo, B. T., Novotney, J. L., Colson, J. W., Uribe-Romo, F. J., Gutierrez, G. D., Clancy, P. & Dichtel, W. R. *J. Am. Chem. Soc.* **133,** 19416 (2011).

21. Sing, K. S. W., Everett, D. H., Haul, R. A. W., Moscou, L., Pierotti, R. A., Rouquérol, J. & Siemieniewska, T. *Pure Appl. Chem.* **57,** 603 (1985).

22. Tang, C., Lennon, E. M., Fredrickson, G. H., Kramer, E. J. & Hawker, C. J. *Science* **322,** 429 (2008).

CHAPTER 3 - APPENDIX

SUPPLEMENTARY INFORMATION

A. Materials and Instrumentation. All reagents were purchased from commercial sources and used without further purification. Zn octahydroxyphthalocyanine **1**[1], pyrene diboronic acid **3**[2], and diphenylbutadiyne diboronic acid **4**[3] were prepared via literature procedures. 1,4-Dioxane and propionic acid were purchased from commercial sources and used without further purification. Other solvents were purchased from commercial sources and purified using a custom-built alumina-column based solvent purification system.

Infrared spectra were recorded on a Thermo Nicolet iS10 with a diamond ATR attachment and are uncorrected.

UV/Vis absorbance spectra were recorded on a Cary 5000 UV-Vis-NIR spectrophotometer with a mercury lamp in either dichloromethane solution or as solids using a praying mantis diffuse reflectance accessory.

Emission and excitation spectra were recorded on a Horiba Jobin Yvon Fluorolog-3 fluorescence spectrophotometer equipped with a 450 W Xe lamp, double excitation and double emission monochromators, a digital photon-counting photomultiplier and a secondary InGaAs detector for the NIR range. Correction for variations in lamp intensity over time and wavelength was achieved with a solid-state silicon photodiode as the reference. The spectra were further corrected for variations in photomultiplier response over wavelength and for the path difference between the sample and the reference by multiplication with emission correction curves generated on the instrument. Solid samples were mounted between quartz slides and mounted on a solid sample holder, and emission was observed using a front face detection accessory.

Powder X-ray diffraction patterns were recorded on a Rigaku Smartlab Powder X-Ray Diffractometer in 2θ medium resolution parallel beam/PSA mode employing CuKα lines focused radiation at 40 kV, 44 mA power and equipped with a Ge crystal detector fitted with a 0.5 mm radiation entrance slit. Samples were mounted on zero background sample holders by dropping powders from a wide-blade spatula and then leveling the sample surface with a glass microscope slide. No sample grinding or sieving was used prior to analysis. Samples were observed using a 0.045º 2θ step scan from 1.0 – 34º (Omega = 1.0º) with an exposure time of 0.4 s per step. No peaks could be resolved from the baseline for 2θ > 34º data, which was therefore not considered for further analysis.

Thermogravimetric analysis from 20-600 °C was carried out on a TA Instruments Q500 Thermogravimetric Analyzer in an N_2 atmosphere using a 10 °C/min ramp without equilibration delay.

Scanning electron microscopy (SEM) was performed on a FEI Strata 400 FE-SEM. Materials were deposited onto a sticky carbon surface on a flat aluminum platform sample holder. No metal sputtering of the sample was necessary. Focused ion beam (FIB) patterning and milling was performed using a FEI Strata 400 FIB Ga^+ LIM system. A 1x10 μm Pt strip (~1 μm thickness) was deposited using the electron gun onto COF films grown on SLG/SiO_2 substrates prior to exposing the sample to the FIB. The sample was then milled with the FIB using a cleaning cross-section. After milling, the samples were imaged at 2 keV using the electron gun. Cross-sectional images were obtained using a stage tilt angle of 52°. Thickness measurements made at

this angle were corrected by multiplying by 1.26. SLG/SiO_2 substrates were grounded to the sample holder using sticky carbon prior to imaging to minimize charging.

Mass spectra were obtained on a Waters MALDI micro MX MALDI-TOF mass spectrometer using positive ionization and a reflectron detector. MALDI samples were prepared by wet deposition of a saturated analyte/dithranol matrix solution onto a metallic sample plate and air dried before loading into the instrument.

Surface area measurements were conducted on a Micromeritics ASAP 2020 Accelerated Surface Area and Porosimetry Analyzer using ca. 20 mg samples degassed at 180 °C for 12 hours. Nitrogen isotherms were generated by incremental exposure to ultra high purity nitrogen up to ca. 1 atm over 28-hour periods in a liquid nitrogen (77 K) bath, and surface parameters were determined using BET adsorption models included in the instrument software (Micromeritics ASAP 2020 V1.05) using the P/P_0 ranges according to consistency criteria for the BET model in frameworks. Non-local density functional theory (NLDFT) model for N_2 at 77 K and oxide surface with cylindrical pore shape integrated in the Micromeritics data reduction software was used to calculate pore size distribution curves from the adsorption branch of the measures isotherms.

NMR spectra were recorded on a Bruker ARX 300 MHz spectrometer using a standard ^{1}H/X Z-PFG probe at ambient temperature with a 20 Hz sample spin rate.

Grazing incidence X-ray diffraction (GIXD) was performed at the G2 station at Cornell High Energy Synchrotron Source (CHESS) using a beam energy of 8.78 ± 0.01 keV (λ = 0.1414 nm), selected using a Be single-crystal monochromator. Motorized slits were used to define a 0.2×2 (V×H) mm^2 beam, with a typical flux of

2×10^{10} photons/s. The data were collected using a 640-element 1D diode-array, of which each element incorporates its own pulse counting electronics capable of count rates of $\sim10^5$ photons/s. A set of 0.1° Soller slits were used on the detector arm to define the in-plane resolution. The scattering geometry is described in detail elsewhere. Each data set was collected by scanning the detector with the sample stationary. The incidence angle α between the beam and sample surface was 0.175°. Axes labels $Q_\perp$ and $Q_\parallel$ are defined using the GISAXS convention $Q_\perp = 4\pi/\lambda\sin(\delta/2)$ and $Q_\parallel = 4\pi/\lambda\sin(\nu/2)$, where δ and ν are the vertical and horizontal scattering angles, respectively. At $\alpha=\delta=0$, $hQ_\parallel$ and $hQ_\perp$ (where h is Planck's constant) are the components of momentum transfer parallel and perpendicular to the sample surface, respectively.

B. Synthetic Procedures.

General procedure for COF powder synthesis and ZnPc-Py COF. Pyrene diboronic acid **3** (17 mg, 0.059 mmol) and Zn octahydroxyphthalocyanine **1** (20 mg, 0.028 mmol) were suspended in a mixture of dioxane and MeOH (2:1, 3 mL) and sonicated for 10 min. The dark green suspension was transferred to a 10 mL pre-scored long-necked glass ampoule, flash-frozen in liquid N_2, and flame-sealed. The ampoule was placed in an oven at 120 ^{o}C for 72 h, and the resulting free-flowing dark green powder was collected by filtration on a Hirsch funnel, washed with anhydrous toluene (1 mL), and air-dried. The resulting **ZnPc-Py COF** powder (10 mg, 52%) was dried under vacuum before characterization by PXRD and IR. **ZnPc-Py COF**: IR (powder, ATR) 3233, 1607, 1459, 1369, 1337, 1271, 1231, 1106, 1078, 1023, 902, 870, 824, 742, 714 cm^{-1}. PXRD [2θ (relative intensity)] 3.22 (100), 6.50 (24), 9.92 (5.6), 13.16 (4.3), 26.62 (6.4). UV-Vis (powder, praying mantis DRA) 711, 377 (sh), 336, 284. Anal. Calcd. for $(C_{64}H_{24}B_4N_8O_8Zn)_n$: C, 67.34; H, 2.12; N, 9.82. Found: C, 63.65; H, 2.20; N, 10.34. The presence of boron was confirmed by a characteristic B 1s peak in the XPS with a binding energy of 190.8 eV.

ZnPc-DPB COF. The above procedure was followed using diphenyl butadiynediboronic acid **4** (17 mg, 0.059 mmol), Zn octahydroxyphthalocyanine **1** (14 mg, 0.020 mmol), and a 3:1 mixture of dioxane and methanol (3:1, 1.3 mL) solvent. 12 mg (53%) of the **ZnPc-DPB COF** were isolated. IR (powder, ATR) 3244, 1607, 1472, 1371, 1338, 1268, 1180, 1081, 1018, 869, 830, 742 cm^{-1}. PXRD [2θ (relative intensity)] 2.66 (100), 3.74 (4.7), 5.45 (15), 8.29 (5.9), 11.04 (1.9), 13.82 (1.3), 16.48 (0.86), 26.83 (2.2). UV-Vis (powder, praying mantis DRA) 713, 361 (sh), 301, 275

(sh). Anal. Calcd for $(C_{64}H_{24}B_4N_8O_8Zn)_n$: C, 67.34; H, 2.12; N, 9.82. Found: C, 54.15; H, 2.19; N, 9.68. The presence of boron was confirmed by a characteristic B 1s peak in the XPS with a binding energy of 191.7 eV.

ZnPc-NDI COF. The above procedure was followed using napthalenediimide diboronic acid **5** (36 mg, 0.071 mmol), Zn octahydroxyphthalocyanine **1** (17 mg, 0.024 mmol), and a 2:1 mixture of dioxane and MeOH (3 mL) solvent. 23 mg (60%) of the **ZnPc-NDI COF** were isolated. **ZnPc-NDI COF**: IR (powder, ATR) 3338, 1714, 1671, 1613, 1582, 1514, 1479, 1451, 1376, 1342, 1272, 1251, 1200, 1119, 1085, 1022, 984, 870, 835, 768, 742, 719 cm^{-1}. PXRD [2θ (relative intensity)] 2.44 (100), 5.00 (27), 7.52 (7.0), 12.52 (3.3), 26.92 (2.6). UV-Vis (powder, praying mantis DRA) 693, 333 (sh), 296. Anal. Calcd for $(C_{84}H_{32}B_4N_{12}O_{16}Zn)_n$: C, 64.10; H, 2.05; N, 10.68. Found: C, 55.41; H, 2.56; N, 11.09. The presence of boron was confirmed by a characteristic B 1s peak in the XPS with a binding energy of 191.3 eV.

ZnPc-PPE COF. The above procedure was followed using PPE diboronic acid **6** (22 mg, 0.060 mmol), Zn octahydroxyphthalocyanine **1** (15 mg, 0.021 mmol), and a 5:1 mixture of dioxane and MeOH (3 mL) solvent. 20 mg (73%) of the **ZnPc-PPE COF** were isolated. **ZnPc-PPE COF**: IR (powder, ATR) 3060, 2930, 1711, 1605, 1472, 1395, 1351, 1270, 1227, 1187, 1042, 1015, 945, 915, 872, 830, 745, 704 cm^{-1}. PXRD [2θ (relative intensity)] 2.28 (100), 4.76 (18), 7.20 (6.9), 9.68 (3.4), 12.16 (2.5), 26.52 (2.3). UV-Vis (powder, praying mantis DRA) 693, 331, 308 nm. Anal. Calcd for $(C_{84}H_{32}B_4N_{12}O_{16}Zn)_n$: C, 70.56; H, 2.49; N, 8.66. Found: C, 59.20; H, 2.58; N, 8.70. The presence of boron was confirmed by a characteristic B 1s peak in the XPS with a binding energy of 191.3 eV.

Scheme S3.1. Synthesis of naphthalene diimide diboronic acid **5**.

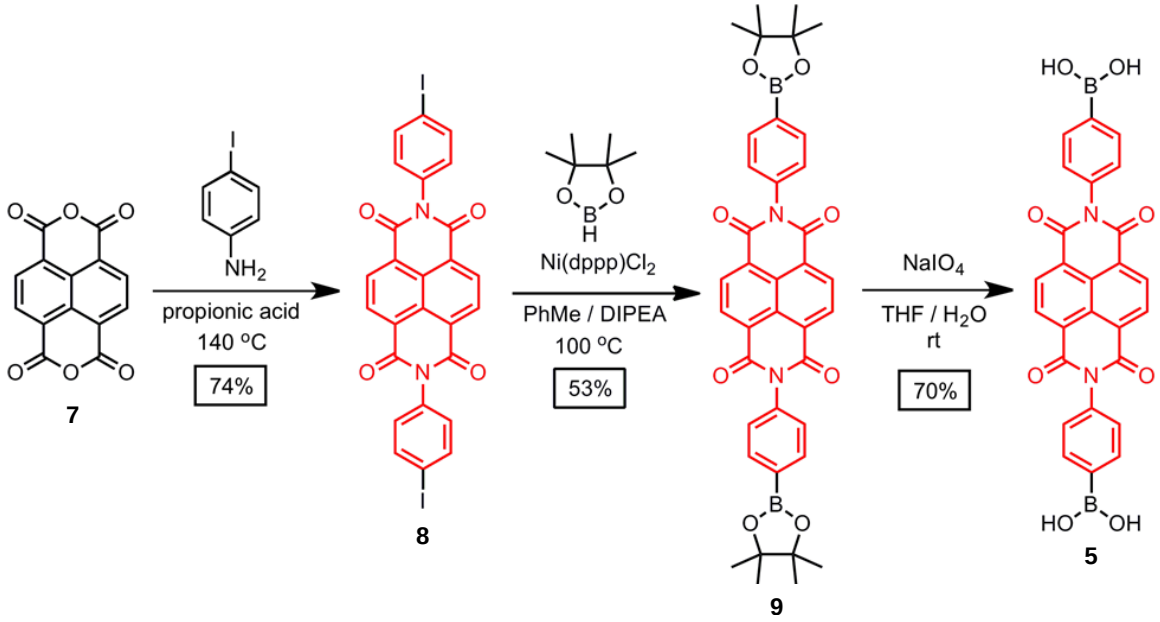

N,N'-bis(4-iodophenyl)naphthalene-1,4,5,8-tetracarboxylic diimide (8). Naphthalene-1,4,5,8-tetracarboxylic dianhydride **7** (1.30 g, 4.85 mmol) and 4-iodoaniline (3.20 g, 10.5 mmol) were refluxed in propionic acid (80 mL) for 18 h under N_2. The brown solution was cooled to rt and the resulting precipitate was collected by filtration and washed with MeOH (4 x 20 mL). The resulting light brown solid **8** (2.40 g, 74%) was used without further purification. Its poor solubility precluded acquisition of a suitable ^{13}C-NMR spectrum. **8**: ^{1}H-NMR (DMSO-d_6, 300 MHz) δ 8.72 (s, 4H); 7.94 (d, J = 9 Hz, 4H); 7.30 (d, J = 9 Hz, 4H). MALDI-MS m/z (%) 542.9 (44, M^+-I); 543.9 (52, M^++1-I); 669.8 (100, M^+); 670.8 (53, M^++1). IR (powder, ATR) 3100, 3068, 3049, 1711, 1670, 1577, 1484, 1446, 1344, 1248, 1198, 1118, 1006, 980, 884, 850, 827, 766, 741 cm^{-1}. UV-Vis [λ / nm (log ε / M^{-1} cm^{-1}], 6.9 μM in DMF] 380 (4.43), 360 (4.43), 340 (4.34). Anal. Calcd for ($C_{26}H_{12}I_2N_2O_4$): C, 46.60; H, 1.80; N, 4.18. Found: C, 47.77; H, 1.84; N, 4.22.

Naphthalenediimide dipinacolatoboronic ester (9). Naphthalene diimide diiodide **8** (138 mg, 0.206 mmol) and nickel(II) diphenylphosphinopropane dichloride (9.0 mg, 0.017 mmol) were heated to reflux in toluene (2 mL) and N,N-diisopropylethylamine (1 mL) under N_2. Pinacol borane (100 µL, 0.69 mmol) was added by syringe and the mixture was stirred for 12 h. After cooling to rt, saturated aq. NH_4Cl (30 mL) was added to the dark brown mixture. The biphasic liquid was diluted with EtOAc (40 mL) and was washed with H_2O (3 x 40 mL). The organic layer was evaporated to provide a pale yellow solid, which was suspended in EtOAc (10 mL) and centrifuged for 30 min at 4000 rpm. This suspension/centrifugation procedure was repeated twice. The tan solid **9** (73 mg, 53%) was dried under vacuum and used without further purification. **9**: ^{1}H-NMR ($CDCl_3$, 300 MHz) δ 8.84 (s, 4H); 8.04 (d, *J* = 9 Hz, 4H); 7.36 (d, *J* = 9 Hz, 4H); 1.38 (s, 24H). ^{13}C-NMR ($CDCl_3$, 300 MHz) δ 163, 138, 136, 132, 130, 128, 128, 127, 84, 25. IR (powder, ATR) 3088, 2980, 2940, 1713, 1675, 1607, 1581, 1447, 1399, 1359, 1342, 1321, 1246, 1213, 1198, 1169, 1143, 1120, 1086, 1022, 983, 963, 860, 824, 794, 769, 717 cm^{-1}. UV-Vis [λ / nm (log ε / M^{-1} cm^{-1}), 8.1 µM in DMF] 380 (4.43), 360 (4.42), 343 (4.25). Anal. Calcd for ($C_{38}H_{36}B_2N_2O_8$): C, 68.09; H, 5.41; N, 4.18. Found: C, 68.05; H, 5.39; N, 4.28.

Naphthalenediimide diboronic acid (5). Ester **9** (30 mg, 0.045 mmol) and $NaIO_4$ (20 mg, 0.094 mmol) were suspended in a 4:1 THF:H_2O solution (0.6 mL). The resulting tan mixture was stirred for 2 h, after which aq. HCl (1M, 1 mL) was added. The pale yellow suspension was stirred for 18 h and diluted with H_2O (5 mL), filtered, and rinsed with another 5 mL H_2O. The resulting tan solid was dried under vacuum to provide the diboronic acid **5** (16 mg, 70 %). **5**: ^{1}H-NMR (DMSO-d_6, 300 MHz) δ 8.72

(s, 4H); 8.23 (s, 4H); 7.94 (d, *J* = 6 Hz, 4H); 7.42 (d, *J* = 6 Hz, 4H). ^{13}C-NMR (DMSO-d_6, 300 MHz) δ 164, 138, 135, 131, 130, 129, 128, 127. IR (powder, ATR) 3479, 3378, 1711, 1664, 1606, 1577, 1437, 1416, 1366, 1341, 1275, 1250, 1199, 1151, 1127, 1061, 1028, 1015, 984, 890, 854, 828, 767, 752, 719 cm^{-1}. UV-Vis [λ / nm (log ε / M^{-1} cm^{-1}), 15.0 μM in DMF] 380 (4.40), 360 (4.38), 345(sh) (4.21). Anal. Calcd for ($C_{26}H_{16}B_2N_2O_8$): C, 61.71; H, 3.19; N, 5.54.Found: C, 62.31; H, 3.21; N, 5.39.

Scheme S3.2. Synthesis of phenylbis(phenylethynyl)diboronic acid **6**.

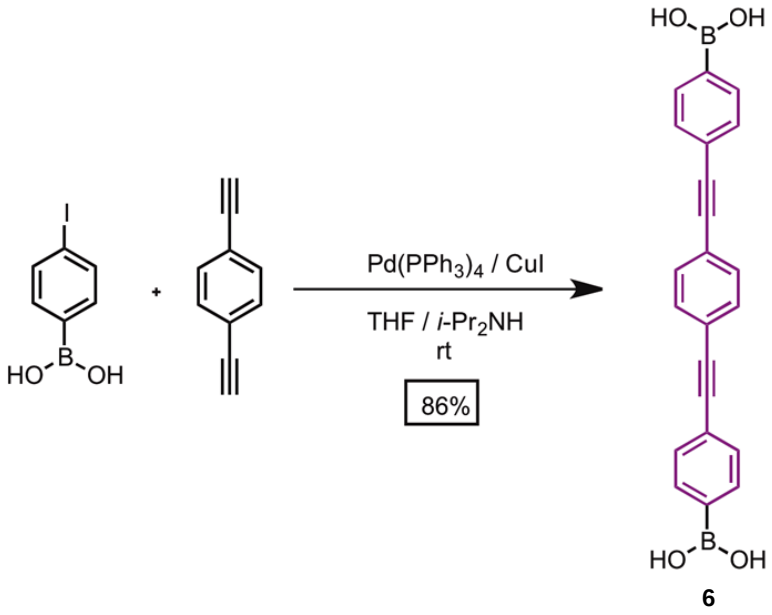

Benzene-1,4-bis(phenylethynyl) diboronic acid (6). 4-iodophenylboronic acid (880 mg, 3.55 mmol) and 1,4-diethynylbenzene (205 mg, 1.63 mmol) were dissolved in THF (25 mL) and ethyldiisopropylamine (10 mL) and the solution was sparged with N_2 for 30 min. CuI (63 mg, 0.33 mmol) and $Pd(PPh_3)_4$ (43 mg, 0.037 mmol) were added and the solution was sparged with N_2 for another 30 min. The resulting pale yellow mixture was stirred at rt for 12 h, during which a white precipitate formed. The pale yellow solid was recovered by filtration and rinsed with EtOAc (20 mL). The

solid was suspended in EtOAc (30 mL), which washed with brine (30 mL) and H_2O (3 × 30 mL), and the solvent removed to yield 513 mg (86%) of the PPE diboronic acid **6** as a white solid. **6**: ^{1}H-NMR (DMSO-d_6, 300 MHz) δ 8.20 (s, 4H); 7.84 (d, *J* = 7.5 Hz, 4H); 7.60 (d, J = 3 Hz, 4H); 7.54 (d, *J* = 7.5 Hz, 4H). ^{13}C-NMR (DMSO-d_6, 300 MHz) δ 135, 133, 130, 123, 122, 92,90. MALDI-MS m/z (%) 365.1 (43, M^+); 366.1 (100, M^++1); 367.1 (27, M^++2), 368.1 (6, M^++3). IR (powder, ATR) 3351, 1701, 1658, 1592, 1576, 1505, 1491, 1434, 1401, 1358, 1256, 1199, 1183, 1143, 1088, 1021, 957, 857, 831, 808, 743, 693 cm^{-1}. UV-Vis [λ / nm (log ε / M^{-1} cm^{-1}), 9.4 μM in DMF] 350 (4.63), 329 (4.83), 321(sh) (4.75). Em (λ / nm in DMF, λ_{ex} = 350 nm) 376, 387, 400(sh). Anal. Calcd for ($C_{22}H_{16}B_2O_4$): C, 72.20; H, 4.41. Found: C, 69.62; H, 4.37.

Graphene Growth. Single-layer graphene was grown on 25 μm-thick copper foil using previously reported chemical vapor deposition methods[4]. A layer of PMMA (50 nm) was spin-coated on top of the graphene and the copper was etched using aq. $FeCl_3$. The graphene was then transferred to fused SiO_2 and the PMMA removed by washing first with chloroform then isopropyl alcohol. The SLG/SiO_2 was finally calcined at 300 °C for 2.5 h.

General procedure for ZnPc COF film growth on SLG. The appropriate diboronic acid (0.109 mmol) and zinc octahydroxyphthalocyanine (0.035 g, 0.050 mmol) were added to a 15 mL cylindrical pressure vessel and suspended in a mixture of 1,4-dioxane, methanol, N,N-dimethylacetamide, and 1,2-dichlorobenzene (v/v 3:1:2:1; 3.0 mL). After capping, the mixture was sonicated for 30 minutes and a graphene-containing substrate was added. The sealed vessel was heated in a 120 °C oven for 24 h. The vessel was cooled to room temperature and the resulting green powder was

recovered by filtration and dried under vacuum. The graphene-containing substrate was submerged in anhydrous toluene and sonicated for 5 seconds, and finally dried under vacuum.

C. NMR Spectra.

Figure S3.1. ^{1}H-NMR spectrum of NDI diiodide **8** in DMSO-d_6.

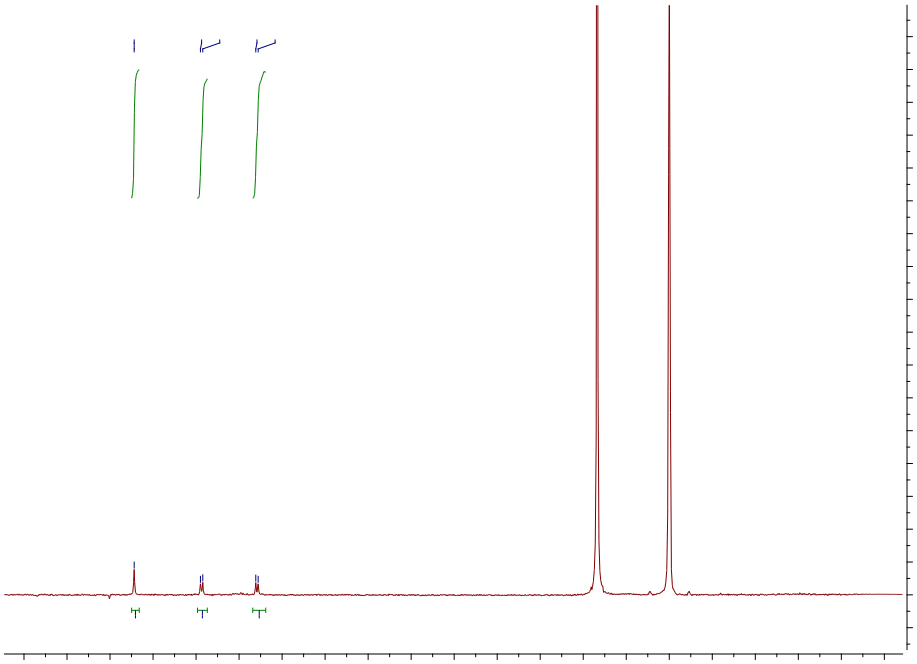

Figure S3.2. ^{1}H-NMR spectrum of NDI ester **9** in $CDCl_3$.

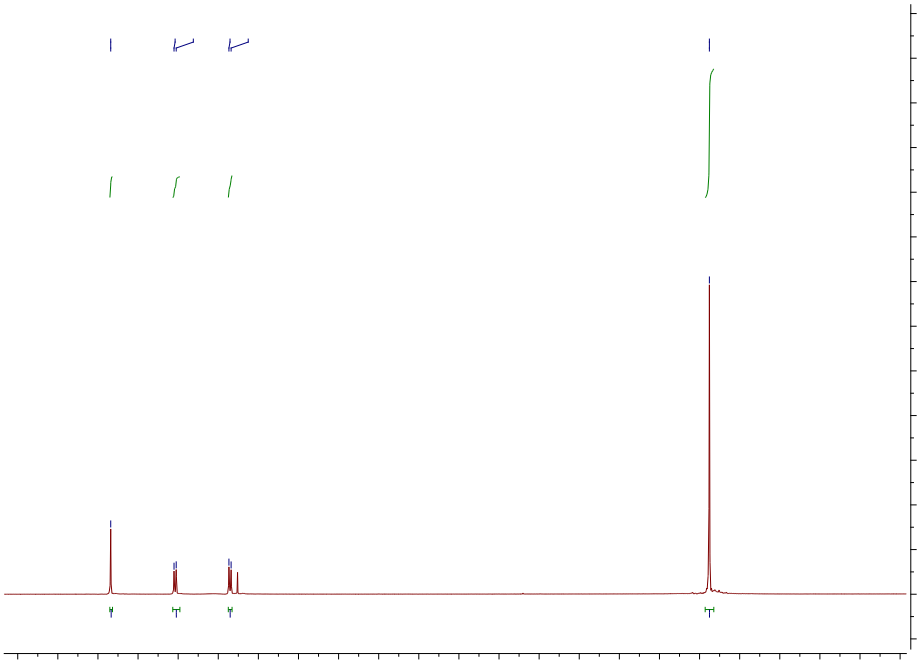

Figure S3.3. ^{13}C-NMR spectrum of NDI ester **9** in $CDCl_3$.

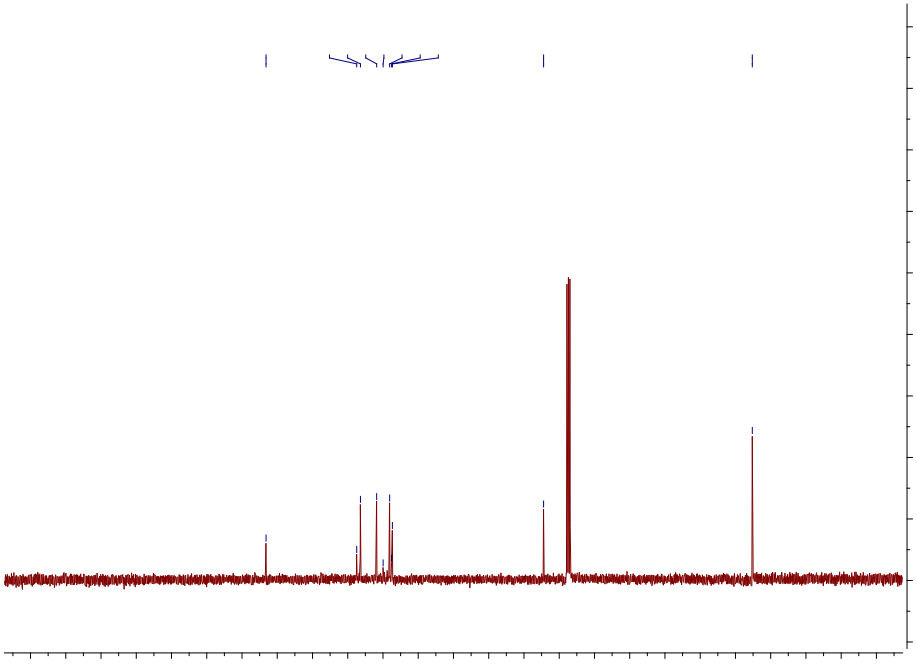

Figure S3.4. ^{1}H-NMR spectrum of NDI diboronic acid **5** in DMSO-d_6.

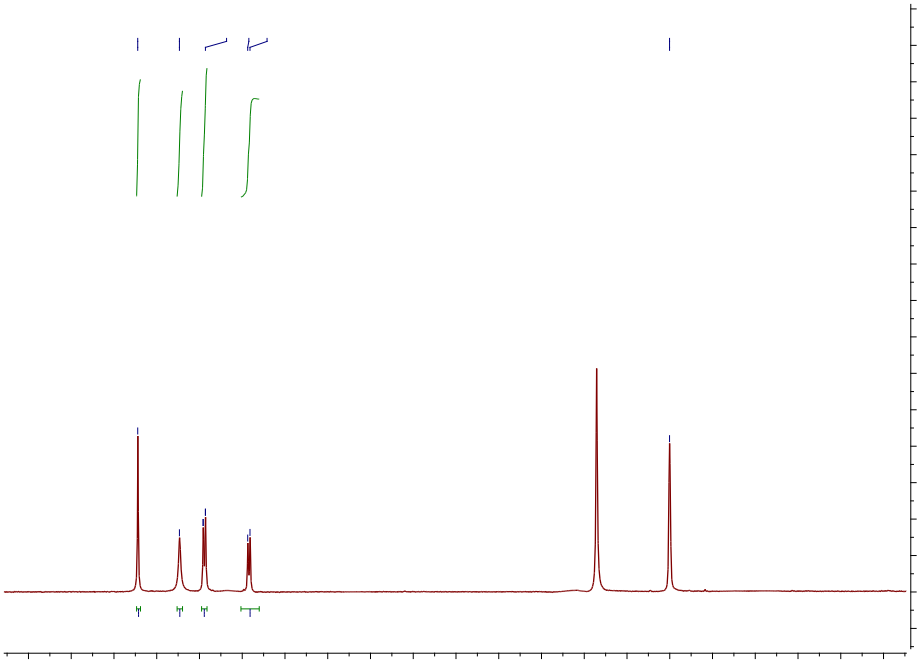

Figure S3.5. ^{13}C-NMR spectrum of NDI diboronic acid **5** in DMSO-d_6.

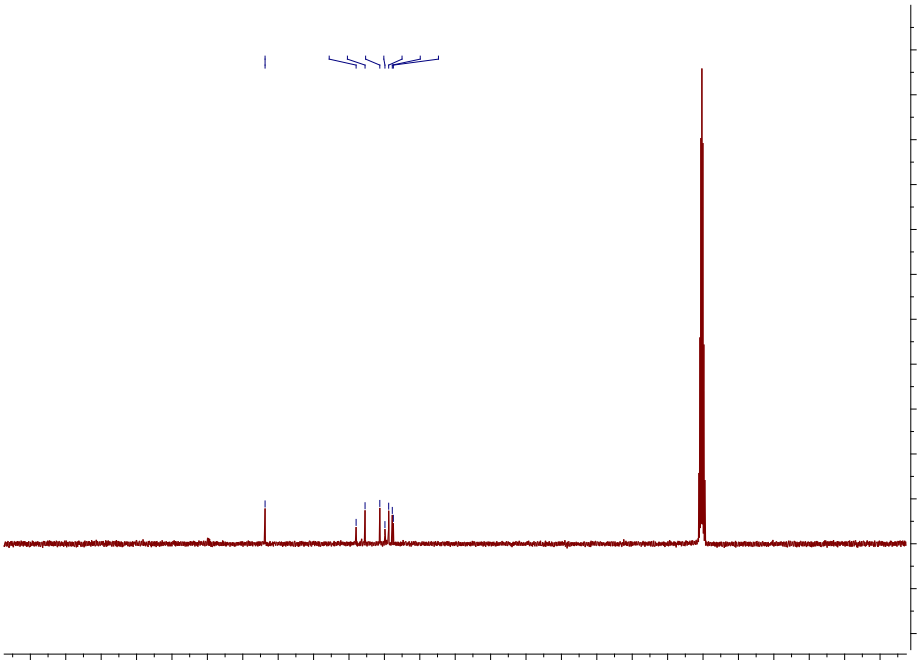

Figure S3.6. ^{1}H-NMR spectrum of PPE diboronic acid **6** in DMSO-d_6.

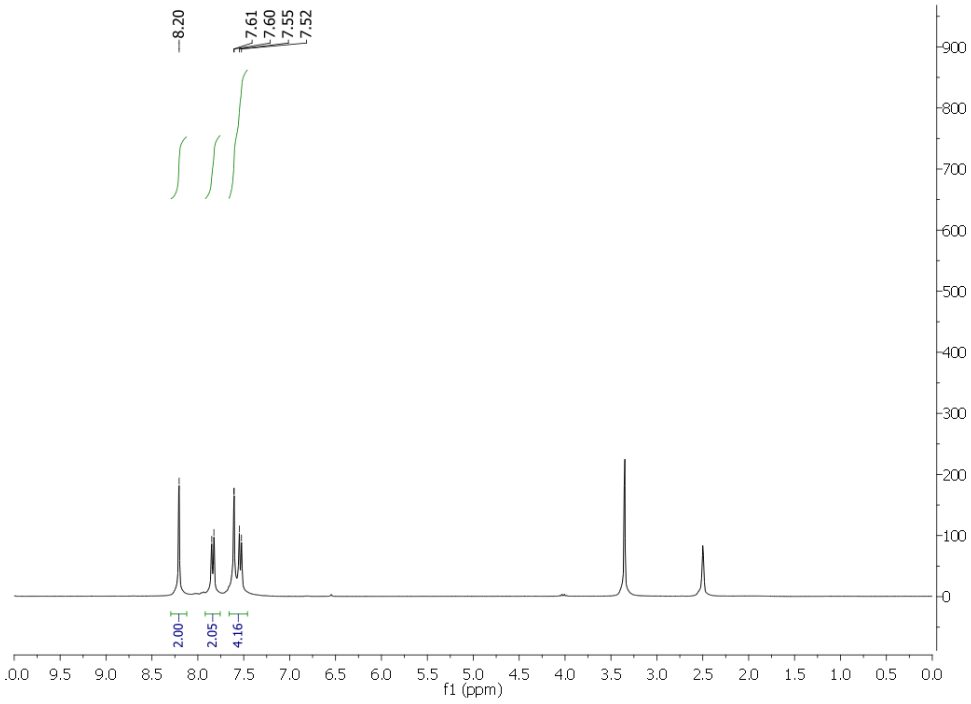

Figure S3.7. ^{13}C-NMR spectrum of PPE diboronic acid **6** in DMSO-d_6.

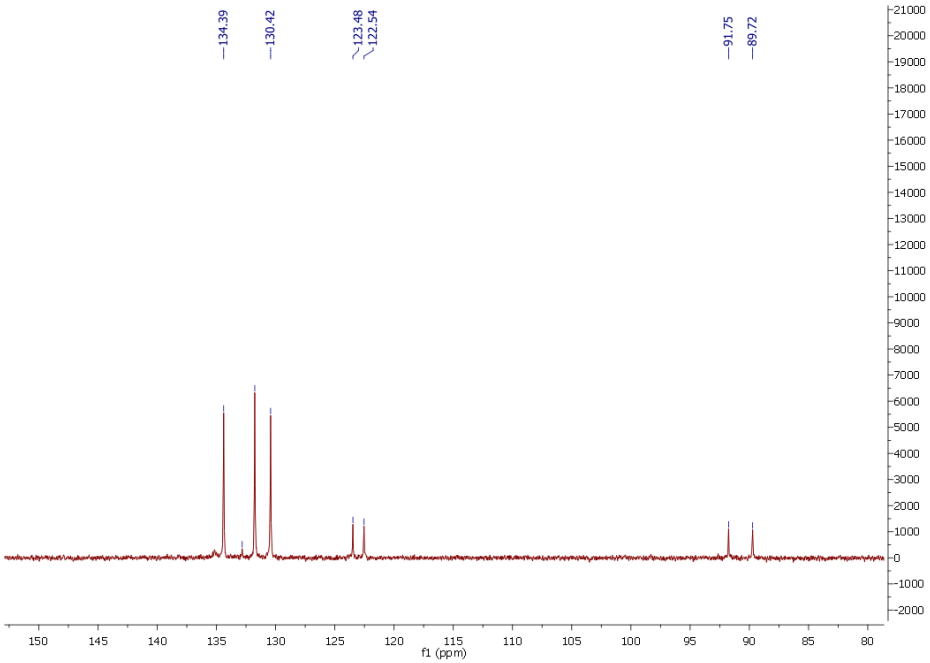

D. FT-IR Spectra.

Figure S3.8. FT-IR of pyrene diboronic acid **3** (blue) and **ZnPc-Py COF** (red).

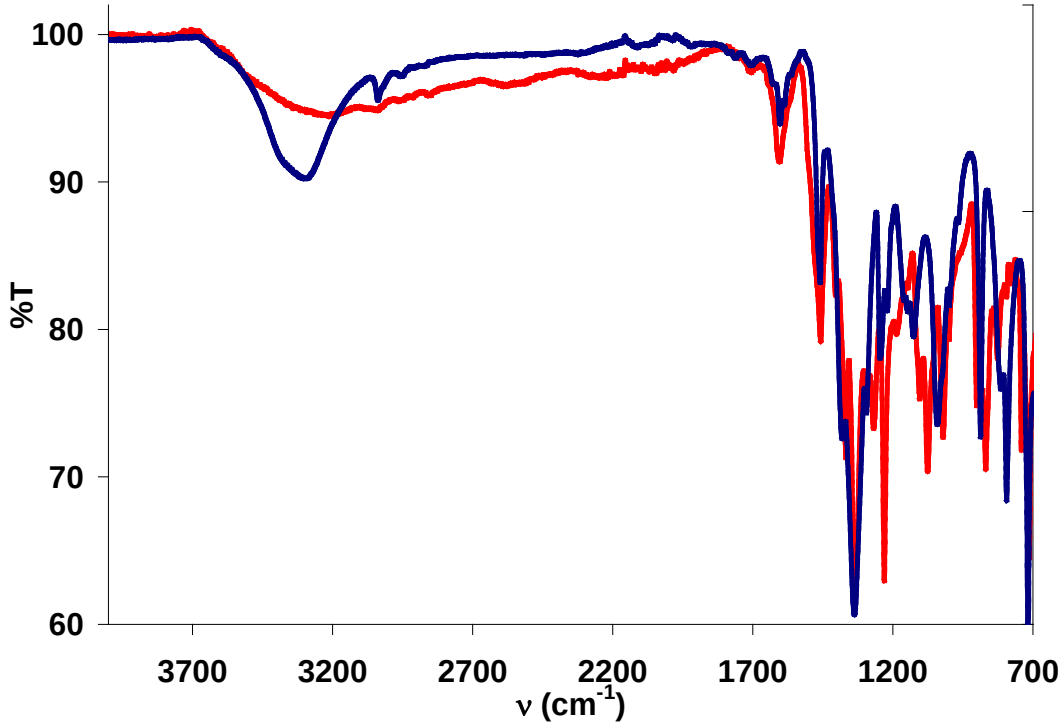

Figure S3.9. Expansion of 700-1800 cm^{-1} region of the above spectrum.

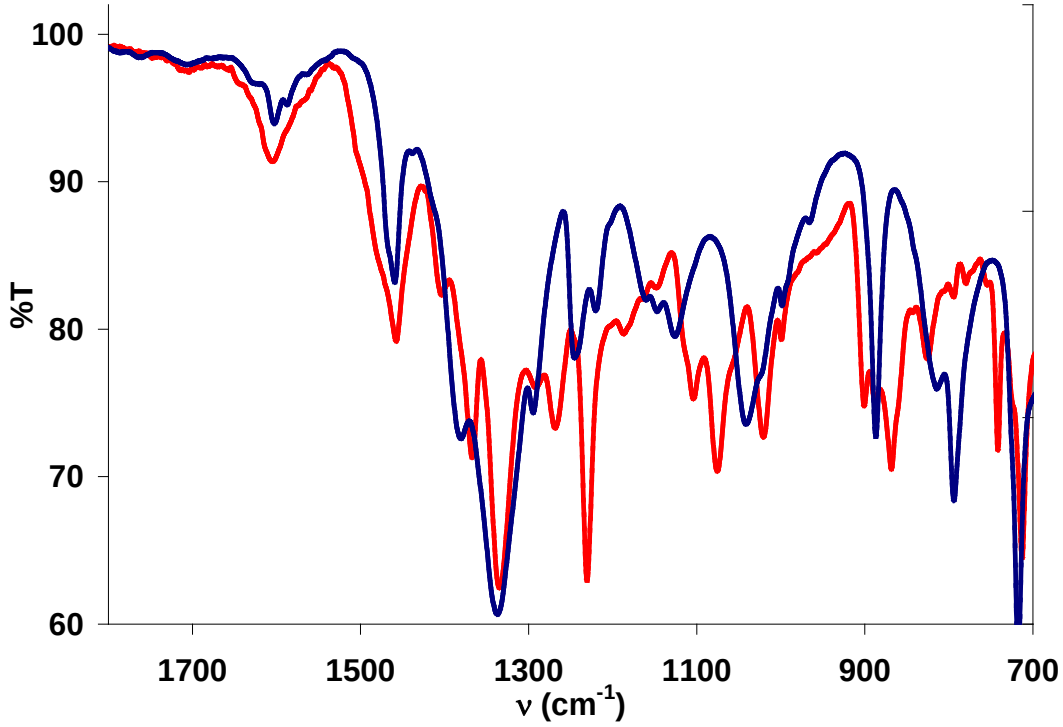

Figure S3.10. FT-IR of DPB acid **4** (blue) and **ZnPc-DPB COF** (red).

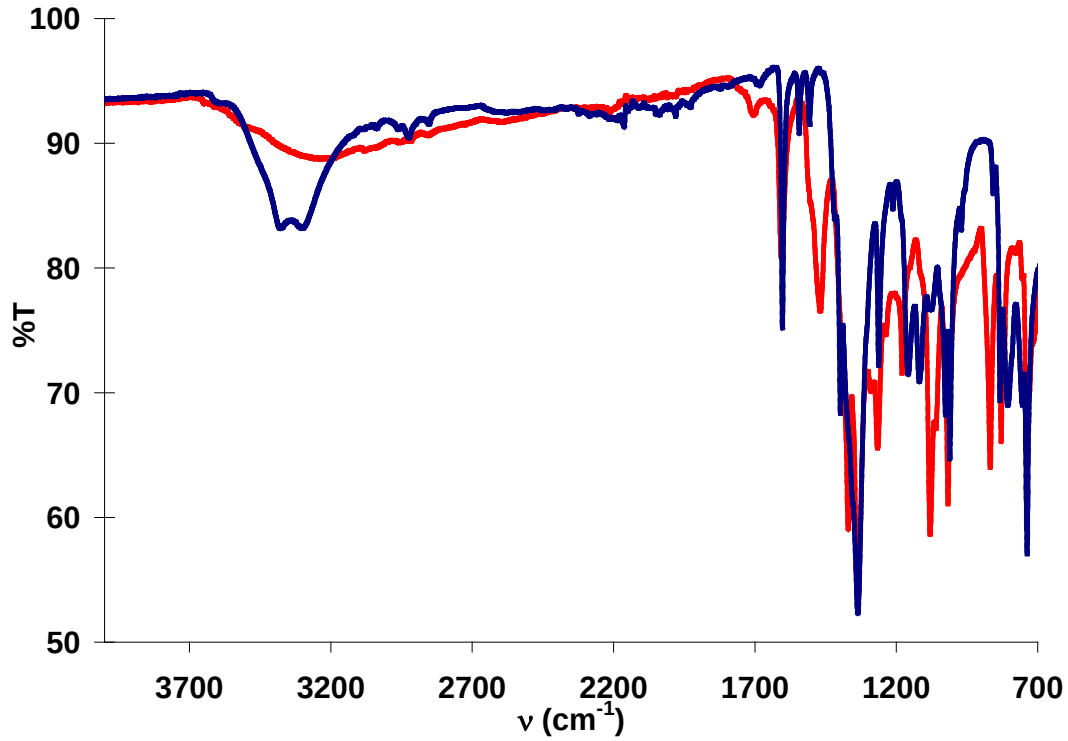

Figure S3.11. Expansion of 700-1800 cm^{-1} region of the above spectrum.

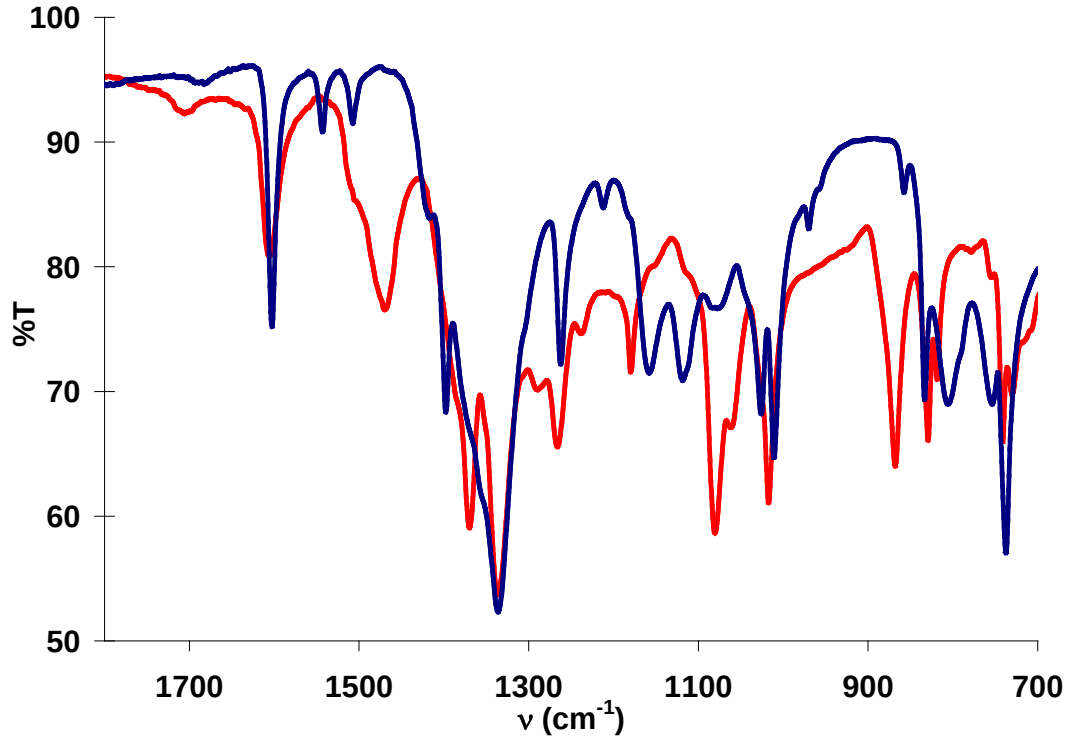

Figure S3.12. FT-IR of NDI diiodide **8** (blue) and pinacolboronate ester **9** (red).

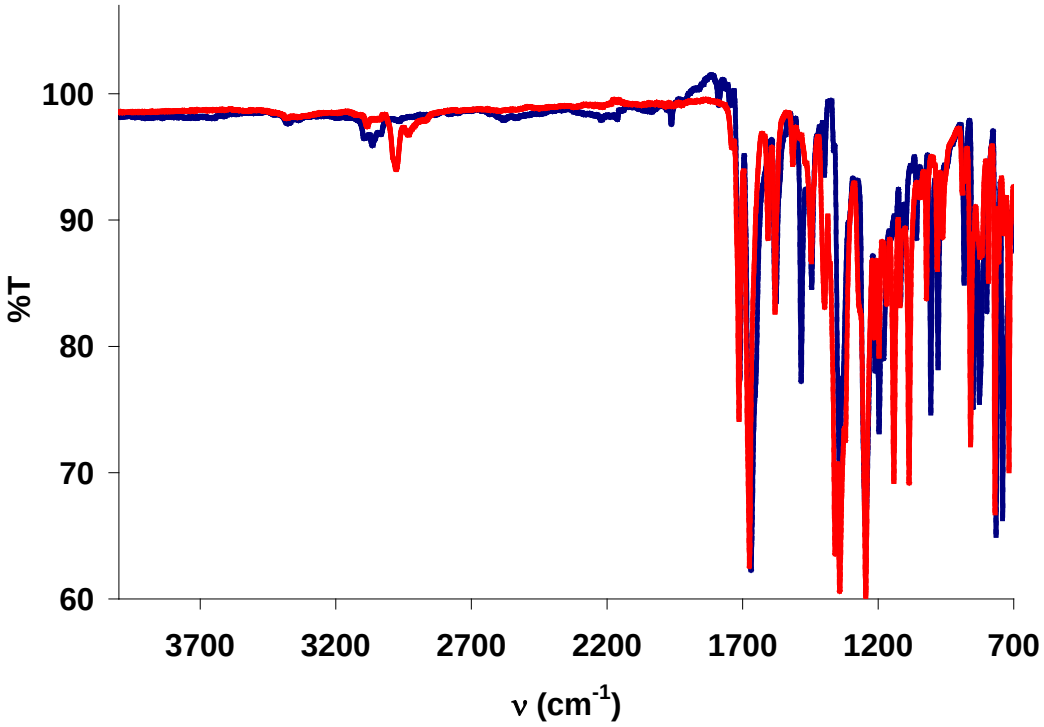

Figure S3.13. Expansion of 700-1800 cm^{-1} region of the above spectrum.

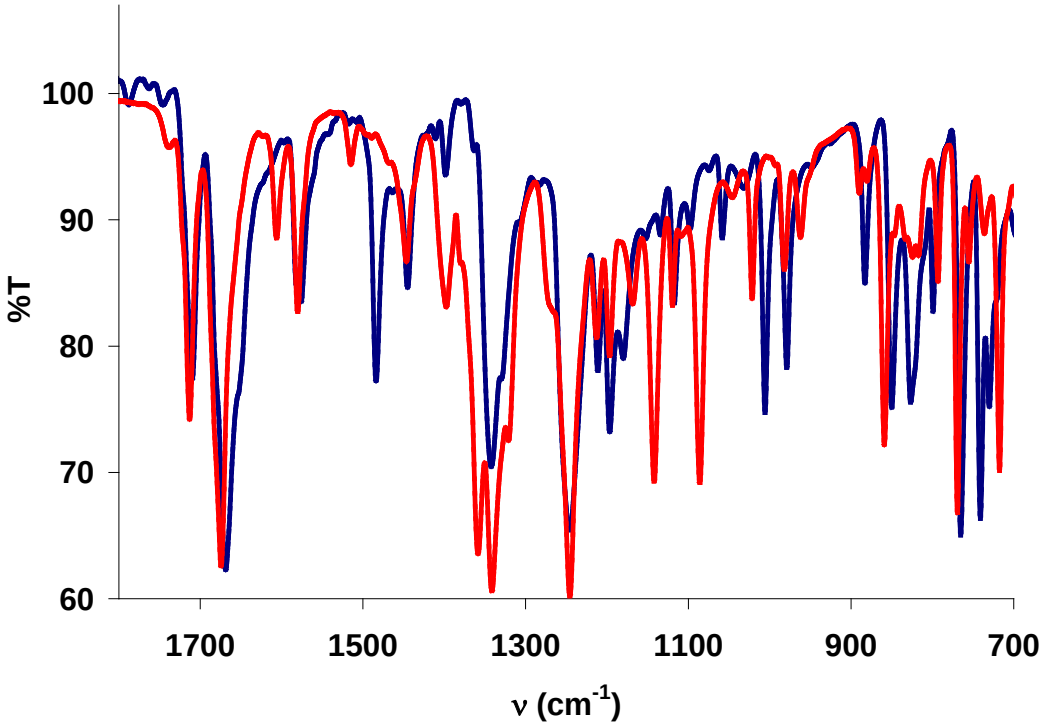

Figure S3.14. FT-IR of NDI acid **5** (blue) and **ZnPc-NDI COF** (red).

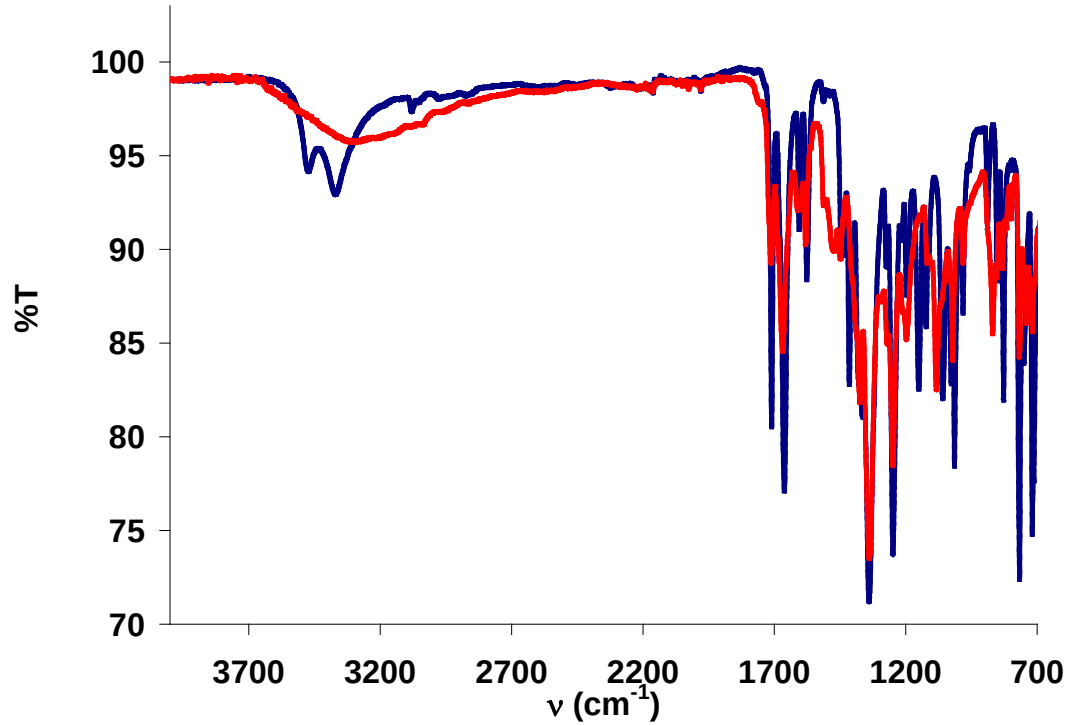

Figure S3.15. Expansion of 700-1800 cm^{-1} region of the above spectrum.

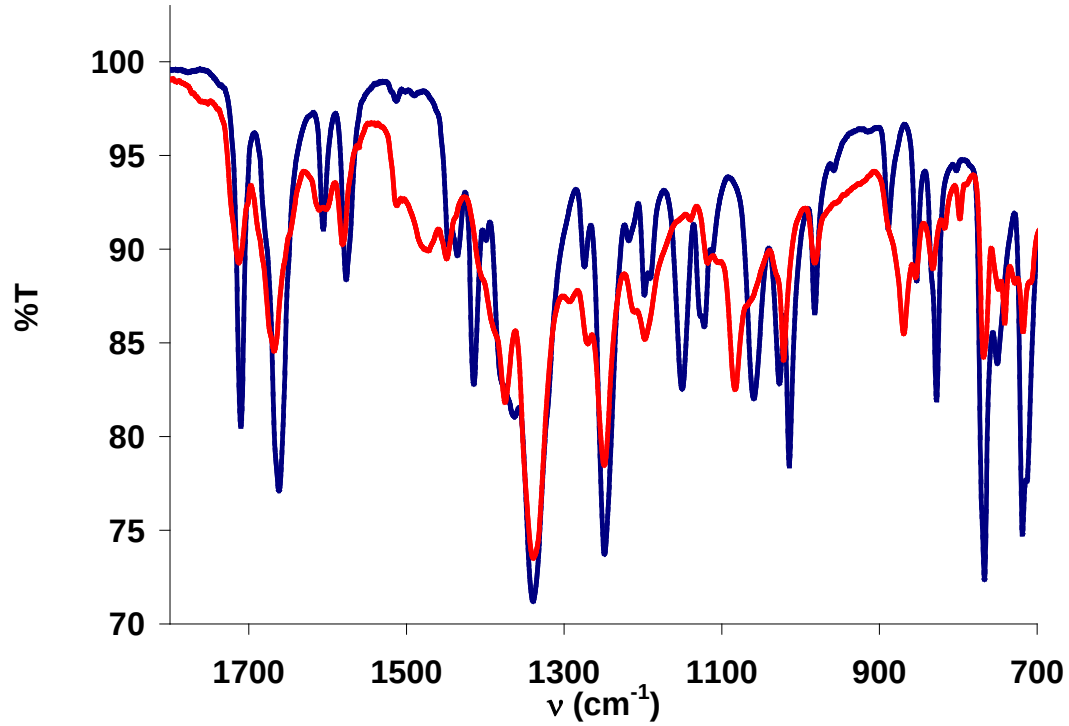

Figure S3.16. FT-IR of diboronic acid **6** (blue) and **ZnPc-PPE COF** (red).

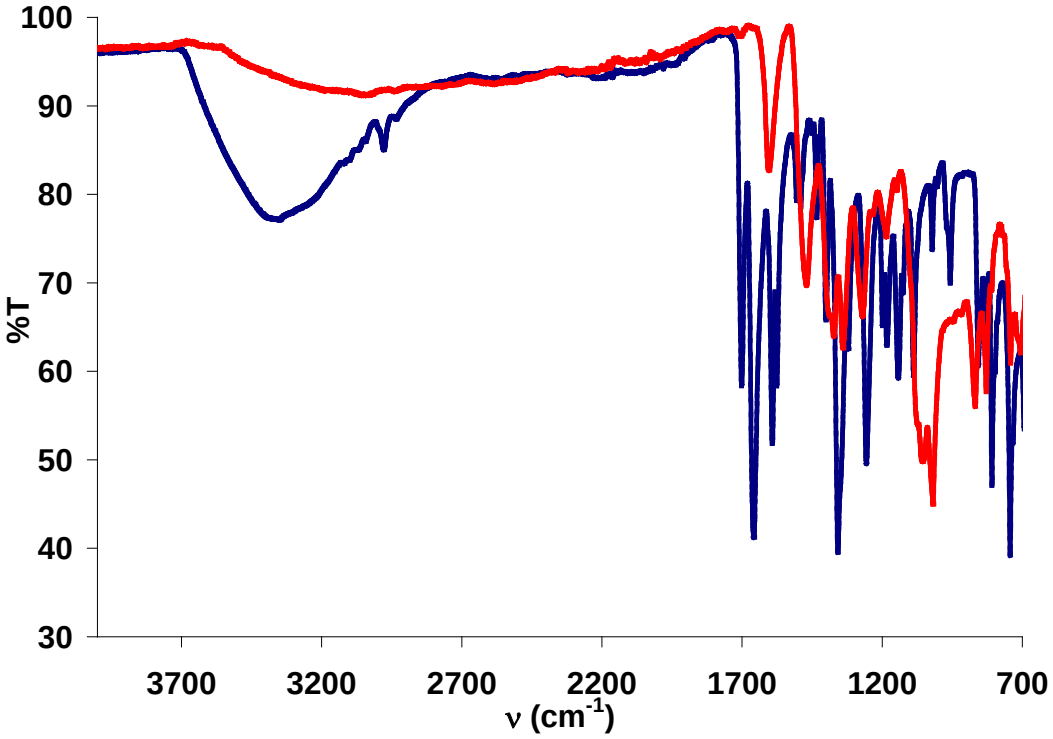

Figure S3.17. Expansion of 700-1800 cm^{-1} region of the above spectrum.

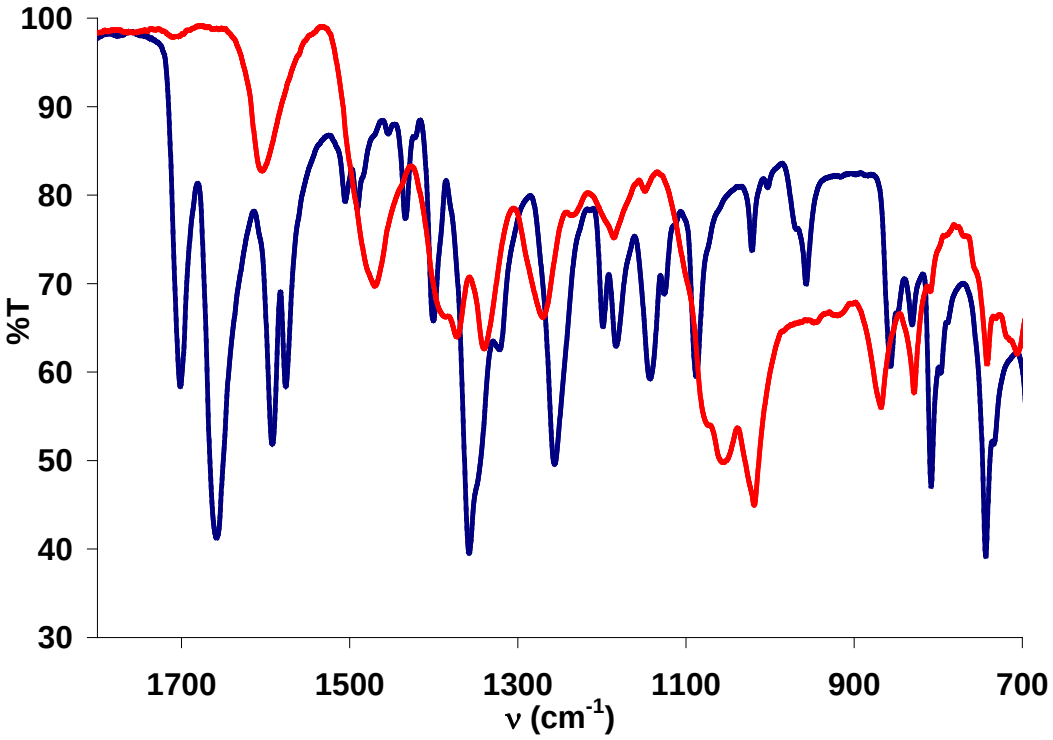

E. UV-Vis-NIR Characterization

Figure S3.18. Diffuse reflectance absorption spectra of **ZnPc-Py COF** (gold), **ZnPc-DPB COF** (blue), **ZnPc-NDI COF** (red) and **ZnPc-PPE COF** (purple) powders.

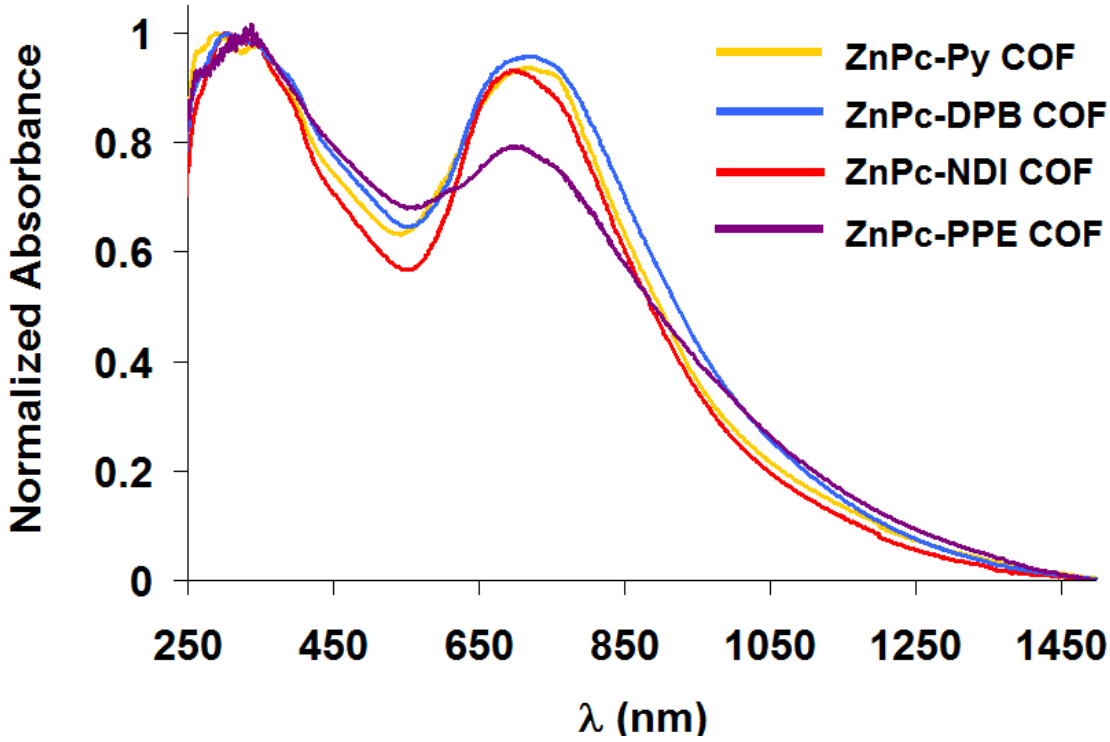

F. Simulation & Refinement of the COF Structures. Crystal modeling of the COFs was carried out using the Materials Studio (ver. 5.0) suite of programs by Accelrys[5]. The initial structures were constructed piecewise starting with a primitive tetragonal unit cell with space group *P*4/*mmm*. The *a* cell parameter was estimated according to the distance between the center of the vertices for each COF as shown in Figure S3.19, and *c* parameter was arbitrarily chosen as 3.35 Å. The structures were optimized using the Geometry Optimization routine including energy minimization with cell parameters optimization, using the parameters from the Universal Force Field. Modeling of the staggered structures was performed in a similar manner but starting with the space group *I*4/*mmm*, and c = 6.70 Å. Calculation of the simulated powder diffraction patterns and Pawley refinements were performed the Materials Studio Reflex Plus Module. The observed diffraction patterns were subjected to Pawley refinement wherein peak profile were refined using the Pseudo-Voigt peak shape function and asymmetry was corrected using the Berar-Baldinozzi function.

Figure S3.19. Precursor structures used for initial modeling of the COF structures.

ZnPc-Py Monomer

ZnPc-DPB Monomer

Figure S3.20. Modeled COF crystals.

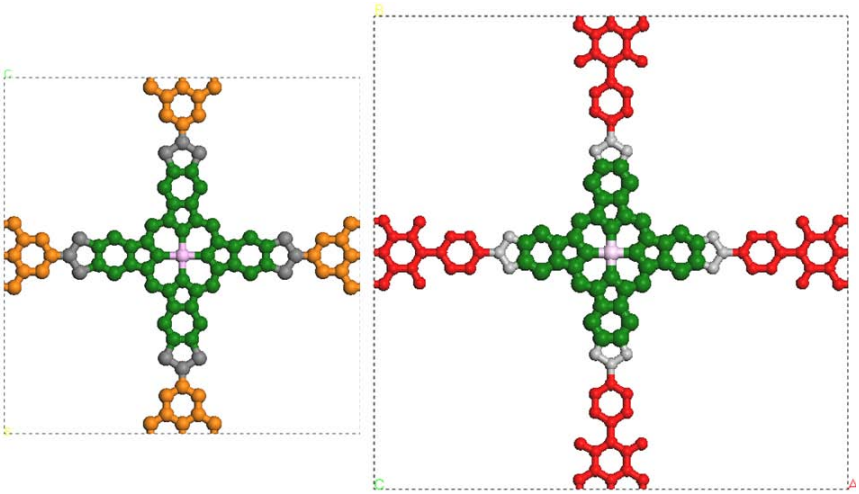

ZnPc-Py COF **ZnPc-NDI COF**

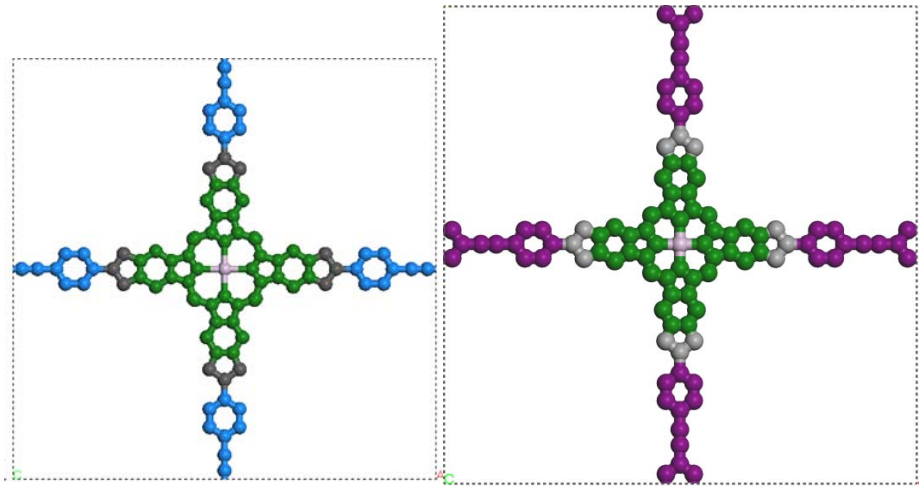

ZnPc-DPB COF **ZnPc-PPE COF**

Figure S3.21. Observed (blue) versus Pawley-refined (red) PXRD pattern profiles for **ZnPc-Py COF**. Residuals are indicated.

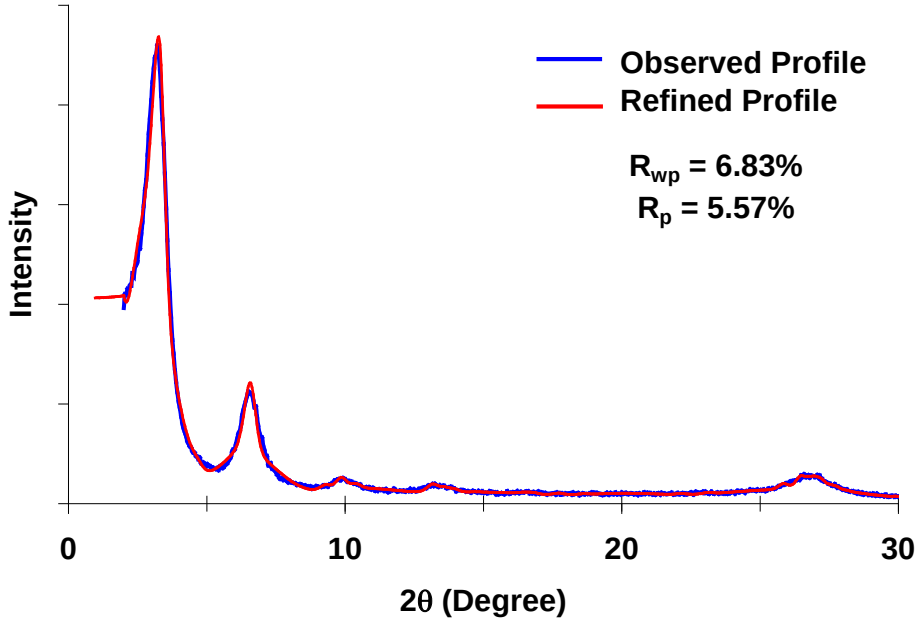

Figure S3.22. Observed (blue) versus Pawley-refined (red) PXRD pattern profiles for **ZnPc-DPB COF**. Residuals are indicated.

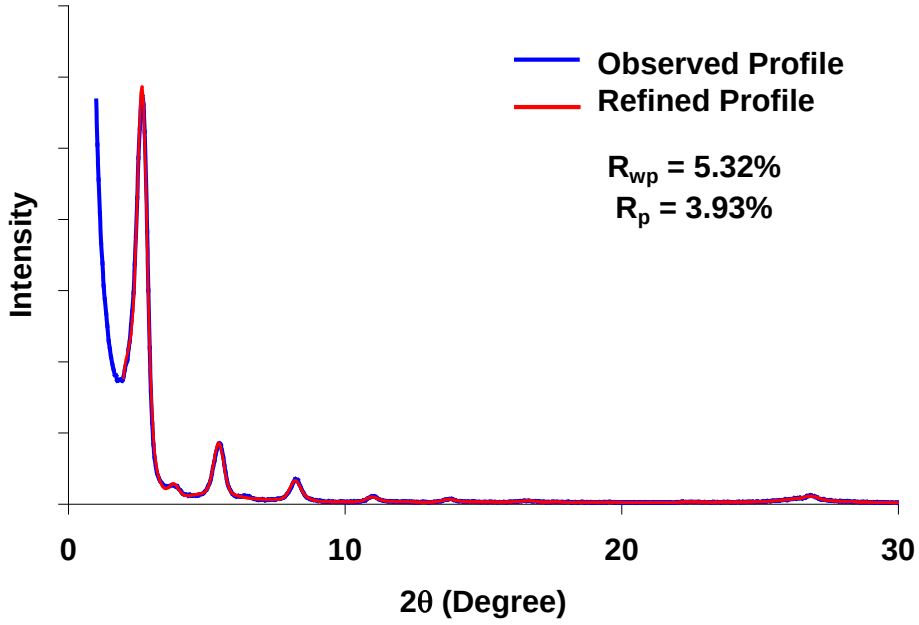

Figure S3.23. Observed (blue) versus Pawley-refined (red) PXRD pattern profiles for **ZnPc-NDI COF**. Residuals are indicated.

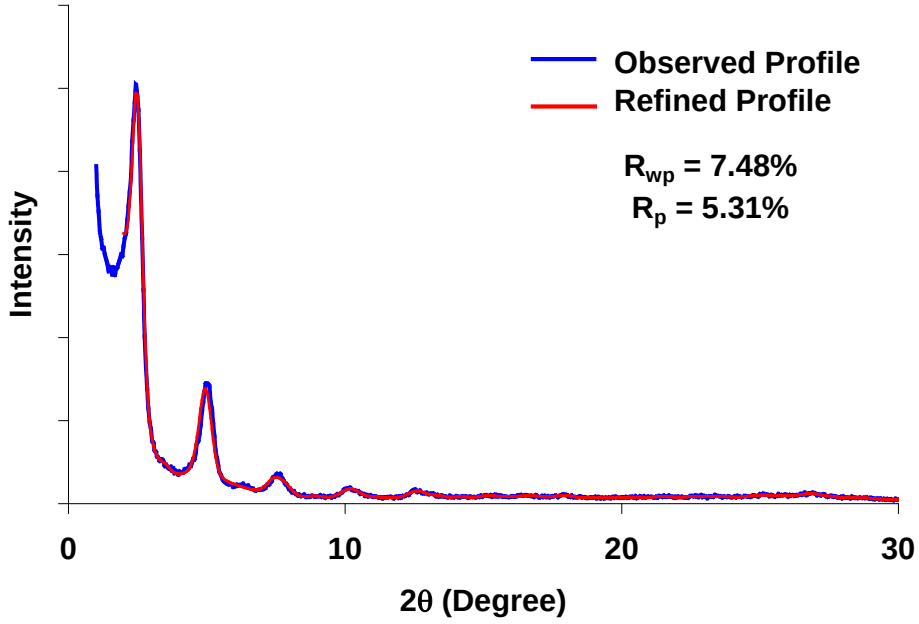

Figure S3.24. Observed (blue) versus Pawley-refined (red) PXRD pattern profiles for **ZnPc-PPE COF**. Residuals are indicated.

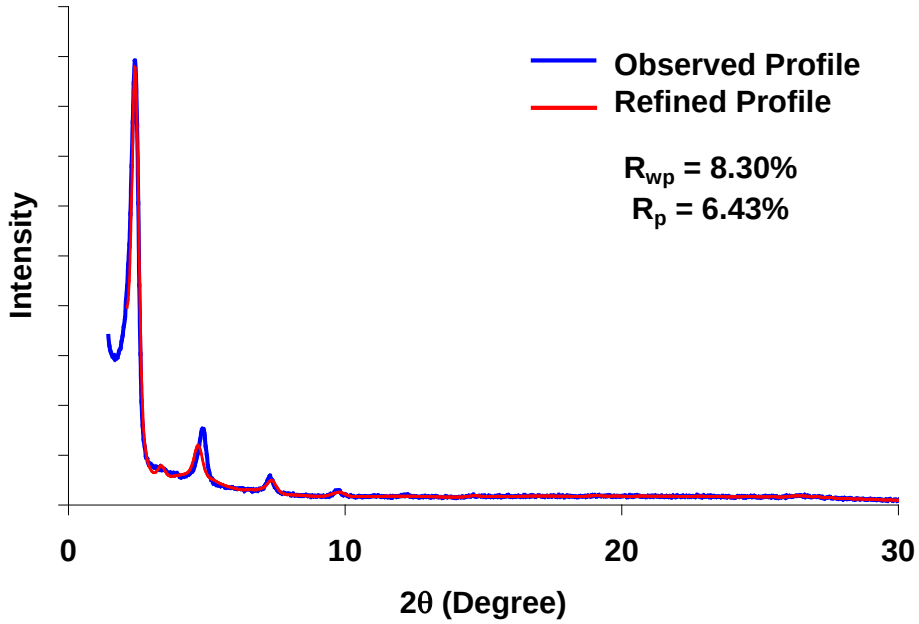

Table S3.1. Comparison of unit cell parameters of the simulated crystals, the *d*-spacing of the 100 diffraction peaks and the refined patterns for each prepared COF.

ZnPc-Py COF	*a* (Å)	*c* (Å)
MS modeling	27.185	3.535
d_{100}	27.056	
Pawley refinement	26.980	3.338

ZnPc-DPB COF	*a* (Å)	*c* (Å)
MS modeling	32.469	3.556
d_{100}	33.060	
Pawley refinement	32.183	3.356

ZnPc-NDI COF	*a* (Å)	*c* (Å)
MS modeling	36.064	3.542
d_{100}	36.176	
Pawley refinement	35.701	3.361

ZnPc-PPE COF	*a* (Å)	*c* (Å)
MS modeling	36.718	3.552
d_{100}	37.403	
Pawley refinement	38.533	3.367

Table S3.2. Fractional atomic coordinates for refined unit cell of **ZnPc-Py COF**.

Tetragonal,
(*P*4/*mmm*)
a = *b* = 26.980 Å, *c* = 3.338 Å

atom	*x*	*y*	*z*
C1	0.027462	0.500000	0.50000
C2	0.027462	0.410860	0.50000
C3	0.053706	0.455430	0.50000
C4	0.105674	0.455430	0.50000
C5	0.131288	0.500000	0.50000
C6	0.265000	0.475000	0.50000
C7	0.309000	0.450000	0.50000
C8	0.355000	0.475000	0.50000
C9	0.401000	0.462000	0.50000
O1	0.212025	0.546591	0.50000
B1	0.182823	0.500000	0.50000
N1	0.430000	0.500000	0.50000
N2	0.416000	0.584000	0.50000
Zn1	0.500000	0.500000	0.50000

Table S3.3. Fractional atomic coordinates for refined unit cell of **ZnPc-DPB COF**.

Tetragonal
(*P*4/*mmm*)
a = *b* = 32.183 Å, *c* = 3.356 Å

atom	*x*	*y*	*z*
C1	0.020491	0.500000	0.50000
C2	0.057698	0.500000	0.50000
C3	0.102075	0.500000	0.50000
C4	0.123748	0.464739	0.50000
C5	0.166807	0.464739	0.50000
C6	0.188528	0.500000	0.50000
C7	0.300642	0.480551	0.50000
C8	0.337406	0.457860	0.50000
C9	0.373823	0.480551	0.50000
C10	0.414478	0.469042	0.50000
O1	0.261315	0.464137	0.50000
B1	0.236652	0.500000	0.50000
N1	0.440321	0.500000	0.50000
N2	0.428054	0.428054	0.50000
Zn1	0.500000	0.500000	0.50000

Table S3.4. Fractional atomic coordinates for unit cell of **ZnPc-NDI COF**.

Tetragonal (*P*4/*mmm*)
a = *b* = 35.701 Å, *c* = 3.361 Å

atom	*x*	*y*	*z*
C1	0.019879	0.500000	0.50000
C2	0.019879	0.433099	0.50000
C3	0.039699	0.466552	0.50000
C4	0.079187	0.466552	0.50000
C5	0.140886	0.500000	0.50000
C6	0.162059	0.466552	0.50000
C7	0.201335	0.466552	0.50000
C8	0.221662	0.500000	0.50000
C9	0.319419	0.480860	0.50000
C10	0.352942	0.460236	0.50000
C11	0.386323	0.480974	0.50000
C12	0.423494	0.470264	0.50000
O1	0.095827	0.435714	0.50000
O2	0.285292	0.467504	0.50000
B1	0.263921	0.500000	0.50000
N1	0.099281	0.500000	0.50000
N2	0.447162	0.500000	0.50000
N3	0.434520	0.434520	0.50000
Zn1	0.500000	0.500000	0.50000

Table S3.5. Fractional atomic coordinates for unit cell of **ZnPc-PPE COF**.

Tetragonal (*P*4/*mmm*)
a = *b* = 38.533 Å, *c* = 3.367 Å

atom	*x*	*y*	*z*
C1	0.018677	0.468853	0.50000
C2	0.038444	0.500000	0.50000
C3	0.078109	0.500000	0.50000
C4	0.110866	0.500000	0.50000
C5	0.150530	0.500000	0.50000
C6	0.170299	0.468853	0.50000
C7	0.207616	0.468853	0.50000
C8	0.227438	0.500000	0.50000
C9	0.327400	0.481973	0.50000
C10	0.359425	0.462877	0.50000
C11	0.391299	0.482008	0.50000
C12	0.426676	0.471666	0.50000
O1	0.293260	0.468194	0.50000
B1	0.270958	0.500000	0.50000
N1	0.437864	0.437864	0.50000
N2	0.448380	0.500000	0.50000
Zn1	0.500000	0.500000	0.50000

Figure S3.25. Crystal models of **ZnPc-Py COF** (top left), **ZnPc-DPB COF** (top right), **ZnPc-NDI COF** (bottom left) and **ZnPc-PPE COF** (bottom right) in a staggered conformation and corresponding simulated PXRD patterns. Similarly colored sheets are in alternating unit cells. Note the lack of match to observed PXRD patterns (*vide supra*).

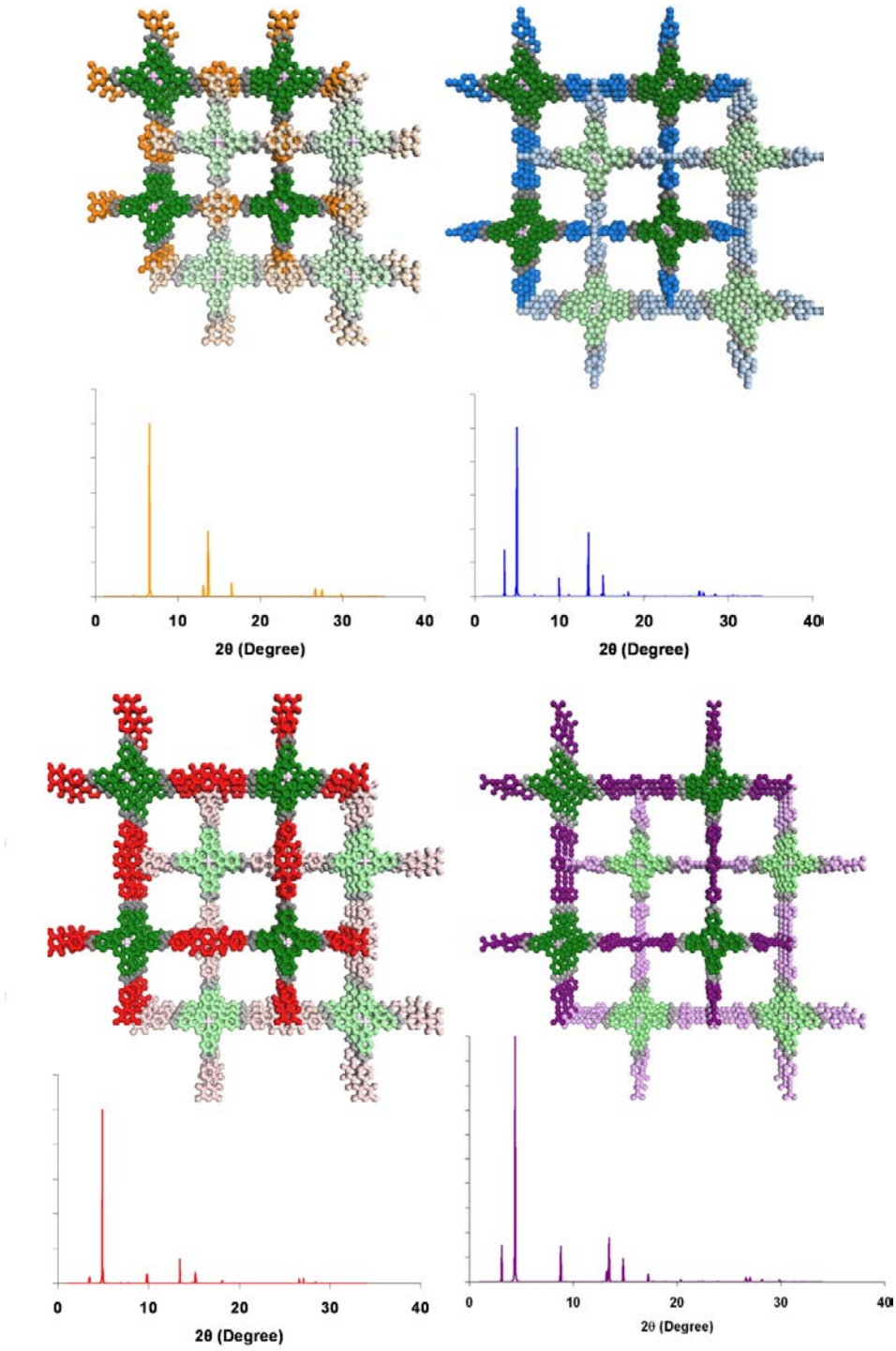

G. Thermogravimetric Analysis.

Figure S3.26. Thermogravimetric traces of **ZnPc-Py COF** (gold), **ZnPc-DPB COF** (blue), **ZnPc-NDI COF** (red) and **ZnPc-PPE COF** (purple).

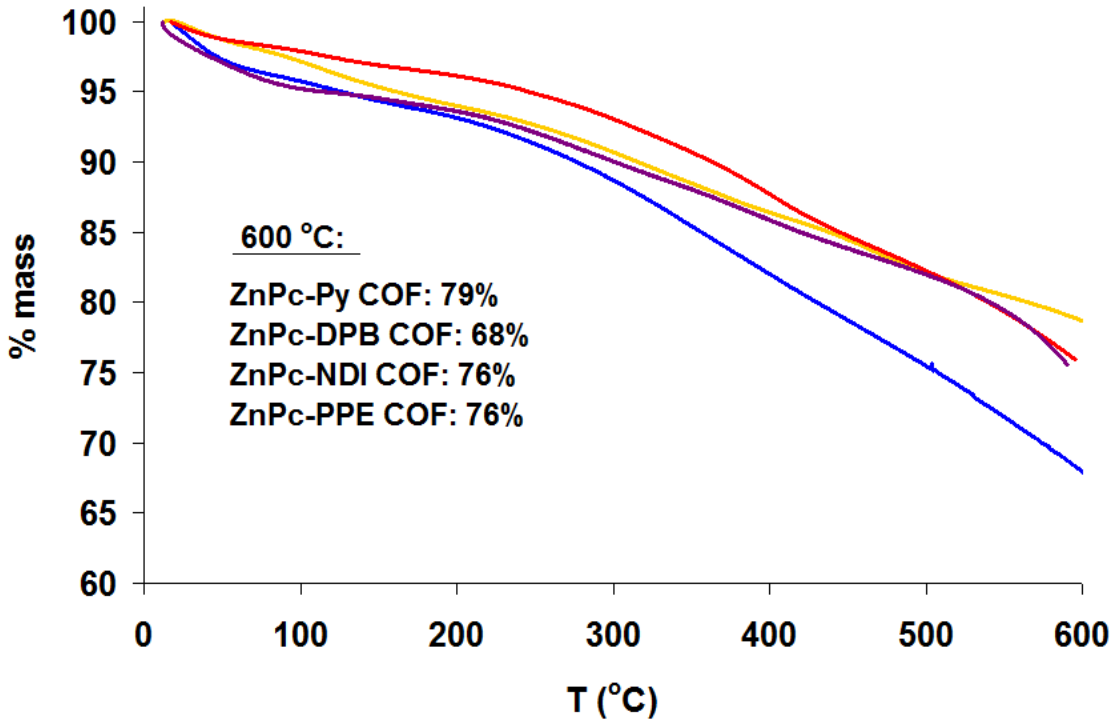

H. Surface Area Measurements.

Figure S3.27. BET plot for **ZnPc-Py COF** calculated from isotherm data.

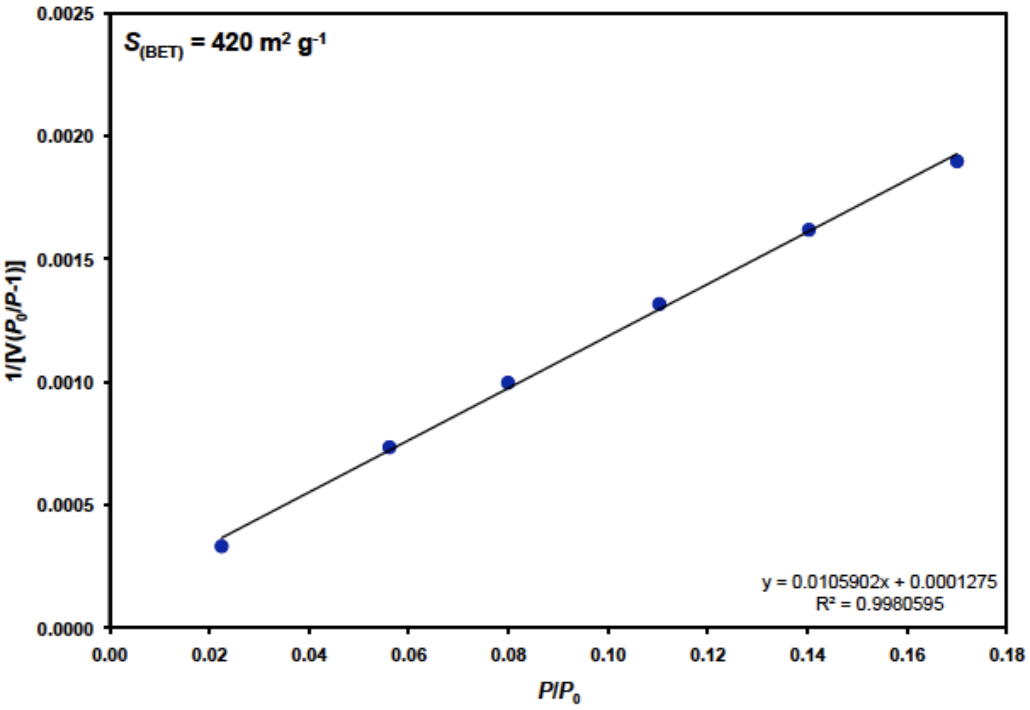

Figure S3.28. BET plot for **ZnPc-DPB COF** calculated from isotherm data.

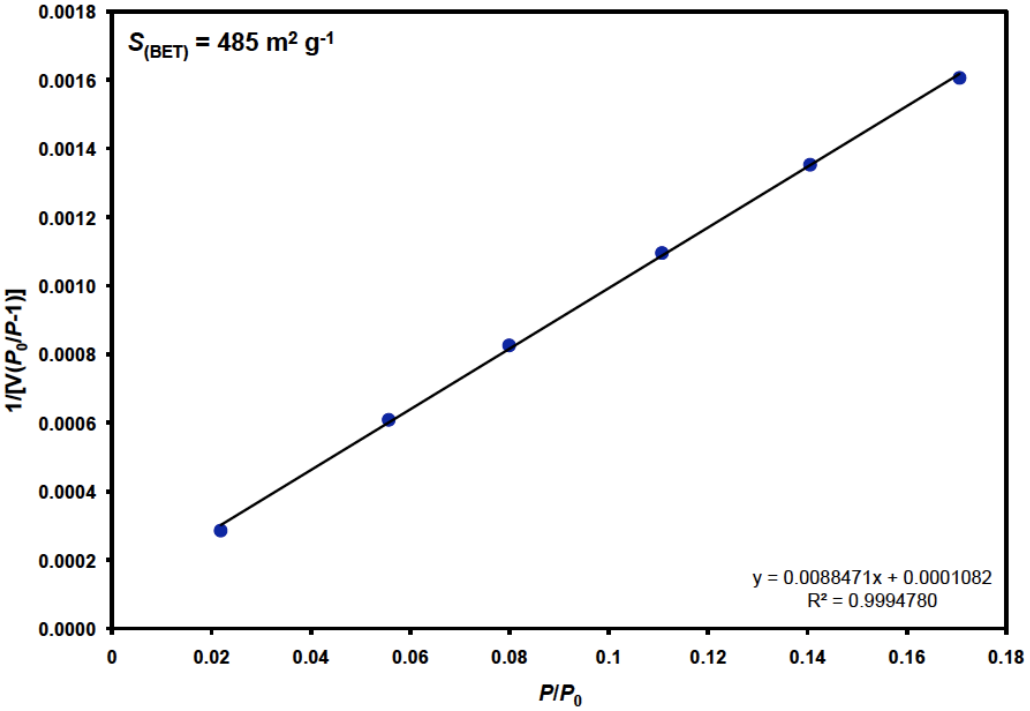

Figure S3.29. BET plot for **ZnPc-NDI COF** calculated from isotherm data.

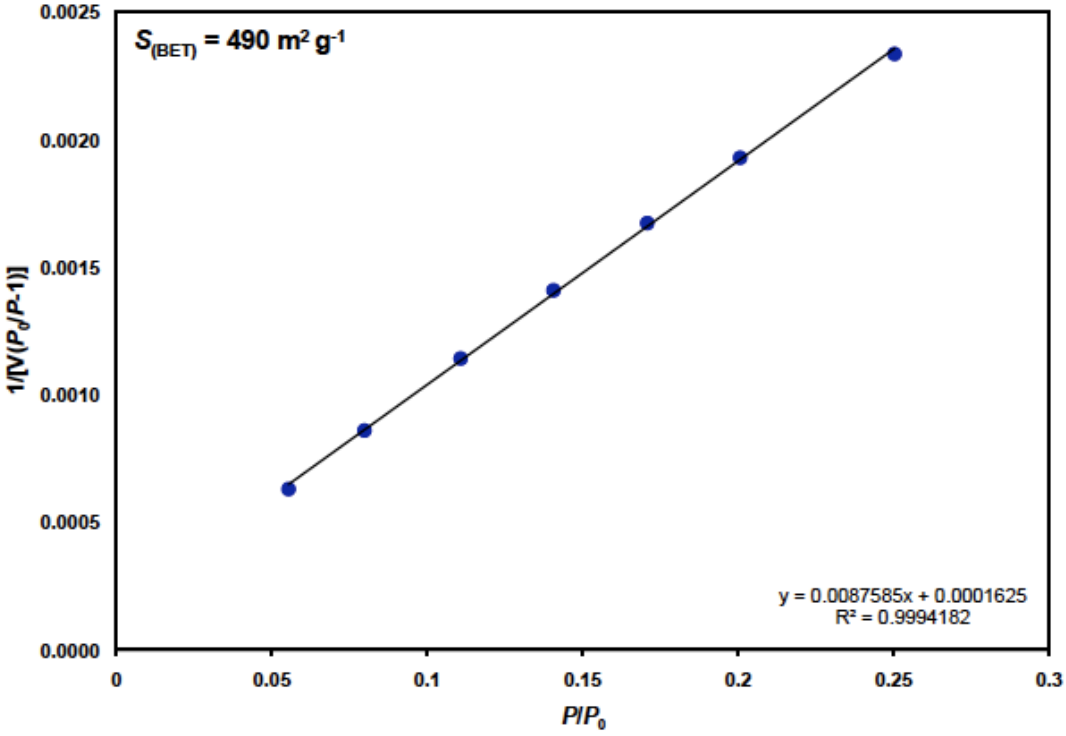

Figure S3.30. BET plot for **ZnPc-PPE COF** calculated from isotherm data.

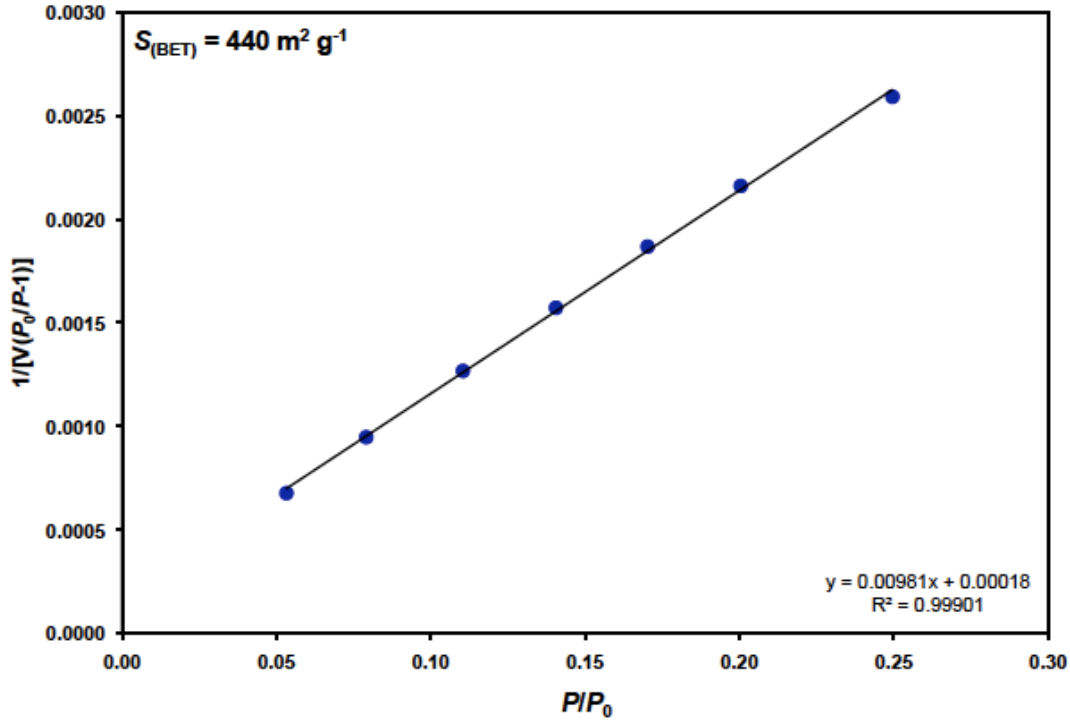

Figure S3.31. Differential (top) and cumulative (bottom) pore size distribution plot of **ZnPc-Py COF** from the application of the NLDFT model to the N_2 isotherm.

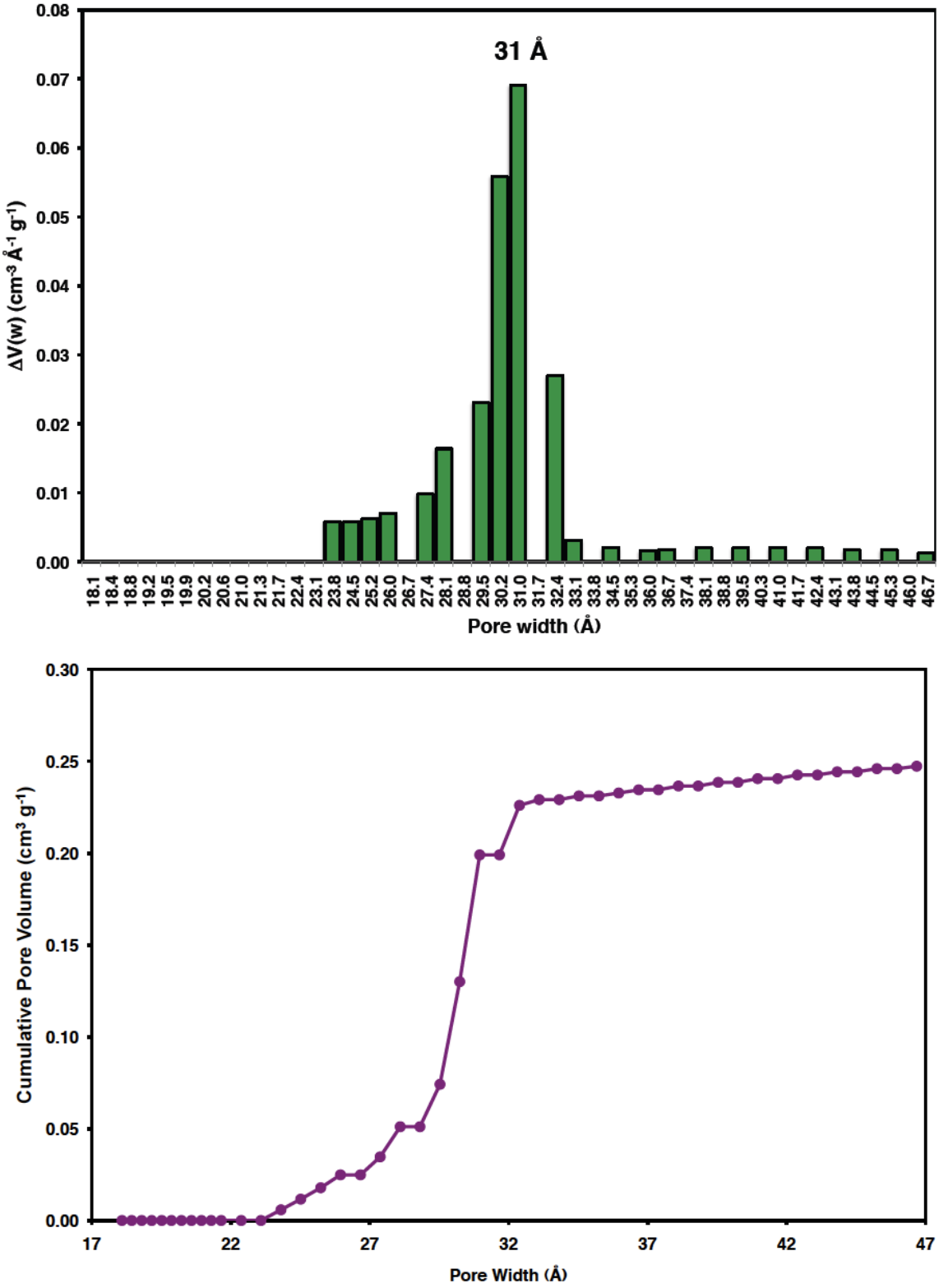

Figure S3.32. Differential (top) and cumulative (bottom) pore size distribution plot of **ZnPc-DPB COF** from the application of the NLDFT model to the N_2 isotherm.

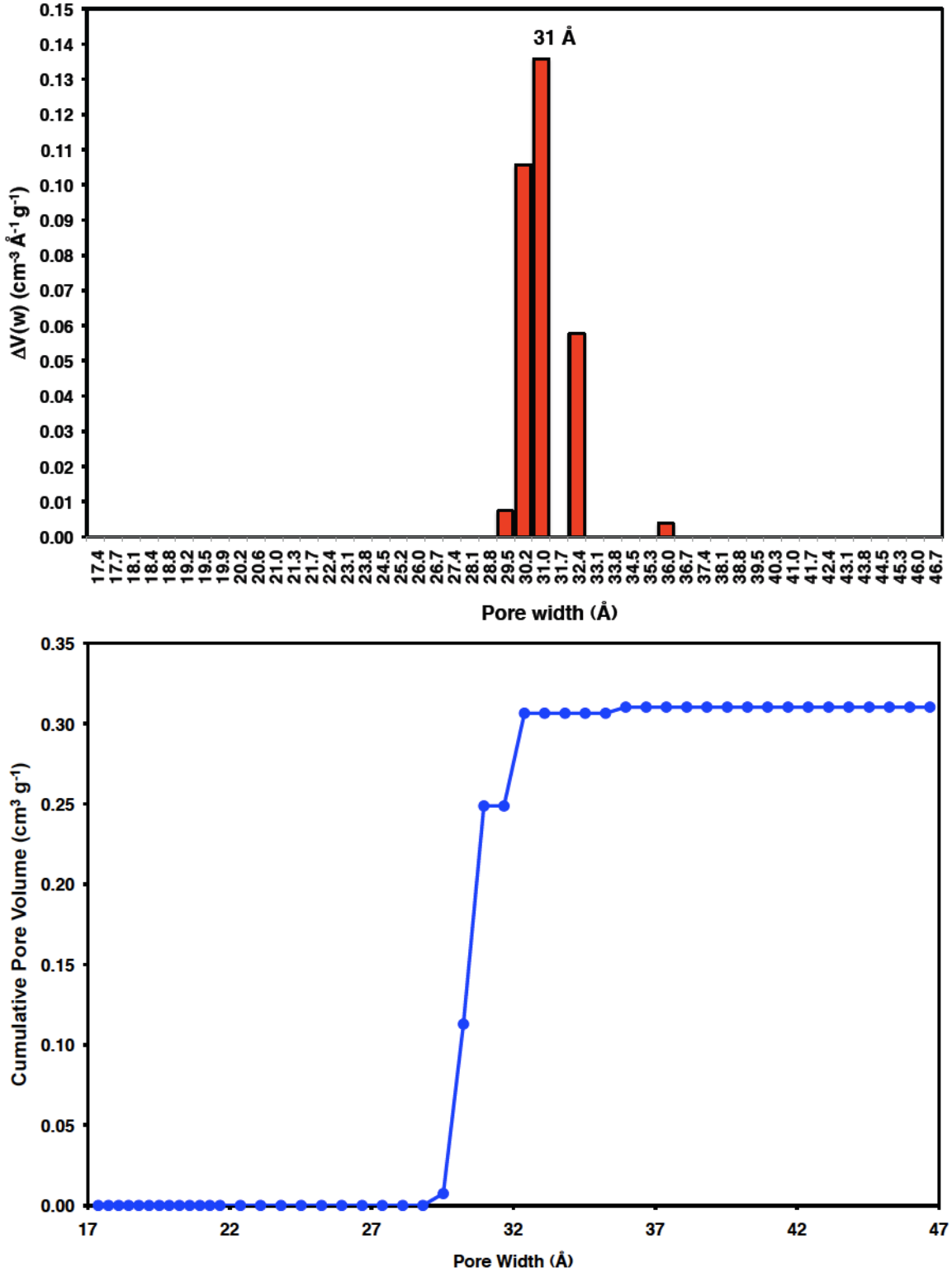

Figure S3.33. Differential (top) and cumulative (bottom) pore size distribution plot of **ZnPc-NDI COF** from the application of the NLDFT model to the N_2 isotherm.

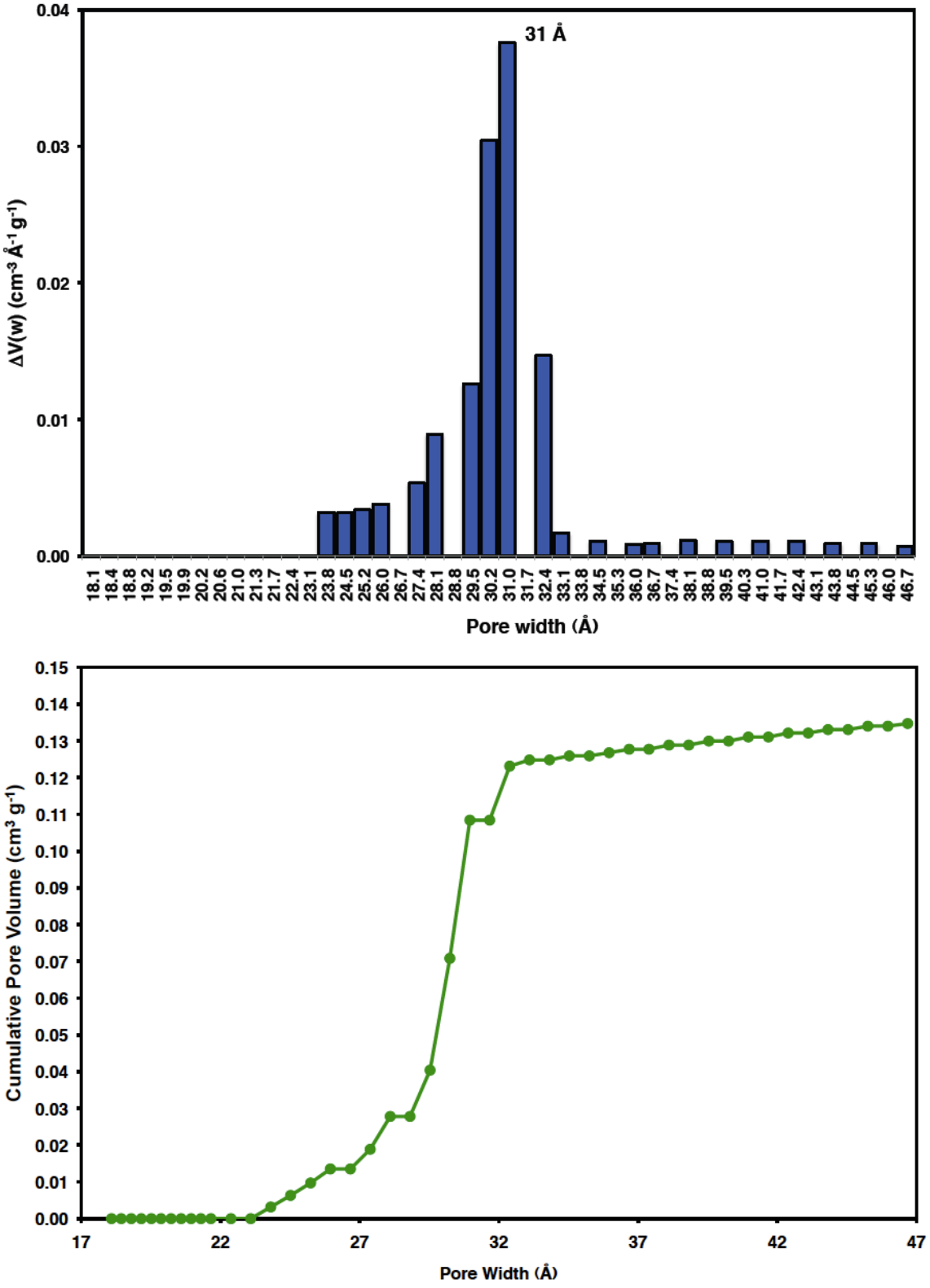

Figure S3.34. Differential (top) and cumulative (bottom) pore size distribution plot of **ZnPc-PPE COF** from the application of the NLDFT model to the N_2 isotherm.

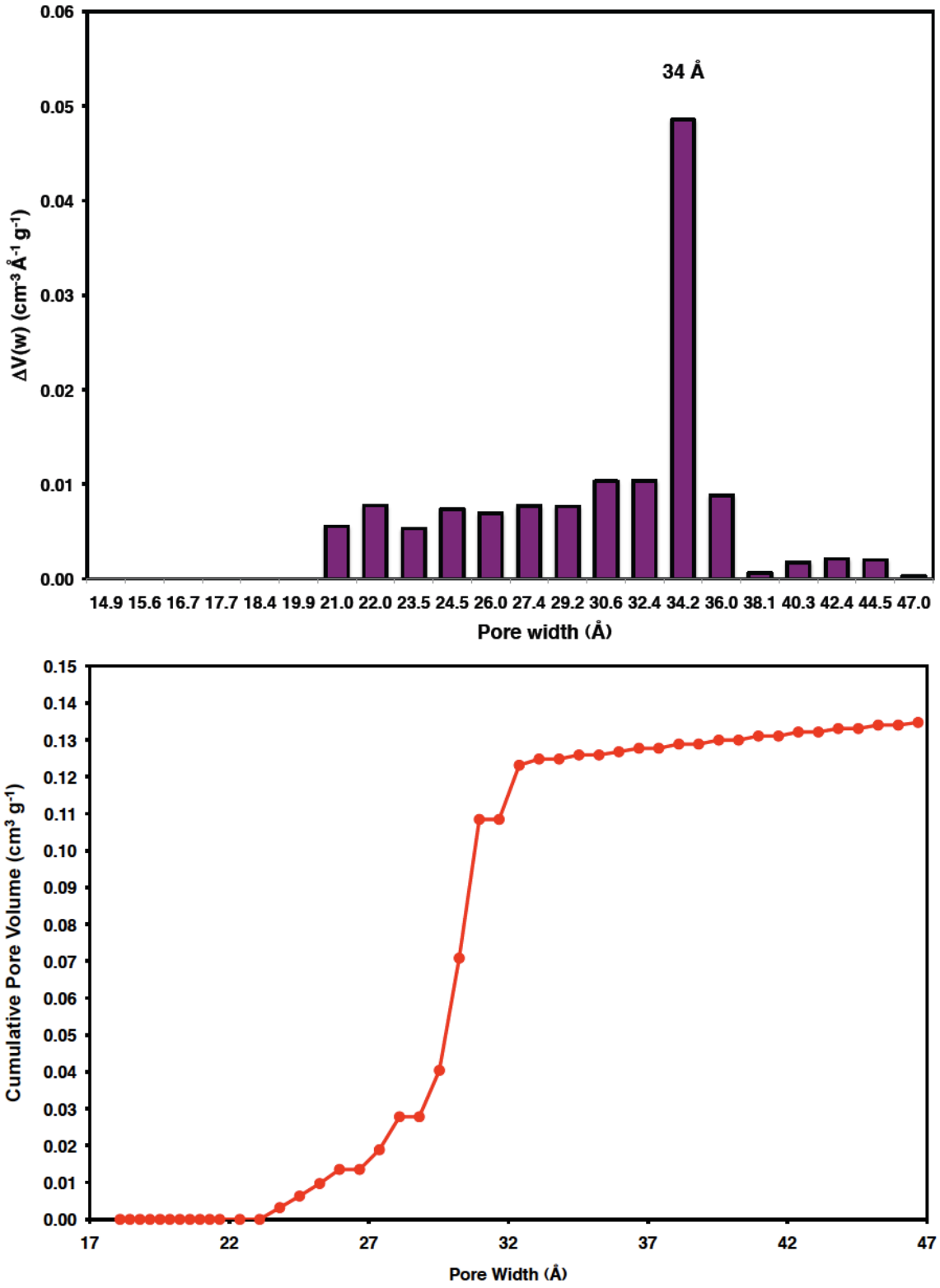

I. Scanning Electron Microscopy

Figure S3.35. Scanning electron micrographs of powder samples of (a) **ZnPc-Py COF,** (b) **ZnPc-DPB COF**, (c) **ZnPc-NDI COF** and (d) **ZnPc-PPE COF**.

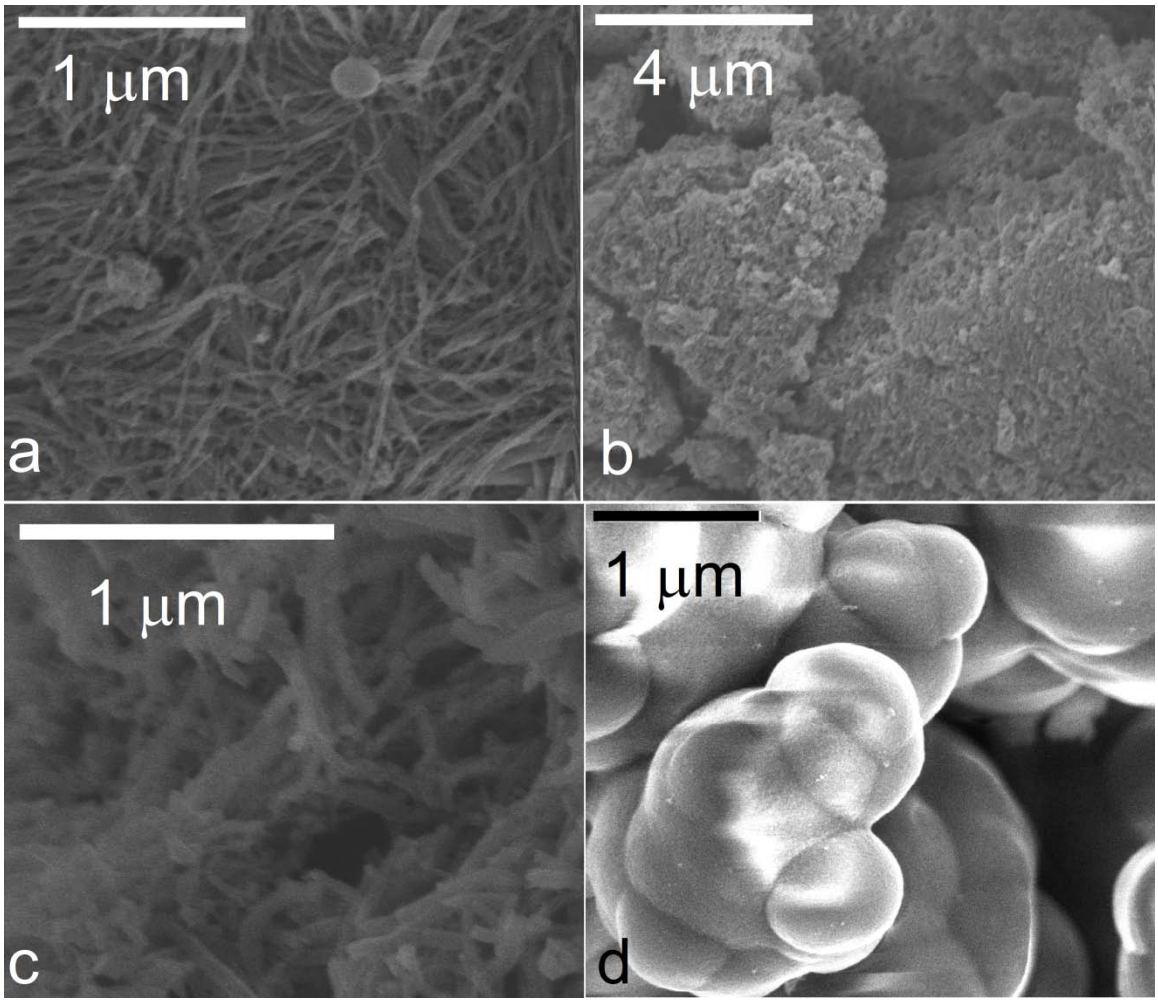

Figure S3.36. Top down SEM of (a) **ZnPc-Py COF** thin film, (b) **ZnPc-DPB COF** thin film, (c) **ZnPc-NDI COF** thin film, and (d) **ZnPc-PPE COF** thin film

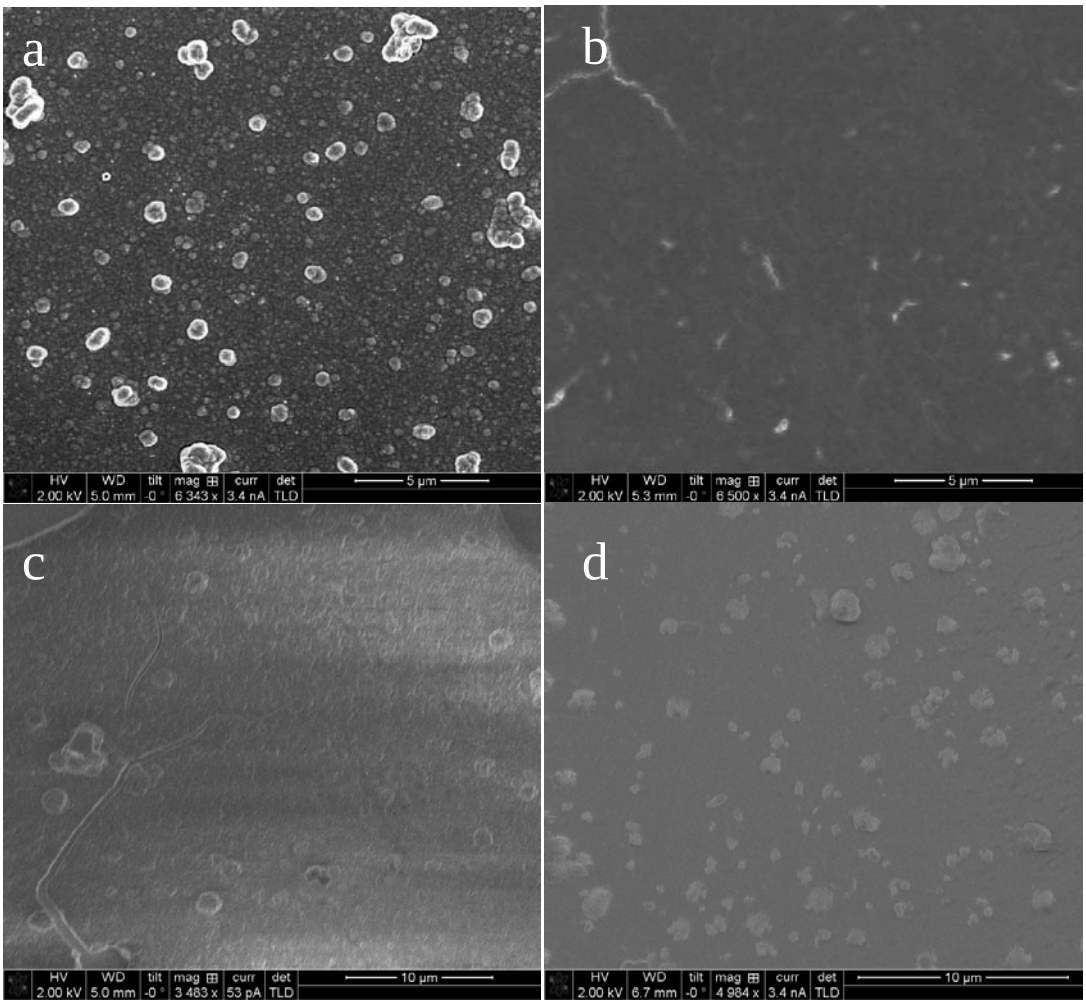

J. Higher Resolution X-ray Reflectivity of ZnPc-DPB COF Film

Figure S3.37. Background subtracted off-specular X-ray reflectivity of **ZnPc-DPB COF** thin film showing improved resolution compared to Fig. 3.6c.

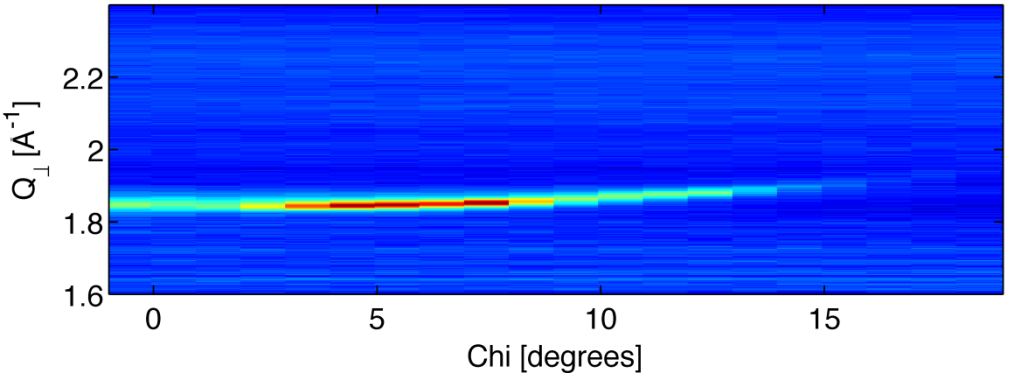

Figure S3.38. 2D projection of the intensity along $Q_\perp$ at Chi = 4.5 degrees. The FWHM of this peak gives the average domain size along the *c*-axis. For this sample, the FWHM is 0.02 Å^{-1} corresponding to a 31 nm (94 layers) correlation length.

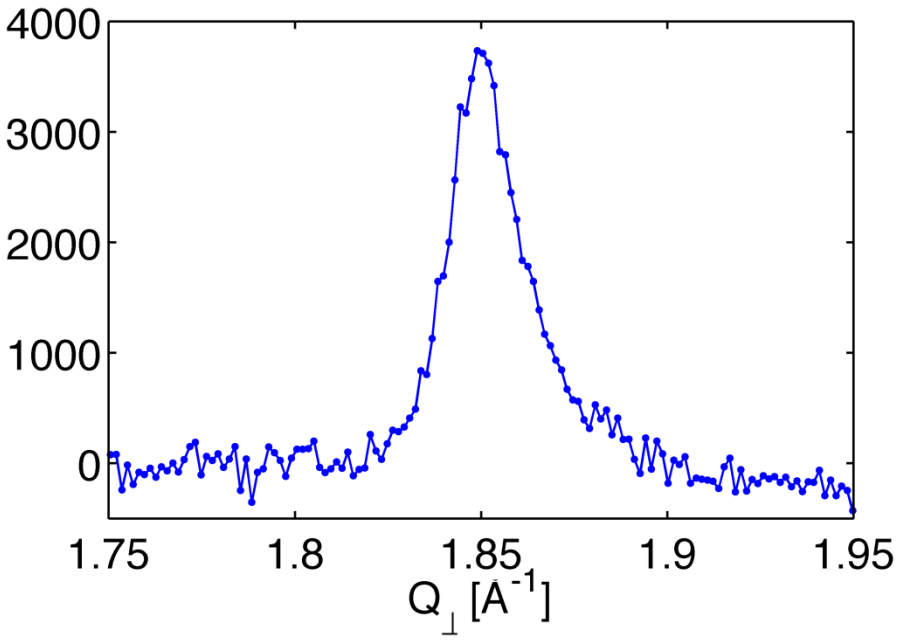

K. Characterization of HHTP-DPB COF film

Figure S3.39. Top down SEM of **HHTP-DPB COF** thin film on SLG (growth time: 24 h).

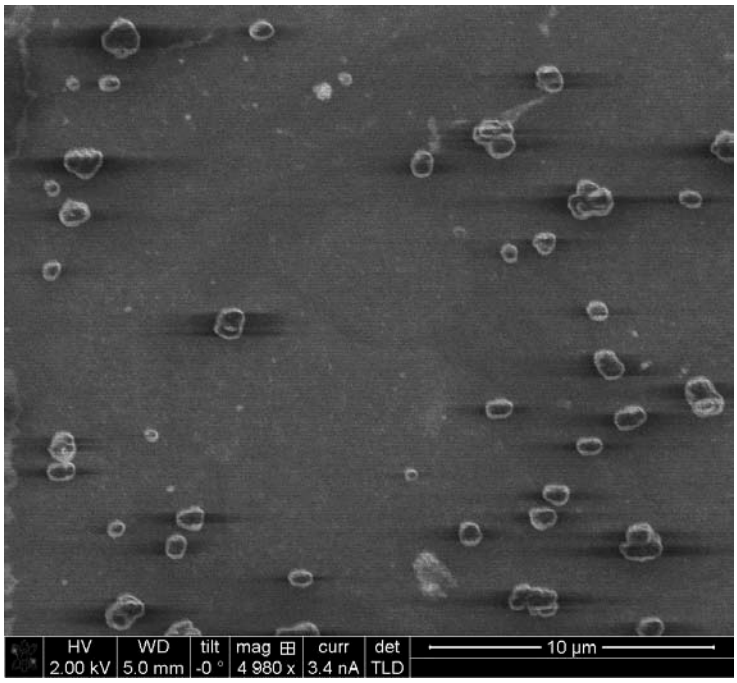

REFERENCES

1. Youssef, T. E. *Polyhedron* **29,** 1776 (2010).

2. Tzschucke, C. C., Murphy, J. M. & Hartwig, J. F. *Org. Lett.* **9,** 761 (2007).

3. Spitler, E. L., Koo, B. T., Novotney, J. L., Colson, J. W., Uribe-Romo, F. J., Gutierrez, G. D., Clancy, P. & Dichtel, W. R. *J. Am. Chem. Soc.* **133,** 19416 (2011).

4. Li, X., Cai, W., An, J., Kim, S., Nah, J., Yang, D., Piner, R., Velamakanni, A., Jung, I., Tutuc, E., Banerjee, S. K., Colombo, L. & Ruoff, R. S. *Science* **324,** 1312 (2009).

5. Materials Studio Release Notes v.5.0 (Accelrys Software, San Diego, 2009).

CHAPTER 4

PATTERNED GROWTH OF ORIENTED 2D COVALENT ORGANIC FRAMEWORK THIN FILMS ON SINGLE-LAYER GRAPHENE

Abstract

Two-dimensional covalent organic frameworks (COFs) are polymer networks that organize molecular building blocks into porous, layered structures of interest for organic optoelectronic and energy storage devices. Current synthetic methods produce these materials as either insoluble, microcrystalline powders or as oriented thin films on various substrates, including single-layer graphene (SLG). Under these conditions, COF thin films form on both the graphene-coated and bare regions of the substrate, suggesting uncontrolled nucleation processes that occur either in solution or nonselectively on different surfaces. Here, we describe modified polymerization conditions that provide COF films selectively on SLG. This finding enables COF films to be grown on lithographically patterned SLG substrates, which provide insight into the uniformity of film growth across the substrate and factors relevant to their nucleation and growth. The ability to grow COF films selectively on lithographically patterned SLG will facilitate their integration into devices.

This work was performed with Jason A. Mann and Catherine R. DeBlase in the Dichtel Research Group and has been submitted for publication in a peer-reviewed journal when this thesis was filed.

Introduction

Covalent organic frameworks (COFs)[1-10] are emerging materials that arrange and align molecular building blocks into crystalline, layered two-dimensional (2D)[1,5,11-14] or three-dimensional (3D)[4,15-20] polymer networks that feature high surface areas, excellent thermal stability, and low densities. 2D COFs have been studied for applications in gas storage[3,16], chemical separations[11], catalysis[21,22], energy storage[12,23], and as active layers in organic photovoltaic (OPV) devices [24]. COFs are usually isolated as polycrystalline powders produced under solvothermal conditions, and the first large single crystals of a 3D network were recently reported[25]. Controlling the morphology of COFs, as well as metal-organic frameworks or porous coordination polymer (MOFs or PCPs)[26-28] will enable new applications. We previously reported the growth of 2D COF films on single-layer graphene (SLG) with preferred crystalline orientations relative to the supporting substrate[29]. Under these conditions, although films grown on SLG showed improved crystallinity and orientational control relative to other substrates, the COF film nevertheless formed over the entire substrate, not just on SLG[30-34]. Strategies that limit growth to one surface material are highly desirable for patterning COF films and integrating them into devices.

Selectively patterned, oriented thin film morphologies broaden the potential applications for framework materials significantly as they might template the formation of other nanomaterials[30,35], enable fabrication of advanced device architectures, or grant access to two-dimensional heterostructures[36,37]. Spatial control and templated MOF/PCP formation has been demonstrated using micropatterned self-assembled monolayers[38-43], inkjet printing[44], and by generating metal ions of the

appropriate oxidation state at a working electrode[45-47]. In contrast, COFs have not been grown selectively onto patterned substrates under solvothermal conditions, and only one study[35] has demonstrated selective COF formation on metal surfaces patterned with NaCl islands under ultrahigh vacuum deposition conditions. Previously, we have grown COF thin films using SLG as substrate[29] and generalized these conditions to a variety of frameworks[7,48]. These thin films deposit across the graphene and also cover any exposed areas of the supporting substrate. For example, the 2D hexagonal network COF-5 forms on many other substrates, including metals such as Au, Pt, Pd, Ti, and Al, as well as on fused SiO_2 (see Chapter 4 appendix Fig. S4.3). Bein and coworkers also reported the growth of oriented COF films on Au, molybdenum oxide, and tin-doped indium oxide (ITO)[34], and demonstrated that ITO-supported thin films are suitable as active layers in OPVs[33]. These results suggest that typical solvothermal growth conditions provide COF films with moderate-to-good crystallinity and orientational control. However, no general approaches to preparing 2D COFs as thin films with simultaneous control over both their orientation and macroscopic pattern have been reported.

Here, we report the selective and patterned growth of a 2D phthalocyanine COF as an oriented thin film using SLG as a template. Graphene has received much attention for its desirable mechanical and electronic properties[49,50], and has been synthesized industrially using a roll-to-roll process to produce sheets with nearly 1 m diagonal length[51]. Moreover, SLG is compatible with established lithographic techniques and is routinely transferred to arbitrary substrates from its metal foil growth substrate[52-54]. Using appropriate solvothermal growth conditions, we show that

COF films form selectively on lithographically patterned graphene. These patterned films reveal important characteristics of COF film growth and could serve as a platform to optimize and develop COF syntheses. These results show that control of surface chemistry and synthetic conditions represents a promising means to direct the growth of COF films.

Results and Discussion

While exploring phthalocyanine (Pc) COF thin films as OPV active layers, we observed that the orientation of the crystallites was strongly influenced by the solvent composition[48] (Figure 4.1). Solvent blends employing *N*,*N*-dimethyl acetamide (DMA) and 1,2-dichlorobenzene (*o*-DCB) (1:2 *v*/*v*) yield thin films comprised of randomly oriented crystallites, whereas mixtures of DMA, *o*-DCB, MeOH, and 1,4-dioxane (Diox) (1:2:1:3 *v*/*v*) provided thin films comprised of layered crystallites whose stacking direction was oriented normal to the substrate. These observations prompted us to explore COF film synthesis in MeOH:Diox (1:3 *v*/*v*) in the absence of DMA and *o*-DCB at 120 °C. These conditions provide crystalline **ZnPc-PBBA COF** powder consistent with previous reports[48], whereas otherwise identical reactions performed at 90 °C provided only amorphous materials[55].

Figure 4.2 compares **ZnPc-PBBA COF** thin films on SLG transferred to fused SiO_2 (SLG/SiO_2) prepared in DMA:*o*-DCB (1:2 *v*/*v*) or MeOH:Diox (1:3 *v*/*v*) using identical initial masses of the monomers and solvent volumes[56]. The **ZnPc-PBBA COF** film prepared in DMA:*o*-DCB uniformly covers the entire SLG/SiO_2 substrate (Fig. 4.2a). In contrast, films prepared in MeOH:Diox form only on the SLG-coated portion of the SLG/SiO_2 substrate (Fig. 4.2b). Grazing incidence X-ray diffraction

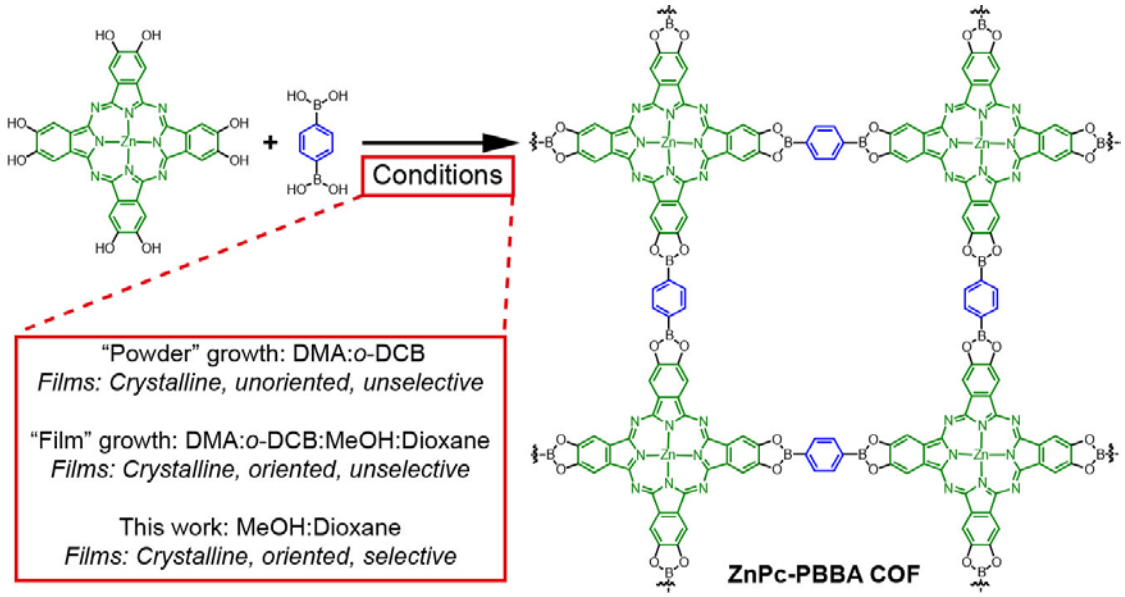

Figure 4.1 | The orientation and substrate selectivity of **ZnPc-PBBA COF** is controlled by varying solvent blend and composition.

(GIXD) performed at the Cornell High Energy Synchrotron Source indicates that films grown in DMA:*o*-DCB (Fig 4.2c) diffract with equal intensity at all out-of-plane angles ($Q_\perp$), which is diagnostic of a randomly oriented crystalline thin film. In contrast, GIXD of films prepared in MeOH:Diox (Fig. 4.2d) show scattering intensity concentrated near $Q_\perp = 0$, indicating that the COF films preferentially orient their π-electron systems parallel to the substrate.

The optical absorption spectra of the **ZnPc-PBBA COF** films obtained from the two synthetic procedures show notable and reproducible differences that may be diagnostic of their crystallinity and vertical orientation. Films prepared using DMA:*o*-DCB exhibit a λ_{max} at 298 nm, corresponding to the ZnPc Soret band, and a broad absorbance centered at 710 nm with a shoulder from 610-620 nm (Fig. 4.2e), corresponding to the phthalocyanine Q band. In contrast, films prepared in MeOH:Diox display local λ_{max} at 300 nm and 598 nm, with a smaller local maximum absorbance at 691 nm (Fig. 4.2f). These maxima more closely match the calculated

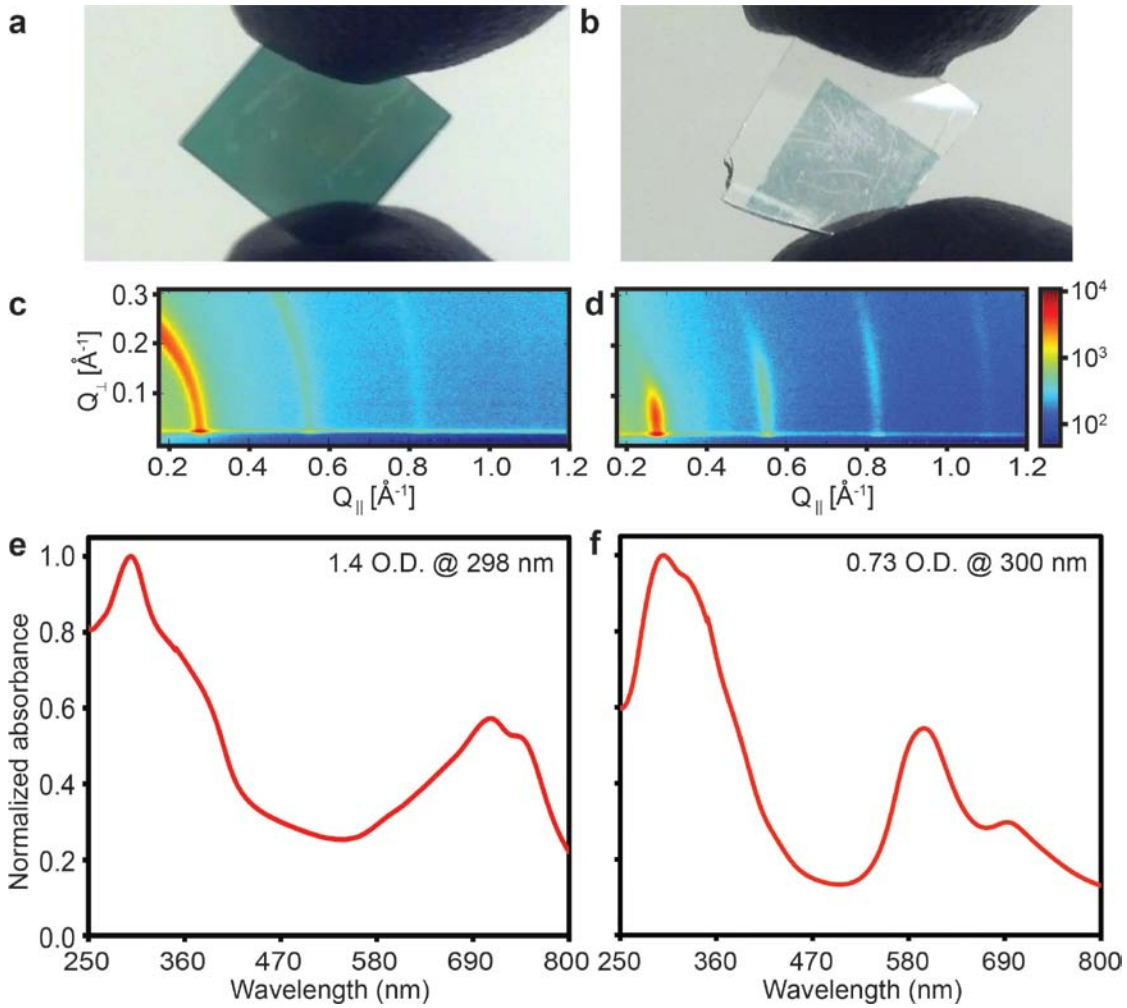

Figure 4.2 | Comparison of COF films prepared in DMA:*o*-DCB and MeOH:Diox. **ZnPc-PBBA COF** on SLG/SiO_2 synthesized in **a)** DMA:*o*-DCB and **b)** MeOH:Diox. GIXD patterns (**c,d**) and UV-Vis spectra (**e,f**) of the of the COF films in a and b, respectively. Samples were prepared at equal concentration.

electronic absorption spectrum of monolayer **NiPc-PBBA COF**[57], which predicts maxima at 302 nm and 563 nm that correspond to LUMO-1-to-HOMO and LUMO-to-HOMO transitions, respectively. Syntheses performed in more dilute DMA:*o*-DCB solvent mixtures (initial [ZnPc] = 1.0 mM) yield only amorphous **ZnPc-PBBA** cross-linked networks. These amorphous materials exhibit UV-Vis spectra that closely resemble the crystalline, unoriented COF films (Fig. 4.2e) prepared from the same solvent mixture (Fig. S4.4). Furthermore, when PBBA is omitted from the

polymerization in DMA:*o*-DCB, films consisting only of adsorbed phthalocyanines also provide absorbance spectra (Fig. S4.5) similar to that shown in Fig. 4.2e. In contrast, nonspecific adsorption of phthalocyanines does not occur from the MeOH:Diox solvent mixture in the absence of PBBA. Therefore, we propose that the crystalline, randomly oriented films prepared in DMA:*o*-DCB are also contaminated by disordered ZnPc monomers or boronate ester-linked oligomers. These contaminants might exist either as a non-selective multilayer on the substrate, as domains distributed throughout the film, or as insoluble species that contaminate the pores. It is currently difficult to determine the percent crystallinity or nature of impurities in COF films, but the differences in UV-Vis spectra between films grown under various conditions might be used to rapidly assess the crystallinity and purity of phthalocyanine-containing COF films in the absence of GIXD data, which we collect at a synchrotron X-ray source.

The above experiments demonstrate simultaneous control of COF film orientation and selectivity and raise questions as to how the polymerizations differ in the two solvent mixtures. Our recent mechanistic study of 2D boronate ester-linked COF formation found that added MeOH inhibited COF formation at concentrations in excess of 15 equiv per boronate ester linkage[58]. The conditions that provide selective growth on SLG employ 300 equiv of MeOH per boronate ester. Therefore, we hypothesize that the SLG adsorbs Pc monomers and/or Pc-PBBA oligomers on its surface, where they condense and nucleate subsequent layers. In contrast, COF powders nucleate readily from solution in DMA:*o*-DCB, and it is likely that the networks formed in solution deposit nonselectively on the substrate with a random

crystallite orientation. Indeed, the optical density of **ZnPc-PBBA COF** prepared for 24 h in MeOH:Diox (Fig. 4.2f) is about half that of a film prepared in DMA:*o*-DCB for 10 h (Fig. 4.2e), indicating that the COF forms much more rapidly in DMA:*o*-DCB. These results suggest that slowing nucleation of COFs in solution, using MeOH or other competing Lewis bases, is a promising way to control both the orientation and selectivity of COF thin films.

The ability to grow COF thin films selectively on SLG enables these materials to be incorporated into specific areas of a substrate or device. Starting from large-area SLG transferred to a Si wafer with a 285 nm thick layer of SiO_2 (SLG/Si), we patterned SLG into squares using photolithography (Fig S4.6). These substrates were subjected to the MeOH:Diox selective COF growth conditions, which provided COF films that retain the underlying SLG pattern (Fig. 4.3a). Selective growth is observed for a wide range of patterned SLG areas: 4–250,000 μm^2 with 1 or 2 μm gaps between squares were patterned over substrates of at least 1 cm^2. SLG is visible by eye on a 285 nm oxide layer such that optical microscopy provides a rapid means to assess both the fidelity of the lithography and selective COF growth. Prior to the polymerization, SLG squares are visible as faint purple patches on a pink background (Fig. 4.3b). After COF synthesis, the squares appear a uniform turquoise-blue across the field of view and show clear contrast between the SLG and supporting substrate (Fig. 4.3c). The height and chemical contrast of the patterned films were characterized with atomic force microscopy (AFM), which reveals that the patterned COFs are significantly thicker (134 ± 6 nm, Fig. 4.3d) than SLG itself (1-2 nm, Fig. S4.7). A phase image of the same region shows a clear contrast between COF covered squares

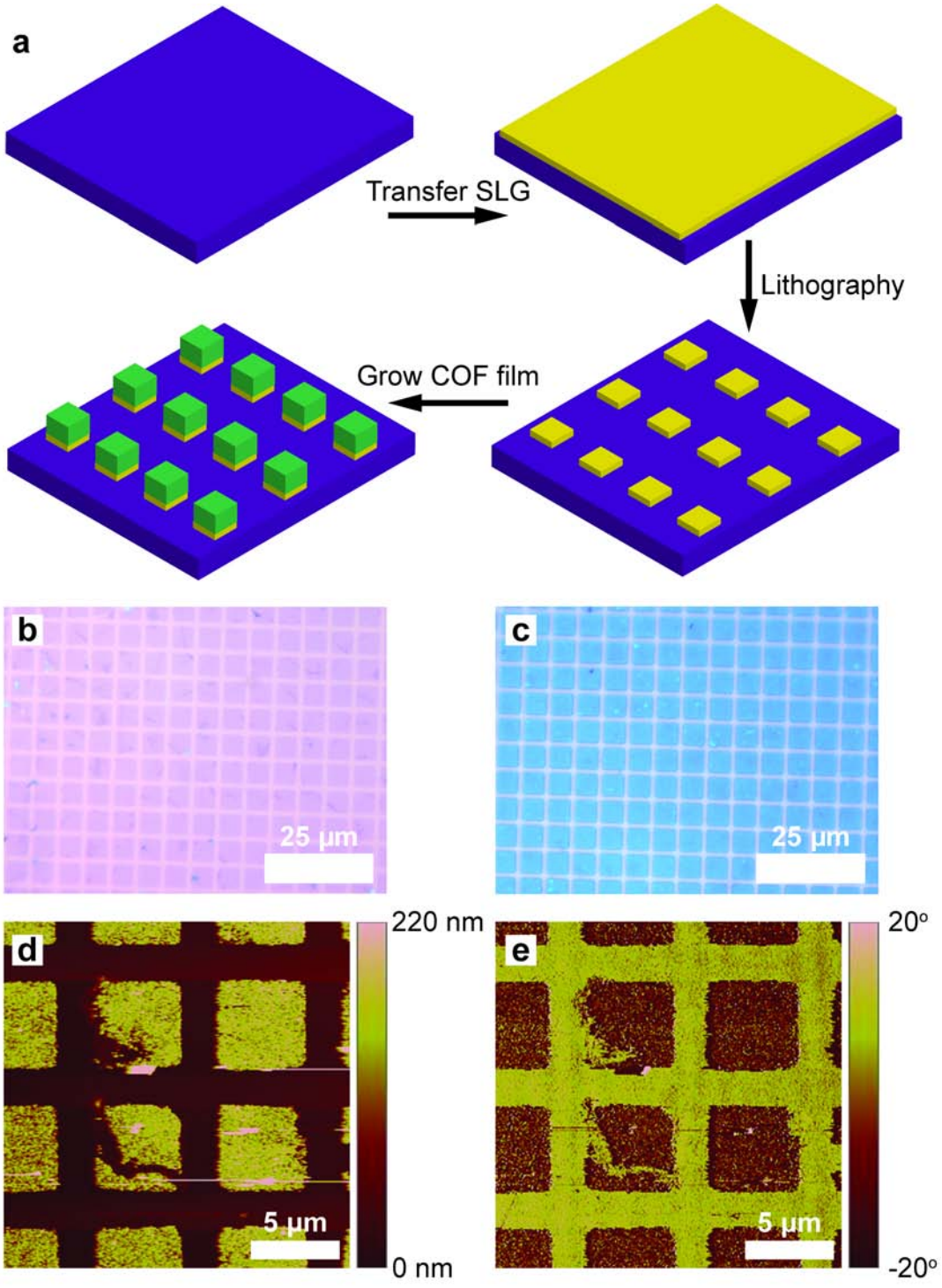

Figure 4.3 | General scheme for patterning **ZnPc-PBBA COF** films on SLG. **a)** Schematic of graphene transfer, patterning, and subsequent COF growth to yield patterned COF. **b)** Bare, patterned SLG prior to COF growth. **c)** Patterned COF after a 24 h synthesis. **d)** AFM height image of COF and its corresponding **e)** phase image (growth time: 20 h). Note that patterned COF also does not grow over occasional tears in the SLG squares.

and the surrounding wafer (Fig. 4.3e). The COF films are crystalline and oriented (Fig.S4.8), albeit with attenuated diffraction intensity, which we attribute to the more sparse coverage of patterned COF on the substrate. The AFM height and phase images also indicate that the COF does not grow on regions of defective or torn graphene squares. Overall, these results demonstrate that COF growth is highly selective for the SLG surface under the MeOH:Diox growth conditions.

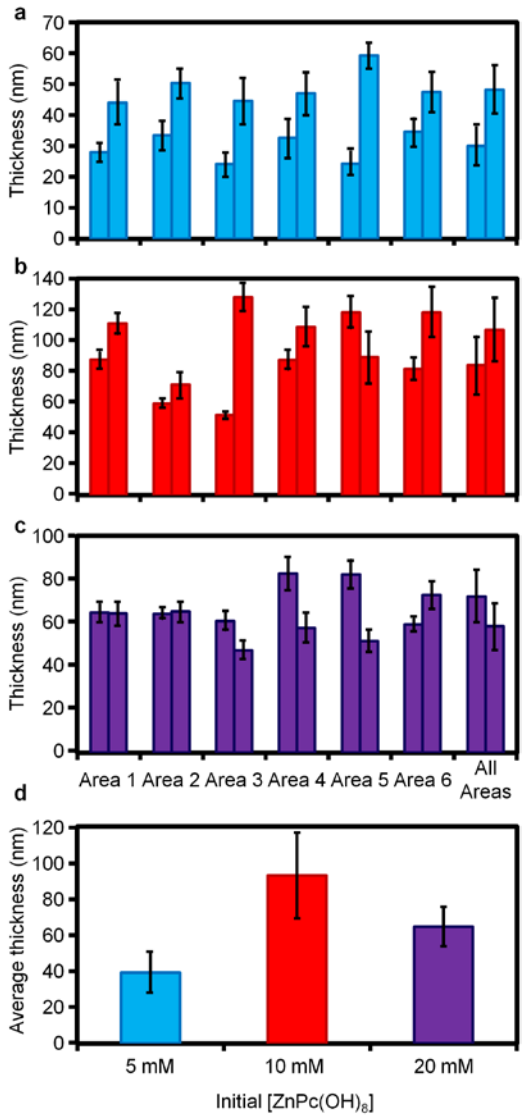

Figure 4.4 | Comparison of film thickness as a function of concentration. Thickness of randomly selected areas of two chips prepared in parallel at **a)** 5 mM **b)** 10 mM and **c)** 20 mM initial phthalocyanine concentration. **d)** Total average film thickness measured at each concentration. Error bars represent one standard deviation.

If each SLG square is considered as a separate growth experiment, patterned substrates represent a highly parallel platform to evaluate how growth conditions influence COF film growth. For example, Fig. 4.4 compares the thickness of patterned **ZnPc-PBBA COF** films grown at nominal 5, 10, and 20 mM initial phthalocyanine concentration, respectively. Although thicker films might be expected as the phthalocyanine concentration is increased, there is no straightforward correlation between film thickness and concentration (Fig. 4.4d), possibly because the heterogeneous reaction mixture maintains a uniform

saturation ZnPc concentration for each. In contrast, stirring the reaction mixtures does influence COF film thickness and film quality, as stirred solutions are much more uniform across a chip than unstirred ones (Figs. S4.12 and S4.13). This observation might arise from variations in local concentration or ZnPc dissolution rate throughout the suspension. It remains unclear what other factors influence film thickness, however, the selective growth conditions described here enable statistically significant numbers of syntheses to be performed in parallel, a key step to understanding these relationships.

Conclusion

We have demonstrated that changes in reaction solvent strongly influence COF nucleation, polymerization, and crystallization processes, which resulted in the first demonstration of patterned COF film growth. Specifically, MeOH:Diox solvent mixtures enable COF growth exclusively on SLG and are general for SLG supported on many substrates. Lithographically patterned graphene indicated uniform COF growth across large areas of the substrate, which will enable further studies of COF film formation in a highly parallel fashion. We anticipate that this approach will be necessary to fully understand and characterize the delicate interplay between monomer concentration, stoichiometry, competitor concentration, agitation, shear forces, and other, as yet unidentified factors that influence COF polymerization and crystallization. Further, the conditions reported here allow COFs to be incorporated into device-relevant geometries, which will be needed for these materials to realize their full potential in optoelectronic and energy storage devices.

REFERENCES

1. Côté, A. P., Benin, A. I., Ockwig, N. W., O'Keeffe, M., Matzger, A. J. & Yaghi, O. M. *Science* **310,** 1166 (2005).

2. Côté, A. P., El-Kaderi, H. M., Furukawa, H., Hunt, J. R. & Yaghi, O. M. *J. Am. Chem. Soc.* **129,** 12914 (2007).

3. Han, S. S., Furukawa, H., Yaghi, O. M. & Goddard, W. A., III. *J. Am. Chem. Soc.* **130,** 11580 (2008).

4. Hunt, J. R., Doonan, C. J., LeVangie, J. D., Côté, A. P. & Yaghi, O. M. *J. Am. Chem. Soc.* **130,** 11872 (2008).

5. Uribe-Romo, F. J., Doonan, C. J., Furukawa, H., Oisaki, K. & Yaghi, O. M. *J. Am. Chem. Soc.* **133,** 11478 (2011).

6. Spitler, E. L. & Dichtel, W. R. *Nature Chem.* **2,** 672 (2010).

7. Spitler, E. L., Koo, B. T., Novotney, J. L., Colson, J. W., Uribe-Romo, F. J., Gutierrez, G. D., Clancy, P. & Dichtel, W. R. *J. Am. Chem. Soc.* **133,** 19416 (2011).

8. Tilford, R. W., Gemmill, W. R., zur Loye, H.-C. & Lavigne, J. J. *Chem. Mater.* **18,** 5296 (2006).

9. Kandambeth, S., Mallick, A., Lukose, B., Mane, M. V., Heine, T. & Banerjee, R. *J. Am. Chem. Soc.* **134,** 19524 (2012).

10. Colson, J. W. & Dichtel, W. R. *Nature Chem.* **5,** 453 (2013).

11. Doonan, C. J., Tranchemontagne, D. J., Glover, T. G., Hunt, J. R. & Yaghi, O. M. *Nature Chem.* **2,** 235 (2010).

12. DeBlase, C. R., Silberstein, K. E., Truong, T.-T., Abruña, H. D. & Dichtel, W. R. *J. Am. Chem. Soc.* **135,** 16821 (2013).

13. Bunck, D. N. & Dichtel, W. R. *J. Am. Chem. Soc.* **135,** 14952 (2013).

14. Berlanga, I., Ruiz-Gonzalez, M. L., Gonzalez-Calbet, J. M., Fierro, J. L., Mas-Balleste, R. & Zamora, F. *Small* **7,** 1207 (2011).

15. El-Kaderi, H. M., Hunt, J. R., Mendoza-Cortés, J. L., Côté, A. P., Taylor, R. E., O'Keeffe, M. & Yaghi, O. M. *Science* **316,** 268 (2007).

16. Furukawa, H. & Yaghi, O. M. *J. Am. Chem. Soc.* **131,** 8875 (2009).

17. Uribe-Romo, F. J., Hunt, J. R., Furukawa, H., Klock, C., O'Keeffe, M. & Yaghi, O. M. *J. Am. Chem. Soc.* **131,** 4570 (2009).

18. Bunck, D. N. & Dichtel, W. R. *Angew. Chem. Int. Ed.* **51,** 1885 (2012).

19. Bunck, D. N. & Dichtel, W. R. *Chem. Commun.* **49,** 2457 (2013).

20. Brucks, S. D., Bunck, D. N. & Dichtel, W. R. *Polymer* **55,** 330 (2014).

21. Xu, H., Chen, X., Gao, J., Lin, J., Addicoat, M., Irle, S. & Jiang, D. *Chem. Commun.* **50,** 1292 (2014).

22. Ding, S. Y., Gao, J., Wang, Q., Zhang, Y., Song, W. G., Su, C. Y. & Wang, W. *J. Am. Chem. Soc.* **133,** 19816 (2011).

23. Liao, H., Ding, H., Li, B., Ai, X. & Wang, C. *J. Mater. Chem. A* **2,** 8854 (2014).

24. Guo, J., Xu, Y., Jin, S., Chen, L., Kaji, T., Honsho, Y., Addicoat, M. A., Kim, J., Saeki, A., Ihee, H., Seki, S., Irle, S., Hiramoto, M., Gao, J. & Jiang, D. *Nature Commun.* **4,** 2736 (2013).

25. Beaudoin, D., Maris, T. & Wuest, J. D. *Nature Chem.* **5,** 830 (2013).

26. Bae, Y.-S. & Snurr, R. Q. *Angew. Chem. Int. Ed.* **50,** 11586 (2011).

27. Stock, N. & Biswas, S. *Chem. Rev.* **112,** 933 (2012).

28. Zhou, H.-C., Long, J. R. & Yaghi, O. M. *Chem. Rev.* **112,** 673 (2012).

29. Colson, J. W., Woll, A. R., Mukherjee, A., Levendorf, M. P., Spitler, E. L., Shields, V. B., Spencer, M. G., Park, J. & Dichtel, W. R. *Science* **332,** 228 (2011).

30. Abel, M., Clair, S., Ourdjini, O., Mossoyan, M. & Porte, L. *J. Am. Chem. Soc.* **133,** 1203 (2011).

31. Zwaneveld, N. A., Pawlak, R., Abel, M., Catalin, D., Gigmes, D., Bertin, D. & Porte, L. *J. Am. Chem. Soc.* **130,** 6678 (2008).

32. Liu, X.-H., Guan, C.-Z., Ding, S.-Y., Wang, W., Yan, H.-J., Wang, D. & Wan, L.-J. *J. Am. Chem. Soc.* **135,** 10470 (2013).

33. Dogru, M., Handloser, M., Auras, F., Kunz, T., Medina, D., Hartschuh, A., Knochel, P. & Bein, T. *Angew. Chem. Int. Ed.* **52,** 2920 (2013).

34. Medina, D. D., Werner, V., Auras, F., Tautz, R., Dogru, M., Schuster, J., Linke, S., Döblinger, M., Feldmann, J., Knochel, P. & Bein, T. *ACS Nano* **8,** 4042 (2014).

35. Clair, S., Ourdjini, O., Abel, M. & Porte, L. *Adv. Mater.* **24,** 1252 (2012).

36. Levendorf, M. P., Kim, C.-J., Brown, L., Huang, P. Y., Havener, R. W., Muller, D. A. & Park, J. *Nature* **488,** 627 (2012).

37. Liu, L., Park, J., Siegel, D. A., McCarty, K. F., Clark, K. W., Deng, W., Basile, L., Idrobo, J. C., Li, A.-P. & Gu, G. *Science* **343,** 163 (2014).

38. Hermes, S., Schröder, F., Chelmowski, R., Wöll, C. & Fischer, R. A. *J. Am. Chem. Soc.* **127,** 13744 (2005).

39. Zacher, D., Baunemann, A., Hermes, S. & Fischer, R. A. *J. Mater. Chem.* **17,** 2785 (2007).

40. Zhuang, J.-L., Ceglarek, D., Pethuraj, S. & Terfort, A. *Adv. Funct. Mater.* **21,** 1442 (2011).

41. Zhuang, J.-L., Lommel, K., Ceglarek, D., Andrusenko, I., Kolb, U., Maracke, S., Sazama, U., Fröba, M. & Terfort, A. *Chem. Mater.* **23,** 5366 (2011).

42. Van Gough, D., Lambert, T. N., Wheeler, D. R., Rodriguez, M. A., Brumbach, M. T., Allendorf, M. D. & Spoerke, E. D. *ACS Appl. Mater. Interfaces* **6,** 1509 (2014).

43. Shekhah, O., Wang, H., Kowarik, S., Schreiber, F., Paulus, M., Tolan, M., Sternemann, C., Evers, F., Zacher, D., Fischer, R. A. & Wöll, C. *J. Am. Chem. Soc.* **129,** 15118 (2007).

44. Zhuang, J.-L., Ar, D., Yu, X.-J., Liu, J.-X. & Terfort, A. *Adv. Mater.* **25,** 4631 (2013).

45. Ameloot, R., Stappers, L., Fransaer, J., Alaerts, L., Sels, B. F. & De Vos, D. E. *Chem. Mater.* **21,** 2580 (2009).

46. Ameloot, R., Pandey, L., Auweraer, M. V. d., Alaerts, L., Sels, B. F. & De Vos, D. E. *Chem. Commun.* **46,** 3735 (2010).

47. Li, M. & Dincă, M. *Chem. Sci.* **5,** 107 (2013).

48. Spitler, E. L., Colson, J. W., Uribe-Romo, F. J., Woll, A. R., Giovino, M. R., Saldivar, A. & Dichtel, W. R. *Angew. Chem. Int. Ed.* **51,** 2623 (2012).

49. Geim, A. K. & Novoselov, K. S. *Nature Mater.* **6,** 183 (2007).

50. Novoselov, K. S., Geim, A. K., Morozov, S. V., Jiang, D., Zhang, Y., Dubonos, S. V., Grigorieva, I. V. & Firsov, A. A. *Science* **306,** 666 (2004).

51. Bae, S., Kim, H., Lee, Y., Xu, X., Park, J.-S., Zheng, Y., Balakrishnan, J., Lei, T., Ri Kim, H., Song, Y. I., Kim, Y.-J., Kim, K. S., Ozyilmaz, B., Ahn, J.-H., Hong, B. H. & Iijima, S. *Nature Nanotech.* **5,** 574 (2010).

52. Li, X., Cai, W., An, J., Kim, S., Nah, J., Yang, D., Piner, R., Velamakanni, A., Jung, I., Tutuc, E., Banerjee, S. K., Colombo, L. & Ruoff, R. S. *Science* **324,** 1312 (2009).

53. Suk, J. W., Kitt, A., Magnuson, C. W., Hao, Y., Ahmed, S., An, J., Swan, A. K., Goldberg, B. B. & Ruoff, R. S. *ACS Nano* **5,** 6916 (2011).

54. Li, X., Zhu, Y., Cai, W., Borysiak, M., Han, B., Chen, D., Piner, R. D., Colombo, L. & Ruoff, R. S. *Nano Lett.* **9,** 4359 (2009).

55. Safety note: Reactions performed at 120 °C are well above the boiling points of the solvent mixture. A reaction vessel rated to withstand elevated pressures, as well as a blast shield, should be employed.

56. The reaction mixtures are heterogeneous, such that the initial monomer concentrations are not known.

57. Zhou, Y., Wang, Z., Yang, P., Zu, X. & Gao, F. *J. Mater. Chem.* **22,** 16964 (2012).

58. Smith, B. J. & Dichtel, W. R. *J. Am. Chem. Soc.* **136,** 8783 (2014).

CHAPTER 4 - APPENDIX

SUPPLEMENTARY INFORMATION

A. Materials and Instrumentation. All reagents were purchased from commercial sources and used without further purification. Zn octahydroxyphthalocyanine[1] was prepared via literature procedures. 1,4-Dioxane, N,N-dimethylacetamide, MeOH and 1,2-dichlorobenzene were purchased from commercial sources and used without further purification. PhMe was purchased from commercial sources and purified using a custom-built alumina-column based solvent purification system.

UV-Vis absorbance spectra were recorded on a Cary 5000 UV-Vis-NIR spectrophotometer with a mercury lamp in either dichloromethane solution or as solids using a praying mantis diffuse reflectance accessory.

Powder X-ray diffraction patterns were recorded on a Scintag Theta-Theta Powder X-Ray Diffractometer in reflectance Bragg-Brentano geometry employing Cu Kα line focused radiation at 2200 W (45 kV, 40 mA) power and equipped with a Ge crystal detector fitted with a 0.3 mm radiation entrance slit. Samples were mounted on zero background sample holders by dropping powders from a wide-blade spatula and then leveling the sample surface with a glass microscope slide. No sample grinding or sieving was used prior to analysis. Samples were observed using a 0.04º 2θ step scan from 2 – 30º with an exposure time of 0.4 s per step. No peaks could be resolved from the baseline for $2\theta > 34$º data and was therefore not considered for further analysis.

Scanning electron microscopy (SEM) was performed on a Zeiss Ultra SEM operating at 1-2 kV. Films were deposited onto double-sided copper tape on a flat aluminum platform sample holder. No metal sputtering of the sample was necessary.

Atomic force microscopy (AFM) was performed on either a Veeco Dimension 3100 or Veeco Icon ambient AFM operating in tapping mode using coated silicon tips (15

nm diamond-like-coating) with resonant frequency 300 ± 100 kHz and force constant 40 N/m. Height and phase images were collected simultaneously. Data were processed using the Nanoscope Analysis program provided with the AFM. Height profiles were corrected for bow and leveled across each row of squares. COF square thicknesses were tabulated in Microsoft Excel and the average and standard deviation of the tabulated thicknesses for each image was calculated. Each collected image was binned as an individual "area" as in Figure 4.4.

Mass spectra were obtained on a Waters MALDI micro MX MALDI-TOF mass spectrometer using positive ionization and a reflectron detector. MALDI samples were prepared by wet deposition of a saturated analyte/dithranol matrix solution onto a metallic sample plate and air dried before loading into the instrument.

Grazing incidence X-ray diffraction (GIXD) was performed at the G2 station at Cornell High Energy Synchrotron Source (CHESS) using a beam energy of 10.06 ± 0.01 keV (λ = 0.1239 nm), selected using a Be single-crystal monochromator. Motorized slits were used to define a 0.2×2 (V×H) mm^2 beam, with a typical flux of 2×10^{10} photons/s. The data were collected using a 640-element 1D diode-array, of which each element incorporates its own pulse counting electronics capable of count rates of $\sim10^5$ photons/s. A set of 0.1° Soller slits were used on the detector arm to define the in-plane resolution. The scattering geometry is described in detail elsewhere. Each data set was collected by scanning the detector with the sample stationary. The incidence angle α between the beam and sample surface was 0.175°. Axes labels $Q_\perp$ and $Q_\parallel$ are defined using the GISAXS convention $Q_\perp = 4\pi/\lambda\sin(\delta/2)$ and $Q_\parallel = 4\pi/\lambda\sin(\nu/2)$, where δ and ν are the vertical and horizontal scattering angles,

respectively. At $\alpha=\delta=0$, $hQ_{\parallel}$ and $hQ_{\perp}$ (where h is Planck's constant) are the components of momentum transfer parallel and perpendicular to the sample surface, respectively.

B. Synthetic Procedures.

General procedure for COF powder and films synthesis. Zn octahydroxyphthalocyanine (10 mg, 0.014 mmol) and 1,4-phenylenebis(boronic acid) (5 mg, 0.030 mmol) were added to a 4 dram vial and suspended in a mixture of dioxane and MeOH (3:1, 2.8 mL). A stir bar was added and the vial placed in a custom-built stainless steel vessel (see below). Substrate supported single-layer graphene was suspended in the solution (see below), the vessel was sealed, and the entire apparatus was heated at 120 °C on a hot plate for the desired time. After cooling, the suspended graphene was removed from solution and briefly (<5 sec) sonicated in dry PhMe. The free-flowing dark green powder remaining in the vial was collected by filtration on a Hirsch funnel and washed with portions of dry PhMe. The resulting **ZnPc-PBBA COF** powder was characterized by PXRD and matched previous reports[2].

Graphene Growth. Single-layer graphene was grown on 25 μm-thick copper foil using previously reported chemical vapor deposition methods[3]. A layer of PMMA (50 nm) was spin-coated on top of the graphene and the copper was etched using aq. $FeCl_3$. The graphene was then transferred to fused SiO_2 (SLG/SiO_2) or silicon (SLG/Si) and the PMMA removed by washing first with chloroform then isopropyl alcohol. For comparison, graphene was purchased from Graphene Supermarket (Calverton, NY). There was no apparent difference in patterning or film growth between the two sources of graphene.

C. Lithographic Patterning of Single-layer Graphene

Photolithography was performed in the cleanroom at the Cornell Nanoscale Science and Technology Facility. A 4-inch silicon wafer with a 285 nm-thick thermal oxide layer was used as substrate for all patterning experiments. After priming in an HMDS vapor prime oven, graphene was transferred to the silicon wafer (see above) and the PMMA was removed by two consecutive acetone soaks (2 h each) followed by an isopropyl alcohol rinse. The substrate was then annealed on a hot plate at 145 °C for two hours and allowed to cool. The wafer was again primed with HMDS and immediately coated with Shipley SPR955-0.9 i-line resist by spin-coating at 3000 rpm for 60 sec. The wafer was baked on a hotplate at 90 °C for 90 sec and then immediately exposed (0.220 sec exposure time) using a GCA Autostep 200 automatic wafer stepper. Following exposure, the wafer was baked at 115 °C for 90 sec then developed using a Hamatech-Steag wafer processor (726 MIF, 60 sec, single-puddle). The developed wafer was then etched in a Glen 1000 oxygen plasma etcher (active mode, sample on grounded shelf below a powered shelf) for 100 sec at 400 watt. After etching, the wafer was then diced and the unexposed resist removed with by soaking in acetone for 2 h, transferred to a fresh acetone bath for 2 h, then rinsed in isopropyl alcohol. Finally, the substrates were annealed in a tube furnace at 375 °C under an H_2 flow for two hours.

D. Reaction Vessel and Experimental Setup

A Parr-type reactor with six independent reaction vessels was built based on a design reported by Coates et al[4].

Figure S4.1. Optical images of the custom-built reactor.

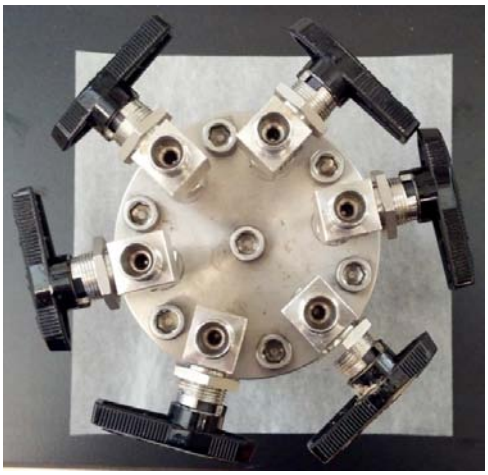

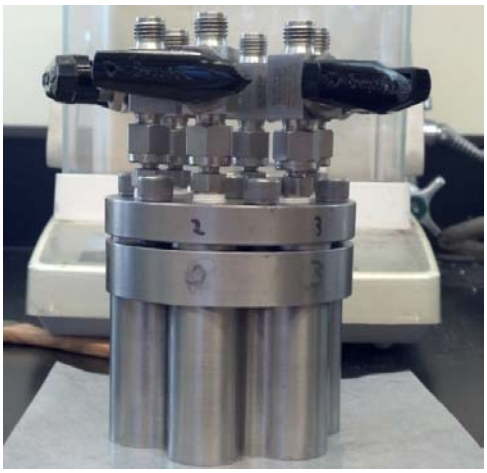

Figure S4.2. Optical images of a suspended SLG/Si chip in a 4 dram vial (stir bar and phthalocyanine omitted for clarity).

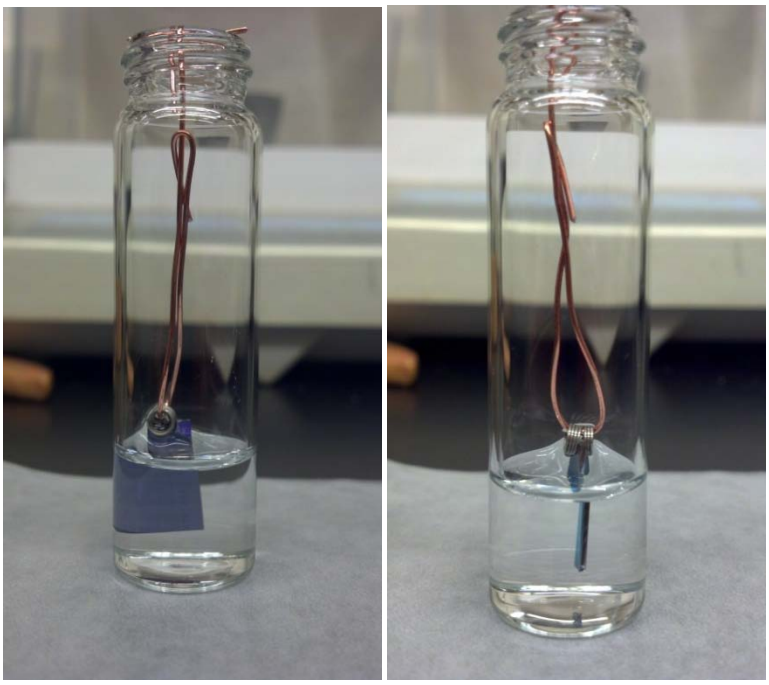

E. Grazing Incidence X-ray Diffraction of COF-5 on Various Substrates

Figure S4.3. GIXD patterns of COF-5 on various substrates.

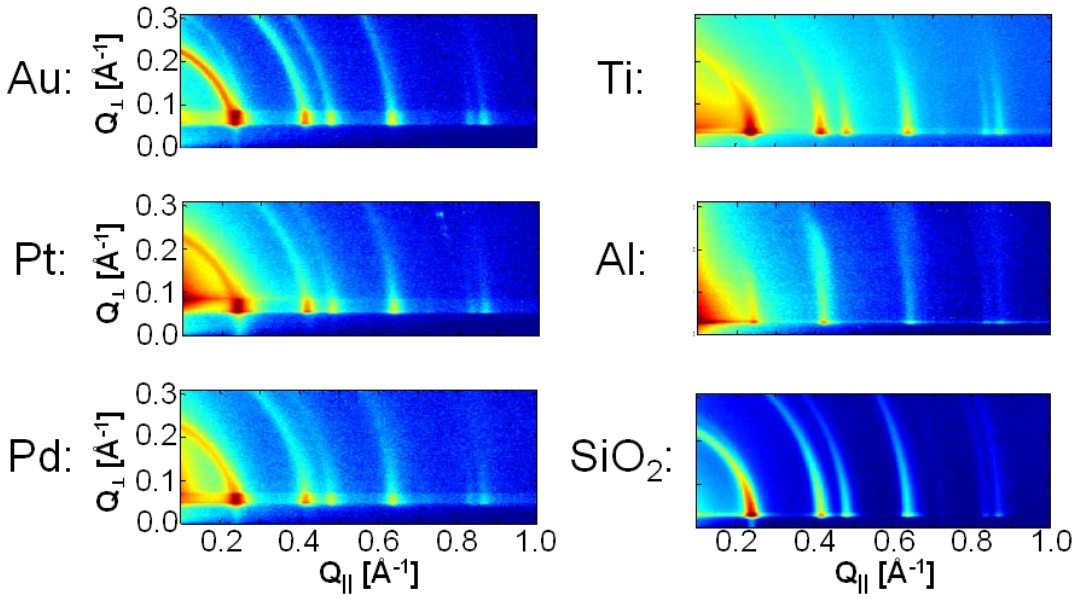

F. Additional UV-Vis Spectra of Films

Figure S4.4. UV-Vis spectra comparing amorphous ZnPc-PBBA polymer prepared at [ZnPc] = 1 mM in DMA:*o*-DCB (blue), crystalline, unoriented **ZnPc-PBBA COF** prepared in DMA:*o*-DCB (red), and crystalline, oriented, **ZnPc-PBBA COF** prepared in MeOH:Diox (green).

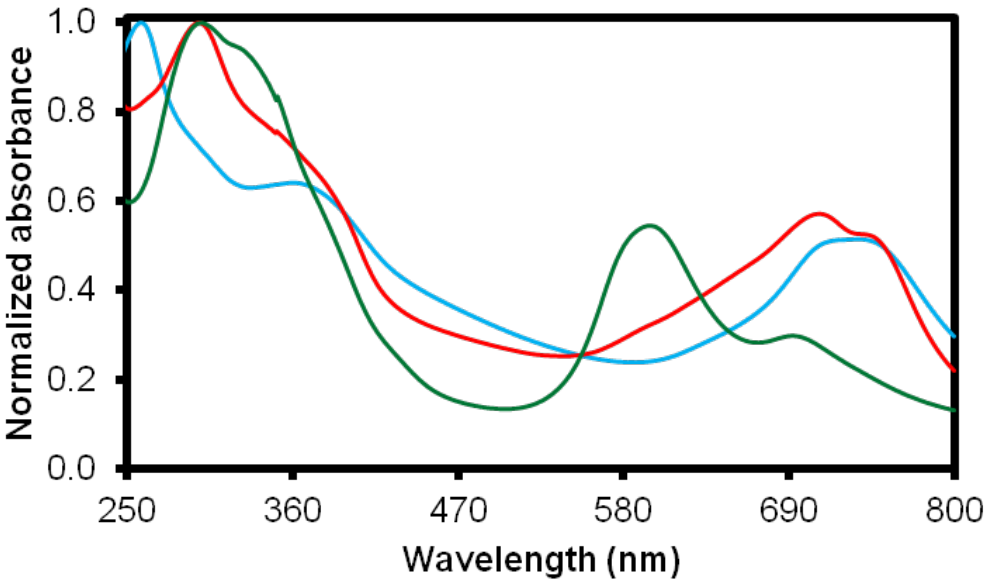

Figure S4.5. UV-Vis spectra of $ZnPc(OH)_8$ films deposited on SLG substrates in the absence of the boronic acid monomer. Film formation conditions: (1 mM $ZnPc(OH)_8$ in DMA:*o*-DCB, heated to 120 °C for 4 h (blue) and 24 h (red).

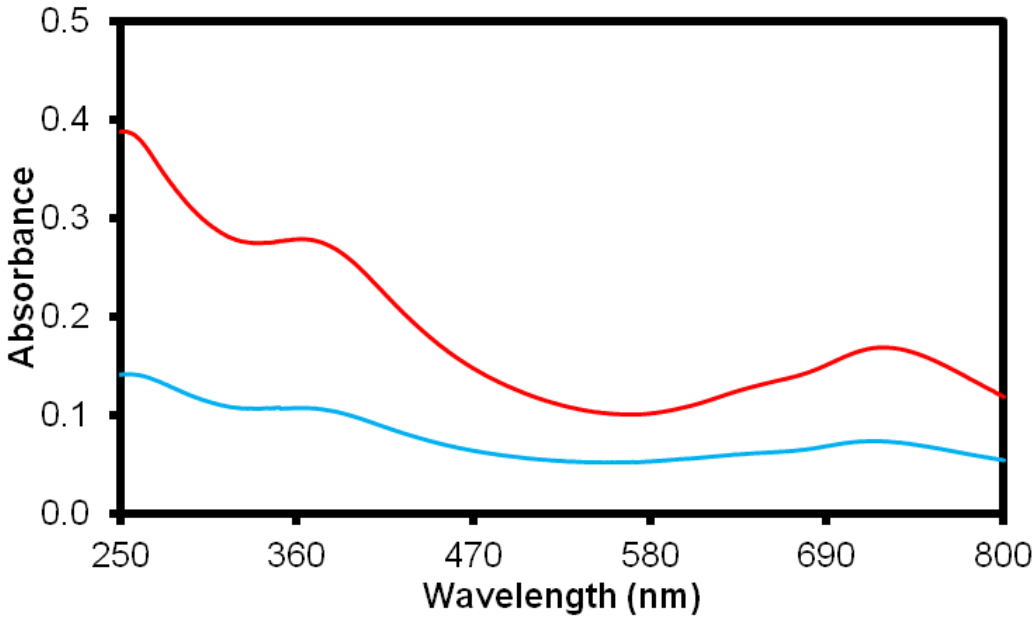

G. Patterned Graphene Characterization

Figure S4.6. Scanning electron micrographs of lithographically patterned SLG on Si with a 285 nm-thick thermal oxide layer. Left: 5 μm x 5 μm squares of SLG with a 1 μm gap between squares. Right 2 μm x 2 μm squares of SLG with a 2 μm gap between squares.

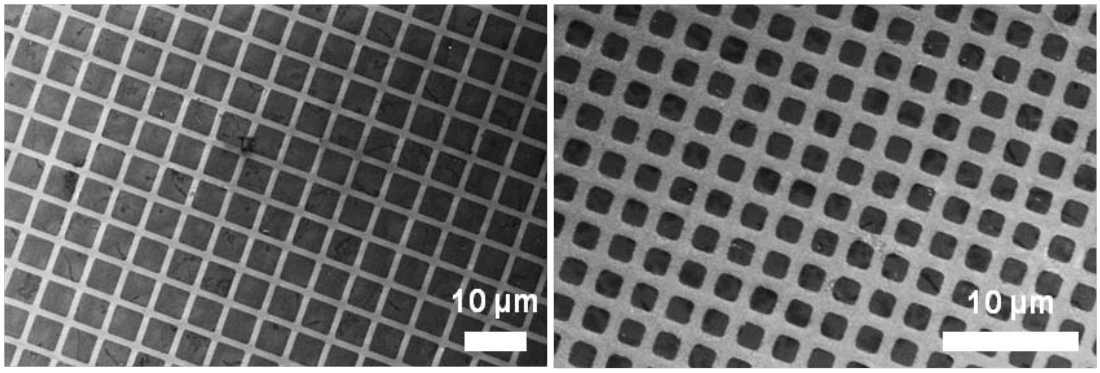

Figure S4.7. AFM height (left) and phase (right) images of SLG/Si patterned to 5 μm x 5μm squares with a 2 μm gap between squares.

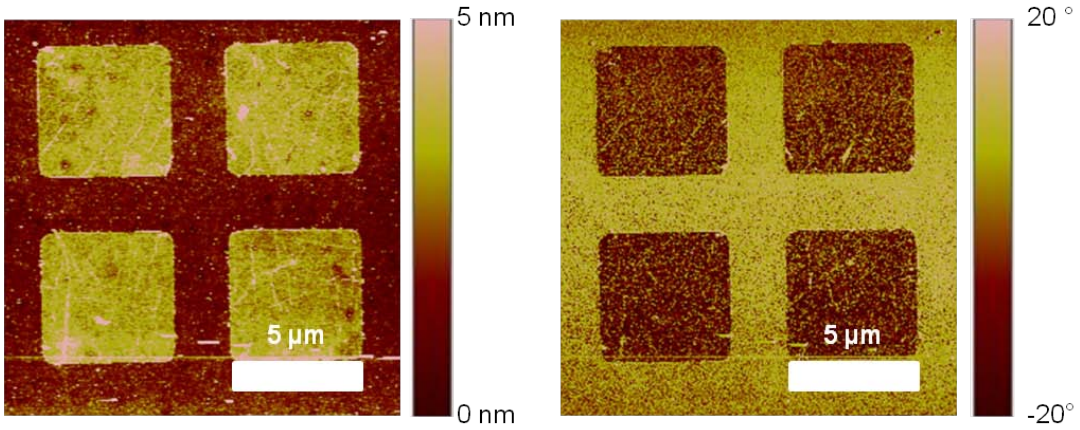

H. Characterization of Patterned COF films

Figure S4.8. GIXD of patterned **ZnPc-PBBA COF** on patterned SLG (growth time: 20 h).

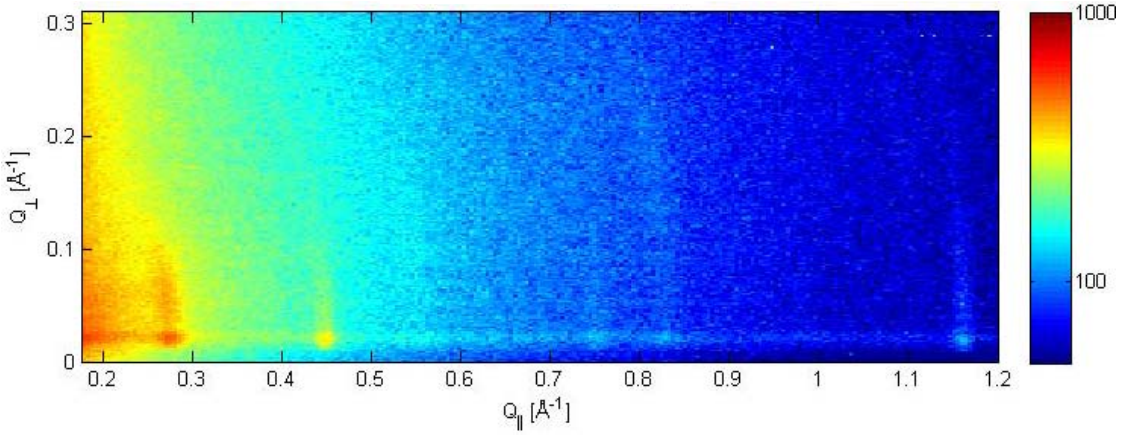

Figure S4.9. AFM height image of **ZnPc-PBBA COF** on SLG patterned into 5 μm x 5 μm boxes with 1 μm spacing (growth time: 24 h).

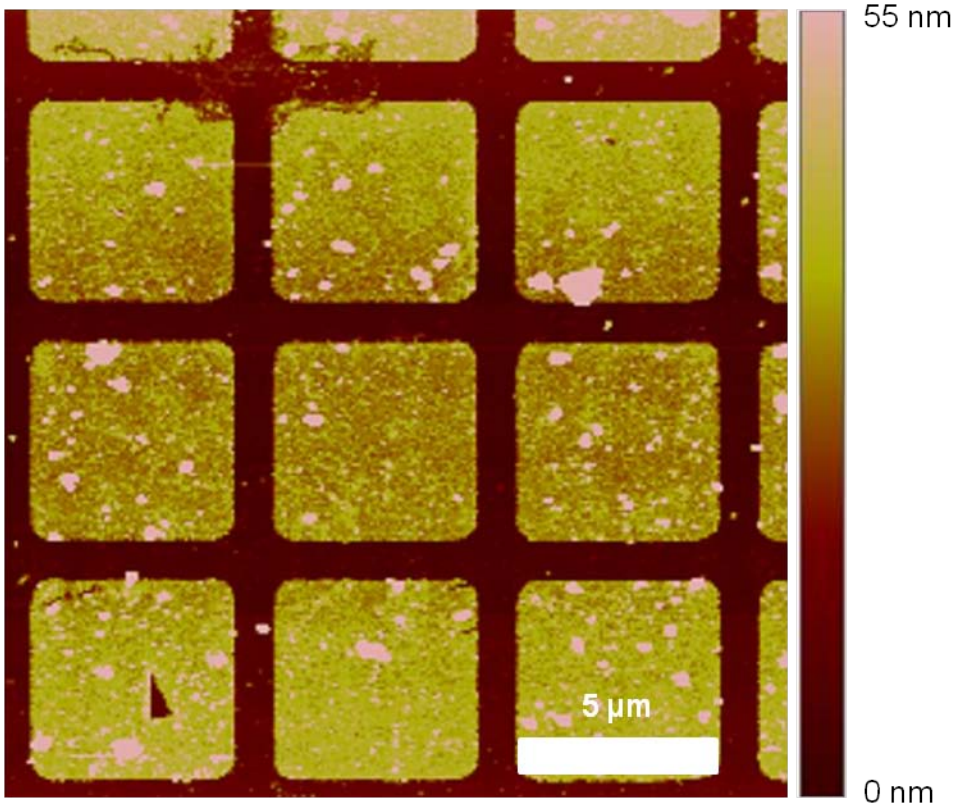

Figure S4.10. AFM height image of **ZnPc-PBBA COF** on SLG patterned into 2 μm x 2 μm squares with 1 μm spacing (growth time: 24 h).

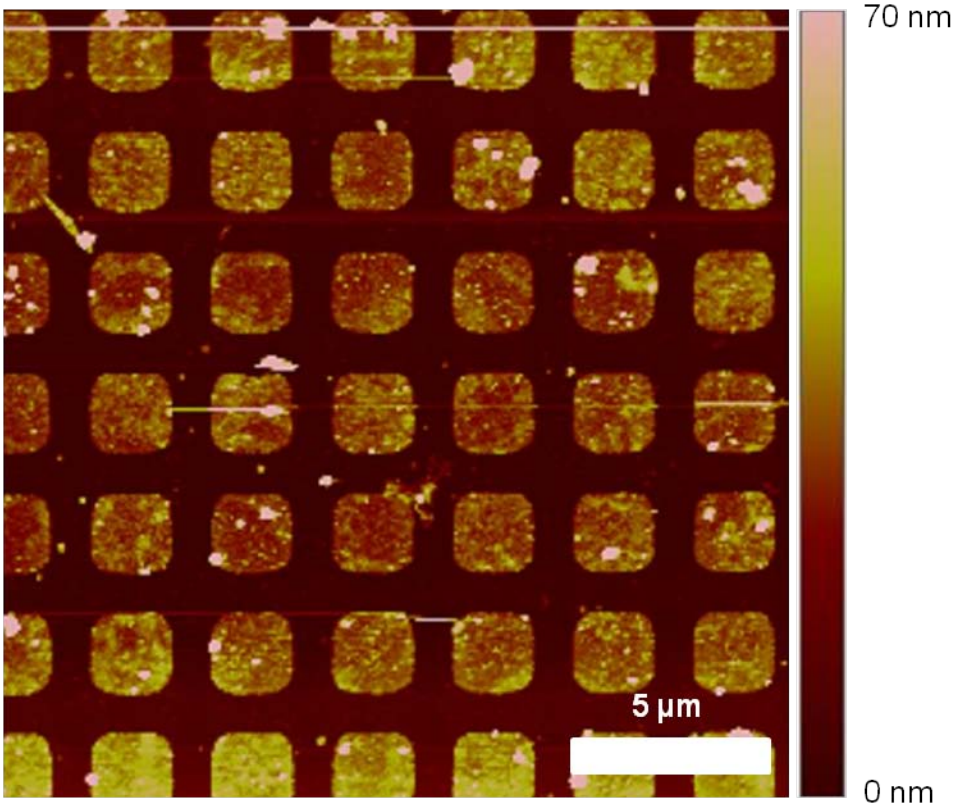

I. Comparison of Film Thickness at Varying Total Reaction Volume

Figure S4.11. Comparison of **ZnPc-PBBA COF** film thickness at equivalent initial $ZnPc(OH)_8$ concentration with varying total reaction volume. **a)** Two samples grown at 5 mM at standard volume (1.133 mL) and **b)** two samples grown at 5 mM at 2X volume (2.267 mL). **c)** Two samples grown at 10 mM at 0.5X volume (1.133 mL) and **d)** two samples grown at 10 mM at standard volume (2.267 mL). Error bars represent one standard deviation measured for each image (12 to 40 individual COF/SLG squares, depending on the size of the squares).

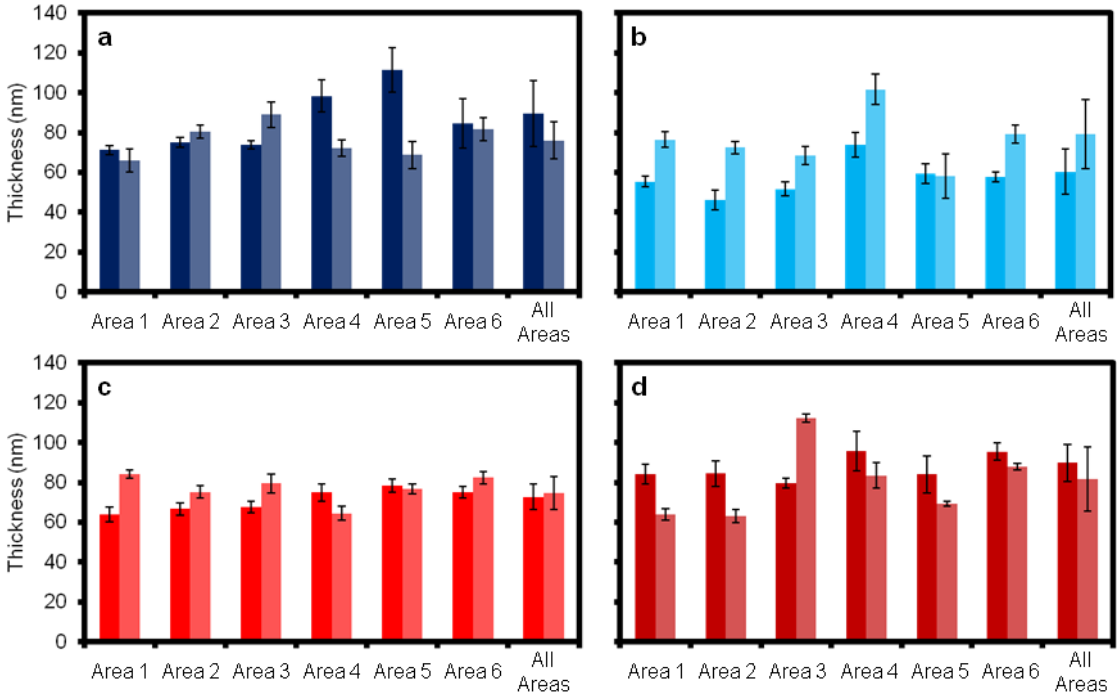

J. Comparison of Stirred and Unstirred COF Synthesis

Figure S4.12. Optical micrograph of a patterned **ZnPc-PBBA COF** film prepared in an unstirred MeOH:Diox suspension (growth time: 24 h). The darker green squares are **ZnPc-PBBA COF**, while blue-purple squares are SLG with little to no COF. In this image, areas in which the graphene is torn are also visible. Stirred suspensions provide much more uniform film thicknesses, as shown in the height measurements and optical micrographs shown in Chapter 4.

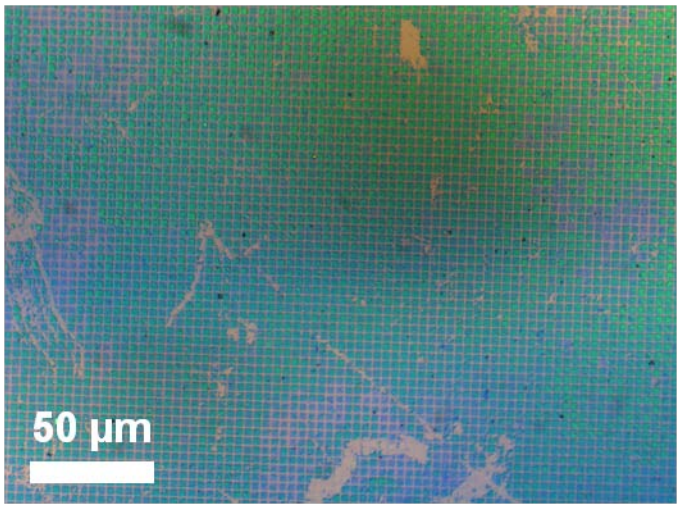

Figure S4.13. Comparison of **ZnPc-PBBA COF** thicknesses at different growth times for 20 h (red) and 24 h (blue). COF grown without stirring **(a,c)** displays a range of thicknesses across the same piece. The thickness **(b,d)** of COF decreases with stirring, but is much more uniform across the substrate. Error bars are one standard deviation. Divisions labeled "All areas" represent the average film thickness measured over all areas of the substrate, while those labeled "Area 1" (etc.) are the average thicknesses of all squares measured in an individual AFM image. The two bars in (d) represent two separate samples grown for 24 h.

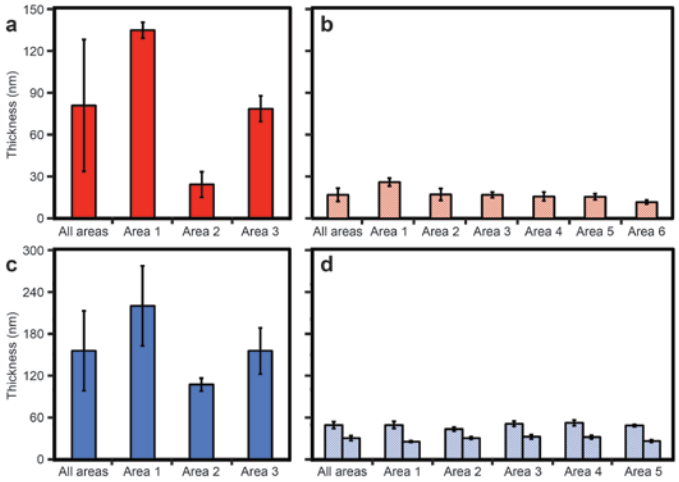

Figure S4.14. Powder X-ray diffraction of **ZnPc-PBBA COF** in unstirred (red) and stirred (blue) suspensions (growth time: 24 h). Equal weight of powder was used to collect the data.

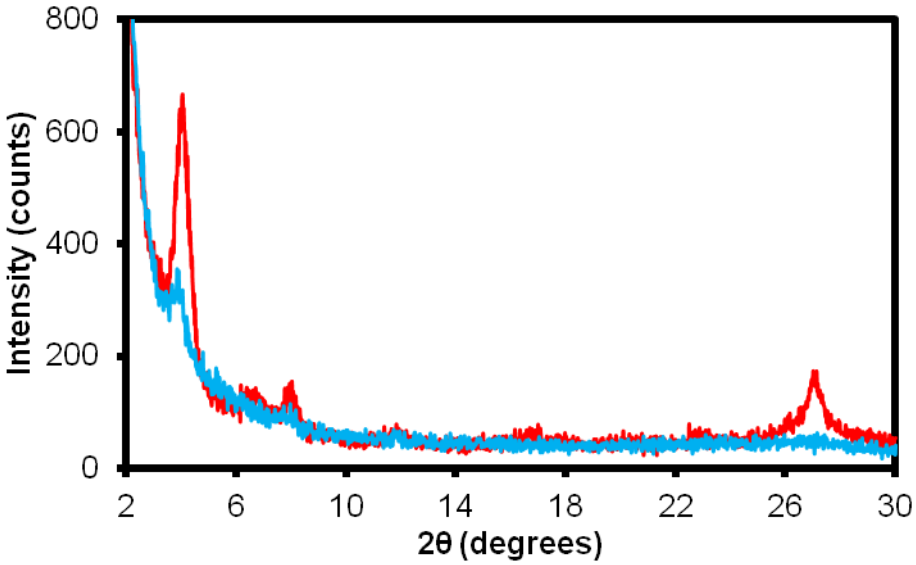

REFERENCES

1. Youssef, T. E. *Polyhedron* **29,** 1776 (2010).

2. Colson, J. W., Woll, A. R., Mukherjee, A., Levendorf, M. P., Spitler, E. L., Shields, V. B., Spencer, M. G., Park, J. & Dichtel, W. R. *Science* **332,** 228 (2011).

3. Li, X., Cai, W., An, J., Kim, S., Nah, J., Yang, D., Piner, R., Velamakanni, A., Jung, I., Tutuc, E., Banerjee, S. K., Colombo, L. & Ruoff, R. S. *Science* **324,** 1312 (2009).

4. Getzler, Y. D. Y. L., Kundnani, V., Lobkovsky, E. B. & Coates, G. W. *J. Am. Chem. Soc.* **126,** 6842 (2004).

CHAPTER 5

2D COVALENT ORGANIC FRAMEWORK THIN FILMS AS ACTIVE LAYERS IN ORGANIC PHOTOVOLTAICS

Abstract

Controlling the nanoscale morphology of the active layer in organic photovoltaic devices (OPVs) remains a significant challenge. As described in this thesis, covalent organic frameworks (COFs) offer a means to simultaneously organize organic semiconductors into programmed topologies with π-orbital overlap. This chapter describes preliminary efforts to develop COFs as active layers in OPVs. Photovoltaic devices that utilize COFs as the active layer have been fabricated and their parameters and external quantum efficiency characterized. Processing parameters relevant to device performance, such as spin speed used to introduce the fullerene solution and annealing temperature will be discussed. Compared to commonly used polymer/fullerene OPVs, devices fabricated with COFs so far exhibit low efficiencies that originate from poor current densities. These results represent progress toward applying these materials in solar energy devices.

This work was performed in collaboration with David T. Moore and Prof. Tobias Hanrath in the School of Chemical and Biological Engineering at Cornell University and with Florian Auras, Mona Calik, and Prof. Thomas Bein in the Department of Chemistry at Ludwig-Maximilians University, Munich.

Introduction

Bulk heterojunction (BHJ) organic photovoltaics (OPVs), in which a *p*-type semiconducting small molecule or polymer electron donor is mixed with a *n*-type (typically fullerene) electron acceptor, are widely studied[1-3]. Extensive empirical screening has revealed how various processing parameters such as donor/acceptor blend ratio[4-6], annealing temperature[7-9], additives[10,11] and solvent composition[12,13] influence the device performance of specific polymer and fullerene combinations. Nevertheless, predicting, designing, and controlling the nanoscale morphology of the active layer in these devices remains a formidable challenge, as subtle changes in chemical structure or modifications to device fabrication often induce major changes in active-layer morphology[14-16] and total efficiency. Thus, materials that simultaneously direct donor and acceptor morphology independently are highly desirable.

Covalent organic frameworks (COFs)[17-22] differ from commonly studied semiconducting polymers in that their topology is dictated by the relative geometries of their polymerizable groups. Thus, COFs organize organic semiconductors in a predictable and predetermined way that will not vary with device processing parameters. This orthogonality provides two significant advantages over photovoltaics prepared from polymer/fullerene blends. First, donors and acceptors are introduced in separate steps that can be optimized individually. For example, solvents and annealing temperatures that yield crystalline and conductive fullerene domains may be incompatible with the polymer component of BHJ blends. By introducing the electron acceptor in a second step, the crystallinity can be optimized without affecting the

morphology of the electron donor. Second, since small molecule organization is predefined and deterministic, processing procedures, donor/acceptor ratios, and other critical device fabrication parameters can be rationally varied without altering the overall topology. These advantages might enable future fundamental studies of charge transport, charge separation, and overall device performance across devices with consistent morphologies.

Utilizing boronate ester-linked hexahydroxytriphenylene (HHTP)[20,23] and zinc phthalocyanine (Pc)[24] COF films as donors, we have fabricated COF-based organic photovoltaic devices using a soluble fullerene derivative, phenyl-C_{61}-butyric acid methylester ($PC_{60}BM$, or its C_{71} equivalent, $PC_{70}BM$), as the acceptor. This chapter describes efforts to optimize processing parameters and discusses device performance. The OPVs fabricated thus far exhibit lower efficiencies than their soluble polymer counterparts, likely because this class of COFs is insufficiently conductive. Future experiments will help illuminate the processes occurring in the active layer, and will point the way forward to optimizing COF-based OPVs.

Results and Discussion

Traditional bulk heterojunction OPVs are fabricated by mixing a soluble semiconducting donor polymer and an electron acceptor in a suitable solvent and spin coating or inkjet printing them onto a transparent conducting oxide anode. The device is annealed to an optimum polymer/fullerene morphology, and an electron extracting layer and top contact (cathode) is evaporated onto the film. The active layer in COF OPVs employs an electron donating COF with pores backfilled with a fullerene derivative (Fig. 5.1a). Because COFs are inherently insoluble in organic solvents, we

first studied COF films synthesized on single-layer graphene[25] transferred to an indium-doped tin oxide (ITO) substrate. After film deposition, PCBM was spin coated on top and a Ca/Al top contact evaporated. However, we have so far found that all OPVs fabricated on SLG provide short-circuited devices. The origin of this problem is not understood, but was mitigated by synthesizing the COF films directly on ITO substrates coated with a NiO or MoO_x electron blocking layer. Following COF film growth, $PC_{60}BM$ or $PC_{70}BM$ was spin coated at 550 rpm for 40 s from a 25 mg/mL solution in 1,2-dichlorobenzene (*o*-DCB) or chlorobenzene with 1 vol % 1,8-diiodooctane as an additive (CB/DIO). The COF/PCBM films were next annealed for 10 min at 80 - 175 °C to aid infiltration of the COF pores and to remove residual solvent. Lastly, a 1 nm LiF hole blocking and electron extraction layer was evaporated on top followed by an 80 nm Ca/Al cathode to complete the device (Fig. 5.1b for device fabrication).

Parameters such as spin speed and dwell time were determined to impact COF OPV performance. Spin speeds ≥1000 rpm prevent PCBM from adhering to the COF surface, while a 20 sec dwell time prior to spinning is critical, likely allowing PCBM to penetrate the COF pores. We find that devices prepared using *o*-DCB display improved device characteristics compared to CB/DIO presumably due to the lower volatility and enhanced solubility of PCBM in *o*-DCB versus CB/DIO which leads to better pore wetting and infiltration. Additionally, $PC_{70}BM$ devices perform better than their $PC_{60}BM$ counterparts, possibly due to improved infiltration and a slower crystallization rate in the COF pores, or as a result of advantageous energy level alignment or enhanced mobility within the pore. The exact reasons for this behavior

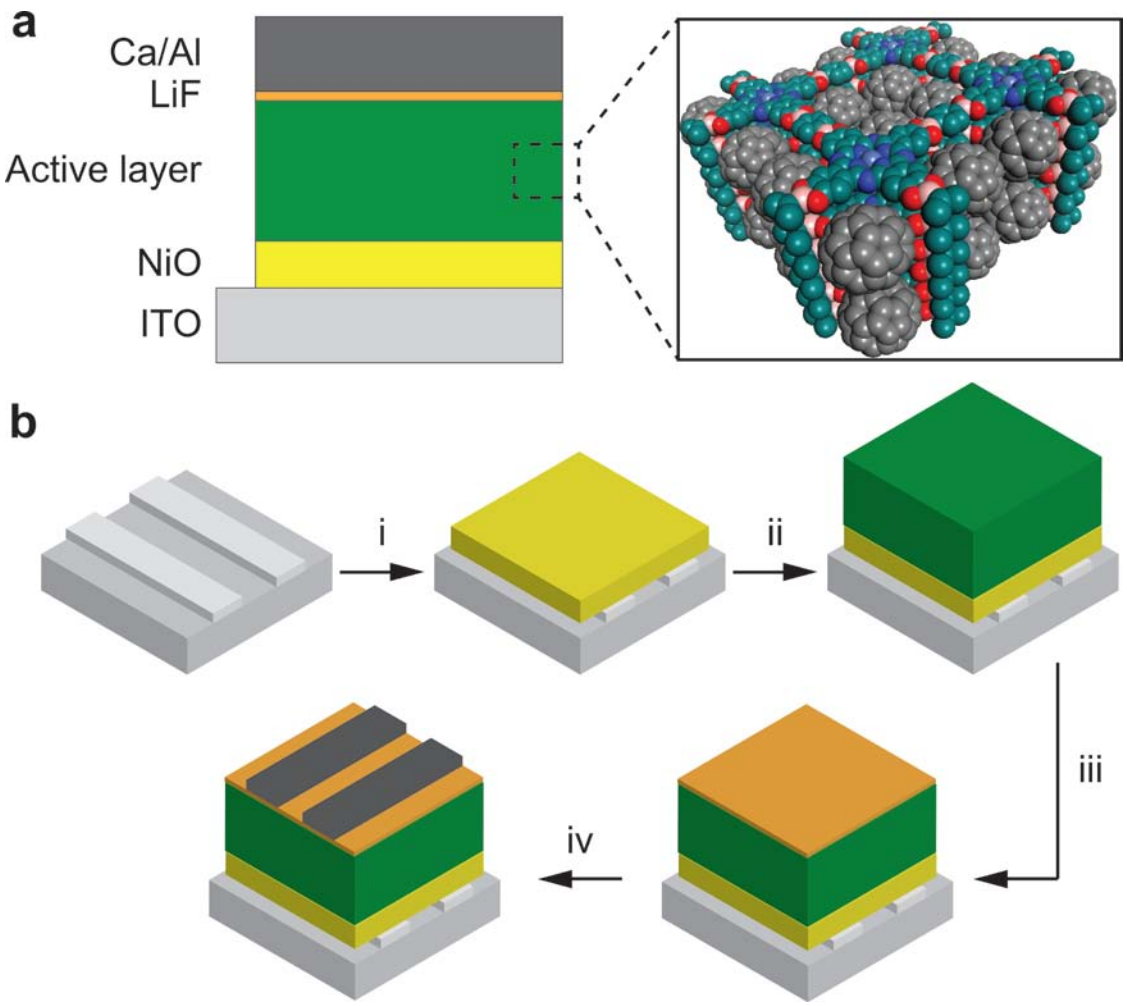

Figure 5.1 | Fabrication and device layout of COF-based OPVs. **a)** Side view of a COF OPV device (left) and the idealized COF/PCBM active layer (right). **b)** General fabrication scheme. Patterned ITO stripes are (**i**) covered with a NiO hole extraction layer, (**ii**) the COF film is grown on the NiO then PCBM is spin-coated on top and annealed, (**iii**) a LiF electron extraction layer is evaporated, and (**iv**) a Ca/Al top electrode is evaporated. The Al/ITO cross hatches define the active device area.

will be the subject of future study. The discussion which follows utilizes devices fabricated with $PC_{70}BM$.

J-V curves and device characteristics for a variety of COF OPVs were measured and their best and average values determined (Fig. 5.2). The open-circuit voltage (V_{OC}), short-circuit current density (J_{sc}), fill factor (FF) and total photocurrent efficiency (PCE) of the best performing COF OPVs are summarized in Table 5.1. These efficiencies are comparable to previously reported COF film OPVs[26]

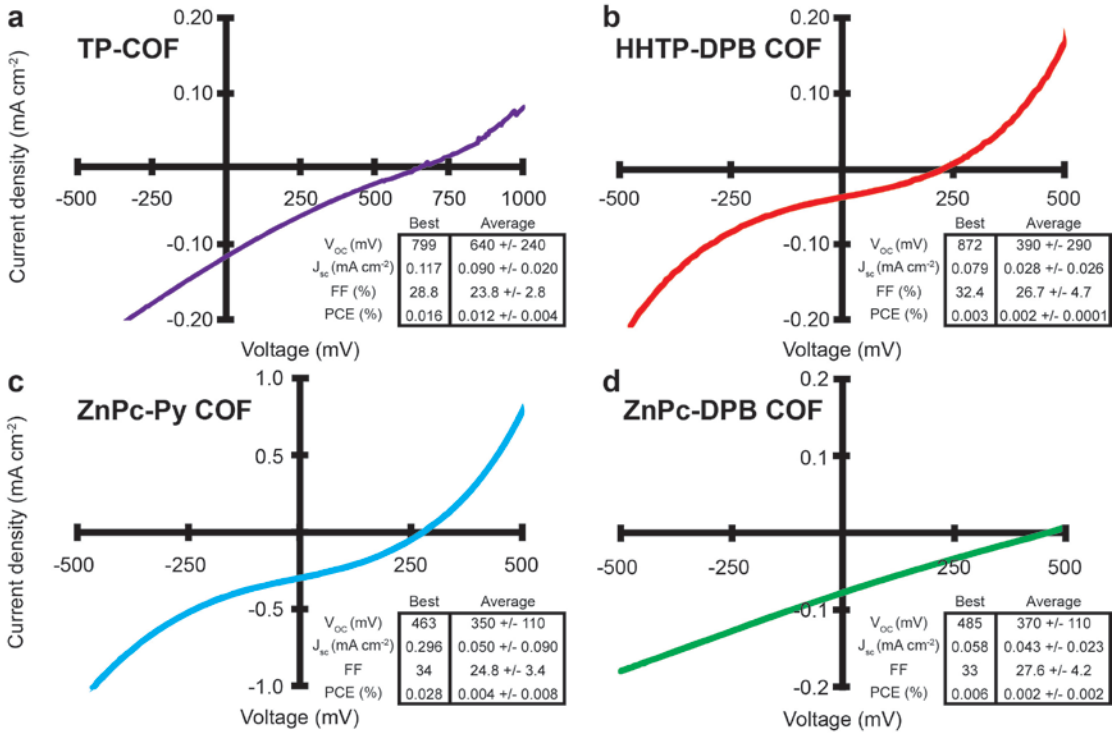

Figure 5.2 | Typical J-V curves and device characteristics of COF OPVs. The highest efficiency devices for **a) TP-COF** (purple), **b) HHTP-DPB COF** (red), **c) ZnPc-Py COF** (blue), and **d) ZnPc-DPB COF** (green) are shown along with best and average measured device parameters.

COF	PCE (%)	V_{oc} (mV)	J_{sc} (mA cm^{-2})	FF
TP-COF	0.016	648	0.117	21.3
HHTP-DPB COF	0.0026	225	0.036	32.4
ZnPc-Py COF	0.028	278	0.296	34.0
ZnPc-DPB COF	0.0064	402	0.067	23.7

Table 5.1 | Key device parameters for the most efficient COV OPVs

but are several orders of magnitude less efficient than devices prepared from COF powders[27] and traditional semiconducting polymer-based devices, which reach efficiencies around 10%[28].

The devices were further characterized by measuring the external quantum efficiency (EQE, Fig. 5.3), which provides information regarding the origin of charge carriers generated in the active layer. For both HHTP-based OPVs, the EQE spectra are nearly identical (Figs. 5.3a,b) and do not overlap with the reported UV-Vis

spectra[20,23], indicating that the observed photocurrent originates from light absorption and charge separation in the PCBM domains and suggesting that these COFs are not mediating long-lived charge separation. However, it is possible that due to limitations in the EQE setup, which cannot measure wavelengths shorter than 300 nm, we are unable to observe some photogenerated current farther into the UV region. In contrast, EQE spectra of Pc-based COF OPVs are broad across the 350 - 500 nm region (**ZnPc-Py COF**, Fig. 5.3c) or 350 - 650 region (**ZnPc-DPB COF**, Fig. 5.3d). These spectra provide evidence that the COFs are generating photocurrent in modest amounts, though the EQE is still dominated by PCBM. The rationale for these observations is still unclear and will be the focus of continued study for these and other COFs.

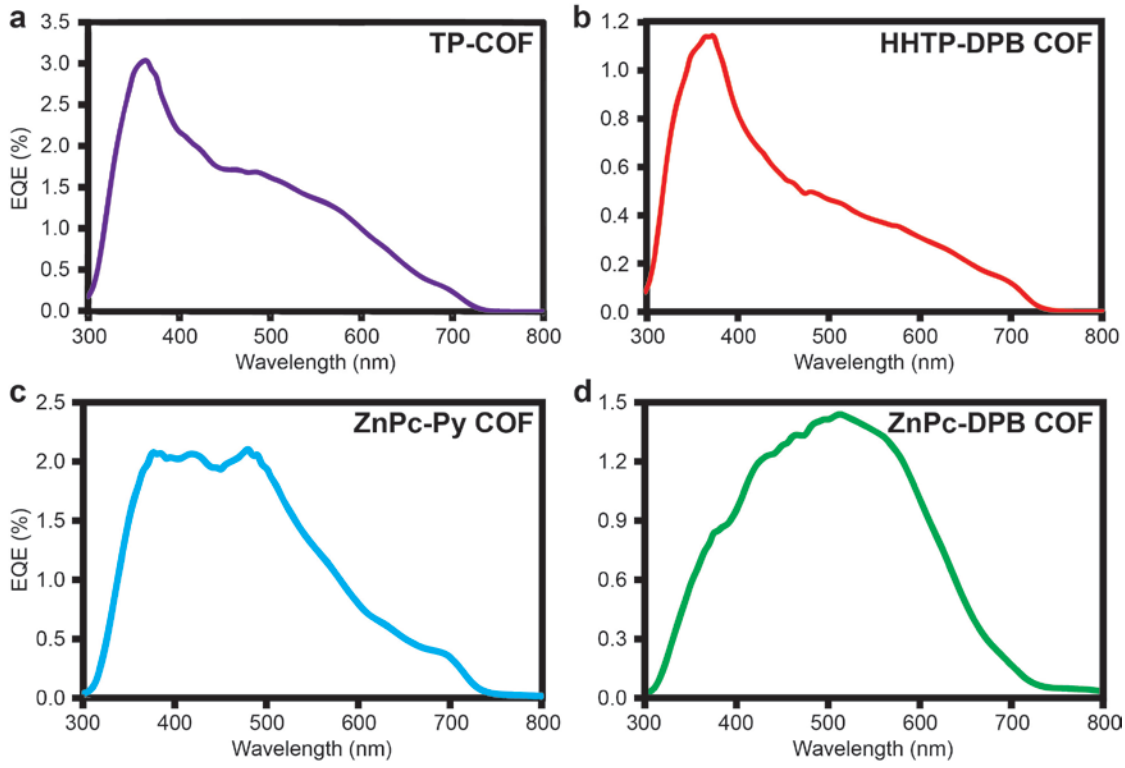

Figure 5.3 | External quantum efficiency of COF OPVs. The EQE of **a) TP-COF** (purple), **b) HHTP-DPB COF** (red), **c) ZnPc-Py COF** (blue), and **d) ZnPc-DPB COF** (green). EQE spectra are measured using the same devices as shown in Figure 5.2

Compared to other semiconducting polymer blends, BHJs prepared with COF films display very low efficiencies, attributable to low short-circuit currents and fill factors. This may result from a partly disordered active layer morphology that contains grain boundaries and impurities within and between layers which can act as charge traps and increase the resistance through the device. Alternatively, the high surface area pore may facilitate significant charge recombination, limiting the number of separated charges that can be collected at the electrodes. Further, it is unknown the extent to which PCBM is penetrating the COF pores, if at all. If the COF/PCBM active layer more closely resembles a bilayer, then many of the photogenerated excitons will be generated too far from the COF/fullerene interface to result in electron transfer. These latter possibilities are less likely, as a fused azine-linked COF recently demonstrated improved current density and a total photocurrent efficiency of ~1%[27].

Interestingly, we observe the open-circuit voltage to vary widely between identical devices. The V_{OC} in OPVs is most strongly dependent on the HOMO-LUMO offset of the donor and acceptor in the active layer, respectively[29,30], though other factors such as temperature, illumination, electrode work function, and active layer microstructure may impact V_{OC}[31]. Because temperature, light intensity, and active-layer blend are identical for a given COF device, we expect V_{OC} to remain constant among devices fabricated with identical COFs, assuming the donor HOMO and acceptor LUMO do not vary dramatically between films. That V_{OC} fluctuates widely between devices suggests that the electrode/active layer and/or donor/acceptor energy level alignment is variable from sample to sample, perhaps due to heterogeneity at the electrode/active layer interface or impurities incorporated throughout the active layer

and in the pores. Both scenarios lead to increased charge trapping and recombination, resulting in a significant decrease in V_{OC}. Further studies to understand the energy level alignment and impact of impurities in COFs and COF/acceptor blends will shed light on this surprising behavior.

Conclusions

Optimizing and improving ncreasing COF photovoltaic devices will depend on fundamental studies of the photophysical processes occurring in the COF active layer. Further work to understand the energy landscape, charge separation processes, carrier lifetimes, and degree of charge trapping will enable rational tuning and device optimization, and may suggest new COF designs which are more amenable to efficient devices. While COF OPVs performance still lags behind traditional BHJ OPVs, the results reported here represent preliminary evidence toward incorporating and evaluating COFs in efficient OPVs.

REFERENCES

1. Thompson, B. C. & Fréchet, J. M. J. *Angew. Chem. Int. Ed.* **47,** 58 (2008).

2. Li, C., Liu, M., Pschirer, N. G., Baumgarten, M. & Müllen, K. *Chem. Rev.* **110,** 6817 (2010).

3. Guo, X., Baumgarten, M. & Müllen, K. *Prog. Polym. Sci.* **38,** 1832 (2013).

4. Barrau, S., Andersson, V., Zhang, F., Masich, S., Bijleveld, J., Andersson, M. R. & Inganäs, O. *Macromolecules* **42,** 4646 (2009).

5. Sanyal, M., Schmidt-Hansberg, B., Klein, M. F. G., Munuera, C., Vorobiev, A., Colsmann, A., Scharfer, P., Lemmer, U., Schabel, W., Dosch, H. & Barrena, E. *Macromolecules* **44,** 3795 (2011).

6. van Bavel, S. S., Bärenklau, M., de With, G., Hoppe, H. & Loos, J. *Adv. Funct. Mater.* **20,** 1458 (2010).

7. Yang, X., Loos, J., Veenstra, S. C., Verhees, W. J. H., Wienk, M. M., Kroon, J. M. Michels, M. A. J. & Janssen, R. A. J. *Nano Lett.* **5,** 579 (2005).

8. Chen, D., Nakahara, A., Wei, D., Nordlund, D. & Russell, T. P. *Nano Lett.* **11,** 561 (2011).

9. Yuan, Y., Zhang, J., Sun, J., Hu, J., Zhang, T. & Duan, Y. *Macromolecules* **44,** 9341 (2011).

10. Lee, J. K., Ma, W. L., Brabec, C. J., Yuen, J., Moon, J. S., Kim, J. Y., Lee, K., Bazan, G. C. & Heeger, A. J. *J. Am. Chem. Soc.* **130,** 3619 (2008).

11. Peet, J., Kim, J. Y., Coates, N. E., Ma, W. L., Moses, D., Heeger, A. J. & Bazan, G. C. *Nature Mater.* **6,** 497 (2007).

12. Li, H., Tang, H., Li, L., Xu, W., Zhao, X. & Yang, X. *J. Mater. Chem.* **21,** 6563 (2011).

13. Gu, Y., Wang, C. & Russell, T. P. *Adv. Energy Mater.* **2,** 683 (2012).

14. Wang, E., Hou, L., Wang, Z., Ma, Z., Hellström, S., Zhuang, W., Zhang, F., Inganäs, O. & Andersson, M. R. *Macromolecules* **44,** 2067 (2011).

15. Lei, T., Wang, J.-Y. & Pei, J. *Chem. Mater.* **26,** 594 (2014).

16. Liu, F., Gu, Y., Shen, X., Ferdous, S., Wang, H.-W., Russell, T. P. *Prog. Polym. Sci.* **38,** 1990 (2013).

17. Côté, A. P., Benin, A. I., Ockwig, N. W., O'Keeffe, M., Matzger, A. J. & Yaghi, O. M. *Science* **310,** 1166 (2005).

18. El-Kaderi, H. M., Hunt, J. R., Mendoza-Cortés, J. L., Côté, A. P., Taylor, R. E., O'Keeffe, M. & Yaghi, O. M. *Science* **316,** 268 (2007).

19. Spitler, E. L. & Dichtel, W. R. *Nature Chem.* **2,** 672 (2010).

20. Spitler, E. L., Koo, B. T., Novotney, J. L., Colson, J. W., Uribe-Romo, F. J., Gutierrez, G. D., Clancy, P. & Dichtel, W. R. *J. Am. Chem. Soc.* **133,** 19416 (2011).

21. Uribe-Romo, F. J., Hunt, J. R., Furukawa, H., Klock, C., O'Keeffe, M.& Yaghi, O. M. *J. Am. Chem. Soc.* **131,** 4570 (2009).

22. Uribe-Romo, F. J., Doonan, C. J., Furukawa, H., Oisaki, K. & Yaghi, O. M. *J. Am. Chem. Soc.* **133,** 11478 (2011).

23. Wan, S., Guo, J., Kim, J., Ihee, H. & Jiang, D. *Angew. Chem. Int. Ed.* **47,** 8826 (2008).

24. Spitler, E. L., Colson, J. W., Uribe-Romo, F. J., Woll, A. R., Giovino, M. R., Saldivar, A. & Dichtel, W. R. *Angew. Chem. Int. Ed.* **51,** 2623 (2012).

25. Colson, J. W., Woll, A. R., Mukherjee, A., Levendorf, M. P., Spitler, E. L., Shields, V. B., Spencer, M. G., Park, J. & Dichtel, W. R. *Science* **332,** 228 (2011).

26. Dogru, M., Handloser, M., Auras, F., Kunz, T., Medina, D., Hartschuh, A., Knochel, P. & Bein, T. *Angew. Chem. Int. Ed.* **52,** 2920 (2013).

27. Guo, J., Xu, Y., Jin, S., Chen, L., Kaji, T., Honsho, Y., Addicoat, M. A. Kim, J., Saeki, A., Ihee, H., Seki, S., Irle, S., Hiramoto, M., Gao, J. & Jiang, D. *Nat. Commun.* **4,** 2736 (2013).

28. Su, Y.-W., Lan, S.-C. & Wei, K.-H. *Mater. Today* **15,** 554 (2012).

29. Brabec, C. J., Cravino, A., Meissner, D., Sariciftci, N. S., Fromherz, T., Rispens, M. T., Sanchez, L. & Hummelen, J. C. *Adv. Funct. Mater.* **11,** 374 (2001).

30. Scharber, M. C., Mühlbacher, D., Koppe, M., Denk, P., Waldauf, C., Heeger, A. J. & Brabec, C. J. *Adv. Mater.* **18,** 789 (2006).

31. Qi, B. & Wang, J. *J. Mater. Chem.* **22,** 24315 (2012).